Advanced applications of Raman spectroscopy and super-resolution imaging of biological and plant materials

by

Sadie Joyce Burkhow

A dissertation submitted to the graduate faculty

in partial fulfillment of the requirements for the degree of

DOCTOR OF PHILOSOPHY

Major: Analytical Chemistry

Program of Study Committee:
Emily A. Smith, Major Professor
Robbyn Anand
Young-Jin Lee
Basil J. Nikolau
Jacob W. Petrich

The student author, whose presentation of the scholarship herein was approved by the program of study committee, is solely responsible for the content of this dissertation. The Graduate College will ensure this dissertation is globally accessible and will not permit alterations after a degree is conferred.

Iowa State University

Ames, Iowa

2021

DEDICATION

This dissertation is dedicated to my dearest Travis and our families (moms, dads, and siblings). Thank you for the love, support, patience, and understanding while I have been discovering my dreams and passions for the past 9 years. I would also like to honorably mention the following subscriptions: Netflix, HBO, Amazon Prime, Hulu, Spotify, and Audible. Without all of you, I would have been lost in the infernal unknown of cable and FM radio.

TABLE OF CONTENTS

ACKNOWLEDGEMENTS

I want to thank my committee chair, Dr. Emily Smith, for the opportunity to be a member of her research group. I would also like to thank my committee members Drs. Robbyn Anand, Young-Jin Lee, Jacob W. Petrich, Basil J. Nikolau, and Robert S. Houk (RHS served as part of my committee for three years) for their guidance and support throughout my time here.

To the Smith group members with whom I had the privilege of knowing and call dear friends: Dr. Deyny Mendivelso-Perez, Dr. Avinash Singh, Dr. Charles Nyamekye, Dr. Brett Boote, Dr. Jon Bobbitt, Danny Freppon, Jingzhe Li, Dr. Chamari Wijesooriya, Dr. Qiaochu Zhu, and Nicole Stephens. Thank you for teaching me so much about chemistry, spectroscopy, professionalism, and camaraderie. I will appreciate the memories and laugher from the "good" Smith group days for the rest of my life. Furthermore, to my cherished best friend Deyny, you have taught me so much about life, love, friendship, food and have helped me grow into the woman I am today. A special thank you to all of my research collaborators (Sangki, Dilini, Amy, Alireza, and Linda) from over the years, you all have taught me so much about your fields of expertise and helped me become very well-rounded and experienced in collaborative work, and it was a real joy to work with you all.

I would also like to thank all those who have helped me discover my true passion, teaching. To the Iowa State University chemistry department for having rigorous teaching assistant training and the many opportunities to be a teaching assistant. To the Preparing for Future Faculty program, which has given me a chance to learn more about my passion and decide the right path for me and giving me all of the resources and tools to do so. I want to especially thank Karen Bovenmyer for all her love, support, and encouragement. You have given me the courage to pursue my passions and opened new doors to others with similar values and

passions. I also would like to thank my exceptional Preparing for Future Faculty mentors, Drs. Joe Burnett and Jake Petrich. I have learned so much about teaching, life as an instructor and faculty member, and so much more.

An incredibly special thank you to Jake. Working and teaching side-by-side as colleagues for a semester was indeed a highlight of my time spent here. Thank you for everything and all the time we spent preparing, discussing, grading, demonstrations, and everything along the way. I will never forget on the very first day of class with you and 200 students watching me almost start the ceiling on fire and then the biggest hydrogen-helium balloon explosion in Gilman demo history. I thought I would be banned from all demonstrations forever, but your excitement, enthusiasm, and laughter ensured me of the opposite. I wish you all the best for the rest of your time here and retirement. You deserve the best of the best.

I would like to thank my family: Mom, Dad, Candice, Megan, Tim, Diane, and Dana, for all the love and support throughout the years, and I love you. To my dearest, loving, and amazing Travis. You are my greatest inspiration and have always encouraged and supported me to find my dreams and passions without any question. We have grown much during my time here, and I am so proud of whom we both have become. I cannot wait for what our future entails, and I love you.

A special thank you to a few persons' pivotal roles on my journey. Without their guidance, I would never have known that this path was available or even an opportunity for me. To Catherine Haslag, my general chemistry instructor at Riverland Community College who suggested to pursue the pre-veterinarian or chemistry program at the University of Wisconsin River Falls because I was unsure about the path forward in my life at that moment and I love animals, so I thought it was a logical path. During the class/degree sign-up day at UW-River

Falls, I realized that I could either go with an Animal Science degree or Pre-Professional Biochemistry degree in pursuance of getting into veterinarian school. At that moment, I decided to go to the chemistry route because I noticed there were so many more chemistry and math classes (which I adored) and went on. It was not until I was almost finished at River Falls when I had to do a research-related class, my academic and research advisor, Dr. Stacey Stoffregen, suggested I think about graduate school for chemistry. I had never known anyone in graduate school, nor anything about it or what it meant. She and many other faculty members suggested Iowa State University, their Ph.D. alma mater, and explained a little more about what it was like. Getting close to finishing at River Falls, I had fallen in love with my chemistry classes and wanted to keep learning more about chemistry and decided to apply to Iowa State University, and now here I am many years and tears later. Without guidance from these two pivotal persons, my path could have ended up very differently, and I wanted to thank them here.

Finally, I would like to thank myself. You have learned so much about yourself during your time here and grown into the woman I believe you are meant to be. You did this incredible feat and persevered even though you would never have thought that you could or that it was even in your realm of possibilities or opportunities. You are a very hard worker, a leader, a friend to many, generous, kind, caring, funny, joyful, a little crazy, and deserve happiness and love in your life. I am so proud of you.

ABSTRACT

Plants are an essential resource for the Earth, yet there is still a significant lack of knowledge about the cells, tissues, and organs of plants compared to the human body. There is a great need for sensitive methods to analyze plants and biological materials to gain an *in situ* understanding of processes at the molecular and cellular level. Raman spectroscopy has many advantages as an analytical method to help fill this knowledge gap: it can differentiate chemical structures with high sensitivity, it is non-destructive, it requires minimal sample preparation compared to many other techniques, and it can reveal quantitative chemical abundances. For these reasons, Raman spectroscopy can non-destructively identify and semi-quantify valuable and essential plant metabolites. In combination with a microscope and mechanized stage, Raman spectroscopy can also reveal the spatial dependence of plant metabolites. In this dissertation, the following three topics are discussed: a developed multimodal imaging method to study gene function in plants, the potential for Raman spectroscopy to infer relative plant metabolite content for optimal harvest, and the prospects of using inorganic semiconductor quantum dots with saturated excitation microscopy for subdiffraction imaging in biological materials. Also four collaborative research projects are discussed that use fluorescence microscopy and Raman spectroscopy to characterize inorganic materials.

The first topic introduces a multimodal imaging method that harnesses Raman spectroscopy and mass spectrometry to reveal the cellular-level biochemical changes from virus-induced gene silencing (VIGS). VIGS is a powerful technique to study gene function, but few tools can study the spatial dependence of its effects at the cellular level. The combined imaging methods uncovered the spatial distribution of the effects from silencing the *phytoene desaturase* gene within maize via the *Foxtail mosaic virus* vector. Raman spectroscopy revealed that the

localized downstream carotenoid expression was reduced in the silenced locations but not eliminated. The complementary mass spectrometry signal for phytoene showed an abundance within the same locations. This is the first instance in which biochemical changes resulting from VIGS at the cellular level were spatially characterized by traditional analytical instrumentation. The imaging method is advantageous for studying plant tissues, including for the biochemical changes that result from gene silencing at the cellular level of expression in stems, leaves, and roots.

The second topic discusses how Raman spectroscopy was developed as a fast and simple alternative method for determining relative plant metabolite abundance *in situ*. The Raman peak area ratio analysis was performed on KI110 and Native spearmint to infer the optimal harvest time for rosmarinic acid extraction. The rosmarinic acid abundance revealed a cellular structure dependence within epidermal cells and trichomes on the adaxial leaf surface. The relative abundance of rosmarinic acid with reference to leaf age was also investigated and found to be statistically different in some instances. A chemometric model was developed to establish a quantitative relationship between Raman and high-performance liquid chromatography (HPLC) analyses of plant leaves and subsequently extracted rosmarinic acid, respectively. This calibration model was built with partial least-squares regression and can relay a quantitative rosmarinic concentration for new plant leaf samples in milligram per gram values. Raman spectroscopy can be a faster alternative to HPLC and has the potential to be used in the field for quick analysis of the relative abundance of rosmarinic acid to harvest with the highest yield.

The third topic introduces the feasibility of using inorganic semiconductor CdSe/ZnS quantum dots (QDs) as a luminescent probe in biological cells with a lab-built saturated excitation (SAX) microscope for subdiffraction imaging. This is the first instance in which these

QDs were tested as a luminescent probe for subdiffraction biological imaging with SAX microscopy. The excitation modulation frequency (ω) was demodulated for signal detection at higher harmonics ($n\omega, n$ = 2, 3, *etc*.). To test the practicality of the QDs, control experiments were completed to mimic the same conditions that were subsequently used for cellular studies that included dried on a glass substrate and an aqueous environment. The QDs revealed different saturation characteristics based upon the sample environment (dried versus aqueous). The dried environment achieved a high harmonic signal with relatively low saturation intensities, but the cellular preparation in a dried environment was not tested. The aqueous environment required the saturation intensity to be very high, which is unfavorable for cellular experiments. The aqueous cells labeled with the QDs was measured and the image constructed using the fundamental frequency; imaging with higher harmonics was not possible without sample damage. This work has laid the foundation for understanding the photoluminescence saturation of these QDs and their compatibility for use within targeted cellular studies to obtain subdiffraction imaging with SAX microscopy.

In summary, this dissertation emphasizes Raman spectroscopy and SAX microscopy for novel application analyses of plants and targeted cellular studies. Two collaborative research works are also reviewed within this dissertation in which fluorescence microscopy and Raman spectroscopy aid in the characterization of inorganic materials and catalysts.

CHAPTER 1. GENERAL INTRODUCTION

Over four-hundred thousand plant species in the world[1] have been identified and studied, and used for many millennia. There is still an incredible number of unknowns about plants and their functions. Plants have been used for a multitude of applications, including building materials, food, heat, pharmaceuticals, *etc*. The tools to study plants are far-reaching, and analytical and genetic techniques are continually evolving. Raman spectroscopy and microscopy supply a method to further explore plants and their properties.

Raman spectroscopy is an analytical technique discovered in 1928 when scientists Krishnan and Raman demonstrated that molecules could have inelastic scattering of light.[2] A fingerprint of molecular functional groups can be ascertained by Raman spectroscopy due to the excitation of vibrational modes, which corresponded to the change in the scattered light frequency. A change in polarizability of the molecule during vibrational excitation must happen for Raman scattering to occur. Since Krishnan and Raman's discovery of inelastic scattering of light, there are now more than 25 different types of known Raman spectroscopy techniques.[3] Companies such as Renishaw, Anton Paar, Horiba, Shimadzu, BaySpec, Kaiser Optical Systems, Thermo Fisher Scientific, and Bruker have commercialized Raman instruments for research and clinical use. Due to this commercialization, the applications of Raman spectroscopy are increasing and far-reaching.[4]

Raman spectroscopy has become a popular characterization technique for biological and plant research areas. Raman spectroscopy is advantageous because it is label-free, reveals chemical and compositional information, and is commonly bridged with microscopy to disclose cellular-level information.[5-6] Raman microscopy or microspectroscopy is often done by coupling traditional Raman instrumentation components and detection with a microscope. Conventional

optical microscopy methods are inherently restricted spatially by Abbe's[7] diffraction limit, $d \approx \frac{\lambda}{NA}$, where λ is the wavelength of light, and NA is the numerical aperture of the microscope objective. Raman microscopy has the same fundamental properties as conventional optical microscopy, however, chemical information that is spatially correlated can be observed. The Raman laser is focused down with an objective to a spot that can be a few hundred nanometers to microns in size. Raman imaging occurs when the sample is raster-scanned, often with a motorized stage, to reveal spatially-correlated chemical information.

Raman spectroscopy has been able to reveal new information about plants, including the quantity and spatial distribution of molecules intrinsic to the plant as well as downstream effects from chemical or mechanical stressors.[6, 8-9] Both qualitative and quantitative chemical information can be acquired about the plants based on the unique pattern within a spectrum. The relative metabolite or plant component concentration can be interpreted from the Raman peak intensity or area. Cellulose and lignin are the two most common plant structural components that are studied extensively in biomass renewable energy applications with Raman spectroscopy.[10] Schulz and Baranska provided an in-depth review of the Raman and infrared spectra of the most commonly studied plant metabolites. They suggested peak assignments for primary and secondary plant metabolites such as proteins, lipids, carbohydrates, phenolic compounds, terpenoids, alkaloids, nitrile compounds, chlorophylls, *etc*.[8]

In Chapters two and three, the plant metabolites, carotenoids, and rosmarinic acid in maize and spearmint, respectively, were investigated with Raman microscopy. Carotenoids notably have three major vibrational modes in a Raman spectrum. The vibrational modes correspond to in-phase stretching vibrations of the C=C bonds at ~1520 cm^{-1}, the stretching vibrations of C-C bonds at ~1150 cm^{-1}, and the C-H stretching modes at ~1000 cm^{-1}.[9, 11-12]

Rosmarinic acid has a distinct Raman peak at ~1600 cm^{-1} which is most representative of the ring C=C stretching vibrations.[13] Raman spectroscopy provided an alternative method to semi-quantitively measure and spatially correlate carotenoids, and rosmarinic acid, in maize and spearmint plants, respectively.

Microscopy techniques, especially fluorescence, are imperative for the study of biological applications. Often within biology and cellular studies, there are crucial phenomena occurring below Abbe's diffraction limit that need to be investigated to further science. Two strategies are commonly used to circumvent Abbe's diffraction limit to do subdiffraction imaging with luminescence. The first strategy is with the use of spatial or temporal modulation of the excitation light. There are several examples of this first strategy, including stimulated emission-depletion (STED),[14] structured illumination microscopy (SIM),[15] saturated structured illumination microscopy (SSIM),[16] plasmonic structured illumination microscopy (PSIM),[17] and saturated excitation (SAX) microscopy.[18-19] The advantages of these techniques include high spatial and temporal resolution; however, the instrumentation is often complex and costly. The second strategy is to use photoswitchable fluorophores to develop iteratively a composite image. Techniques include photo-activated localization microscopy (PALM)[20] and stochastic optical reconstruction microscopy (STORM).[21] These localization strategies also offer high spatial resolution and often cheaper instrumentation, but temporal resolution depends on the photoswitchable fluorophores, which can limit the applications.

Pioneered and popularized by Fujita and coworkers, SAX microscopy provides a straightforward subdiffraction imaging technique.[18-19] The method involves a high intensity modulated excitation source focused tightly on a sample using a microscope. Improved spatial resolution occurs when the fundamental modulation frequency (ω) is demodulated at higher

harmonics ($n\omega, n$ = 2, 3, *etc.*) using a lock-in-amplifier. Spatial resolution improvement is proportional to the saturation degree and is in theory unlimited, but maximum laser power, sample degradation, and detector efficiency are limiting factors.[18] Common luminescent probes for biological applications with SAX microscopy have included fluorescent dyes,[18] gold nanoparticles,[22] and nanodiamonds.[23]

In Chapter 4, SAX microscopy has been extended to the commercially available CdSe/ZnS core-shell quantum dots (QDs) and its utility as a biological luminescent probe. Inorganic semiconductor QDs were some of the first nanotechnologies incorporated into biological applications[24-25] and have proven to be powerful probes for fluorescence cellular imaging.[26-28] Quantum dots are commercially available and are biocompatible for targeted use by conjugating the surface with antibodies, peptides, or small molecules.[29] QDs have not been used previously in SAX microscopy, but they have been used with other imaging techniques and would provide a commercially available and facile label for cellular studies. Two local environments of the QDs were investigated, aqueous and dried, to mimic hydrated and fixed biological environments. HeLa cells were labeled with biotinylated-phalloidin followed by marking with streptavidin-coated QDs in order to measure actin fibers with the fundamental frequency only, due to the high-power requirements for saturation. The luminescent properties and limits of QDs were determined for cellular studies and proved to be useful in fixed environments.

Overview

This dissertation is organized into seven chapters. A brief introduction to plants and the available analytical instrumentation used to characterize them and an introduction to Raman spectroscopy and subdiffraction imaging for biological samples are discussed in Chapter one.

Chapter two discusses the use of Raman spectroscopy and mass spectrometry imaging to characterize virus-induced gene silencing at the cellular level.

Chapter three presents another method using a Raman spectrum to determine the plant metabolite's relative cellular content of rosmarinic acid in spearmint for the best harvest time.

Discussed in Chapter four is a collaborative project led by Dr. Avinash Singh, the post-doctoral student with the Smith research group at the time. A subdiffraction imaging technique was used to investigate the use of inorganic semiconductor quantum dots as a saturated excitation probe and the possibility of its use in biological samples.

Chapters five and six are collaborative research projects at Iowa State University, and I contributed significantly to the overall scientific studies and for each provided items such as: figure(s), literature review, and results and discussion related to the Raman or luminescence measurements.

In Chapter five, methylammonium lead halide nanocrystals were investigated for their photophysical properties by time-correlated luminescence. My specific contribution included data analysis and figure preparation for Fig. 3 (Page 115), 4 (Page 116), S3 (Page 126), and S4 (127). I assisted in writing the text within the materials and methods, starting with "Nanocrystal Luminescence Microscopy" on Page 104 to the results and discussion on Page 106. I also assisted the first author with the revision process with the corresponding author before submission.

The work described in Chapter six explores the catalytic activity of aminopropyl-functionalized silica nanoparticles within aldol condensations and monitoring the effects of hydrophobic environments. My specific contribution included the measurement optimization of all materials, data analysis, and preparation of Figure S6 (Page 160). I searched and reviewed the

literature of similar catalyst materials and data analyses with Raman spectroscopy in the figure legend. I wrote the manuscript text within the “Raman Spectroscopy” of the materials and methods section on Page 133-4, and contributed the text written within the results and discussion on Page 139, ‘Whereas these observations suggest …… Schiff base intermediate 1’.

General conclusions are presented and discussed in Chapter seven.

References

1. Ungricht, S., How many plant species are there? And how many are threatened with extinction? Endemic species in global biodiversity and conservation assessments. Taxon 2004, 53 (2), 481-484.

2. Raman, C. V.; Krishnan, K. S., A new type of secondary radiation. Nature 1928, 121 (3048), 501-502.

3. Jones, R. R.; Hooper, D. C.; Zhang, L.; Wolverson, D.; Valev, V. K., Raman techniques: fundamentals and frontiers. Nanoscale research letters 2019, 14 (1), 1-34.

4. Das, R. S.; Agrawal, Y., Raman spectroscopy: recent advancements, techniques and applications. Vibrational spectroscopy 2011, 57 (2), 163-176.

5. Butler, H. J.; Ashton, L.; Bird, B.; Cinque, G.; Curtis, K.; Dorney, J.; Esmonde-White, K.; Fullwood, N. J.; Gardner, B.; Martin-Hirsch, P. L., Using Raman spectroscopy to characterize biological materials. Nature protocols 2016, 11 (4), 664-687.

6. Gierlinger, N.; Schwanninger, M., The potential of Raman microscopy and Raman imaging in plant research. Spectroscopy 2007, 21 (2), 69-89.

7. Abbe, E., Beiträge zur Theorie des Mikroskops und der mikroskopischen Wahrnehmung. Archiv für mikroskopische Anatomie 1873, 9 (1), 413-468.

8. Schulz, H.; Baranska, M., Identification and quantification of valuable plant substances by IR and Raman spectroscopy. Vibrational Spectroscopy 2007, 43 (1), 13-25.

9. Baranska, M.; Roman, M.; Dobrowolski, J.; Schulz, H.; Baranski, R., Recent advances in Raman analysis of plants: alkaloids, carotenoids, and polyacetylenes. Curr Anal Chem 2013, 9.

10. Lupoi, J. S.; Gjersing, E.; Davis, M. F., Evaluating lignocellulosic biomass, its derivatives, and downstream products with Raman spectroscopy. Frontiers in bioengineering and biotechnology 2015, 3, 50.

11. Schulz, H.; Baranska, M.; Baranski, R., Potential of NIR-FT-Raman spectroscopy in natural carotenoid analysis. Biopolymers 2005, 77.

12. Withnall, R.; Chowdhry, B. Z.; Silver, J.; Edwards, H. G. M.; Oliveira, L. F. C., Raman spectra of carotenoids in natural products. Spectrochim Acta Part A Mol Biomol Spectrosc 2003, 59.

13. Mariappan, G.; Sundaraganesan, N.; Manoharan, S., Experimental and theoretical spectroscopic studies of anticancer drug rosmarinic acid using HF and density functional theory. Spectrochimica Acta Part A: Molecular and Biomolecular Spectroscopy 2012, 97, 340-351.

14. Hell, S. W.; Wichmann, J., Breaking the diffraction resolution limit by stimulated emission: stimulated-emission-depletion fluorescence microscopy. Optics letters 1994, 19 (11), 780-782.

15. Gustafsson, M. G., Nonlinear structured-illumination microscopy: wide-field fluorescence imaging with theoretically unlimited resolution. Proceedings of the National Academy of Sciences 2005, 102 (37), 13081-13086.

16. Haeberlé, O.; Simon, B., Saturated structured confocal microscopy with theoretically unlimited resolution. Optics communications 2009, 282 (18), 3657-3664.

17. Wei, F.; Liu, Z., Plasmonic structured illumination microscopy. Nano letters 2010, 10 (7), 2531-2536.

18. Fujita, K.; Kobayashi, M.; Kawano, S.; Yamanaka, M.; Kawata, S., High-resolution confocal microscopy by saturated excitation of fluorescence. Physical review letters 2007, 99 (22), 228105.

19. Yonemaru, Y.; Yamanaka, M.; Smith, N. I.; Kawata, S.; Fujita, K., Saturated excitation microscopy with optimized excitation modulation. ChemPhysChem 2014, 15 (4), 743-749.

20. Patterson, G.; Davidson, M.; Manley, S.; Lippincott-Schwartz, J., Superresolution imaging using single-molecule localization. Annual review of physical chemistry 2010, 61, 345-367.

21. Rust, M. J.; Bates, M.; Zhuang, X., Sub-diffraction-limit imaging by stochastic optical reconstruction microscopy (STORM). Nature methods 2006, 3 (10), 793-796.

22. Chu, S.-W.; Su, T.-Y.; Oketani, R.; Huang, Y.-T.; Wu, H.-Y.; Yonemaru, Y.; Yamanaka, M.; Lee, H.; Zhuo, G.-Y.; Lee, M.-Y., Measurement of a saturated emission of optical radiation from gold nanoparticles: application to an ultrahigh resolution microscope. Physical review letters 2014, 112 (1), 017402.

23. Yamanaka, M.; Tzeng, Y.-K.; Kawano, S.; Smith, N. I.; Kawata, S.; Chang, H.-C.; Fujita, K., SAX microscopy with fluorescent nanodiamond probes for high-resolution fluorescence imaging. Biomedical optics express 2011, 2 (7), 1946-1954.

24. Bruchez, M.; Moronne, M.; Gin, P.; Weiss, S.; Alivisatos, A. P., Semiconductor nanocrystals as fluorescent biological labels. science 1998, 281 (5385), 2013-2016.

25. Chan, W. C.; Nie, S., Quantum dot bioconjugates for ultrasensitive nonisotopic detection. Science 1998, 281 (5385), 2016-2018.

26. Grecco, H.; Lidke, K.; Heintzmann, R.; Lidke, D.; Spagnuolo, C.; Martinez, O.; Jares-Erijman, E.; Jovin, T., Ensemble and single particle photophysical properties (two-photon excitation, anisotropy, FRET, lifetime, spectral conversion) of commercial quantum dots in solution and in live cells. Microscopy research and technique 2004, 65 (4-5), 169-179.

27. Antelman, J.; Ebenstein, Y.; Dertinger, T.; Michalet, X.; Weiss, S., Suppression of quantum dot blinking in DTT-doped polymer films. The Journal of Physical Chemistry C 2009, 113 (27), 11541-11545.

28. Pechstedt, K.; Whittle, T.; Baumberg, J.; Melvin, T., Photoluminescence of colloidal CdSe/ZnS quantum dots: the critical effect of water molecules. The Journal of Physical Chemistry C 2010, 114 (28), 12069-12077.

29. Rosenthal, S. J.; Chang, J. C.; Kovtun, O.; McBride, J. R.; Tomlinson, I. D., Biocompatible quantum dots for biological applications. Chemistry & biology 2011, 18 (1), 10-24.

CHAPTER 2. CHARACTERIZING VIRUS-INDUCED GENE SILENCING AT THE CELLULAR LEVEL WITH IN SITU MULTIMODAL IMAGING

Sadie J. Burkhow[a], Nicole M. Stephens[a], Yu Mei[b], Maria Emilia Dueñas[a], Daniel J. Freppon[a], Geng Ding[c], Shea C. Smith[d], Young-Jin Lee[a], Basil J. Nikolau[c], Steven A. Whitham[b], Emily A. Smith[a]

[a]The Ames Laboratory, U.S. Department of Energy, and Department of Chemistry, Iowa State University, Ames, IA 50011-3111, USA; [b]Department of Plant Pathology and Microbiology, Iowa State University, Ames, Iowa 50011; [c]Department of Biochemistry, Biophysics, and Molecular Biology, Center for Metabolic Biology, Iowa State University, Ames, IA 50011, USA; [d]Engineering Research Center for Biorenewable Chemicals, Iowa State University, Ames, IA 50011, USA.

Modified from a manuscript published in *Plant Methods* 14.1 (2018): 37, https://doi.org/10.1186/s13007-018-0306-7.

Abstract

Background: Reverse genetic strategies, such as virus-induced gene silencing, are powerful techniques to study gene function. Currently, there are few tools to study the spatial dependence of gene silencing at the cellular level.

Results: We report the use of multimodal Raman and mass spectrometry imaging methods to study the cellular-level biochemical changes that occur from silencing the *phytoene desaturase* (*pds*) gene using a *Foxtail mosaic virus* (FoMV) vector in maize leaves. The multimodal imaging method allows the localized carotenoid distribution to be measured and reveals differences lost in the spatial average when analyzing a carotenoid extraction of the whole leaf. The nature of the Raman and mass spectrometry signals are complementary: silencing *pds* reduces the downstream carotenoid Raman signal and increases the phytoene mass spectrometry signal.

Conclusions: Both Raman and mass spectrometry imaging techniques show that the biochemical changes from FoMV-*pds* silencing occur with a mosaic spatial pattern at the cellular level, and the Raman images show carotenoid expression was reduced at discrete locations but not eliminated. The data indicate the multimodal imaging method has great utility to study the biochemical changes that result from gene silencing at the cellular spatial level of expression in many plant tissues including the stem and leaf. Our demonstrated method is the first to spatially characterize the biochemical changes as a result of VIGS at the cellular level using commonly available instrumentation.

Keywords: RNA Silencing, Foxtail Mosaic Virus, Phytoene Desaturase, Subcellular Raman Imaging, Mass Spectrometry Imaging, Monocots, Whole-plant analysis, Biochemical Characterization, Mosaic Spatial Pattern, Carotenoids

Introduction

Reverse genetics techniques, such as RNA silencing, have been widely used over the past 20 years to generate loss-of function phenotypes that provide insight into the functions of silenced genes. Virus-induced gene silencing (VIGS) is a method of RNA silencing that takes advantage of the plant's natural antiviral defense mechanisms. VIGS requires a modified viral vector that carries RNA or DNA fragments corresponding to the plant target gene(s). The recombinant virus replicates and moves systemically throughout the plant. Meanwhile the antiviral RNA silencing system is activated against the viral genetic template, which also encompasses the target plant gene fragment, resulting in the silencing of the target gene. The use of VIGS technologies addresses the need for rapid and potentially high-throughput methods for testing gene functions in a wide variety of monocot and dicot plant species.[1-11]

Foxtail mosaic virus (FoMV), belonging to the *Potexvirus* genus, was recently developed as a VIGS vector for use in maize and other important monocot crop species such as wheat.[1-2] The genome organization of FoMV and other potexviruses consists of five major open reading frames (ORFs) encoding: RNA polymerase (ORF1), the triple gene block (ORF2-4), and the coat protein (ORF5),[10, 12] all of which are essential for virus survival and function. In addition, FoMV encodes a unique 5A protein that is not essential for replication or viral infection.[12] Mei et al.[1] developed a DNA-based full-length FoMV VIGS vector by inserting a cloning site after the coat protein. This FoMV vector was used to silence *phytoene desaturase* (*pds)* and other genes in sweet corn and the B73 inbred line of yellow dent corn. Silencing *pds* in tobacco leaves has been shown to produce an easily observed variegated white phenotype.[11] The *pds* enzyme along with other desaturases and isomerases convert the colorless phytoene molecule to downstream carotenoids (Fig. 1).[13-18] These downstream carotenoids have multiple conjugated double bonds that lead to the absorption of light in the visible region (~390 to 700 nm). Zhang et al.[19] utilized a *Bean pod mottle virus* VIGS vector to silence *pds* within soybean leaves. They tagged this VIGS vector with green fluorescent protein (GFP), and confirmed via fluorescence that the vector was spatially correlated to the visual mosaic phenotype produced from silencing *pds.*[19] Juvale et al.[20] performed a similar experiment with transgenic soybeans that constitutively expressed a GFP transgene in all tissues to measure GFP VIGS from a *Bean pod mottle virus* vector.[20] They determined that the GFP transgene was uniformly silenced and suggested the differences between their observation and those reported by Zhang et al.[19] may result from silencing a GFP transgene versus endogenous *pds*. While a fluorescent tag can be used to localize the VIGS vector, the fluorescence signal does not reveal downstream biochemical effects occurring from gene silencing.

Raman and mass spectrometry (MS) imaging are complementary analysis techniques in regard to the nature of the signal, the kind of information measured, and the spatial resolution. Raman spectroscopy provides a fingerprint of functional groups within a molecule and is an ideal tool for carotenoid characterization. Raman scattering results when there is a change in photon energy as a result of exciting vibrations in chemical bonds. Resonance Raman spectroscopy (and pre-resonance Raman spectroscopy) occurs when the laser excitation wavelength falls within the range of wavelengths absorbed by a molecule and the result is an enhanced Raman scattering intensity. Raman imaging is a non-destructive technique that can be performed on whole tissue (such as fruit, leaves, stems, roots) or sections of these tissues and provides spatially-localized chemical information for a variety of compounds. The spatial distribution, relative content, and accumulation of carotenoids within plant tissues can be measured by plotting the area of a Raman peak to generate a Raman image.[21-28] These compounds, however, generally need to be abundant to be measured with Raman techniques. MS imaging is suitable to measure low abundance compounds with a greater chemical selectivity, and has become a valuable analytical tool for analyzing the spatial distribution of a wide range of compounds directly on or within plant tissues.[29-32] Matrix-assisted laser desorption/ionization (MALDI) imaging provides high sensitivity, and chemical versatility. Nanoparticles are efficient matrices for small molecule analysis using MALDI-MS imaging due to their low or negligible matrix background, homogeneous application, and high laser absorption.[33] In particular, silver nanoparticles have been commonly used for analyte cationization of various molecules, such as cholesterol, fatty acids, and other olefin-containing molecules.[34-36]

Herein, a combined Raman and MS imaging approach is presented for the measurement of the cellular spatial dependence of *pds* silencing using the FoMV vector developed by Mei et al.[1] in the leaves of the maize sweet corn variety Golden × Bantam. The goal of this work is to gain a cellular level understanding of a VIGS phenotype using the downstream biochemical changes in carotenoid expression that occur from silencing *pds*. We present a useful methodology suitable to study the spatial dependence of gene silencing at the cellular level using any VIGS virus targeting genes that produce a unique biochemical signature within leaf and stem tissues.

Materials and Methods

FoMV-pds Silenced, FoMV, & Non-Inoculated Sweet Corn Line Golden × Bantam Plants.

Plants were grown and inoculated as described by Mei et al.[1] Plants were grown in a 20 to 22 ºC greenhouse with a 16-h photoperiod. A Biolistic PDS-1000/He system was utilized to inoculate one-week-old plants by particle bombardment with FoMV infectious clones (Bio-Rad Laboratories). The biolistic inoculation used 1 µm gold particles coated with 1 µg of FoMV plasmid DNA at 1100 p.s.i. to rupture disks from a distance of 6 cm. Plants were placed in the dark for 12-h before and after bombardment with the FoMV infectious clones. The infected leaves were ground to sap with 50 mM phosphate buffer (pH 7) and then rubbed onto plants with 600-mesh Carborundum at the two-leaf stage. The rub-inoculated plants were considered the "FoMV-*pds* silenced" plants. The "FoMV" plants were rub-inoculated with the FoMV vector without the sequence encoding the *pds* gene. "Non-Inoculated" plants were not inoculated with the FoMV vector. The following titles FoMV-*pds*, FoMV, and non-inoculated will be used throughout this work to describe the three sample types. Plants were approximately 5-6 weeks old or at the 5-9 leaf stage when measurements were completed. For all imaging experiments, the total leaf length was measured and the position representing half of the total leaf length was used

for measurements. For full information about the VIGS system see Mei et al.[1] Quantitative reverse transcription polymerase chain reaction (aRT-PCR) was used to determine the effectiveness within FoMV-*pds* silenced leaves. In leaves where the variegated phenotype was observed, there was a significant reduction (13.5% to 27.6%) of *pds* expression when compared to the FoMV or non-inoculated leaves.[1] The VIGS methodology is also described in Mei et al.[37]

Transverse Cross Sections of Maize Leaves.

A Leica CTI cryostat was utilized to section the leaves to 45 µm thickness. Leaves 5 and 6 were manually cut with a scalpel into 5 to 8 cm samples at the half leaf length position. The FoMV-*pds* silenced leaves were sectioned at the highest abundance of variegated white areas at the half leaf length position. The cut samples were flash frozen in liquid nitrogen for 30 seconds. The fixed tissues were placed vertically in the cryostat base molds which were filled halfway with distilled water. The samples were left in the cryostat set at -23ºC until the water was frozen. Sectioned samples were placed onto a microscope slide with a drop of distilled water, sealed with a glass coverslip and clear nail polish. Samples were stored in the dark and analyzed within 12 hours of being sectioned.

Fractured Maize Leaves.

Leaves were prepared as outlined previously by Klein et al.[38] Leaves 5 and 6 were manually cut with a scalpel into 3 to 5 cm samples at the half leaf length position. The cut samples were placed on packing tape and vacuum dried. Once dried, the packing tape was folded over, passed through a rolling mill, and the two halves of the leaf were separated.

***Mass Spectrometry (MS) Imaging*.**

The fractured maize leaves were subject to matrix deposition by sputter coating (108 Auto Sputter Coater, Ted Pella INC, Redding, CA, USA) silver at 40 mA for 10 seconds. MS imaging data were collected using a MALDI-linear ion trap (LIT)-Orbitrap mass spectrometer (MALDI-LTQ-Orbitrap Discovery; Thermo Finnigan, San Jose, CA, USA). The instrument was modified to incorporate an external 355-nm frequency tripled Nd: YAG laser (UVFQ; Elforlight, Daventry, UK). TunePlus and XCalibur (ThermoFisher Scientific) were used to define imaging parameters and to acquire data, respectively. Mass spectra were acquired with 10 laser shots per spectrum in positive ion mode using an Orbitrap mass analyzer (resolution 30,000 at m/z 400) for an *m/z* scan range of 100-1,000 and using a 20 µm raster step size. MS images were generated using ImageQuest (ThermoFisher Scientific) with a mass window of ± 0.003 Da. The observed and imaged peak is a silver adduct, $[M+^{107}Ag]^{+}$. MS/MS analysis was performed on a different region of the fractured leaf tissue to the one used for MS imaging. The ion-trap analyzer was used for MS/MS of selected ions with a mass window of 1.5 Da and a normalized collision energy of 35 (arbitrary units). No downstream carotenoids were detected by MS imaging for any of the maize leaves using these experimental conditions suitable for detecting phytoene.

Raman Imaging.

All Raman measurements were performed using a commercially available XploRA Plus Raman confocal upright microscope with a Synapse EMCCD camera (HORIBA Scientific, Edison, New Jersey). An Olympus objective (20×-magnification, 0.4-numerical-aperture) was used to collect images in the epi-direction with a 1200 grooves/millimeter grating and a 1450 cm^{-1} center wavelength, and a 100 µm confocal pinhole. A 532-nm solid-state diode laser produced an 800 W/cm^2 laser irradiance, unless otherwise noted. A 75×50 mm XYZ translational stage

and a step size of 3 μm was utilized for all Raman images. The size (and acquisition time) for the *in situ* whole leaf, leaf transverse cross sections, and fractured leaf Raman images were 50×100 μm (15 s), 120×238 μm (5 s), and 50×50 μm (15 s), respectively. Two measurements per leaf and two separate leaves were measured for each plant type (FoMV-*pds*, FoMV, and non-inoculated). A total of 12 images were collected for the *in situ* whole leaf and leaf transverse cross sections. For the fractured leaf images, 2 areas on each side of the fractured leaf at the half leaf length location were collected for each plant type with a total of 12 images collected. White light optical images of the same area corresponding to the Raman images were collected using the same instrument. ImageJ was used to analyze optical images.

Igor Pro 6.36 (WaveMetrics, Inc., Lake Oswego, OR) scientific analysis and graphing software was used to process the Raman spectra. A Gaussian function with a constant baseline was used to batch fit and extract the ~1520 cm^{-1} peak amplitudes and maxima. In order to generate Raman images, an automated method applied two criteria to the output of the resulting Gaussian fit functions: the peak maximum was between 1515 to 1530 cm^{-1}, and the peak intensity had to be larger than three times the standard deviation of the noise. The noise was quantified within the region of 500 to 600 cm^{-1} where no spectral peaks are located. If any of the criteria were not met, the corresponding pixel was assigned null (a gray pixel) within the Raman image. The Raman images were plotted using a custom MATLAB 2016b script. All reported uncertainties represent one standard deviation.

Histograms of the ~1520 cm^{-1} peak maximum were compiled for all spectra in four Raman images (*in situ* whole leaf and transverse leaf transverse cross sections) or two images (each side of fractured leaf). The bin width of the histogram was 1 cm^{-1}, and was fit to a Gaussian function to obtain the reported distribution mean.

Standard and Supplement Raman Measurements.

ß-carotene (Sigma-Aldrich) and phytoene (Toronto Research Chemicals) standards were diluted to 0.01 mg/mL in chloroform for absorbance and fluorescence measurements. Absorbance measurements were performed on an Agilent 8453 UV-visible spectrophotometer. Fluorescence measurements were carried out on an Agilent Cary Eclipse spectrophotometer. The excitation wavelength for fluorescence measurements was 291 nm for phytoene and 464 nm for ß-carotene. For Raman measurements, the pure standards were diluted to 0.25 mg/mL in chloroform and 3 µL were drop casted (solvent evaporated) onto a clean (soaked in isopropanol and dried under a nitrogen flow) glass microscope cover slip. Raman spectra were collected with a 3 s acquisition, 2 accumulations and 1.66 W/cm^2 laser irradiance.

Lutein (Nature's Bounty©), zeaxanthin (Swanson Ultra©), lycopene (Spring Valley©), and ß-carotene (Nature's Bounty©) liquid capsule dietary supplements were purchased from local retailers. Raman measurements required the contents of an individual capsule to be emptied onto a microscope slide. To collect the Raman spectrum of the supplement mixture, an equal volume of all the supplements was mixed together. The acquisition parameters were: 10 s acquisition, 2 accumulations and 1.66 W/cm^2 laser irradiance.

Results and Discussion

Carotenoid Characterization by Raman Spectroscopy

Raman spectra of phytoene and ß-carotene standards were measured to understand the Raman signal of these compounds and ultimately to enable the interpretation of the Raman images obtained from the maize leaves. The Raman spectrum of phytoene, when collected with a 532 nm laser, showed only a broad background and no Raman peaks (Fig. 2A), whereas the Raman spectrum of ß-carotene showed peaks that are characteristic of carotenoids (Fig. 2B). There were three major vibrational modes (ν) in the Raman spectrum of carotenoids.[22, 26, 39-42]

The most intense ν_1 band corresponded to the in-phase stretching vibrations of C=C bonds, and occurred between 1512 to 1524 cm^{-1}. The ν_2 band corresponded to the stretching vibrations of C-C bonds, and occurred at approximately 1150 cm^{-1}. The lowest intensity ν_3 band corresponded to the C-H stretching modes, and occurred at approximately 1000 cm^{-1}. The absorption spectra reveal the reason for the differences in the Raman spectra measured for phytoene and ß-carotene. Phytoene does not absorb 532 nm light (Fig. 2C) and thus does not exhibit resonant enhancement of the Raman signal, whereas ß-carotene does absorb 532 nm light (Fig. 2D) and will exhibit an enhanced Raman signal, as will any carotenoid that absorbs the excitation wavelength.

Carotenoid supplements were utilized to determine how the Raman peaks were affected by their varying chemical structure (Fig. 2E). All the analyzed carotenoids absorbed 532 nm light to varying extents (Supplemental Fig. S1, Additional File 1) and produced a strong Raman signal under these experimental conditions. There were few differences in the Raman peaks below 1450 cm^{-1}. There were, however, differences in the ~1520 cm^{-1} peak maximum, and these may allow changes in carotenoid mixtures to be identified by Raman spectroscopy. The ~1520 cm^{-1} peak maximum depended on the degree of conjugation as well as the substituents on the tetraterpenoid backbone of the carotenoid. Lycopene and ß-carotene possess 11 conjugated double bonds and no hydroxyl substituents and yielded a peak maximum at 1512 to 1513 cm^{-1} (Fig. 2E). The chemical structure of zeaxanthin and lutein have two hydroxyl substituents and the peak maximum was observed at 1521 and 1524 cm^{-1}, respectively (Fig. 2E). The spectral resolution of the Raman instrument determined whether the peak maxima can be distinguished. The instrument used to collect the Raman images in this work had a 5 cm^{-1} spectral resolution based on a spectral calibration with a Ne lamp. Thus, within the same spectrum ß-carotene or lycopene peak maxima could be distinguished from lutein or zeaxanthin. A mixture of all four

supplements had a peak maximum at 1521 cm^{-1} with a Gaussian peak shape and no evidence of spectrally overlapping peaks (Fig. 2E). For carotenoid mixtures, the peak maximum is expected to depend on the chemical composition and concentration of the constituents.

Cellular Spatial Distribution of Carotenoids: Whole Leaf Measurements

Overlays of the optical (white light illumination) and Raman images collected *in situ* on whole leaves are shown in Fig. 3A and Supplemental Fig. S2, Additional File 1. The intensity of the ~1520 cm^{-1} carotenoid peak was the largest and used to generate the Raman images to ensure the best sensitivity. The cell types visualized in the optical images were epidermal and guard cells. The white, primarily horizontal, stripes observed in all the optical images were only visible when the light was illuminating the leaf on the same side as the detector (epi-illumination) as opposed to when the illumination and detector were on opposite sides (trans-illumination) (Supplemental Fig. S4, Additional File 1). This indicated the striped features were generated from light reflection or scattering from the exterior (cuticle) layer of the leaf. A representative camera image of the FoMV-*pds*, FoMV, and non-inoculated leaves with *pds* silenced areas outlined within the FoMV-*pds* plant type is shown within Supplemental Fig. S5, Additional File 1). Within the FoMV-*pds* silenced leaf, the carotenoid signal was not measured in most of the pixels at the bottom of the image where the FoMV mosaic pattern was visually observed (Fig. 3A). (Optical images of the areas adjacent to where the Raman images were collected are shown in Supplemental Fig. S3, Additional File 1). This indicated a reduction in carotenoid expression within these measured areas. The few pixels that showed a carotenoid signal in the variegated white phenotype area were located where the scattering/reflection of light at the leaf surface was the lowest and may represent areas where the excitation light penetrates farther into the plant tissue. For the FoMV and non-inoculated samples (Fig. 3A), the carotenoid signals were

distributed more evenly throughout the Raman image. The peak maximum histograms for the FoMV-*pds* silenced, FoMV, and non-inoculated leaves (Fig. 3B) had a mean ranging from 1521 to 1522 cm^{-1}, suggesting when carotenoids were present there was a similar carotenoid composition.

Cellular Spatial Distribution of Carotenoids: Transverse Cross Sections and Leaf Fractures

As mentioned above, the excitation laser may have probed through different tissue depths at different locations on the leaf, and the *in situ* whole leaf measurements were not ideal for obtaining information about internal cellular structures including the mesophyll and vascular bundles. Raman images of transverse cross sections of the leaf revealed the internal cellular structures (Fig. 4). Each image showed at least two vascular bundles with the surrounding mesophyll, and epidermal cells present on the left and right of the vascular bundles (Fig. 4A). The FoMV and non-inoculated optical and Raman images of the transverse cross sections showed a correlation between chloroplast location and carotenoid signal. The overall carotenoid signal from replicates of the same plant type (FoMV-*pds*, FoMV, and non-inoculated) (Supplemental Fig. S6, Additional File 1), showed extreme variability, for this reason all conclusions were based on the data obtained for the *in situ* whole and fractioned leaf. The correlation of chloroplast location and carotenoid signal were in agreement with the location of carotenoid biosynthesis.[43] The ~1520 cm^{-1} peak maximum histograms generated from the transverse cross section data (Fig. 4B) were consistent with the values obtained for the *in situ* whole leaf measurements (Fig. 3B) with a distribution maximum between 1521 to 1522 cm^{-1}, indicating a similar carotenoid composition is present within the internal cellular contents on the leaf.

Complementary Raman and Mass Spectrometry Imaging of Fractured Maize Leaves

Fracturing the leaves provided a way to consistently correlate the Raman signal from internal leaf structures and the visible phenotype observed from the exterior of the leaf, although some cellular structures may have been altered from the fracturing process (Fig. 5). Raman images collected on the variegated white areas of the FoMV-*pds* silenced fractured leaves showed low, but not zero, levels of carotenoid Raman signal (Fig. 5A); whereas the green areas (Fig. 5B) showed carotenoid signals consistent with the FoMV (Fig. 5C) and non-inoculated (Fig. 5D) fractured leaves with a moderately uniform carotenoid signal. The ~1520 cm^{-1} peak maximum histogram mean ranged from 1523 to 1525 cm^{-1} for the FoMV-*pds* silenced, FoMV, and non-inoculated fractured leaves.

Phytoene did not produce an appreciable Raman signal with the experimental conditions used for this study, therefore MS imaging was used to detect phytoene and confirm the spatial localization within the fractured leaves. A sputter coated silver matrix was used for detection. The *m/z* assignment (*m/z* 651.405, $[M+^{107}Ag]^+$) was based on accurate mass measurement, and confirmed by MS/MS [44] (Supplemental Fig. S7, Additional File 1). Low phytoene signal was present in the MS image of the FoMV and non-inoculated fractured leaf, indicating there was no appreciable buildup of phytoene (Fig. 6). On the contrary, there was a specific localization of phytoene signal within the FoMV-*pds* silenced fractured leaf originating from the accumulation of phytoene.

High performance liquid chromatography (HPLC) was performed on the leaf samples to quantify the concentration of selected carotenoids (Supplemental Table S1, Additional File 1). The concentration of phytoene extracted from the FoMV-*pds* leaf and analyzed by HPLC was 0.4 ± 0.2 µg/g of fresh weight (extraction method see Additional File 1). Phytoene was not

detected by HPLC in the extract of the non-inoculated leaves and was measured at a very low concentration 0.011 ± 0.005 µg/g of fresh weight within two of the replicates for the FoMV leaf. (The HPLC instrumentation limit of detection for phytoene was 0.003 µg/g of fresh weight.) The quantification performed with the extract was consistent with the MS images that showed a very low phytoene signal across the FoMV and non-inoculated leaf. The downstream carotenoids (Fig. 1) measured in the non-inoculated leaf were: lutein (61 ± 3 µg/g), α and ß-carotene (22 ± 1 µg/g), violaxanthin/neoxanthin (10 ± 2 µg/g), and zeaxanthin (7 ± 5 µg/g). Comparing the FoMV leaf to the non-inoculated leaf, the only statistically significant difference ($p < 0.05$) was a lower concentration of α and ß-carotene within the FoMV leaf. Comparing the FoMV-*pds* leaf to the non-inoculated leaf there were no statistically significant differences in the downstream carotenoid concentrations. This observation justifies a need for chemical imaging to provide biochemical information at specific spatially-correlated locations to measure changes in the local carotenoid expression that were lost in the spatially-averaged signal that is obtained from the extract analysis.

Discussion

The most common method used to analyze the effectiveness of VIGS is quantitative reverse transcription polymerase chain reaction.[1, 9] The mRNA transcript levels are generally measured using a large amount of tissue (i.e., spatially averaged) and are reported as a percentage change relative to non-inoculated tissue. While visual inspection of the plant tissue can reveal the macroscopic variegation that results from *pds* silencing, such a simple analysis cannot reveal details at the cellular level, provide information about specific biochemical compounds, nor easily differentiate varying low levels of response. Typical methods used to analyze VIGS, including qRT-PCR, are unequivocally the go-to analysis for determining gene

silencing, but these techniques are not able to reveal downstream biochemical effects occurring as a result of VIGS at the cellular level. FoMV-*pds* suppresses expression of the mRNA transcripts encoding the *pds* enzyme and this is expected to result in the accumulation of the colorless phytoene in leaves.[11, 45] The accumulation of phytoene cannot be detected by a visible phenotype. The analysis of the extracted carotenoids from these leaves demonstrates an increase in phytoene within the FoMV-*pds* silenced leaf. MS imaging revealed an increased phytoene signal that was spatially correlated within the FoMV-*pds* plants. The phytoene signal is spatially localized within the variegated areas of the fractured leaves of the FoMV-*pds* silenced leaves (Fig. 6), which agrees with the reduced carotenoid Raman signal within the same area (Fig. 5). The FoMV and non-inoculated fractured leaf MS images display a low non-localized phytoene signal. Even though *pds* silencing does not result in the complete elimination of the expression within FoMV-*pds* tissues,[1] the multimodal imaging technique still measures the biochemical changes in carotenoid expression that occurred from the achieved level of gene silencing. The measurable changes are expected to be easier to quantify by the outlined imaging approach presented here when the silencing levels are higher.

The carotenoid extract shows no statistically significant differences in any of the carotenoids measured by HPLC when comparing the non-inoculated and FoMV-*pds* leaves. This is not surprising when considering the mosaic pattern of infection and *pds* silencing only affects a small area of the overall leaf. It is difficult to quantify small differences in the bulk of the extracted components. Imaging approaches, on the other hand, allow for a localized distribution to be measured and reveal spatially-correlated differences lost in the average when analyzing an extraction. The percentage of pixels that have a detectable carotenoid signal within the Raman images for the FoMV-*pds* silenced *in situ* whole leaves is 22 ± 5% (n=4) in the areas measured.

The percentage of pixels that have a detectable carotenoid signal for FoMV and non-inoculated *in situ* whole leaves are 57 ± 9% and 70 ± 10%, respectively. The fractured leaf images reveal similar results. The percentage of pixels that have a detectable carotenoid signal for FoMV-*pds* silenced, FoMV, and non-inoculated fractured leaves are 22 ± 2% (n=2), 99.1 ± 0.3%, 80 ± 8%, respectively. Within the region that produces a visible mosaic phenotype, the carotenoid expression is reduced but not eliminated and is most evident in the fractured leaf images.

The most abundant downstream carotenoids reported in the literature for the leaves of maize and other monocots are lutein, ß-carotene, and violaxanthin.[46-50] The extracted carotenoids measured by HPLC are (in order of abundance): lutein, □ and □-carotene, violaxanthin/neoxanthin, and zeaxanthin. Other carotenoids may also be present as a comprehensive HPLC analysis has not been performed. The histograms of the ~1520 cm^{-1} Raman peak maximum provide information about the nature of the carotenoids present. The 1521 to 1522 cm^{-1} peak maximum measured for the *in situ* whole leaf and transverse cross section is consistent with a mixture consisting of primarily lutein and ß-carotene. The fractured leaves have a 1 to 5 cm^{-1} higher mean peak maximum compared to the *in situ* whole leaf and transverse cross section measurements, which is not likely the result of biologically relevant differences in chemical compositions since the same samples were analyzed for the three leaf preparation methods. Carotenoids are susceptible to oxidation, especially if the plant is under stressors including excess light or dehydration,[51-55] The preparation of a fractured leaf requires dehydration, unlike the other two sample preparation methods, and oxidation of the carotenoids upon fracturing the leaf may explain the shift in the peak maximum to higher wavenumbers.

Raman and MS imaging are complementary imaging approaches in many aspects: (1) non-destructive versus destructive sampling; (2) subcellular resolution of ~1 µm versus a cellular

resolution of ~10 μm; (3) knowledge of functional groups present versus the mass of the molecules present; and (4) molecular sensitivity to resonance with the excitation laser for Raman imaging versus a high ionization efficiency with MS imaging. Whereas the differential sensitivity of MS imaging enables the imaging of phytoene, the precursor to downstream carotenoids, Raman imaging provides high selectivity for downstream carotenoids.

Conclusions

In summary, a multimodal Raman and MS imaging method has been successfully demonstrated in the current study to measure the spatial dependence of gene silencing at the cellular level. This information is vital in gaining a complete understanding of the loss-of function phenotypes produced by VIGS. The most common analysis of VIGS efficacy provides an average percentage change in the mRNA levels with no spatial correlation at the cellular level. We report in regions of the leaf that show a visible mosaic phenotype, the carotenoid expression is reduced but not completely eliminated. The presented multimodal imaging approach will be useful to study the silencing of plant genes that produce a unique biochemical signature even if the gene silencing does not produce a visible phenotype. If the phenotype is not visible, it is advisable to sample multiple locations, possibly multiple tissues, to ensure heterogeneous biochemical responses are measured. We have measured up to six locations on the same leaf (data not shown) without observing any signal degradation, and more measurements should be possible on the same leaf. Our proof-of-concept study used the common VIGS marker gene, *pds*, which is easily detected by the characteristic variegated phenotype. We propose our method should be used in conjunction with gene expression analysis (e.g., qRT-PCR) to confirm that gene silencing was successful. The imaging approach can then be applied to measure resulting biochemical changes that result from the reduced gene expression. For example, the resulting biochemical changes may be measured for plant genes that alter the synthesis of lignin,

cellulose, or carotenoids. Raman and MS imaging [56] can provide spatially-correlated biochemical compositions in the leaf, and stem of monocots (Supplemental Fig. S9, Additional File 1) and dicots (Supplemental Fig. S10, Additional File 1). In addition, the presented approach will also be useful for measuring biochemical changes that result, for example, from biotic and abiotic stresses.

Declarations

Acknowledgements

The WM Keck Metabolomics Research Laboratory (Iowa State University, Ames, IA) is acknowledged for providing access to instrumentation and discussion in the HPLC-DAD-MS analyses. SJB, NMS, DJF and EAS are supported by and thank the U.S. Department of Energy, Office of Science, Office of Biological and Environmental Research (BER) through the Ames Laboratory. The Ames Laboratory is operated for the U.S. Department of Energy by Iowa State University under Contract No. DE-AC02-07CH11358. MED, GD, YJL, and BJN are supported by and thank BER through award DESC0014038 to Iowa State University. YM and SAW are supported by the Iowa State University Plant Sciences Institute and the USDA NIFA Hatch Project No. 3808.

Figures

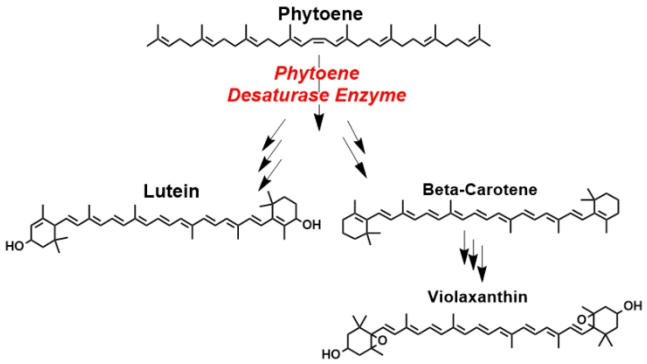

Fig. 1. Simplified carotenoid biosynthesis pathway in higher plants: phytoene (absorption & emission λ, 291, 360 nm, respectively), ß-carotene (absorption & emission λ, 465, 542 nm, respectively), lutein (absorption & emission λ, 456, 525 nm, respectively), and violaxanthin (absorption & emission λ reported by Gruszecki et al. [57], 410, 555 nm, respectively).

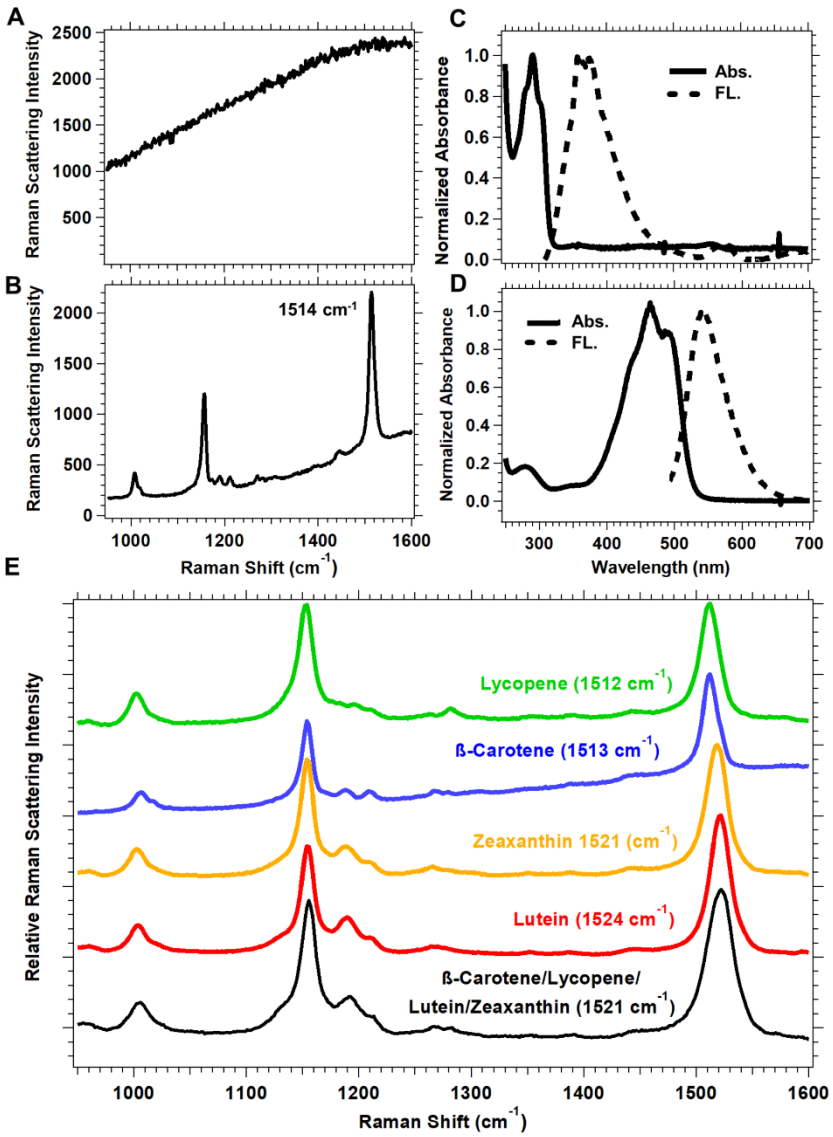

Fig. 2. Spectra of selected carotenoid (A-D) standards and (E) supplements. (A) Raman and (C) absorption and fluorescence spectra of phytoene. (B) Raman and (D) absorption and fluorescence spectra of ß-carotene. The phytoene absorption maximum is ~291 nm, which is not resonantly enhanced with a 532 nm laser, leading to a lack of peaks in the Raman spectrum. (E) Raman spectra of lycopene, ß-carotene, zeaxanthin, lutein, and a mixture of the supplements with corresponding peak maxima.

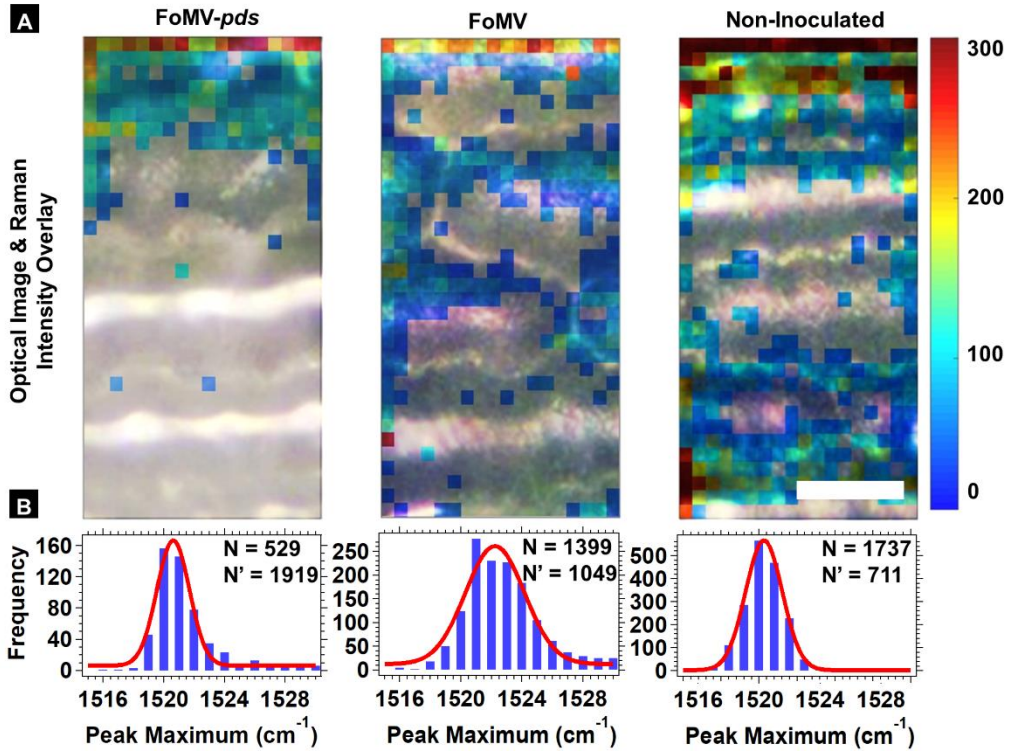

Fig. 3. (A) Merged optical and ~1520 cm^{-1} Raman images of *in situ* whole maize leaves. From left to right the images correspond to FoMV-*pds* silenced, FoMV, and non-inoculated leaves. The color scale at right represents the Raman scattering intensity and is the same for all images. The scale bar is 25 µm and is the same for all images. (B) Histograms of the ~1520 cm^{-1} peak maximum were generated from each pixel in the Raman images shown in (A) and Supplemental Fig. S2, Additional File 1. The histograms were fit to a Gaussian function (red solid line). N is the number of pixels that were positive for carotenoids and N' is the number of pixels that were null (not included in the histogram). Additional *in situ* whole leaf Raman images are shown in Supplemental Fig. S2, Additional File 1, and optical images of an expanded area around where the Raman images were collected are shown in Supplemental Fig. S3, Additional File 1.

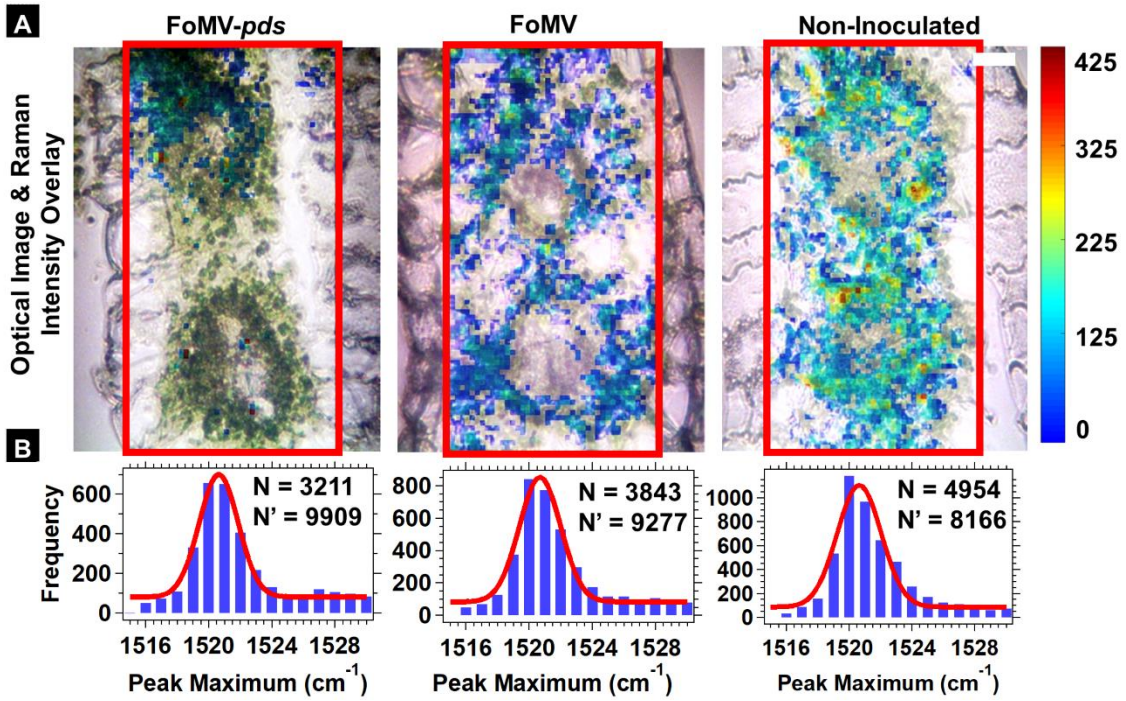

Fig. 4. (A) Merged optical and ~1520 cm^{-1} Raman images (outlined in red) of maize leaf transverse cross sections. From left to right the images correspond to FoMV-*pds* silenced, FoMV, and non-inoculated leaves. The color scale represents the Raman scattering intensity as shown in the scale at right. The scale bar is 25 µm. (B) Histograms of the ~1520 cm^{-1} peak maximum were generated from each pixel in the Raman images shown in (A) and Supplemental Fig. S6, Additional File 1. The histograms were fit to a Gaussian function (red solid line). N is the number of pixels that were positive for carotenoids and N' is the number of pixels that were null (not included in the histogram). Additional transverse section Raman images are shown in Supplemental Fig. S6, Additional File 1.

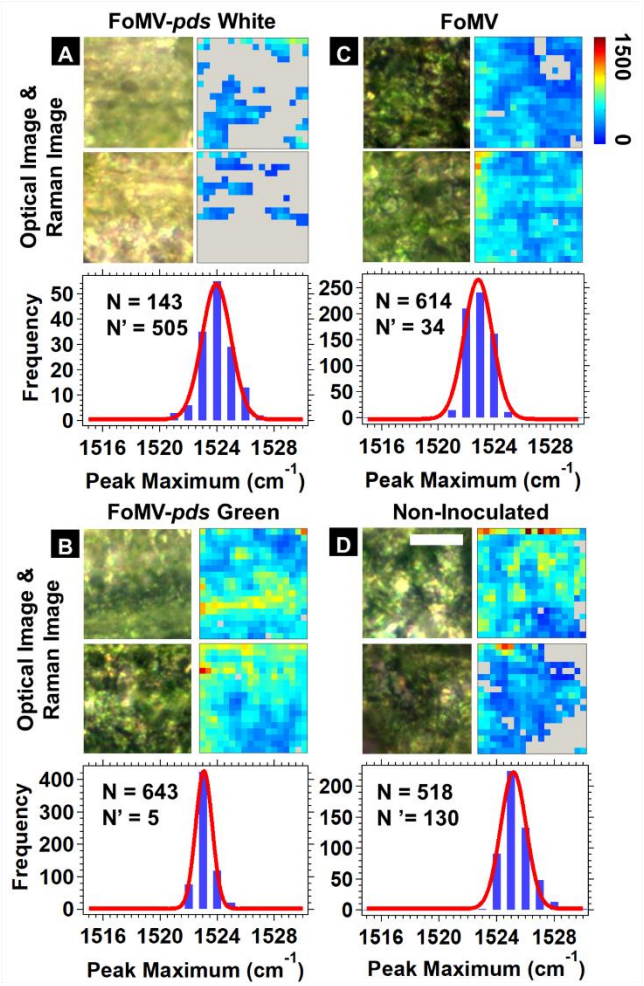

Fig. 5. (A-D) Optical images, ~1520 cm^{-1} Raman images of fractured maize leaves, and histograms of the ~1520 cm^{-1} peak location generated from each pixel within the Raman images. The fracturing process splits the leaf into two halves lengthwise. For each panel, the top optical and Raman image corresponds to one side of the fractured leaf, and the bottom optical and Raman image corresponds to the other side of the fractured leaf. Two areas at the half leaf location were analyzed for the FoMV-*pds* leaf: (A) variegated white area and (B) a green area. The scale bar is 25 µm. The histograms were fit to a Gaussian function (red solid line). (C, D) represent the area measured for the FoMV and non-inoculated fractured leaves, respectively. N is the number of pixels that were positive for carotenoids and N' is the number of pixels that were null (colored gray and were not included in the histogram).

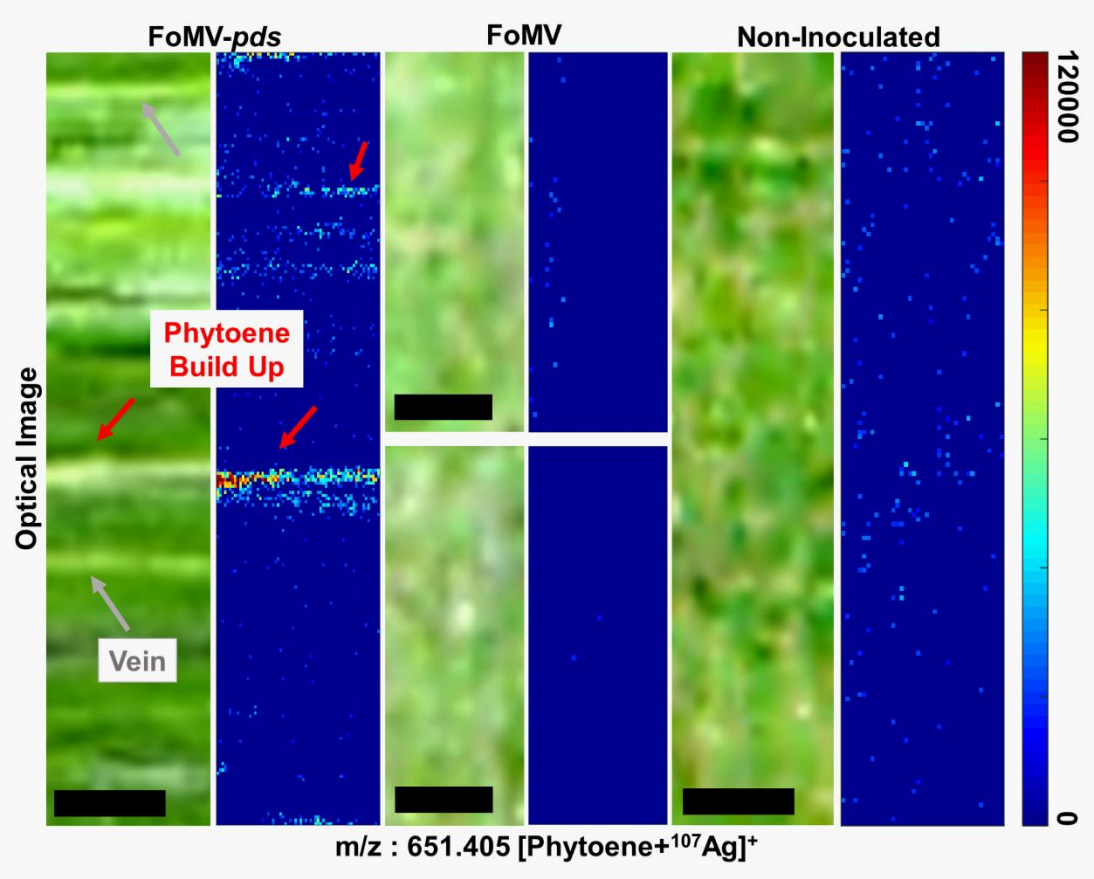

Fig. 6. Mass spectrometry (MS) images of fractured FoMV-*pds* silenced, FoMV and non-inoculated maize leaves. The images are generated using the phytoene mass-to-charge (*m/z*) ratio 651.405, which is a silver adduct [Phytoene+^{107}Ag]$^{+}$. The ion intensity is shown using the color scale shown on the right. The leaf vein was easily identifiable from the FoMV-*pds* silenced variegated white areas because the leaf vein(s) were present throughout the entire length of the leaf and the variegation was not. The leaf vein(s) were identifiable (gray arrows) because they were present along the entire length of the leaf. The FoMV-*pds* silenced variegated white areas (red arrows) however were not present along the entire length of the leaf. The resolution of the camera collecting the optical images on the MSI instrument is low, however an additional optical image collected prior to imaging is provided in Supplemental Fig. S8, Additional File 1. Scale bar is 500 µm for all images.

References

1. Mei, Y.; Zhang, C.; Kernodle, B. M.; Hill, J. H.; Whitham, S. A., A Foxtail mosaic virus Vector for Virus-Induced Gene Silencing in Maize. *Plant Physiology* **2016,** *171* (2), 760-772.

2. Liu, N.; Xie, K.; Jia, Q.; Zhao, J.; Chen, T.; Li, H.; Wei, X.; Diao, X.; Hong, Y.; Liu, Y., Foxtail Mosaic Virus-Induced Gene Silencing in Monocot Plants. *Plant Physiology* **2016,** *171* (3), 1801-1807.

3. Liou, M.-R.; Huang, Y.-W.; Hu, C.-C.; Lin, N.-S.; Hsu, Y.-H., A dual gene-silencing vector system for monocot and dicot plants. *Plant Biotechnology Journal* **2014,** *12* (3), 330-343.

4. Liu, Z.; Kearney, C. M., An efficient Foxtail mosaic virus vector system with reduced environmental risk. *BMC Biotechnology* **2010,** *10* (1), 88.

5. Scofield, S. R.; Huang, L.; Brandt, A. S.; Gill, B. S., Development of a Virus-Induced Gene-Silencing System for Hexaploid Wheat and Its Use in Functional Analysis of the Lr21-Mediated Leaf Rust Resistance Pathway. *Plant Physiology* **2005,** *138* (4), 2165-2173.

6. Lu, H.-C.; Chen, H.-H.; Tsai, W.-C.; Chen, W.-H.; Su, H.-J.; Chang, D. C.-N.; Yeh, H.-H., Strategies for Functional Validation of Genes Involved in Reproductive Stages of Orchids. *Plant Physiology* **2007,** *143* (2), 558-569.

7. Ding, X. S.; Schneider, W. L.; Chaluvadi, S. R.; Mian, M. A. R.; Nelson, R. S., Characterization of a Brome mosaic virus Strain and Its Use as a Vector for Gene Silencing in Monocotyledonous Hosts. *Molecular Plant-Microbe Interactions* **2006,** *19* (11), 1229-1239.

8. Purkayastha, A.; Mathur, S.; Verma, V.; Sharma, S.; Dasgupta, I., Virus-induced gene silencing in rice using a vector derived from a DNA virus. *Planta* **2010,** *232* (6), 1531-1540.

9. Wang, R.; Yang, X.; Wang, N.; Liu, X.; Nelson, R. S.; Li, W.; Fan, Z.; Zhou, T., An efficient virus-induced gene silencing vector for maize functional genomics research. *The Plant Journal* **2016,** *86* (1), 102-115.

10. Bruun-Rasmussen, M.; Madsen, C. T.; Johansen, E.; Albrechtsen, M., Revised sequence of foxtail mosaic virus reveals a triple gene block structure similar to potato virus X. *Archives of Virology* **2008,** *153* (1), 223-226.

11. Kumagai, M. H.; Donson, J.; della-Cioppa, G.; Harvey, D.; Hanley, K.; Grill, L. K., Cytoplasmic inhibition of carotenoid biosynthesis with virus-derived RNA. *Proceedings of the National Academy of Sciences of the United States of America* **1995,** *92* (5), 1679-1683.

12. Robertson, N. L.; French, R.; Morris, T. J., The open reading frame 5A of foxtail mosaic virus is expressed in vivo and is dispensable for systemic infection. *Archives of Virology* **2000,** *145* (8), 1685-1698.

13. Hannoufa, A.; Hossain, Z., Regulation of carotenoid accumulation in plants. *Biocatalysis and Agricultural Biotechnology* **2012,** *1* (3), 198-202.

14. Wurtzel, E.; Cuttriss, A.; Vallabhaneni, R., Maize Provitamin A Carotenoids, Current Resources, and Future Metabolic Engineering Challenges. *Frontiers in Plant Science* **2012,** *3* (29).

15. Bartley, G. E.; Scolnik, P. A., Plant carotenoids: pigments for photoprotection, visual attraction, and human health. *The Plant Cell* **1995,** *7* (7), 1027-1038.

16. Bartley, G. E.; Scolnik, P. A.; Giuliano, G., Molecular Biology of Carotenoid Biosynthesis in Plants. *Annual Review of Plant Physiology and Plant Molecular Biology* **1994,** *45* (1), 287-301.

17. Beyer, P.; Mayer, M.; Kleinig, H., Molecular oxygen and the state of geometric isomerism of intermediates are essential in the carotene desaturation and cyclization reactions in daffodil chromoplasts. *European Journal of Biochemistry* **1989,** *184* (1), 141-150.

18. Chen, Y.; Li, F.; Wurtzel, E. T., Isolation and Characterization of the Z-ISO Gene Encoding a Missing Component of Carotenoid Biosynthesis in Plants. *Plant Physiology* **2010,** *153* (1), 66-79.

19. Zhang, C.; Bradshaw, J. D.; Whitham, S. A.; Hill, J. H., The Development of an Efficient Multipurpose Bean Pod Mottle Virus Viral Vector Set for Foreign Gene Expression and RNA Silencing. *Plant Physiology* **2010,** *153* (1), 52.

20. Juvale, P. S.; Hewezi, T.; Zhang, C.; Kandoth, P. K.; Mitchum, M. G.; Hill, J. H.; Whitham, S. A.; Baum, T. J., Temporal and spatial Bean pod mottle virus-induced gene silencing in soybean. *Molecular Plant Pathology* **2012,** *13* (9), 1140-1148.

21. Gierlinger, N.; Schwanninger, M., The potential of Raman microscopy and Raman imaging in plant research. *Spectroscopy* **2007,** *21* (2), 69-89.

22. Schulz, H.; Baranska, M.; Baranski, R., Potential of NIR-FT-Raman spectroscopy in natural carotenoid analysis. *Biopolymers* **2005,** *77* (4), 212-221.

23. Baranska, M.; Schulz, H.; Rosch, P.; Strehle, M. A.; Popp, J., Identification of secondary metabolites in medicinal and spice plants by NIR-FT-Raman microspectroscopic mapping. *Analyst* **2004,** *129* (10), 926-930.

24. Baranski, R.; Baranska, M.; Schulz, H., Changes in carotenoid content and distribution in living plant tissue can be observed and mapped in situ using NIR-FT-Raman spectroscopy. *Planta* **2005,** *222* (3), 448-457.

25. Weissflog, I.; Vogler, N.; Akimov, D.; Dellith, A.; Schachtschabel, D.; Svatos, A.; Boland, W.; Dietzek, B.; Popp, J., Toward in Vivo Chemical Imaging of Epicuticular Waxes. *Plant Physiology* **2010,** *154* (2), 604-610.

26. Baranska, M.; Roman, M.; Cz. Dobrowolski, J.; Schulz, H.; Baranski, R., Recent Advances in Raman Analysis of Plants: Alkaloids, Carotenoids, and Polyacetylenes. *Current Analytical Chemistry* **2013,** *9* (1), 108-127.

27. Strehle, M. A.; Rösch, P.; Baranska, M.; Schulz, H.; Popp, J., On the way to a quality control of the essential oil of fennel by means of Raman spectroscopy. *Biopolymers* **2005,** *77* (1), 44-52.

28. Roman, M.; Marzec, K. M.; Grzebelus, E.; Simon, P. W.; Baranska, M.; Baranski, R., Composition and (in)homogeneity of carotenoid crystals in carrot cells revealed by high resolution Raman imaging. *Spectrochimica Acta Part A: Molecular and Biomolecular Spectroscopy* **2015,** *136*, 1395-1400.

29. Dueñas, M. E.; Klein, A. T.; Alexander, L. E.; Yandeau-Nelson, M. D.; Nikolau, B. J.; Lee, Y. J., High-Spatial Resolution Mass Spectrometry Imaging reveals the genetically programmed, developmental modification of the distribution of thylakoid membrane lipids among individual cells of the maize leaf. *The Plant Journal* **2017,** *89* (4), 825-838.

30. Sturtevant, D.; Lee, Y.-J.; Chapman, K. D., Matrix assisted laser desorption/ionization-mass spectrometry imaging (MALDI-MSI) for direct visualization of plant metabolites in situ. *Current Opinion in Biotechnology* **2016,** *37*, 53-60.

31. Lee, Y. J.; Perdian, D. C.; Song, Z.; Yeung, E. S.; Nikolau, B. J., Use of mass spectrometry for imaging metabolites in plants. *The Plant Journal* **2012,** *70* (1), 81-95.

32. Feenstra, A. D.; Alexander, L. E.; Song, Z.; Korte, A. R.; Yandeau-Nelson, M.; Nikolau, B. J.; Lee, Y.-J., Spatial Mapping and Profiling of Metabolite Distributions During Germination. *Plant Physiology* **2017**.

33. Chiang, C.-K.; Chen, W.-T.; Chang, H.-T., Nanoparticle-based mass spectrometry for the analysis of biomolecules. *Chemical Society Reviews* **2011,** *40* (3), 1269-1281.

34. Dufresne, M.; Thomas, A.; Breault-Turcot, J.; Masson, J.-F.; Chaurand, P., Silver-Assisted Laser Desorption Ionization For High Spatial Resolution Imaging Mass Spectrometry of Olefins from Thin Tissue Sections. *Analytical Chemistry* **2013,** *85* (6), 3318-3324.

35. Jun, J. H.; Song, Z.; Liu, Z.; Nikolau, B. J.; Yeung, E. S.; Lee, Y. J., High-Spatial and High-Mass Resolution Imaging of Surface Metabolites of Arabidopsis thaliana by Laser Desorption-Ionization Mass Spectrometry Using Colloidal Silver. *Analytical Chemistry* **2010,** *82* (8), 3255-3265.

36. Sekula, J.; Niziol, J.; Rode, W.; Ruman, T., Silver nanostructures in laser desorption/ionization mass spectrometry and mass spectrometry imaging. *Analyst* **2015,** *140* (18), 6195-6209.

37. Mei, Y.; Whitham, S. A., Virus-Induced Gene Silencing in Maize with a Foxtail mosaic virus Vector. In *Maize: Methods and Protocols*, Lagrimini, L. M., Ed. Springer New York: New York, NY, 2018; pp 129-139.

38. Klein, A. T.; Yagnik, G. B.; Hohenstein, J. D.; Ji, Z.; Zi, J.; Reichert, M. D.; MacIntosh, G. C.; Yang, B.; Peters, R. J.; Vela, J.; Lee, Y. J., Investigation of the Chemical Interface in the Soybean–Aphid and Rice–Bacteria Interactions Using MALDI-Mass Spectrometry Imaging. *Analytical Chemistry* **2015,** *87* (10), 5294-5301.

39. Pascal, A. A.; Ruban, A. V.; Robert, B., Antenna Protein Conformational Changes Revealed by Resonance Raman Spectroscopy. In *Non-Photochemical Quenching and Energy Dissipation in Plants, Algae and Cyanobacteria*, Demmig-Adams, B.; Garab, G.; Adams Iii, W.; Govindjee, Eds. Springer Netherlands: Dordrecht, 2014; pp 245-257.

40. Ermakov, I. V.; Sharifzadeh, M.; Ermakova, M.; Gellermann, W., Resonance Raman detection of carotenoid antioxidants in living human tissue. *Journal of Biomedical Optics* **2005,** *10* (6), 064028-064028.

41. Withnall, R.; Chowdhry, B. Z.; Silver, J.; Edwards, H. G. M.; de Oliveira, L. F. C., Raman spectra of carotenoids in natural products. *Spectrochimica Acta Part A: Molecular and Biomolecular Spectroscopy* **2003,** *59* (10), 2207-2212.

42. Ladislav, F.; Feltl, L.; Pacakova, V.; Stulik, K.; Volka, K., Reliability of Carotenoid Analyses: A Review. *Current analytical chemistry* **2005,** *1* (1), 93-102.

43. Joyard, J.; Ferro, M.; Masselon, C.; Seigneurin-Berny, D.; Salvi, D.; Garin, J.; Rolland, N., Chloroplast Proteomics and the Compartmentation of Plastidial Isoprenoid Biosynthetic Pathways. *Molecular Plant* **2009,** *2* (6), 1154-1180.

44. Sherrod, S. D.; Diaz, A. J.; Russell, W. K.; Cremer, P. S.; Russell, D. H., Silver Nanoparticles as Selective Ionization Probes for Analysis of Olefins by Mass Spectrometry. *Analytical Chemistry* **2008,** *80* (17), 6796-6799.

45. Liu, Y.; Schiff, M.; Dinesh-Kumar, S. P., Virus-induced gene silencing in tomato. *The Plant Journal* **2002,** *31* (6), 777-786.

46. Wolf, F. T., Effects of Light and Darkness on Biosynthesis of Carotenoid Pigments in Wheat Seedlings. *Plant Physiology* **1963,** *38* (6), 649-652.

47. Kay, R. E.; Phinney, B., Plastid Pigment Changes in the Early Seedling Leaves of Zea Mays L. *Plant Physiology* **1956,** *31* (3), 226-231.

48. Kay, R. E.; Phinney, B. O., The Control of Plastid Pigment Formation by a Virescent Gene, Pale-Yellow-1, of maize. *Plant Physiology* **1956,** *31* (6), 415-420.

49. Arvayo-Enriquez, H.; Mondaca-Fernandez, I.; Gortarez-Moroyoqui, P.; Lopez-Cervantes, J.; Rodriguez-Ramirez, R., Carotenoids extraction and quantification: a review. *Analytical Methods* **2013,** *5* (12), 2916-2924.

50. Takagi, S., Determination of Green Leaf Carotenoids by HPLC. *Agricultural and Biological Chemistry* **1985,** *49* (4), 1211-1213.

51. Merzlyak, M. N.; Gitelson, A. A.; Pogosyan, S. I.; Lekhimena, L.; Chivkunova, O. B., Light-induced pigment degradation in leaves and ripening fruits studied in situ with reflectance spectroscopy. *Physiologia Plantarum* **1998,** *104* (4), 661-667.

52. Shi, J., Lycopene in Tomatoes: Chemical and Physical Properties Affected by Food Processing. *Critical Reviews in Biotechnology* **2000,** *20* (4), 293-334.

53. Ramel, F.; Mialoundama, A. S.; Havaux, M., Nonenzymic carotenoid oxidation and photooxidative stress signalling in plants. *Journal of Experimental Botany* **2013,** *64* (3), 799-805.

54. Mattila, H.; Khorobrykh, S.; Havurinne, V.; Tyystjärvi, E., Reactive oxygen species: Reactions and detection from photosynthetic tissues. *Journal of Photochemistry and Photobiology B: Biology* **2015,** *152*, 176-214.

55. Havaux, M., Carotenoid oxidation products as stress signals in plants. *The Plant Journal* **2014,** *79* (4), 597-606.

56. Dong, Y.; Li, B.; Malitsky, S.; Rogachev, I.; Aharoni, A.; Kaftan, F.; Svatoš, A.; Franceschi, P., Sample Preparation for Mass Spectrometry Imaging of Plant Tissues: A Review. *Frontiers in Plant Science* **2016,** *7* (60).

57. Gruszecki, W. I.; Zelent, B.; Leblanc, R. M., Fluorescence of zeaxanthin and violaxanthin in aggregated forms. *Chemical Physics Letters* **1990,** *171* (5), 563-568.

58. Bino, R. J.; De Vos, C. H. R.; Lieberman, M.; Hall, R. D.; Bovy, A.; Jonker, H. H.; Tikunov, Y.; Lommen, A.; Moco, S.; Levin, I., The light-hyperresponsive high pigment-2dg mutation of tomato: alterations in the fruit metabolome. *New Phytologist* **2005,** *166* (2), 427-438.

59. López-Ráez, J. A.; Charnikhova, T.; Gómez-Roldán, V.; Matusova, R.; Kohlen, W.; De Vos, R.; Verstappen, F.; Puech-Pages, V.; Bécard, G.; Mulder, P.; Bouwmeester, H., Tomato strigolactones are derived from carotenoids and their biosynthesis is promoted by phosphate starvation. *New Phytologist* **2008,** *178* (4), 863-874.

60. Lupoi, J. S.; Gjersing, E.; Davis, M. F., Evaluating Lignocellulosic Biomass, Its Derivatives, and Downstream Products with Raman Spectroscopy. *Frontiers in Bioengineering and Biotechnology* **2015,** *3*, 50.

Appendix. Supplemental Information

Additional File 1 Supplemental Data

Materials and Methods

Carotenoid Extraction. Sample preparation was modified from previously described methods.[58-59] Leaf 5 of each maize plant was cut into ~100 mg aliquots at the half leaf length position and flash frozen in liquid nitrogen. Samples were pulverized to fine powders in liquid nitrogen using

a mortar and pestle. A solution of 2-mL methanol/chloroform (5:4) containing 0.1% butylated hydroxytoluene (BHT, Sigma-Aldrich) and 20 µL of 1 mg/mL of canthaxanthin as an internal standard (Sigma-Aldrich) were added to the powder samples. Samples were incubated on ice for 10 minutes; 1.1 mL of 1 M NaCl (prepared with 0.1 M Tris-HCl buffer pH 7.5) was added to the samples and incubated on ice for another 10 minutes. The samples were centrifuged (1350 × *g*) for 10 minutes at room temperature. The organic fraction was collected, and the aqueous layer was centrifuged with an additional 1 mL aliquot of chloroform containing 0.1% BHT. The combined organic fractions were dried under a stream of nitrogen and the residue was dissolved in 200 µL ethyl acetate containing 0.1% BHT for future analysis.

An Agilent 1100 series high performance liquid chromatograph (HPLC) with photodiode array and mass selective (MS) detectors was used for carotenoid separation and identification. A Spherisorb® 5 µm ODS2 column (250×4.6 mm) (Phenomenex) heated to 40 ºC was utilized with a sample injection volume of 20 µL. The mobile phase consisted of 0.1% acetic acid (v:v) in acetonitrile/methanol/water (84:9:7v:v:v; eluent A), and 0.1% acetic acid (v:v) in methanol/ethyl acetate (68:32v:v; eluent B). The separation gradient with a flow rate of 1 mL/min was as follows: 0 min 0% B, 15 min 100% B, 28 min 100% B, 30 min 0% B, post run (5 min). A photodiode array detector was used for absorption-based detection. An atmospheric pressure chemical ionization source in positive mode was utilized with an ion trap mass spectrometer. The MS conditions were as follows: nebulizing nitrogen gas flow: 12 L/min; nebulizing gas pressure: 25 p.s.i.; dry temperature: 350 °C, vaporizer temperature: 400 °C; maximum accumulation time: 300 ms; mass scan range: 150 to 700 m/z; and corona: 3900 nA.

Quantification of all carotenoids were processed with DataAnalysis and QuantAnalysis software (Bruker Daltonics). Lutein (Sigma-Aldrich) and zeaxanthin (Sigma-Aldrich) were

identified using commercial standards. Violaxanthin/neoxanthin, α-carotene, and β-carotene were identified by the m/z values of the molecular ions and by MS/MS analysis of the generated fragments. Retention times for carotenoids were as follows: violaxanthin/neoxanthin (8.1 min); lutein (9.9 min); zeaxanthin (10.2 min); canthaxanthin (10.9 min); α-carotene (19.9 min); and β-carotene (20.2 min). α and β-carotene could not be individually quantified due to overlapping peaks. The phytoene signal was too low to be measured in the FoMV and non-inoculated leaves with the utilized HPLC conditions and equipment. All reported uncertainties represent one standard deviation.

Supplemental Table

Table S1. Average measured value (µg/g of fresh weight) by HPLC of the indicated carotenoids in maize leaf extract with uncertainty representing on standard deviation.[1]

	FoMV-*pds*[2]	FoMV[3]	Non-inoculated
α- & ß-carotene	20 ± 3 (p = 0.5)	11 ± 2 (p = 0.004)	22 ± 1
Phytoene	0.4 ± 0.2	0.011 ± 0.005	Not Detected[4]
Violaxanthin	8 ± 3 (p= 0.6)	7 ± 2 (p= 0.2)	10 ± 2
Lutein	54 ± 5 (p = 0.2)	40 ± 10 (p = 0.2)	61 ± 3
Zeaxanthin	2.4 ± 0.5 (p = 0.3)	1 ± 1 (p= 0.3)	7 ± 5

[1] All measurements were collected from one leaf with 2 to 3 tissue replicates.
[2] p-values comparing FoMV-*pds* vs. Non-Inoculated.
[3] p-values comparing FoMV vs. Non-Inoculated.
[4] The phytoene detection limit for this analysis is 0.003 µg/g of fresh weight

Supplemental Figures

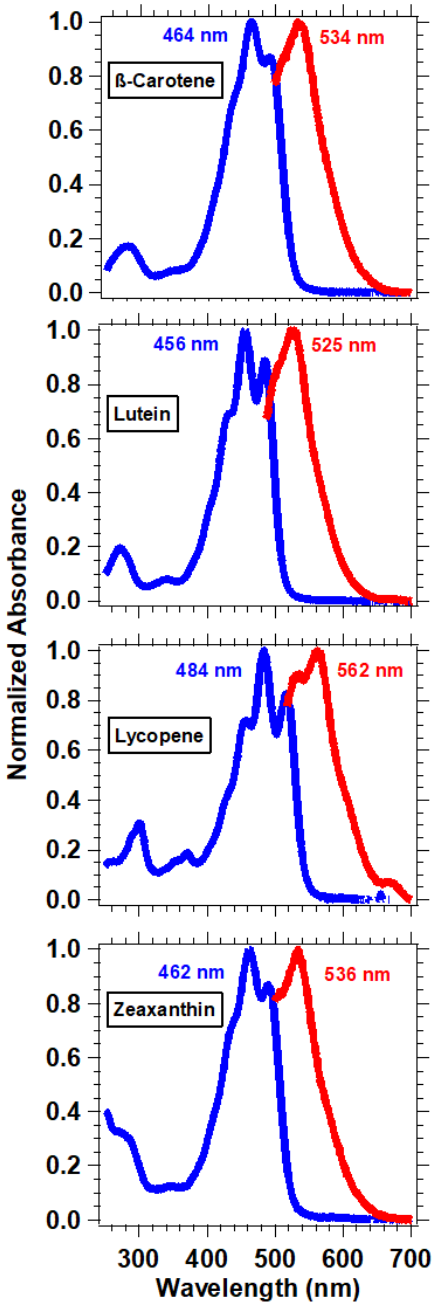

Supplemental Fig. S1. Absorbance (blue) and fluorescence (red) spectra for ß-carotene, lutein, lycopene, and zeaxanthin dietary supplements. All supplements were diluted to 0.01 mg/mL in chloroform. Absorbance measurements were performed on an Agilent 8453 UV-visible spectrophotometer. Fluorescence measurements were carried out on an Agilent Cary Eclipse spectrophotometer. The corresponding wavelength of maximum absorbance and fluorescence is listed in each spectrum. The wavelength of maximum absorbance (fluorescence) was used as the excitation (emission) wavelength to collect the fluorescence (excitation) spectrum.

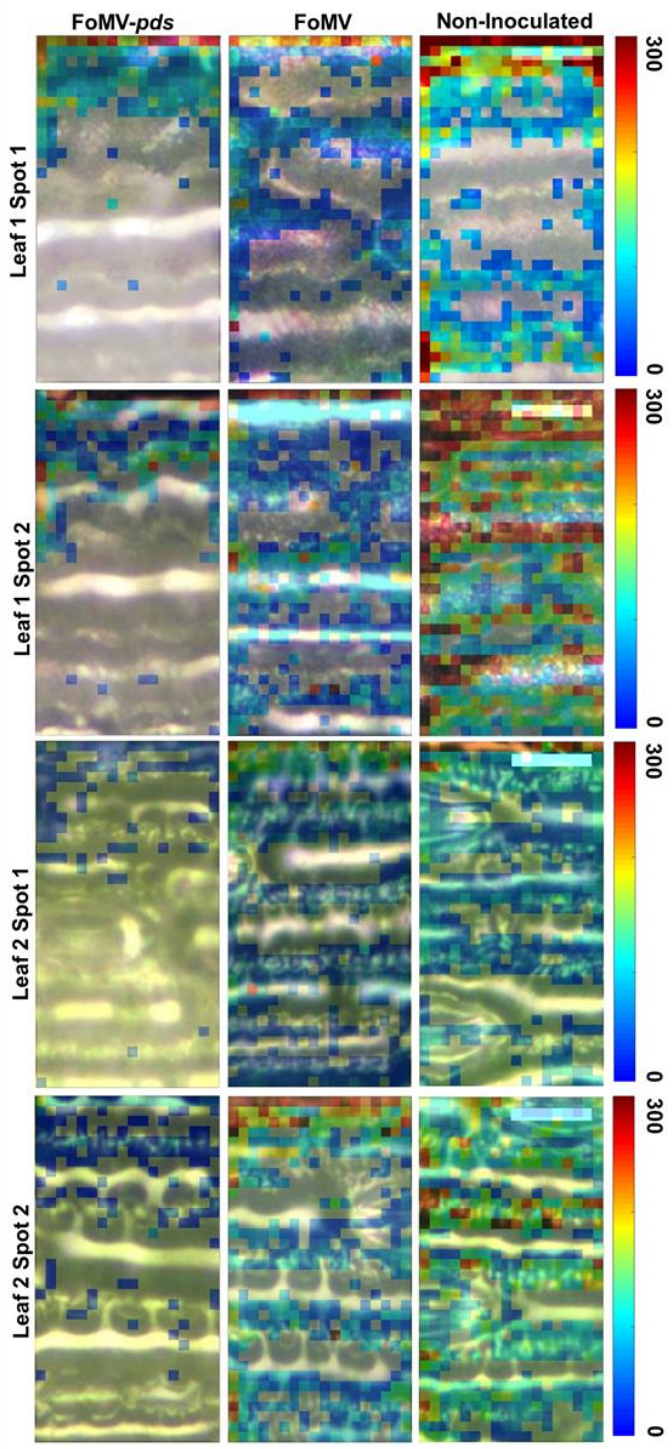

Supplemental Fig. S2. Merged optical and ~1520 cm^{-1} Raman images (color scale) of *in situ* whole maize leaves. All maps were scaled to the same intensities. The scale bar is 25 µm. Optical images of an expanded area around where the Raman images were collected is seen in Supplemental Fig. S3.

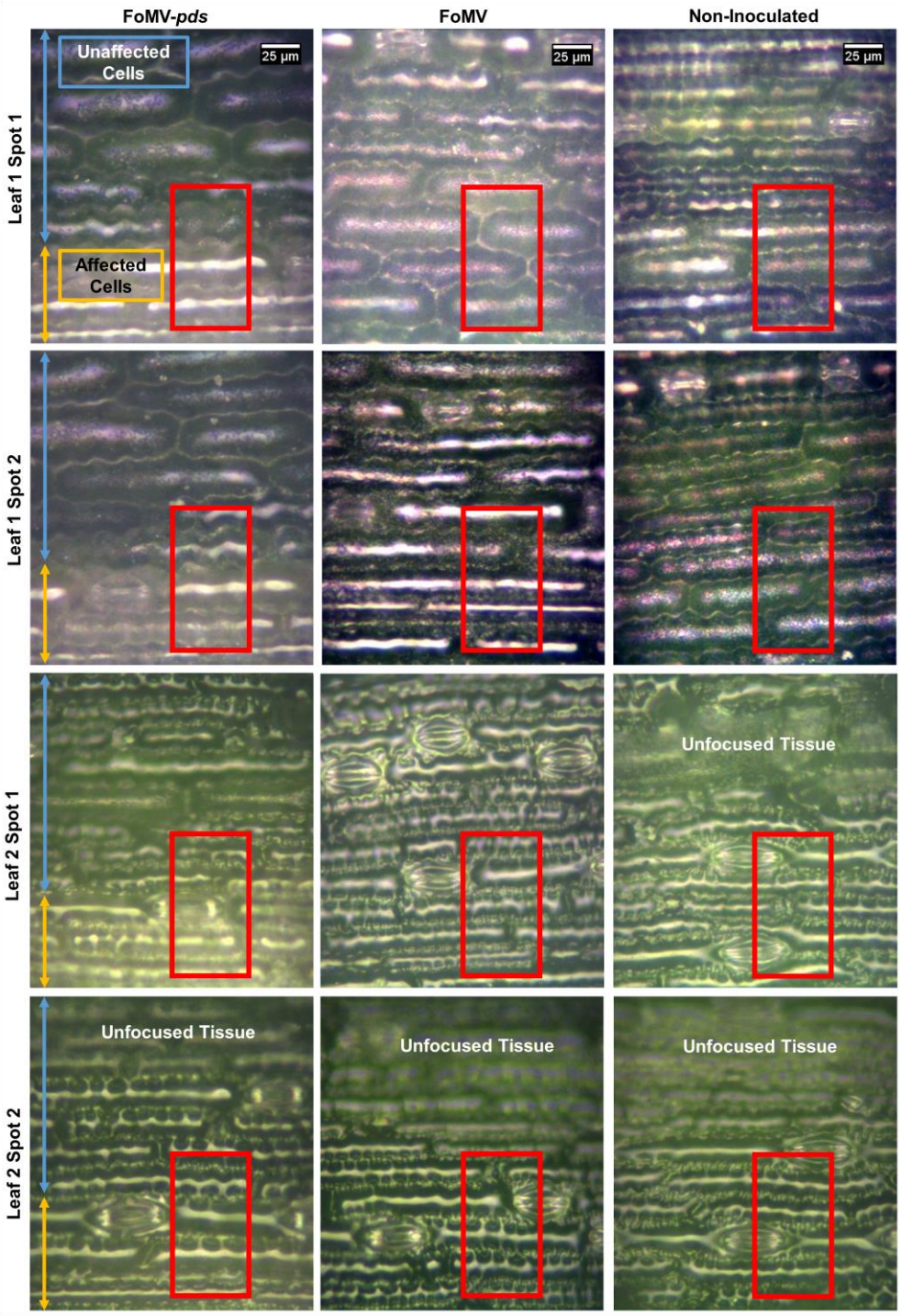

Supplemental Fig. S3. Optical images showing the location (red box) where the *in situ* whole leaf measurements presented in Figure 3 and Supplemental Fig. S2 were collected. Within the FoMV-*pds* optical images, the variegated white phenotype is shown with a yellow arrow and the unaffected area is shown with a blue arrow. The leaf is not optically flat, and some regions are out of focus (as noted).

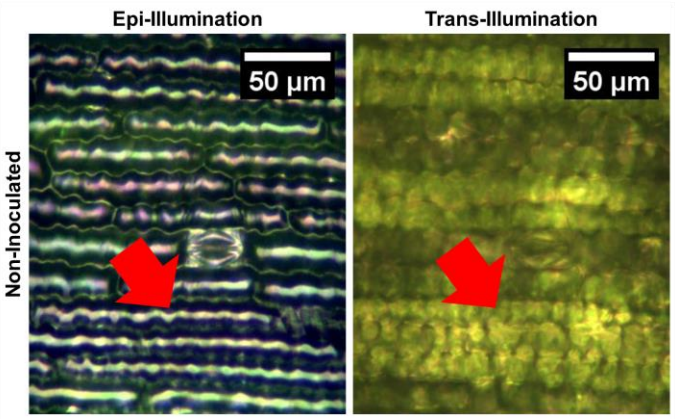

Supplemental Fig. S4. White light optical images of a non-inoculated leaf with epi-illumination (incident light and reflected light on the same side of the sample) and trans-illumination (incident light and transmitted light on opposite sides of the sample). The red arrow highlights the same location of the leaf in both images.

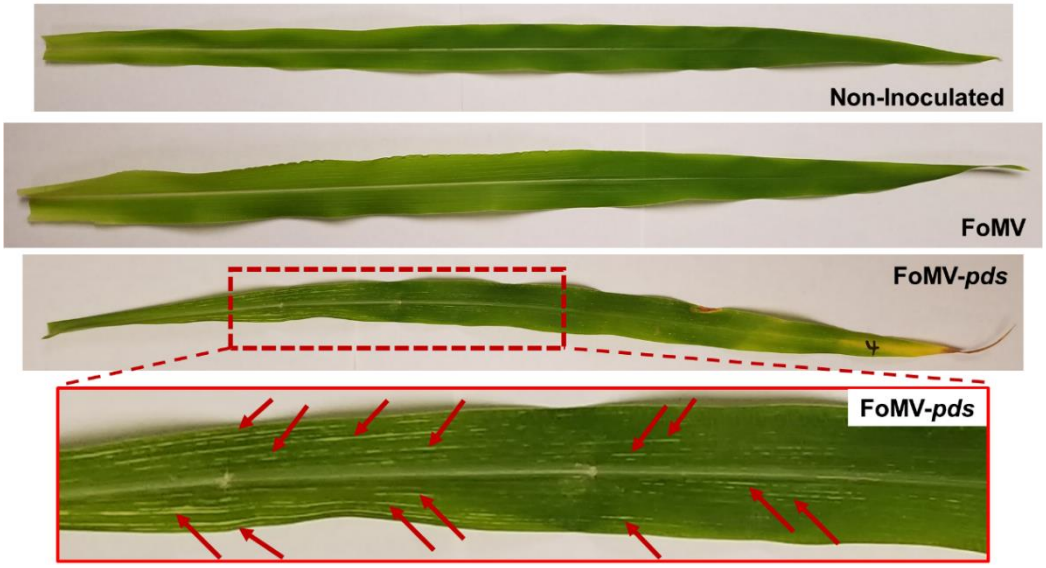

Supplemental Fig. S5. Representative optical images of the entire leaf of the three plant types. The total leaf length ranged between 12-18 inches. Within the FoMV-*pds* magnified optical image (bottom image), example variegated areas are highlighted with red arrows. The percentage of the FoMV-*pds* leaf exhibiting the variegated area within the lower optical image was 13%. This was measured using ImageJ and by applying a color threshold to identify the areas lacking green coloration. The total white area identified by the color threshold was divided by the total leaf area. The variegated areas of the FoMV-*pds* leaf do not provide information about the biochemical composition or microscopic information, information that is measured with the presented imaging approach.

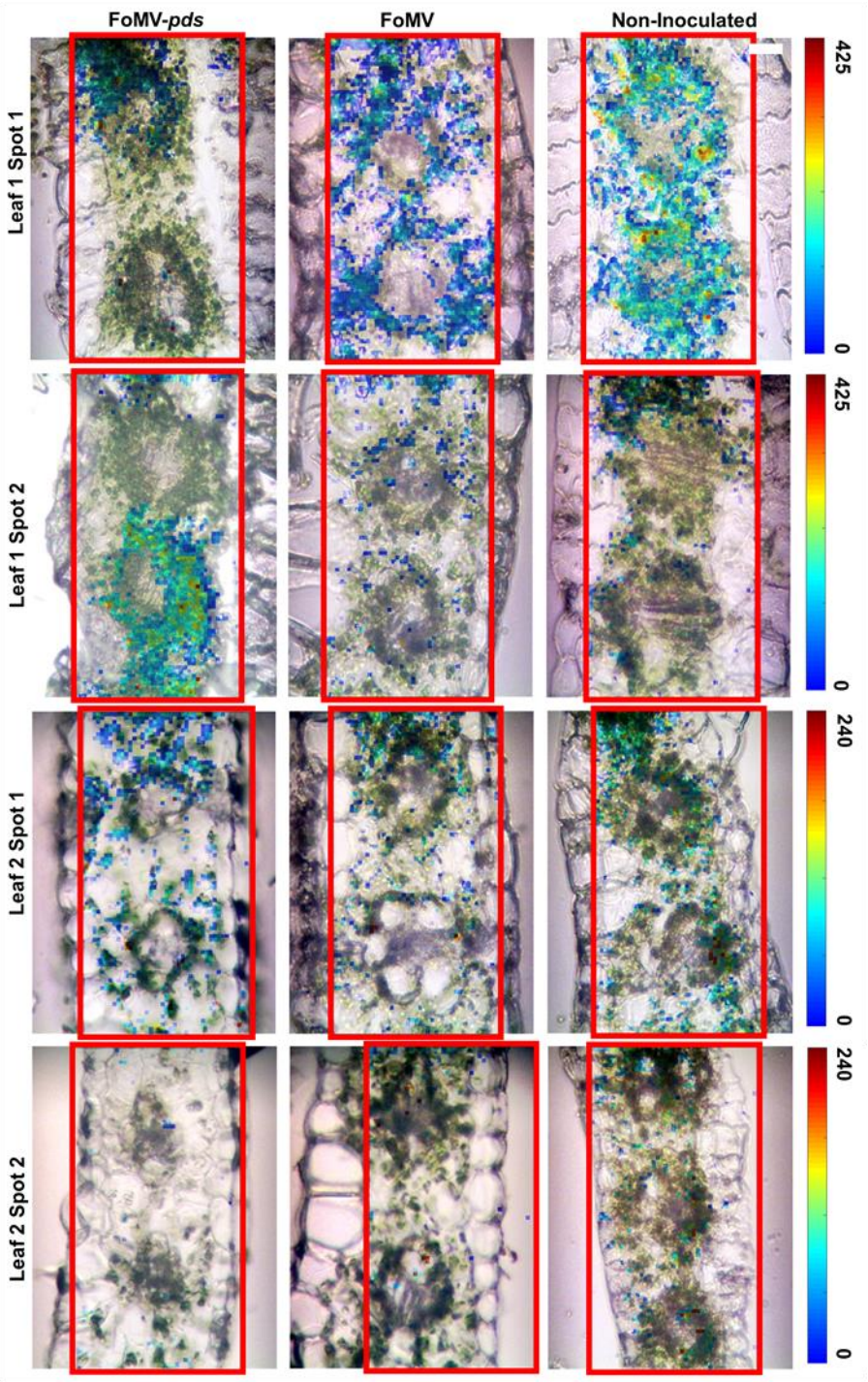

Supplemental Fig. S6. Merged optical and ~1520 cm^{-1} Raman images (color scale and outlined in red) of maize leaf transverse cross sections. Scale bar is 25 µm.

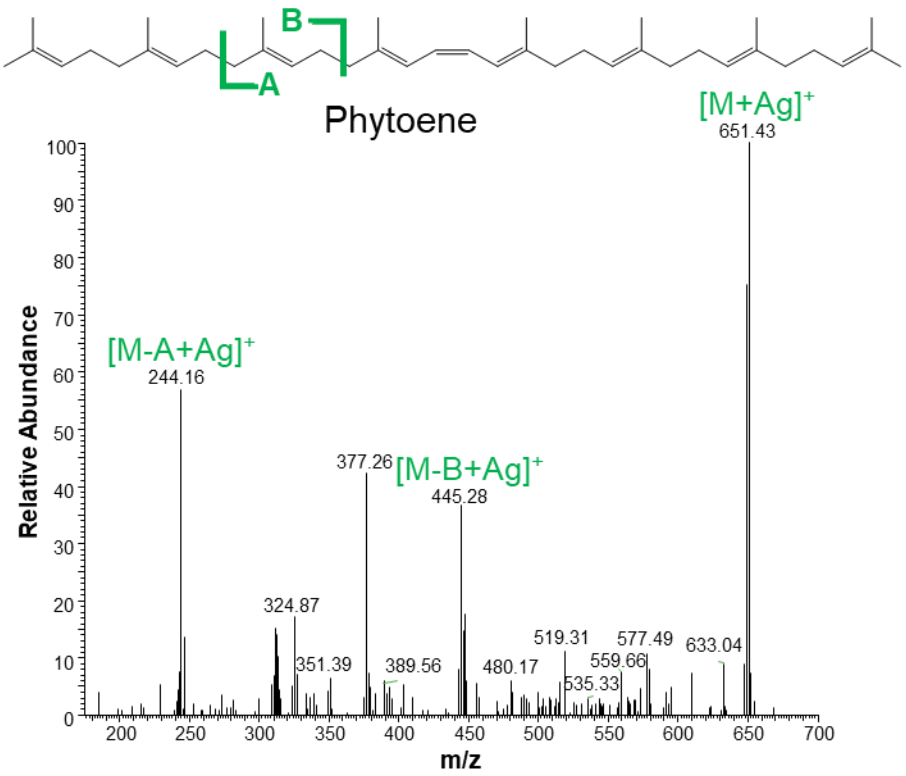

Supplemental Fig. S7. Tandem (MS/MS) mass spectrum of phytoene, (*m/z* 651.405, $[M+^{107}Ag]^+$) from FoMV-*pds* fractured leaves.

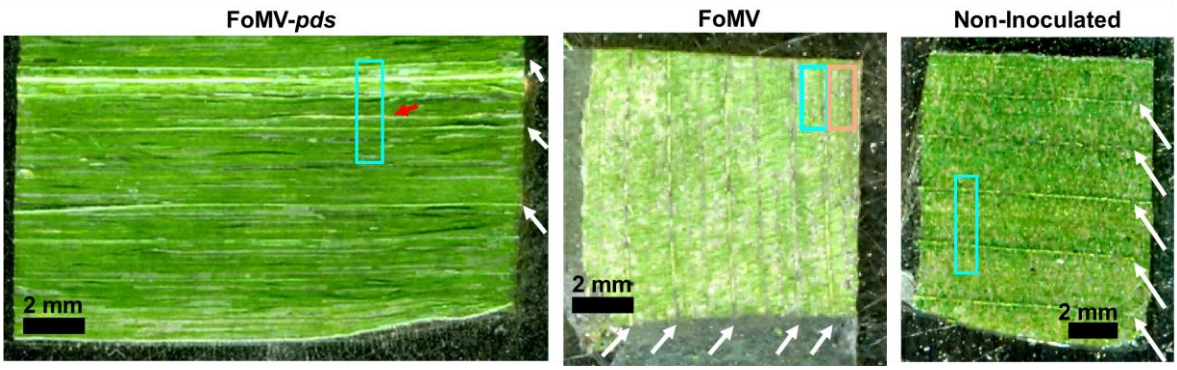

Supplemental Fig. S8. Larger optical images showing the locations (light blue & orange boxes) where the fractured leaf MS imaging measurements presented in Fig. 6 were collected. Within the FoMV optical image, the orange box indicates the top MS image within Fig. 6, and the light blue represents the bottom MS image. The leaves are orientated in the same direction as shown in Fig. 6. The leaf veins within all three plant types are outlined with white arrows. Within the FoMV-*pds* optical image, an example variegated white area is highlighted with a red arrow. Note these leaf fractures were less than 2 inches in length; sample optical images of an entire leaf are shown in Supplemental Fig. S5.

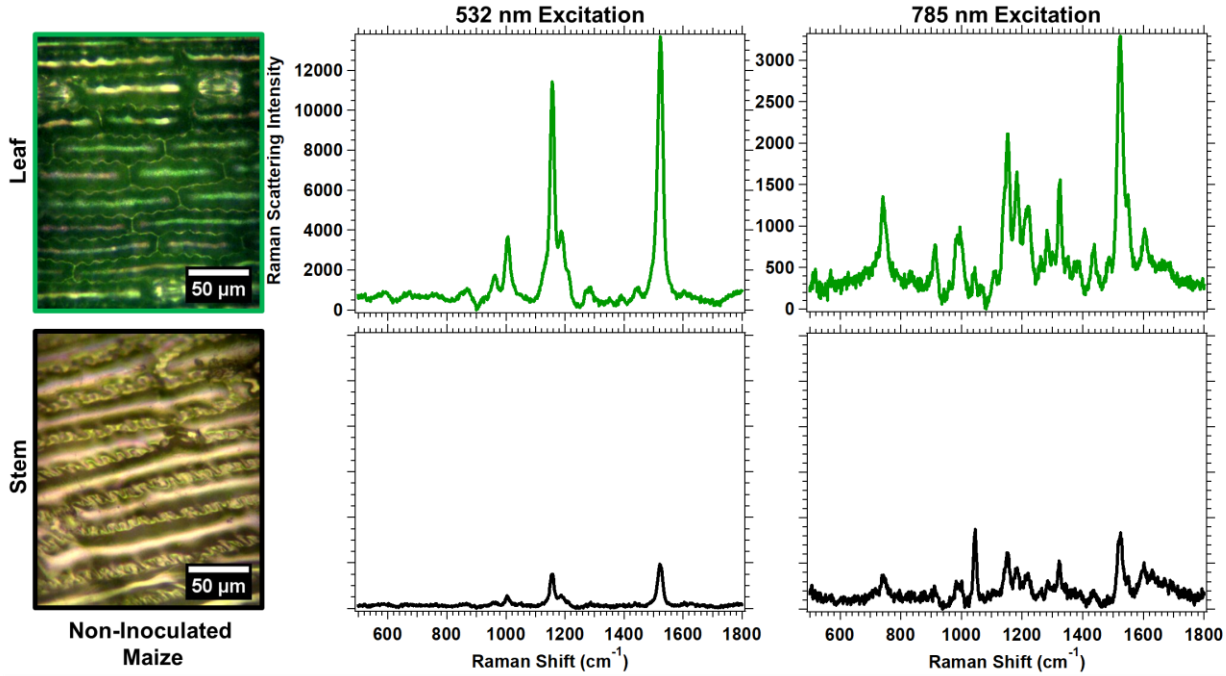

Supplemental Fig. S9. Maize (monocot) leaf and stem tissues. (Left) optical image of selected regions of the indicated tissue and background subtracted Raman spectra collected with (middle) 532 nm and (right) 785 nm excitation. Using 532 nm excitation, the Raman spectrum is dominated by carotenoid peaks (~1520, ~1150, and ~1000 cm^{-1}). Using 785 nm excitation, the Raman signal includes the polysaccharide, lignin (e.g., the lignin peak at ~1605 cm^{-1}), and other biomolecule peaks.[60]

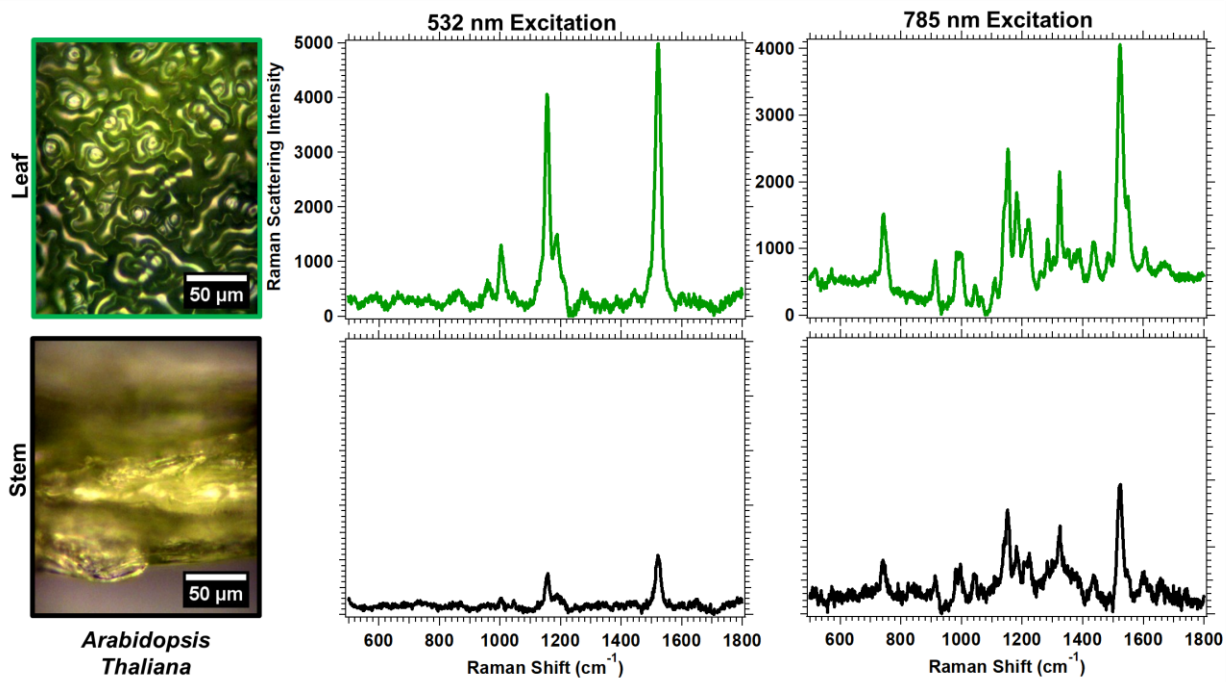

Supplemental Fig. S10. *Arabidopsis thaliana* (dicot) leaf and stem tissues. (Left) optical image of selected regions of the indicated tissue and background subtracted Raman spectra collected with (middle) 532 nm and (right) 785 nm excitation. Using 532 nm excitation, the Raman spectrum is dominated by carotenoid peaks (~1520, ~1150, and ~1000 cm^{-1}). Using 785 nm excitation, the Raman signal includes polysaccharides (e.g., the ~1043 cm^{-1} peak commonly assigned to cellulose that is prominent in the leaf spectrum), lignin, and other biomolecule peaks.[60]

CHAPTER 3. MEASURING PLANT METABOLITE ABUNDANCE WITH RAMAN SPECTRA TO DETERMINE OPTIMAL HARVEST TIME

Sadie J. Burkhow,[ab] Linda K. B. Brown,[c] Beatrice Y. Collet,[c] John A. Greaves,[c] Emily A. Smith[ab*]

[a]Department of Chemistry, Iowa State University, Ames, IA 50011-3111, USA.

[b]Chemical and Biological Science Division, The Ames Laboratory, Ames, IA, 50011, USA.

[c]Kemin Industries, 1900 Scott Avenue, Des Moines IA 50317, USA.

Modified from a manuscript that is in preparation for journal submission

Abstract

A fast and straightforward method that implemented Raman spectroscopy to determine the optimal harvest time of plants in order to obtain the highest abundance of target metabolites is presented. Raman peak area ratio analyses of commercial 'Native' and the Kemin proprietary clonal line 'KI110' spearmint (*Mentha spicata* L.) leaves yielded qualitative rosmarinic acid abundances relative to a non-varying plant metabolite. The ratios were statistically at least 6-fold higher (p-values < 0.0001) for the trichomes compared to the epidermal cells on the adaxial leaf surface of KI110 plants. This is the first report of a plant-leaf cellular-structure correlation of rosmarinic acid abundance. In some instances, rosmarinic acid abundance may also be dependent on the age of the leaf in the same plant, which is critical to know for accurate sampling. In order to determine the concentration of rosmarinic acid within the leaf, partial least squares regression was used to develop a calibration model with Raman spectroscopy and high-performance liquid chromatography. The calibration model had an R^2 of 0.96 and an estimated mean squared prediction error of 0.000067. Combining Raman spectroscopy and the calibration model, the optimal spearmint harvest time can be determined rapidly and in real time, using this micro-remote sensing method.

Introduction

There is a need for rapid analysis methods to confirm the optimal plant harvest time in order to extract metabolites found within the tissues. Primary and secondary plant metabolites include amino acids, lipids, flavonoids, polyphenols, alkaloids, nitriles, and chlorophylls, to name a few. Unlike harvesting fruits or a flowering plant, where a visual cue is easily observed, there is often no visual cue when harvesting a vegetative plant for a target metabolic component. Typical methods to investigate the plant metabolite concentration include extraction from the tissue followed by high-performance liquid chromatography (HPLC) quantification. Such an analysis cannot be performed in the field, requires lengthy and labor-intensive liquid sample preparation, and often requires abundant tissue (on the order of grams) for the analysis. Metabolite expression and accumulation is dependent on many biotic and abiotic factors, including temperature, humidity, soil type, amount of sunlight.[1] As a result, the best harvest time also depends on many factors and is not necessarily predictable. Thus, an alternative rapid analysis method to determine the plant metabolite concentration for optimal harvest time is needed.

Raman spectroscopy could be an alternative method to determine promptly when a plant is ready to harvest in order to obtain the most extractable metabolite(s). Raman spectroscopy is a non-destructive analytical technique that provides information on molecular functional groups. Many plant metabolites can be differentiated based on characteristic vibrational peaks.[2] The sample preparation for Raman spectroscopy is usually minimal; analyses can often be performed on whole leaves or other tissues. A spectrum can be acquired within seconds in many cases and directly interpreted or screened with spectral libraries. Also, handheld commercial Raman spectrometers can be carried directly to a greenhouse or field and used with minimal training.[3]

Quantitation with Raman spectroscopy is possible because the intensity of the Raman scattered light from the sample, $I(v)_R$ is proportional to the number of molecules producing the scattered light, N. In other words, $I(v)_R \propto$ N.[4] There are two standard methods to obtain quantitative information with Raman spectroscopy. Univariate calibration is the first quantitative method wherein a calibration curve is constructed with the Raman peak amplitude or area of prepared standard solutions. Several research groups have demonstrated the potential of using Raman spectroscopy and univariate calibration for real-time monitoring of lignocellulosic bioethanol production, including pretreatment, hydrolysis, and fermentation steps.[5-10]

The second standard method for developing a calibration model with Raman spectroscopy incorporates chemometrics, such as multivariate regression analysis. The sample must be measured with Raman spectroscopy and another technique (such as HPLC) that provides the metabolite concentration. In this way, each method's instrument response can be directly correlated to the metabolite concentration using regression-based analysis. Several authors used PLSR with Raman spectroscopy to determine the concentration of a plant metabolite.[11-17] Akpolat and coworkers used a handheld Raman spectrometer and chemometrics, including PLS, soft independent modeling of class analogy (SIMCA), and artificial neural networks (ANNs) to quantify all-trans-lycopene content in tomato fruit varieties.[12] They used HPLC and UV/visible spectrophotometry to profile and quantify the seven types of carotenoids present. Anastasaki and coworkers determined that Raman spectroscopy could be a rapid screening tool for saffron (crocetin esters) quality.[13] They used HPLC and UV/visible spectrophotometry to measure concentrations of the crocetin esters and correlated those data with Raman spectra of the same materials using PLSR. When creating a multivariate regression calibration for Raman data, a large sample size is recommended to capture sufficient variance and produce better prediction

models. Based on experiments published in the literature with biomass materials, a sample size of at least 100 is typical to build a reliable model.[11-17] Additionally, Raman spectra often require preprocessing before developing a chemometric model. Examples of preprocessing methods include the use of one or more of the following: normalization, derivatization, background subtraction, mean-centering, smoothing, interpolation to areas of interest. The preprocessing method that produces the best chemometric model is often found by trial and error and can significantly impact its reliability.

In this work, Raman spectroscopy was demonstrated to be a rapid, non-invasive technique to monitor metabolite expression for the determination of optimal crop harvest time. To illustrate this, we focused on rosmarinic acid in 'KI110'[18-19] and commercial 'Native' spearmint plants. Rosmarinic acid, a polyphenol plant metabolite (Supplemental Figure S1), has many uses in support of human health when taken as a nutritional supplement.[20] It is most notably used as an antioxidant,[21] anti-inflammatory,[22] anti-mutagen,[23] and an astringent.[24] Rosmarinic acid is commonly extracted from the *Lamiaceae* (i.e., mint or sage*)* and *Boraginaceae* plant families.[25] Sik *et al.* discussed various extraction and analysis methods of rosmarinic acid from multiple plants.[25] We used the Raman peak area to measure the relative abundance of rosmarinic acid within the spearmint leaves. The relationship between cellular structures or leaf age with the relative abundance of rosmarinic acid was investigated. In addition, a chemometric model was used to develop a calibration model to quantify the concentration of rosmarinic acid within a leaf using Raman spectroscopy. A similar calibration model can be used for future rapid in situ Raman measurements to quantify the concentration of metabolites in many plant types.

Materials and Methods

Materials

Native and KI110 spearmint (*Mentha spicata* L.) plants were used in this study. The KI110 clonal line was developed to accumulate up to 10% rosmarinic acid on a dry weight basis, whereas the commercial Native spearmint plant accumulates <2% rosmarinic acid in leaf tissue under field conditions in early June. The plants were vegetatively propagated to produce multiple genetically identical clones in 4-inch pots. These plots were grown at the Kemin Specialty Crop Improvement research far near Kelley, Iowa, as well as inside Kemin's greenhouses in Des Moines, Iowa. The plants were harvested at approximately three months of age from August to October 2019 and were also provided in 4-inch pots for measurements.

Nine sets of pots were measured (labeled I to IX). Within each set, there were varying amounts of pots that were measured. Sets I to IV consisted of the following number of KI110 pots: 5, 7, 4, and 5, respectively. The remaining sets V to IX consisted of the following number of Native spearmint pots 2, 3, 2, 7, and 7, respectively. Sets IV, VII, VIII, and IX, were grown in the greenhouse, and all others were grown in field plots.

High-Performance Liquid Chromatography (HPLC)

An HPLC instrument with a Quad pump, an autosampler, a thermostat column compartment and a diode array detector (Agilent 1100) was used. All measurements were collected using a 5 µL injection volume and a flow rate of 1 mL/min. A stock solution was made of 0.8652 mg/mL rosmarinic acid in acetonitrile. The following solutions were then made by dilution with acetonitrile: 0.2163, 0.4326, 0.6589, 0.7354, and 0.8651 mg/mL. A calibration curve was made using the peak eluding at ~5 minutes. For HPLC analysis, the entire leaf mass from each pot was combined to extract the rosmarinic acid. The rosmarinic acid extraction process used proprietary Kemin Industries method using the following extraction solution,

KH_2PO_4 buffer:reagent alcohol (1:1 v/v). Rosmarinic acid concentrations (mg/g) measured by HPLC are shown in Supplemental Figure S2.

Raman Measurements

The Raman spectra were measured with an XploRA Plus Raman confocal upright microscope (HORIBA Scientific, Edison, New Jersey) with a Synapse EMCCD camera. An irradiance of 17 kW/cm^2 with a 785-nm solid-state laser was used for all materials. An Olympus objective (20× magnification, 0.4 numerical aperture) was used to collect optical images and Raman data in the epi-direction. Raman measurements were collected with a 600 grooves/millimeters (resolution ± 10 cm^{-1}) grating. A 300 µm monochromator slit and 100 µm confocal pinhole were used for data collection.

Supplemental Figure S3 outlines how Raman measurements were performed for each pot. A total of 3,774 Raman spectra were collected, half (1,887) for the KI110 plants and half (1,887) for the Native plants. The number of measurements for each set are shown in Supplemental Table S1. A leaf was cut from the plant and placed on a coverslip coated with double-sided tape to ensure it laid flat. The leaf was measured immediately with the adaxial leaf surface facing the air. This process was repeated for leaf positions 3, 4, and 5 that were analyzed. Raman spectra were acquired with an acquisition time of fifteen seconds and four accumulations. White-light optical images were analyzed with the imaging analysis software ImageJ. The same acquisition parameters were used to collect a Raman spectrum of rosmarinic acid powder placed on a glass coverslip (Sigma-Aldrich) and is included in Figure 1A. The rosmarinic acid spectrum is an average of 3 replicates.

Data and Statistical Analysis

Raman Data Analysis. The 741, 990, 1521, and 1598 cm^{-1} Raman peaks were fit with a Gaussian and constant baseline to extract the peak amplitude, peak maximum, and peak area using IGOR Pro 6.37 (Wavemetrics, Inc., Lake Oswego, OR, USA). The extracted Gaussian fit was further analyzed in Microsoft Excel with the following criteria. Firstly, the Raman peak amplitude had to be greater than three times the standard deviation of the noise, as determined in a spectral region where no Raman peaks were present (2000-2025 cm^{-1}). Secondly, the peak maximum had to be within the range of 1554-1650 cm^{-1}. If both criteria were met, then the peak amplitude or area was used for further analysis, and if not, then a zero value was assigned for further analysis. Within the Native and KI110 datasets, 243 and 1 spectra were excluded, respectively.

Statistical Analysis. One-way analysis of variance (ANOVA) was calculated using Microsoft Excel. The confidence interval was 95%, with an alpha (α) value of 0.05. Data that were not statistically similar had a $p \geq 0.05$ and were annotated with n.s. Data that were statistically different had the following: $p < 0.05$ annotated with plus (+) sign, $p < 0.01$ annotated with (++), and $p < 0.0001$ annotated with (++++). Supplemental Table S2 lists all *p*-values.

Chemometric Analysis. MATLAB 2019b (MathWorks, Natick, MA, USA) was used to preprocess Raman spectra and perform chemometric analyses. All Raman spectra were preprocessed by interpolating the raw spectral data from 50-2500 cm^{-1} to 200-1800 cm^{-1} to remove unneeded points where no useful spectral peaks were present. The principal component analysis was done as a first step for exploratory data analysis using the built-in MATLAB

function, [coeff, score, latent, tsquared, explained, mu] = pca(). There were no similarities or differences seen in the scores and loadings plots (not shown).

Partial least squares regression (PLSR)[26] was used with built-in MATLAB functions, [XL, YL, XS, YS, BETA] = plsregress(X,Y, ncomp,..). This calibration model used the SIMPLS algorithm[27] for a PLSR.[28] The input data consisted of nine correlated HPLC-determined rosmarinic-acid concentrations and nine Raman spectra that were averages of spectra collected for sets I to IX. The calibration model was cross-validated with the model-building data with the leave-one-out method. Three principal components were used to build the model. The PLS weight versus variable (wavenumber) is shown in Supplemental Figure S4A. The estimated mean squared prediction error (MSEP) for three components was 0.000067, as shown in the plot in Supplemental Figure S4B.

Results and Discussion

Raman Spectra and Assignments of Rosmarinic Acid and Spearmint Plants.

Spearmint plants vary tremendously for extractable rosmarinic acid.[29] KI110 and a commercial Native spearmint clonal line were included in this study. The KI110 plants were bred to have higher concentrations of rosmarinic acid, and using both Native and KI110 plants enabled a larger range of rosmarinic acid concentrations to be included in the study. Rosmarinic acid is found within the roots, stems, and leaves of plants that synthesize this metabolite.[29] Leaves have the highest concentration of rosmarinic acid, followed by the stems and then the roots.[30] Leaves were the sole focus of this study to mimic what is most important to the commercial harvest of rosmarinic acid from the proprietary KI110 clonal line.

Representative Raman spectra of the KI110 (set I to IV) and Native (set V to IX) plant leaves are displayed in Figure 1A. There are many peaks present, and peak assignments are shown in Supplemental Table S3. The primary difference between the KI110 and Native plant

spectra is the 1598 ± 4 cm^{-1} (n = 3,774) peak amplitude, hereafter listed as the 1600 cm^{-1} peak. There are also variations within each plant type, with a difference of 13% in the KI110 plant and 12% in the Native plant. The rosmarinic acid spectrum's most intense peak at 1601 cm^{-1} is assigned to the ring C=C stretching vibrations.[31] For rosmarinic acid solutions, there is a linear increase in the 1600 cm^{-1} peak amplitude with increased rosmarinic acid concentration (data not shown). It is assumed that the peak amplitude difference measured for the KI110 and Native plants reflects, in part, differences in rosmarinic acid concentration. In plant tissues, the 1600 cm^{-1} peak is often assigned to aromatic species, including the phenylpropanoid-based lignin polymer.[32] Lignin is not typically prevalent in the cell wall of plant leaves (although it is found in the stem), however, other aromatic species may be present. A variety of essential oils are commonly found within spearmint. The most abundant essential oil in Native spearmint is carvone,[33] which has a Raman peak at 1623 cm^{-1} that is assigned to the ring C=C stretching vibrations.[34] The percentage of carvone relative to all extracted essential oils in Native spearmint grown in India and Illinois were 46.9-76.6%[35] and 70.9%,[36] respectively. The cultivars used within the current study were bred to have minimal carvone (data not shown).

Correlation of the 1600 cm^{-1} Peak Amplitude and Peak Area to Relative Rosmarinic Acid Abundance

Sampling differences caused by leaf thickness or surface roughness can affect the Raman spectrum and complicate quantitative analyses. Sampling variation can sometimes be accounted for by computing a ratio of the peak area for the varying component and a peak area representing a non-varying component. Several Raman peak area ratios were analyzed to see if they correlated with a simple linear regression to the rosmarinic acid concentration measured with HPLC. Table 1 shows the normalized ratios for the 1600 cm^{-1} peak relative to the 741, 990, and

1521 cm^{-1} peaks, which were primarily assigned to chlorophyll, cellulose, and carotenoids, respectively.[37] Similar values were obtained for all three ratios (a notable exception is the KI110 set II).

The normalized 1600 cm^{-1}/990 cm^{-1} ratios showed the best correlation to rosmarinic acid concentration with an R^2 value of 0.93. The 1600 cm^{-1} peak amplitude had an R^2 of 0.92, which is nearly as good as the 1600 cm^{-1}/990 cm^{-1} ratio, suggesting that sampling differences were not a significant issue with these leaves. Overall, these correlations were surprisingly good, given the many differences between the Raman measurement and the HPLC measurement. Raman spectroscopy measures the abundance of rosmarinic acid within the leaf, which is not necessarily the amount available for extraction. Extraction is rarely 100% efficient and must be performed before the HPLC analysis. In addition, the Raman analysis likely measures only the rosmarinic acid near the adaxial surface since absorption and scattering limit the light penetration through the leaf. However, the results suggest that Raman peak area ratios can be used to determine the relative abundance of rosmarinic acid without having to perform an HPLC analysis.

Factors Affecting Sampling and Raman Spectra: Cellular Structure and Leaf Age

There were two relevant structures within the spearmint adaxial leaf surface, epidermal cells and trichomes. Optical images of representative epidermal cells and a trichome are displayed in Figure 1B. Figure 2 shows the 1600 cm^{-1}/990 cm^{-1} ratios for KI110 and Native trichomes and epidermal cells. As expected, comparing the epidermal cells or trichomes, the ratios of the KI110 plants were statistically larger than the Native plants, with the *p*-value less than 0.0001. The ratios for the KI110 plants were larger for the trichomes compared to the epidermal cells. In Native cells, however, this increase was not measured.

These data indicate that rosmarinic acid abundance varies within the cellular structures of the leaves. This conclusion is useful for two reasons: first, the same cellular structures should be measured when comparing different plant populations. Second, spatially dependent physiological information about rosmarinic acid has been gained using Raman spectroscopy. This could benefit future breeding efforts. As typical for plants, there were several outliers in the data (Figure 2). Most outliers were toward larger ratios and presumably higher rosmarinic acid abundance. Although not the goal of this work, this highlights that Raman measurements may be useful in future plant breeding efforts aimed at achieving high metabolite concentrations.

The rosmarinic acid abundance as a function of leaf age was explored to see if there was variation between younger and older leaves. There are typically hundreds of leaves on each plant. New leaves emerge from the top of the seedling, and the leaves farther down the stem are older. In this study, the leaves were counted from the top of the plant, as the older leaves can be the first to die and may not be consistent from plant to plant. Leaf 3 was the third leaf from the top of the plant stalk, and so on for leaf 4 and 5. Figure 3 shows the 1600 cm^{-1}/990 cm^{-1} ratio distribution and statistical differences within the KI110 and Native plants for leaves 3, 4, and 5. There were no statistical differences in the ratio for the KI110 or Native epidermal cells with different leaf ages (Figure 3A and 3C). For the trichomes (Figure 3B and 3D), the ratio increased when comparing leaves 3 and 4, and 3 and 5. Although the differences in the ratios are relatively small, the difference in the rosmarinic acid concentration may be significant. To explore this, a calibration of the Raman peak area ratio was performed.

Rosmarinic Acid Concentration Determination from Raman Spectra with Partial Least Squares Regression (PLSR).

Univariate calibration with standard rosmarinic acid solutions was explored. Ultimately, this analysis was not possible since the 1600 cm^{-1} peak amplitude measured for the leaves was 7.5-times larger than the peak amplitude for a saturated rosmarinic acid solution (data not shown). As a result, chemometrics was used to obtain rosmarinic concentrations from the Raman spectra.

As stated above, Raman spectra often need to be preprocessed to obtain a reliable chemometric model. Principal component analysis was used for exploratory analysis of KI110 and Native spectra (data not shown), and no clusters or trends were observed from these raw data. Preprocessing methods such as normalization, interpolation, and derivatization on the Raman spectra were tested to see if trends or clusters formed in the loadings and scores plots from PCA; however, there were none and moved to PLSR analysis. For the PLSR model, Raman spectra without preprocessing were used first (data not shown). The PLSR model was cross-validated with the leave-one-out method. Then interpolation was performed as a preprocessing step, and the resulting PLSR model had a higher R^2 (0.96) and lower estimated mean squared error of prediction (MSEP, 0.0000674) compared to the model using spectra without preprocessing and only interpolation as a preprocessing step was used in further analysis. The MSEP versus components plot is in Supplemental Figure S4B, which shows that three principal components produce the best model. The region of the Raman spectra that most influenced the model (where the most variation was between spectra) was around the 1600 cm^{-1} Raman peak, as seen in Supplemental Figure S4A. From the data in Table 2, the predicted concentrations were relatively close to the measured concentrations. The largest percent error

calculated was for the Native sets V and Vl, with 28% and 64%, respectively. Similarly, in comparison to the Raman peak area ratios in Table 1, the set II concentration from PLSR was lower than the HPLC determined concentration. The calibration model developed using PLSR successfully predicts rosmarinic acid concentration using the Raman spectrum. The current proof-of-concept study used a model that was built and validated with 9 data points. For a real-world implementation, the model should ideally contain more data points.

Conclusions

In summary, it is possible to semi-quantitatively report a plant metabolite's relative abundance using Raman peak area ratios in a fraction of the time it takes to perform an HPLC analysis. While this does not reveal the metabolite's absolute concentration, a relative abundance can be quickly ascertained, which may be ideal for determining the optimal time to harvest. This method can be used directly with no sample preparation and can measure leaves, stems, and roots.[38] These studies used a Raman microscope. A suggested future avenue to investigate is the use of a handheld Raman spectrometer for measurements in the field or greenhouse. A handheld Raman spectrometer typically has a working distance of about 5-10 mm and spot size on the order of hundreds of microns. As mentioned above, it is also recommended that similar Raman measurements may be useful for future plant breeding efforts aimed at developing plants that produce a large amount of the metabolite.

Declarations

Acknowledgments

The U.S. Department of Energy supported this research, Office of Science, Office of Biological and Environmental Research (BER) through Ames Laboratory. The Ames Laboratory is operated for the U.S. Department of Energy by Iowa State University under Contract No. De-

AC02-07CH11358. The authors also thank Dr. Yumou Qiu from the statistics department at Iowa State University for his guidance with PLSR.

Conflict of Interest Statement

Kemin Industries, Inc., has a financial interest in using the developed methods.

Figures and Tables

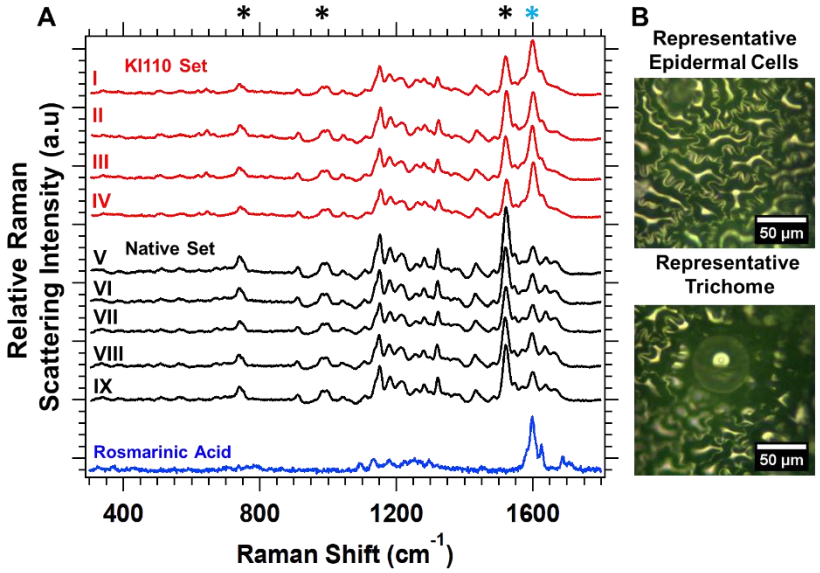

Figure 1. A) Average Raman spectra of KI110 (red) and Native sets (black) and rosmarinic acid (blue). The number of replicates for each average spectrum is listed in the experimental section. The Raman peak at 1600 cm^{-1} (indicated with a blue asterisk) is assigned, in part, to rosmarinic acid. The spectra have been offset and background subtracted for clarity. B) Representative optical images of epidermal cells and a trichome (also showing some epidermal cells) on an adaxial leaf surface where Raman measurements were collected. The spectra shown in panel A were averages of both epidermal cells and trichomes.

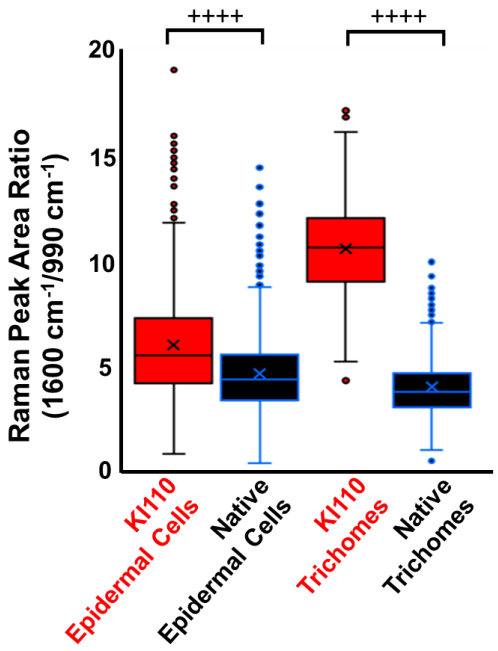

Figure 2. The relative rosmarinic acid abundance determined from the 1600 cm^{-1}/990 cm^{-1} ratios within the epidermal cells and trichomes of KI110 and Native plants. *p*-values were obtained by one-way ANOVA and are shown in Supplemental Table S2. $p < 0.0001$ was represented with ++++. Three outliers with values between 20-25 were removed from the plot for better clarity.

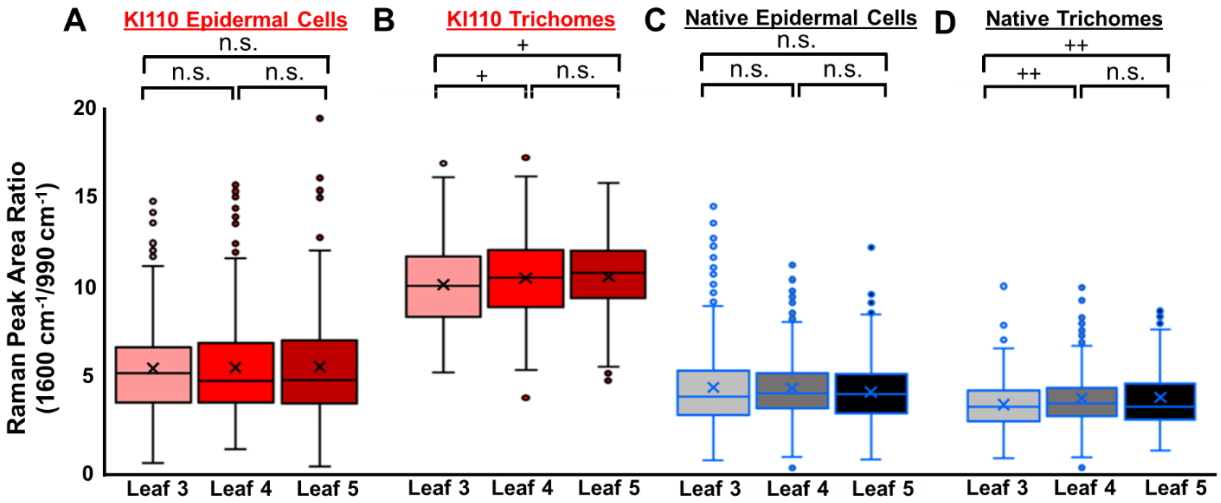

Figure 3. The relative rosmarinic acid abundance determined from the 1600 cm^{-1}/990 cm^{-1} ratios as a function of leaf age for the A) KI110 epidermal cells, B) KI110 trichomes, C) Native epidermal cells, and D) Native trichomes. *p*-values were obtained by one-way ANOVA and are shown in Supplemental Table S2. $p < 0.05$ was represented with +, $p < 0.01$ was represented with ++, and values that were not statistically different ($p \geq 0.05$) were represented with (n.s.). Three outliers with values between the 20-25 ratios were removed from the plot for better clarity.

Table 1. Normalized Raman peak area ratios, 1600 cm^{-1} peak amplitudes, and HPLC derived rosmarinic acid concentrations.[4]

	(1600 cm^{-1} /741 cm^{-1}) Normalized Ratios[1]	(1600 cm^{-1} /990 cm^{-1}) Normalized Ratios [1]	(1600 cm^{-1} /1521 cm^{-1}) Normalized Ratios [1]	1600 cm^{-1} Normalized Raman Peak Amplitude (a.u) [1]	Normalized HPLC Rosmarinic Acid Concentration (mg/g) [2]
KI110 Set					
I	1.00	1.00	1.00	0.99	0.91
II	0.53	0.76	0.62	0.87	1.00
III	0.83	0.83	0.83	0.97	0.82
IV	0.96	0.97	1.00	1.00	0.94
Native Set					
V	0.07	0.09	0.08	0.39	0.14
VI	0.09	0.12	0.11	0.43	0.12
VII	0.12	0.08	0.12	0.36	0.26
VIII	0.14	0.11	0.14	0.48	0.25
IX	0.10	0.09	0.11	0.41	0.32
R^2	0.83[3]	0.93[3]	0.87[3]	0.92[3]	---

[1] Averages from all plants within sets I, II, III, *etc*., including epidermal cells and trichomes. Peak areas were determined by fitting the 741, 990, 1521, and 1600 cm^{-1} Raman peaks to a Gaussian.
[2] Average value from three replicate measurements
[3] R^2 is from the linear correlation between values in this column and the mean rosmarinic acid concentration measured by HPLC.
[4] Supplemental Table S4 contains the Raman values prior to normalization.

Table 2. PLSR Results with Raman Spectroscopy and HPLC for Rosmarinic Acid Concentration

	HPLC Measured Rosmarinic Acid Concentration (mg/g)	Predicted Rosmarinic Acid Concentration (mg/g) from PLSR of Raman spectra	Percent Error
KI110 Set			
I	0.046	0.047	3
II	0.050	0.042	19
III	0.041	0.046	10
IV	0.047	0.047	0
Native Set			
V	0.007	0.009	28
VI	0.006	0.004	64
VII	0.013	0.011	16
VIII	0.013	0.015	16
IX	0.016	0.017	6

$R^2 = 0.96$

Estimated Mean Squared Prediction Error (MSEP) (3 component) = 0.000067

Percent Error = $\frac{|(Predicted\ Concentation - HPLC\ Concentration)|}{HPLC\ Concentration} * 100$

Calculated Prior to Rounding Values

References

1. Akula, R.; Ravishankar, G. A., Influence of abiotic stress signals on secondary metabolites in plants. Plant signaling & behavior 2011, 6 (11), 1720-1731.

2. Schulz, H.; Baranska, M., Identification and quantification of valuable plant substances by IR and Raman spectroscopy. Vibrational Spectroscopy 2007, 43 (1), 13-25.

3. Chandler, L.; Huang, B.; Mu, T. T. In A smart handheld Raman spectrometer with cloud and AI deep learning algorithm for mixture analysis, Next-Generation Spectroscopic Technologies XII, International Society for Optics and Photonics: 2019; p 1098308.

4. Pelletier, M., Quantitative analysis using Raman spectrometry. Applied spectroscopy 2003, 57 (1), 20A-42A.

5. Gray, S. R.; Peretti, S. W.; Lamb, H. H., Real-time monitoring of high-gravity corn mash fermentation using in situ raman spectroscopy. Biotechnology and bioengineering 2013, 110 (6), 1654-1662.

6. Iversen, J. A.; Ahring, B. K., Monitoring lignocellulosic bioethanol production processes using Raman spectroscopy. Bioresource technology 2014, 172, 112-120.

7. Shih, C.-J.; Lupoi, J. S.; Smith, E. A., Raman spectroscopy measurements of glucose and xylose in hydrolysate: role of corn stover pretreatment and enzyme composition. Bioresource technology 2011, 102 (8), 5169-5176.

8. Shih, C.-J.; Smith, E. A., Determination of glucose and ethanol after enzymatic hydrolysis and fermentation of biomass using Raman spectroscopy. Analytica chimica acta 2009, 653 (2), 200-206.

9. Ewanick, S.; Schmitt, E.; Gustafson, R.; Bura, R., Use of Raman spectroscopy for continuous monitoring and control of lignocellulosic biorefinery processes. Pure and Applied Chemistry 2014, 86 (5), 867-879.

10. Ewanick, S. M.; Thompson, W. J.; Marquardt, B. J.; Bura, R., Real-time understanding of lignocellulosic bioethanol fermentation by Raman spectroscopy. Biotechnology for biofuels 2013, 6 (1), 1-8.

11. Lawaetz, A. J.; Christensen, S. M.; Clausen, S. K.; Jørnsgaard, B.; Rasmussen, S. K.; Andersen, S. B.; Rinnan, Å., Fast, cross cultivar determination of total carotenoids in intact carrot tissue by Raman spectroscopy and partial least squares calibration. Food Chemistry 2016, 204, 7-13.

12. Akpolat, H.; Barineau, M.; Jackson, K. A.; Akpolat, M. Z.; Francis, D. M.; Chen, Y.-J.; Rodriguez-Saona, L. E., High-Throughput Phenotyping Approach for Screening Major Carotenoids of Tomato by Handheld Raman Spectroscopy Using Chemometric Methods. Sensors 2020, 20 (13), 3723.

13. Anastasaki, E. G.; Kanakis, C. D.; Pappas, C.; Maggi, L.; Zalacain, A.; Carmona, M.; Alonso, G. L.; Polissiou, M. G., Quantification of crocetin esters in saffron (Crocus sativus L.) using Raman spectroscopy and chemometrics. Journal of agricultural and food chemistry 2010, 58 (10), 6011-6017.

14. Lee, K.-M.; Herrman, T. J.; Yun, U., Application of Raman spectroscopy for qualitative and quantitative analysis of aflatoxins in ground maize samples. Journal of Cereal Science 2014, 59 (1), 70-78.

15. Lupoi, J. S.; Hackley, P. C.; Birsic, E.; Fritz, L. P.; Solotky, L.; Weislogel, A.; Schlaegle, S., Quantitative evaluation of vitrinite reflectance in shale using Raman spectroscopy and multivariate analysis. Fuel 2019, 254, 115573.

16. Suhandy, D.; Yulia, M., The use of partial least square regression and spectral data in UV-visible region for quantification of adulteration in Indonesian palm civet coffee. International journal of food science 2017, 2017.

17. Ur Rehman, N.; Al-Harrasi, A.; Boqué, R.; Mabood, F.; Al-Broumi, M.; Hussain, J.; Alameri, S., FT-NIRS Coupled with PLS Regression as a Complement to HPLC Routine Analysis of Caffeine in Tea Samples. Foods 2020, 9 (6), 827.

18. Greaves, J. A.; Narasimhamoorthy, B.; Wildgen, S.; Barkley, R.; Ruden, S., Spearmint plant denominated KI-MsEM0110. Google Patents: 2017.

19. Narasimhamoorthy, B.; Zhao, L.; Liu, X.; Yang, W.; Greaves, J., Differences in the chemotype of two native spearmint clonal lines selected for rosmarinic acid accumulation in comparison to commercially grown native spearmint. Industrial Crops and Products 2015, 63, 87-91.

20. Luo, C.; Zou, L.; Sun, H.; Peng, J.; Gao, C.; Bao, L.; Ji, R.; Jin, Y.; Sun, S., A Review of the Anti-Inflammatory Effects of Rosmarinic Acid on Inflammatory Diseases. Frontiers in Pharmacology 2020, 11, 153.

21. Ly, T. N.; Shimoyamada, M.; Yamauchi, R., Isolation and characterization of rosmarinic acid oligomers in Celastrus hindsii Benth leaves and their antioxidative activity. Journal of agricultural and food chemistry 2006, 54 (11), 3786-3793.

22. Kelm, M.; Nair, M.; Strasburg, G.; DeWitt, D., Antioxidant and cyclooxygenase inhibitory phenolic compounds from Ocimum sanctum Linn. Phytomedicine 2000, 7 (1), 7-13.

23. Martins-Gomes, C.; Nunes, F. M.; Sampaio, A.; Souto, E. B.; Silva, A. M., Rosmarinic acid: Sources, bioactivities and health benefits. Phytochemicals: Plant Sources and Potential Health Benefits; Ryan, I., Ed 2019, 109-146.

24. Lee, S. Y.; Xu, H.; Kim, Y. K.; Park, S. U., Rosmarinic acid production in hairy root cultures of Agastache rugosa Kuntze. World Journal of Microbiology and Biotechnology 2008, 24 (7), 969-972.

25. Sik, B.; Kapcsándi, V.; Székelyhidi, R.; Hanczné, E. L.; Ajtony, Z., Recent advances in the analysis of rosmarinic acid from herbs in the Lamiaceae family. Natural Product Communications 2019, 14 (7), 1934578X19864216.

26. Wold, S.; Sjöström, M.; Eriksson, L., PLS-regression: a basic tool of chemometrics. Chemometrics and intelligent laboratory systems 2001, 58 (2), 109-130.

27. De Jong, S., SIMPLS: an alternative approach to partial least squares regression. Chemometrics and intelligent laboratory systems 1993, 18 (3), 251-263.

28. Wold, S.; Martens, H.; Wold, H., The multivariate calibration problem in chemistry solved by the PLS method. In Matrix pencils, Springer: 1983; pp 286-293.

29. Shekarchi, M.; Hajimehdipoor, H.; Saeidnia, S.; Gohari, A. R.; Hamedani, M. P., Comparative study of rosmarinic acid content in some plants of Labiatae family. Pharmacognosy magazine 2012, 8 (29), 37.

30. Fletcher, R. S.; Slimmon, T.; Kott, L. S., Environmental factors affecting the accumulation of rosmarinic acid in spearmint (Mentha spicata L.) and peppermint (Mentha piperita L.). The Open Agriculture Journal 2010, 4 (1).

31. Mariappan, G.; Sundaraganesan, N.; Manoharan, S., Experimental and theoretical spectroscopic studies of anticancer drug rosmarinic acid using HF and density functional theory. Spectrochimica Acta Part A: Molecular and Biomolecular Spectroscopy 2012, 97, 340-351.

32. Lupoi, J. S.; Gjersing, E.; Davis, M. F., Evaluating lignocellulosic biomass, its derivatives, and downstream products with Raman spectroscopy. Frontiers in bioengineering and biotechnology 2015, 3, 50.

33. Kokkini, S.; Karousou, R.; Lanaras, T., Essential oils of spearmint (Carvone-rich) plants from the island of Crete (Greece). Biochemical Systematics and Ecology 1995, 23 (4), 425-430.

34. Schulz, H.; Özkan, G.; Baranska, M.; Krüger, H.; Özcan, M., Characterisation of essential oil plants from Turkey by IR and Raman spectroscopy. Vibrational Spectroscopy 2005, 39 (2), 249-256.

35. Chauhan, R.; Kaul, M.; Shahi, A.; Kumar, A.; Ram, G.; Tawa, A., Chemical composition of essential oils in Mentha spicata L. accession [IIIM (J) 26] from North-West Himalayan region, India. Industrial crops and products 2009, 29 (2-3), 654-656.

36. Wu, Z.; Tan, B.; Liu, Y.; Dunn, J.; Martorell Guerola, P.; Tortajada, M.; Cao, Z.; Ji, P., Chemical Composition and Antioxidant Properties of Essential Oils from Peppermint, Native Spearmint and Scotch Spearmint. Molecules 2019, 24 (15), 2825.

37. Gierlinger, N.; Schwanninger, M., The potential of Raman microscopy and Raman imaging in plant research. Spectroscopy 2007, 21 (2), 69-89.

38. Burkhow, S. J.; Stephens, N. M.; Mei, Y.; Dueñas, M. E.; Freppon, D. J.; Ding, G.; Smith, S. C.; Lee, Y.-J.; Nikolau, B. J.; Whitham, S. A., Characterizing virus-induced gene silencing at the cellular level with in situ multimodal imaging. Plant methods 2018, 14 (1), 1-12.

39. Heraud, P.; Beardall, J.; McNaughton, D.; Wood, B. R., In vivo prediction of the nutrient status of individual microalgal cells using Raman microspectroscopy. FEMS microbiology letters 2007, 275 (1), 24-30.

40. Wiley, J. H.; Atalla, R. H., Band assignments in the Raman spectra of celluloses. 1987.

41. Schulz, H.; Baranska, M., Identification and quantification of valuable plant substances by IR and Raman spectroscopy. Vibrational Spectroscopy 2007, 43 (1), 13-25.

42. Larsen, K. L.; Barsberg, S., Theoretical and Raman spectroscopic studies of phenolic lignin model monomers. The Journal of Physical Chemistry B 2010, 114 (23), 8009-8021.

43. Mariappan, G.; Sundaraganesan, N.; Manoharan, S., Experimental and theoretical spectroscopic studies of anticancer drug rosmarinic acid using HF and density functional theory. Spectrochimica Acta Part A: Molecular and Biomolecular Spectroscopy 2012, 97, 340-351.

44. Ralph, J.; Landucci, L., Lignin and lignans: advances in chemistry. Heitner C 2010, 137.

45. Agarwal, U. P., An overview of Raman spectroscopy as applied to lignocellulosic materials. Advances in lignocellulosics characterization 1999, 201-225.

Appendix. Supplemental Information

Supplemental Figures and Tables.

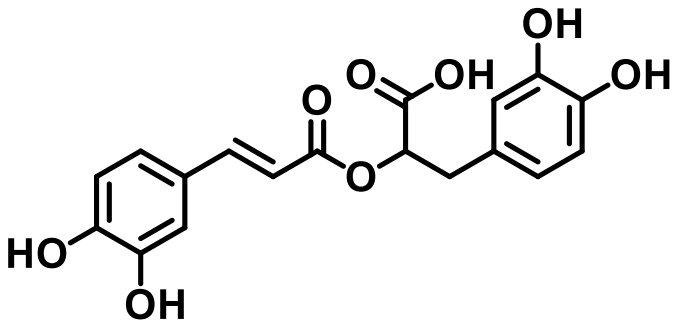

Supplemental Figure S1. Chemical structure of pure rosmarinic acid.

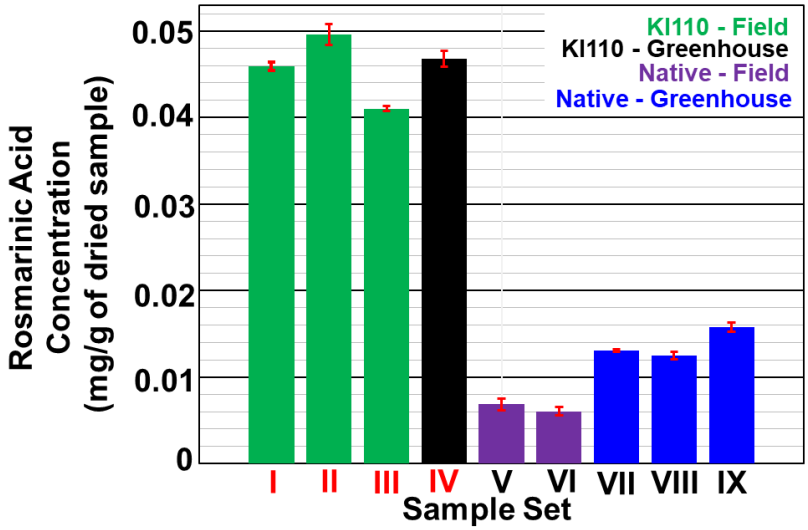

Supplemental Figure S2. HPLC results of extracted rosmarinic acid concentration (mg/g of dried sample) from the nine (I to IX) sets. The plants obtained from the field are colored purple, and green. The plants obtained from the greenhouse are colored blue and black. The rosmarinic acid concentrations from the HPLC analysis were not dependent on where the KI110 plants were grown but did matter for the Native plants. No dependencies were observed where the plants were grown with the Raman analyses discussed in the main manuscript file. The error bars are in red represent one standard deviation (σ) from the sample replicate's average.

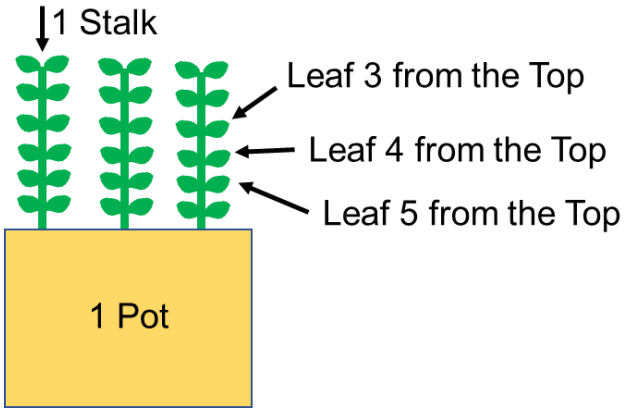

Supplemental Figure S3. Schematic showing the leaf numbering system for Raman spectroscopy measurements. Twenty-one pots of KI110 plants and 21 pots of Native plants were used for Raman measurements. Three stalks and five leaves per stalk were measured for each pot: leaf position 3 and 4 from the top (2 leaves each), and leaf position 5 from the top (1 leaf)). Three epidermal cells and three trichomes on each leaf were collected to ensure a representative signal. Most pots had more than three stalks, so three stalks were chosen randomly within a given pot. All stalks had many more leaves than what is represented in this schematic.

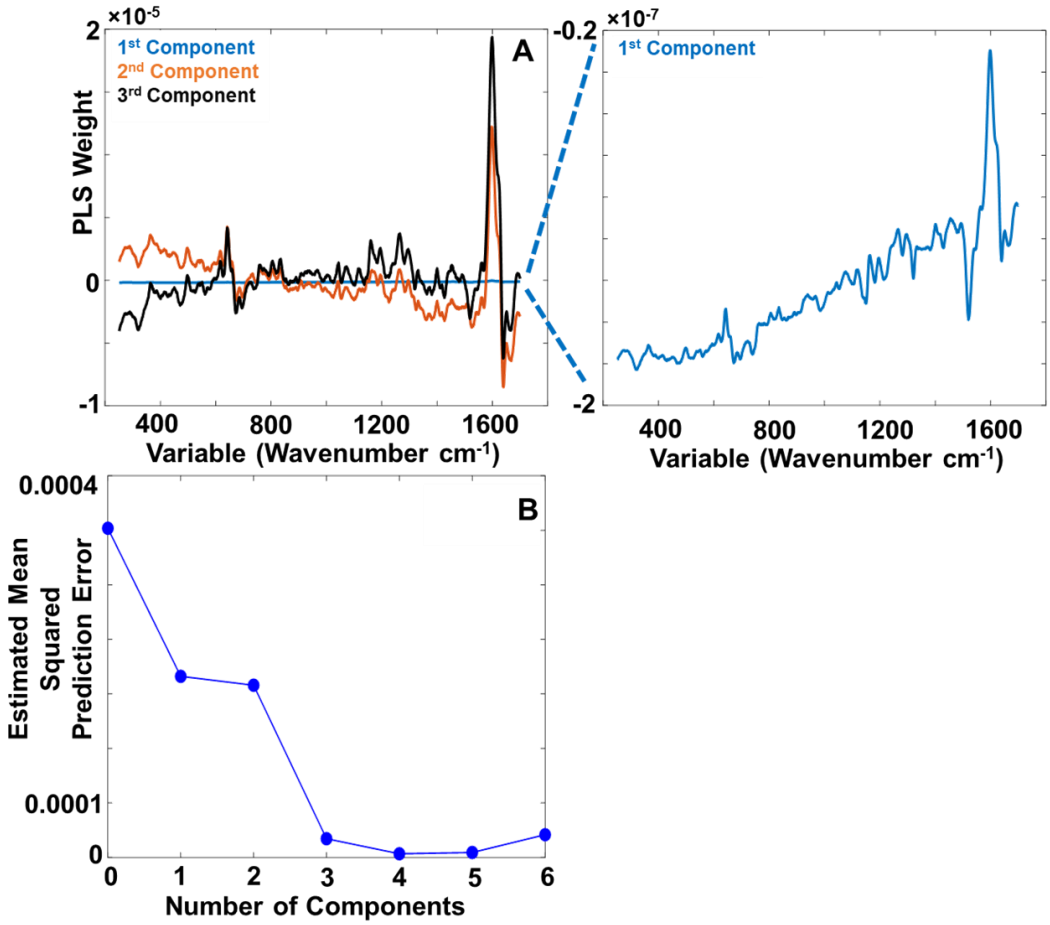

Supplemental Figure S4. Partial least squares regression (PSLR) validation results. A) PLS weight versus original variables (wavenumber, cm^{-1}) reveals how much each component in the PLSR model varies across the variable ranges. In the first three components, the strongest correlation depends on the 1600 cm^{-1}, which is the wavenumber of the most dominant peak in the rosmarinic acid spectrum. B) displays the estimated mean squared prediction error (MSEP) versus the number of principal components. From the MSEP, three or four components were best for model development. In this case, three components were used without possibly overfitting by using more components than necessary.

Supplemental Table S1. The number of measurements and pots for each sample set.

	Number of Pots	Number of Raman Measurements*	Number of HPLC Measurements**
KI110 Set			
I	5	450	3
II	7	630	3
III	4	360	3
IV	5	450	3
Native Set			
V	2	174	3
VI	3	270	3
VII	2	180	3
VIII	7	630	3
IX	7	630	3

*Figure 1 shows the average Raman spectra for each set
**A sample mass from all pots within a set was collected and divided into three for HPLC measurements.

Supplemental Table S2. Calculated *p*-values from ANOVA and the number of measurements that were within manuscript Figures 2 and 3.

Figure 2	***p*-value**	**Number of Measurements (in parenthesis)**
KI110 vs. Native Epidermal Cells	4.3×10^{-34}	KI110 (944) : Native (865)
KI110 vs. Native Trichomes	0	KI110 (945) : Native (776)
Figure 3		
A. Leaf 3 vs. Leaf 4	0.79	Leaf 3 (376) : Leaf 4 (378)
A. Leaf 4 vs. Leaf 5	0.89	Leaf 4 (378) : Leaf 5 (190)
A. Leaf 3 vs. Leaf 5	0.71	Leaf 3 (376) : Leaf 5 (190)
B. Leaf 3 vs. Leaf 4	0.029	Leaf 3 (378) : Leaf 4 (378)
B. Leaf 4 vs. Leaf 5	0.73	Leaf 4 (378) : Leaf 5 (189)
B. Leaf 3 vs. Leaf 5	0.032	Leaf 3 (378) : Leaf 5 (189)
C. Leaf 3 vs. Leaf 4	0.78	Leaf 3 (334) : Leaf 4 (343)
C. Leaf 4 vs. Leaf 5	0.24	Leaf 4 (343) : Leaf 5 (188)
C. Leaf 3 vs. Leaf 5	0.25	Leaf 3 (334) : Leaf 5 (188)
D. Leaf 3 vs. Leaf 4	0.0024	Leaf 3 (308) : Leaf 4 (300)
D. Leaf 4 vs. Leaf 5	0.69	Leaf 4 (300) : Leaf 5 (168)
D. Leaf 3 vs. Leaf 5	0.0099	Leaf 3 (308) : Leaf 5 (168)

Supplemental Table S3. Selected Raman peak assignments from literature.

Wavenumber (cm^{-1})*	**Assignment**	**Associated Plant Metabolite(s)**
740 ± 1	δH-C-O, δN-C-C	Chlorophyll[39]
990 ± 1	νC-C, νC=O	Cellulose[40]
1150 ± 4	νC-C	Carotenoids[41]
1190 ± 4	δH-C-O-C	Lignin[42]/Rosmarinic Acid[43]
1320 ± 1	aliphatic νOH	Lignin[44]/Rosmarinic Acid[43]
1440 ± 1	ring νC=C, δC-H	Lignin[44]/Rosmarinic Acid[43]
1520 ± 1	νC=C	Carotenoids[41]
1600 ± 2	ring νC=C	Lignin45/Rosmarinic Acid[43]

δ, bending
ν, stretching
*n=9 and one standard deviation (σ) from average, and these data were from Figure 1 in the main manuscript file.

Supplemental Table S4. Representative average Raman peak areas and ratios (before normalization) for data shown in Table 1 of the manuscript. The averages and standard deviations were calculated for the 741, 990, 1521 cm^{-1} Raman peak area columns and are at the bottom of the table.

	Raman Peak Area 741 cm^{-1}	**Raman Peak Area 990 cm^{-1}**	**Raman Peak Area 1521 cm^{-1}**	**Raman Peak Area 1600 cm^{-1}**	**1600 cm^{-1} Raman Peak Amplitude (a.u)**	**(1600 cm^{-1} / 741 cm^{-1}) Ratios**	**(1600 cm^{-1} / 990 cm^{-1}) Ratios**	**(1600 cm^{-1} / 1521 cm^{-1}) Ratios**
KI110 Set								
I	20465	14445	72060	193880	3476	9.47	13.42	2.69
II	30129	14864	90405	151430	3048	5.03	10.19	1.68
III	23569	16589	82489	185170	3380	7.86	11.16	2.24
IV	20943	14624	70635	189840	3494	9.06	12.98	2.69
Native Set								
V	38164	20335	111020	23928	1355	0.63	1.18	0.22
VI	34624	17827	93196	28069	1493	0.81	1.57	0.30
VII	20322	19833	73009	22566	1267	1.11	1.14	0.31
VIII	23433	20970	78530	31000	1667	1.32	1.48	0.39
IX	27949	22352	90551	26487	1441	0.95	1.18	0.29
Column Average	27000	18000	80000	----		----	----	----
Column Standard Deviation (1σ)	6000	3000	10000	----		----	----	----

CHAPTER 4. INORGANIC SEMICONDUCTOR QUANTUM DOTS AS A SATURATED EXCITATION (SAX) PROBE FOR SUBDIFFRACTION IMAGING

Avinash Kumar Singh[a], Sadie J. Burkhow[ab], Chamari Wijesooriya[b], Brett W. Boote[ab], Jacob W. Petrich[ab], Emily A. Smith*[ab]

[a]The Ames Laboratory, U.S. Department of Energy, Chemical and Biological Sciences Division, 311 Iowa State University, Ames IA 50011, United States

[b]Department of Chemistry, Iowa State University, Ames IA 50011, United States

*Corresponding Author E-mail: esmith1@iastate.edu

Modified from a manuscript published in *ChemPhotoChem* (2020), https://doi.org/10.1002/cptc.202000195.

Abstract

The photoluminescence (PL) saturation of CdSe/ZnS core/shell inorganic semiconductor quantum dots (QDs) and its utility as a probe for saturated excitation (SAX) microscopy are reported. Under saturating excitation power densities, the PL signal was demodulated and recorded at harmonics of the fundamental frequency. For commercially available Qdot® 655 ITK™ QDs, the power density required to achieve saturation was dependent upon the local environment of the QDs. For QDs deposited and dried on a glass substrate, the excitation power density required for PL saturation was less than 1 kW/cm^2. Compared to this, saturation of PL for QDs dispersed in water required an excitation power density greater than 200 kW/cm^2. This observation is manifested as a limitation in the imaging of hydrated samples, as demonstrated for HeLa cells labelled with biotinylated-phalloidin followed by labelling with streptavidin-coated QDs. As saturation affects the obtained spatial resolution in several imaging formats, including confocal imaging, the provided data will aid in obtaining the optimal spatial resolution when using QD probes to image biological samples.

Introduction

Subdiffraction microscopy techniques enable accurate measurements of sample features smaller than the Abbe diffraction limit, which is approximately a couple of hundred of nanometers using visible light. Generally, there are two strategies employed in experiments designed to obtain subdiffraction imaging with luminescence: (i) use of spatial or temporal modulation of the excitation light to reduce the point spread function (PSF); or (ii) generation of a composite image from localized, photoswitchable fluorophores in an iterative manner. Examples of excitation modulation-based sub-diffraction techniques include stimulated emission-depletion (STED) microscopy,[1] structured illumination microscopy (SIM),[2] saturated structured illumination microscopy (SSIM),[3] plasmonic structured illumination microscopy (PSIM),[4] and saturated excitation (SAX) microscopy.[5-6] Common examples of localization-based sub-diffraction techniques are photo-activated localization microscopy (PALM)[7] and stochastic optical reconstruction microscopy (STORM).[8] Many of these techniques have been shown to push the spatial resolution well below 100 nanometers, facilitating the routine imaging of previously unresolvable cellular structural details.[9] Compared to the other subdiffraction imaging techniques that require pulsed excitation schemes, complex optical setups, careful selection of caged/photoswitching fluorophores, or extensive post processing of large data files, SAX microscopy is easier to implement.

SAX microscopy, pioneered by Fujita and coworkers,[5-6] is a simple approach to subdiffraction imaging using saturation of the relevant transition for resolution improvement. SAX imaging has been successfully implemented in fluorescence as well as Raman-based methods.[5, 10] A high intensity modulated excitation source is tightly focused on the sample. Nonlinearity in the PL is produced when the intense illumination results in saturation of the population difference between ground and the excited states.[11] For a Gaussian excitation beam,

this phenomenon occurs in the central, most intense region of the focal spot thereby reducing the effective PSF.[5] Demodulation of the signal at higher harmonics ($n\omega$, where n is a positive integer) of the fundamental modulation frequency (ω)) using a lock-in-amplifier and subsequent image construction yields an image with improved spatial resolution.[5-6, 12-14] The higher the harmonic used to construct the image, the better the expected spatial resolution, but also the lower the signal that is obtained when using the same excitation power density. The improvement of the spatial resolution is theoretically unlimited, though finite laser power, sample integrity, and detector efficiency all contribute to a limit of observable resolution gain.[5] The high laser irradiances required for SAX microscopy, in particular, pose a challenge in the form of photobleaching of traditional organic fluorophores. SAX microscopy has been demonstrated for high-resolution imaging of biological samples using fluorescent dyes,[5] gold nanoparticles,[15] and fluorescent nanodiamonds.[12]

In this work, SAX microscopy has been extended to inorganic semiconductor QDs. The photostability and bright PL of the inorganic semiconductor QDs make them a favorable candidate for SAX microscopy experiments where high laser irradiance is required to achieve saturation and to recover higher harmonics of the signal. Commercially available CdSe/ZnS core/shell QDs (Qdot® 655 ITK™, Thermo Fisher Scientific) were used for the present study. These QDs have superior optical properties over QDs that are surface passivated by organic molecules.[16] In addition to their optimal optical properties, QDs have flexibility in their surface modification, and commercially available QDs have become an attractive choice as labels in cellular imaging.[17-20] While QDs have previously been used to produce sub-diffraction images through second- and third-order photon antibunching,[21] this mechanism is different than that of saturated excitation, which is used in the present work.

Understanding PL saturation of QDs also has implications for other imaging formats. Theoretical and experimental studies performed by Brakenhoff and coworkers showed that fluorescence saturation leads to a deterioration in the sectioning capability in a confocal microscope.[22] Ultimately, in this case saturation results in a degradation of spatial resolution. In addition, the PL saturation characteristics of QDs have been recently probed for their viability in schemes like STED, where the saturation intensity of the fluorophore determines the achieved lateral spatial resolution.[23-24] Thus, our results presented here have implications for achieving the best spatial resolution in several optical imaging formats.

Materials and Methods

Materials

The 200-nm orange fluorescent beads (FluoSpheres™ Carboxylate-Modified Microspheres, 0.2 µm, orange fluorescent (540 nm excitation/560 nm emission) 2% solids), Qdot® 655 ITK™ quantum dots (emission maximum ~655 nm) with carboxyl modifications, and Qdot® 655 ITK™ Streptavidin-conjugate QDs were purchased from ThermoFisher Scientific. It has been shown previously for this class of QDs that surface functionalization does not have a significant effect on the photophysics.[36]

Steady-state and time-correlated, single-photon counting (TCSPC)

The absorption spectra were collected using an Agilent 8453 UV-visible spectrometer and the photoluminescence spectra were collected using an Agilent Cary Eclipse fluorescence spectrophotometer. The quantum yields of the photoluminescence were measured relative to that of a standard sample, Atto 590 in ethanol using a method reported in literature.[27] For aqueous samples, a standard absorption measurement suffices for quantifying the number of input photons for the yield measurement. Such a measurement is problematic, however, for the solid sample. A standard transmission measurement overestimates the absorption by lengthening the

pathlength of the sample and increasing the contribution from scattered light. Consequently, for solid samples, fluorescence-excitation spectra were used to determine the absorption.

The PL lifetimes were recorded using a time-correlated single-photon counting (TCSPC) setup based on a SPC-830 TCSPC module (Becker & Hickl GmbH). The excitation wavelngth was 531 nm delivered by an LDH-D-TA-530 PicoQuant pulsed laser diode head (Berlin Germany). Use of 531 nm excitation was a restriction imposed by the available source. However, we do not expect significant differences in the excited state dynamics of the QDs upon changing the excitation wavelength from 532 nm to 531 nm. For all the experiments the repetition rate was set to 5 Mhz with the PDL 800-B PicoQuant laser control module (Berlin Germany). The samples were placed on a custom-built sample holder on an inverted microscope (Nikon, Ti) with a 60× oil-immersion microscope objective (1.49 N.A. APO TIRF). The excitation pulse was fed into the back port of the microscope using a dichroic mirror (LDP02-532RU-25-Semrock) and the PL was collected in the epi direction with a long-pass emission filter placed in front of the single-photon counting detector (SPCM-AQR-16, Excelitas) to eliminate any residual excitation light. The average laser power was measured in the sample plane of the microscope. The PL decays were analyzed with a commercially available software package (SPCImage 8.1).

Saturated photoluminescence

An instrument schematic of the saturated PL setup is shown in the supplementary information (Figure S4). The modulation of the excitation source was achieved using a Mach-Zehnder interferometer. The output of a 150-mW 532-nm diode laser (Coherent, Santa Clara, CA) was separated into two arms using a 50:50 nonpolarizing beam splitter cube (Stock #11-289, Edmond optics), which then passed through two acousto-optic modulators (AOM-402AF1, IntraAction Corp, Bellwood, IL) operating at 40.00 MHz and 40.01 MHz. The first-order

diffracted beams from the AOMs were selected by an aperture and recombined at a second identical beam splitter cube, which results in a sinusoidal modulation of the laser beam at the difference frequency of the two AOMs (in this case, 10 kHz). One arm emanating from the recombination beam splitter passed through a neutral density filter to an avalanche photodiode (APD, C12703, Hamamatsu). The APD output was coupled to the reference input of the lock-in amplifier (SR865A, Stanford Research Systems). A home-built 10× beam expander expands the second arm from the recombination beam splitter. The expanded beam is fed into the back port of an inverted microscope (Nikon Eclipse Ti2) equipped with a Plan Apo DC 100× Oil (1.40 NA) objective. The PL signal was collected in the epi-direction and detected confocally with a 25-µm pinhole. Excitation light was blocked using a notch filter (NF01-532U-25, Semrock) and a bandpass filter (FF01-630/92-25, Semrock) before signal detection with a photomultiplier tube (PMT1001, Thorlabs). Signal from the PMT was sent into the lock-in amplifier for extracting the signal readings at the fundamental (10 kHz), second harmonic (20 kHz) and third harmonic (30 kHz). Image acquisition was performed by scanning the sample over the excitation beam using a xyz-nanopositioning stage (Nano-LP200, Madcity Labs) and demodulating the signal at each pixel at the desired frequency. The image acquisition software (GPScan VI)37 is based on Labview and a National Instruments multifunction I/O device (PCIe-6353, National Instruments, Austin, TX). Graphs were generated within the scientific and analysis graphing software Igor Pro 6.36 (Wavemetrics, Inc., Lake Oswego, OR). MATLAB 2018b was used to generate the images.

Sample Preparation

Preparation of QD samples for saturation experiments: Carboxyl-functionalized Qdot® 655 ITK™ QDs (8 µM) were diluted until an optical density of 0.2 at 532 nm was achieved (40 µL in 3 ml deionized water) which is approximately 100 nM. Adhesive-backed

rubber wells were fixed on a clean glass coverslip and filled with the QD dispersion. The dried QD sample was made by drop casting the QDs on a clean glass coverslip. After evaporation, a film of QDs was obtained on the coverslip.

Preparation of cells for imaging: HeLa cells (human cervical cancer cell line) were used for the study, and actin fibers were selected as the imaging target. DMEM medium supplemented with 10% fetal bovine serum, 12.5 mM streptomycin, and 36.5 mM penicillin was used as the culturing medium for this cell line. Cells were subcultured every other day and maintained at 37 °C in a water-jacketed CO_2 (5%) incubator. For the imaging experiment, cells were grown on coverslips to obtain an approximately 40% confluence level. The cell samples were washed twice with pre-warmed phosphate-buffered saline (PBS, pH 7.4) and fixed using a 4% formaldehyde solution in PBS for 15 minutes at room temperature. Cells were washed twice with PBS buffer and incubated with 0.1% TritonTM X-100 (Sigma-Aldrich) in PBS for 15 minutes. Then the cells were washed three times with PBS buffer. 20 µL of Biotin-XX phalloidin (Invitrogen, Thermo Fisher Scientific) methanolic stock solution (20 µM) was diluted in 200 µL PBS with 1% bovine serum albumin (BSA), and the cells were incubated with this solution for 15 minutes. The streptavidin-coated quantum dot solution was prepared by mixing 2.5 µL of 2 µM Qdot® 655 ITK™ Streptavidin Conjugate (Thermo Fisher Scientific) with 100 µL of Qdot® incubation buffer (2% BSA in 50 mM borate buffer, pH 8.3, containing 0.05% sodium azide, Thermo Fisher Scientific) and 100 µL PBS. Cells were incubated with this solution for 30 minutes. The cell sample was subsequently washed several times and imaged in PBS buffer.

Results and Discussion

Photophysical properties of Qdot® 655 ITK™ quantum dots

The primary motivation of this work was to investigate the photophysical and saturation properties of core/shell QDs as a luminescent labelling agent for SAX microscopy of biological

samples. To this effect, photophysical and saturation characteristics of QDs were investigated at different excitation power densities. The excitation power densities affect the onset of saturation as well as the relative strength of the harmonic signal. The PL spectra of the QDs were measured in aqueous media and dried on a glass substrate, and no significant shifts in the PL spectra were observed (Figure 1). The concentration of the QDs in the aqueous media was set to a value where the deviations from the linear behavior of PL with increasing excitation power density were captured, while keeping the PL signal levels within the linear regime of the detector. The final optical density of the QD solution was 0.2 at 532 nm.

In order to understand the PL saturation behavior of QDs, it is useful to consider the relationship between the PL lifetime and saturation. The saturation intensity I_{Sat} is defined as $I_{Sat} = 1/\sigma\tau$ where σ is the absorption cross section and τ is the excited state lifetime of the luminescence.[23] Since the QD PL lifetime is environmentally dependent, a comparison was made between the PL lifetimes of QDs in aqueous media and dried on a glass substrate.

As shown in Figure 2, the PL decay traces using two different excitation power densities were satisfactorily fitted with a biexponential model for both QDs dispersed in water and dried on the glass substrate. Wang *et al.* have attributed the faster lifetime component of a few nanoseconds to core-state recombination and the slower lifetime component of tens of nanoseconds to the surface states.[26] While both lifetime components are likely to play a role in PL saturation (also, assuming the absorption cross section of Qdot® 655 ITK™ QDs is the same for both samples and approximately of the order 10^{-18} m^2),[27] it is sufficient to use the average lifetime to understand the trends in PL saturation. For QDs in solution and QDs dried on a glass substrate, the individual lifetime components are similar using an excitation power density of 200 kW/cm^2, although the faster component of approximately 7 ns had a higher amplitude for the

QD sample dispersed in water (Table 1). This results in an overall faster average lifetime of 22.7 ns for the QDs dispersed in water compared to 24.2 ns for the QDs dried on a glass substrate. At a higher excitation power density of 700 kW/cm^2, a shortening in τ_{av} was observed for the QDs dispersed in water. This observation resulted from the decrease in both τ_1 and τ_2 lifetime components. The faster time constant (τ_1) of 6.8 ns reduced to 4.9 ns and the slower time constant (τ_2) reduced from 30.2 ns to 27.5 ns (Table 1). However, the associated amplitudes remain almost unchanged for QDs dispersed in water at the higher power density of 700 kW/cm^2. The decrease in the PL lifetime for QDs at higher excitation power densities has been attributed to biexciton and multiexciton generation.[28-31] At the power density of 700 kW/cm^2 (which is the highest setting for our TCSPC instrument), there was no significant change in τ_{av} for QDs dried on a glass substrate. Based on these lifetimes, it is possible to make a comparison between the expected saturation characteristics of the QDs and organic fluorophores. The QDs used in the current study have an average PL lifetime substantially longer than the typical monoexponential lifetime of organic dyes, for instance Rhodamine 6G (4.1 ns),[32] by a factor of ~5. Also the absorption cross section of these QDs is larger than Rhodamine 6G by two orders of magnitude.[27,33] It is thus expected that the saturation intensity threshold for the QDs will be lower than the typical organic dye, which one expects to correlate with less sample damage. The relative quantum yield of the dried and aqueous QDs reveal a slightly higher quantum yield for the solid sample, which correlates with the PL lifetime data (Table 2). Experimental constraints did not allow the determination of the quantum yields and the respective radiative and nonradiative rate constants at other power densities. However, comparing QDs in solution and dried, it is expected that saturation will be achieved with a dried QD sample at a lower excitation power density.

From an imaging perspective, it is imperative to note that the onset of a second-harmonic signal does not necessarily correspond to an excitation power density that produces a signal level strong enough to construct a satisfactory SAX image. Under identical signal detection parameters (detector gain, lock-in sensitivity and time constant), the second harmonic signal for QDs dispersed in water is weaker than the fundamental signal by approximately an order of magnitude for 1900 kW/cm^2 (Figure 3A). Making a similar estimation for the dried QDs sample is difficult. The is due to the intense PL from the QD film on the glass substrate, which results in detector saturation or damage even before a reasonably strong second harmonic signal is generated. However, these observations clearly demonstrate the difference between the PL saturation threshold for QDs in different environments.

Excitation power dependence of the fundamental (ω) and second harmonic (2ω) frequencies

The intensity of the second harmonic signal as a function of excitation power density is an important guide to the feasibility of using SAX microscopy. The PL saturation behavior was interrogated for the QDs in aqueous media (Figure 3A, B) and dried on a glass substrate (Figure 3C, D) as a function of excitation power density. Examination of the saturation plots revealed the PL of the dried sample departs from linear behavior at a relatively low excitation power density of approximately 0.2 kW/cm^2 (Figure 3C). Comparatively, for QDs dispersed in aqueous media, the saturation in the PL did not occur until the excitation power density was close to 200 kW/cm^2 (Figure 3A). The expanded graph (Figure S1, supplementary information) shows the PL intensity versus excitation power density plot was fairly linear below 200 kW/cm^2. An examination of the second-harmonic signal revealed that the actual saturation set in at somewhat lower excitation power densities as evident from the increase in the second harmonic signal, a direct consequence

of PL saturation (Figure 3B). Using the absorption cross section of the Qdot® 655 ITK™ reported in the literature[27], and the average lifetime of 22.7 ns observed in aqueous media, the saturation intensity was estimated to be < 10 kW/cm^2, which was consistent with the onset of a weak second harmonic signal as shown in Figure S1 (supplementary information). The slightly higher average lifetime observed for the solid sample is consistent with a lower saturation intensity observed for the solid sample (Figure 3C). Nevertheless, based on the inverse relationship between the PL saturation threshold and the PL lifetime as discussed above, the higher threshold of PL saturation for aqueous QDs can be explained by the decrease in the PL lifetime compared to the dried QD sample. It is possible that the concentration of the QDs in the solid sample may explain the high emission intensities. These experiments, however, serve as a good benchmark for the evaluationof the QDs‘ applicability for the SAX microscopy of cells where the medium is aqueous. Also, we rule out the possibility of photobleaching as a cause of loss of linearity in the PL behavior. Using a power density of 235 kW/cm^2 for both aqueous and dry samples, no loss of intensity was observed in a PL intensity vs. time plot (Figure S2, supplementary information).

Resolution calibration of the SAX microscope and imaging of HeLa cells labeled with QDs

A sample was prepared with a dilute QD sample to achieve isolated and small aggregates of QDs spread on a glass substrate, which is necessary to measure the spatial resolution while preventing detector saturation from the intense PL of a dense QD film, as discussed previously. SAX images with a signal-to-noise ratio greater than 22 were collected at the fundamental (10 kHz) and third harmonic frequencies (30 kHz) as shown in Figures 4A, B. The measured spatial resolution is diffraction-limited, as expected, for the image constructed at the fundamental frequency (Figure 4C). There is an average improvement in the spatial resolution of 40 percent

for the third-harmonic image compared to the image constructed by the fundamental frequency (Figure 4C). When imaging 200-nm fluorescent polymer nanoparticles, no statistically significant improvement in spatial resolution was recorded between the SAX image constructed at the fundamental frequency (10 kHz) and that at the second-harmoinc frequency (20 kHz) (Figure S3, Supplementary information). The second-harmonic image of the fluorescent polymer nanoparticles was collected using a 20 kW/cm^2 power density. The highest excitation power density that produced a second harmonic signal without damaging the polymer nanoparticles was 80 kW/cm2. These value are comparable to the excitation intensities reported in the literature for ATTO488, AlexaFluor 488, Rhodamine 6G and Rhodamine B.[34-35] Increasing the excitation intensity to extract higher harmonics for resolution improvement resulted in extensive photobleaching of the polymer nanoparticles, but the photostability of QDs allows much higher excitation intensities to be used without damaging the QDs.

HeLa cells were imaged to examine the utility of the saturation scheme for biological imaging using the QDs. As shown in Figure 5, HeLa cells labeled with QDs were imaged at the fundamental modulation frequency with relative ease. However, within the excitation power limits needed to maintain the cell integrity during image acquisition, a satisfactory second harmonic signal was not measured. As discussed in the previous section for the case of QDs dispersed in water, we suggest that the environment of a hydrated cell affects the excitated state dynamics of the QDs in a way that extraction of the higher harmonic signal is difficult. It is pertinent to note here that the QDs themselves are highly stable under intense irradiation, so the integrity of the fluorescent label is not an issue. This was confirmed by exciting a sample of QD aggregates with an excitation power density in excess of 2 MW/cm^2. At this power level even a satisfactory extraction of third harmonic signal at 30 kHz was facilitated (Figure 4B). QDs are,

thus, a viable option for SAX imaging whenever the sample can withstand similar excitation power densities.

Conclusions

Since saturation depends on the excited-state lifetime, it can be influenced by the environmental factors that affect the excited state dynamics of the luminescent probe. In this case, the CdSe/ZnS quantum dots show distinct behavior in aqueous media compared to when they are in a dried state. When dried, the saturation of PL can be achieved at very low excitation power densities (< 1 kW/cm^2), and a reasonably good third harmonic signal is measured, which facilitates an improvement in the spatial resolution by 40 percent. However, when dispersed in water, the saturation densities needed to extract the second harmonic signal increases by at least two orders of magnitude (>200 kW/cm^2). We suspect that this is due to the shortening of the excited state lifetime of the QDs in the aqueous media. This phenomenon is also manifested when imaging hydrated HeLa cells labeled with QDs. A promising route for SAX imaging of aqueous and biological samples may be found using tailored QDs that have long lifetimes when dispersed in water. We believe that better surface passivation may be a viable route to achieve this. Also, just as for the case for various organic fluorophores, quantum dots of different materials and surface modifications will have correspondingly different saturation efficiencies and ability to generate larger harmonic signals. For example, novel perovskite nanocrystals, which have been shown to have a low saturation[23], can be a potentially suitable candidate.

Declarations

Acknowledgements

This research was supported by the U.S. Department of Energy, Office of Science, Office of Biological and Environmental Research (BER) through the Ames Laboratory. The Ames Laboratory is operated for the U.S. Department of Energy by Iowa State University under

Contract No. DE-AC02-07CH11358. C. W. was supported by the National Science Foundation under Grant Number CHE-1709099.

Figures and Tables

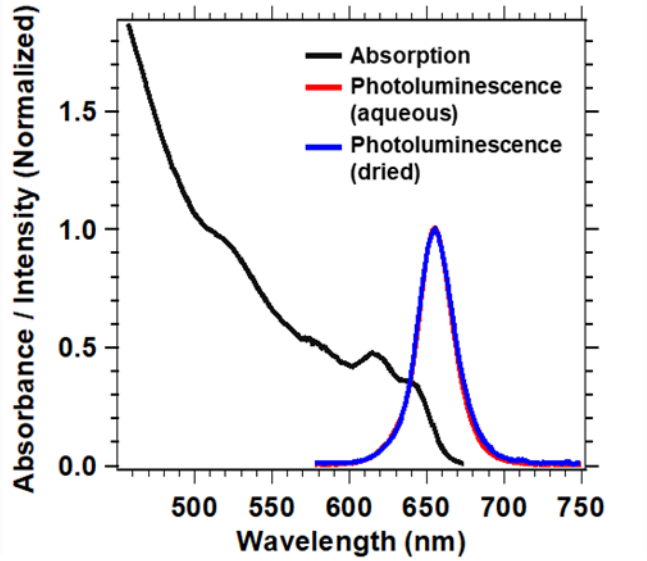

Figure 1. Absorption (black) and PL spectra of Qdot® 655 ITK™ quantum dots in aqueous media (red) and when dried on a glass substrate (blue). PL spectra were collected following 532-nm excitation. The absorption spectrum was normalized at 500 nm and the PL spectra were normalized at the peak maxima of 655 nm.

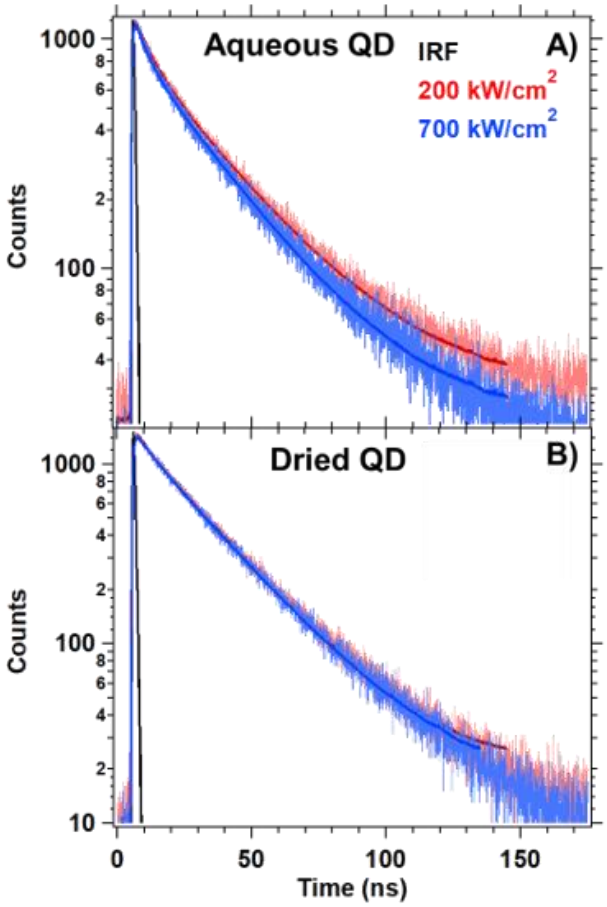

Figure 2. Temporal PL profile of the QDs (**A**) in aqueous media and (**B**) dried on a glass substrate at an excitation power density of 200 kW/cm^2 (red) and 700 kW/cm^2 (blue). The excitation wavelength was 531 nm. The instrument response function (IRF) is the black curve, the exponential fits are the solid red and blue lines.

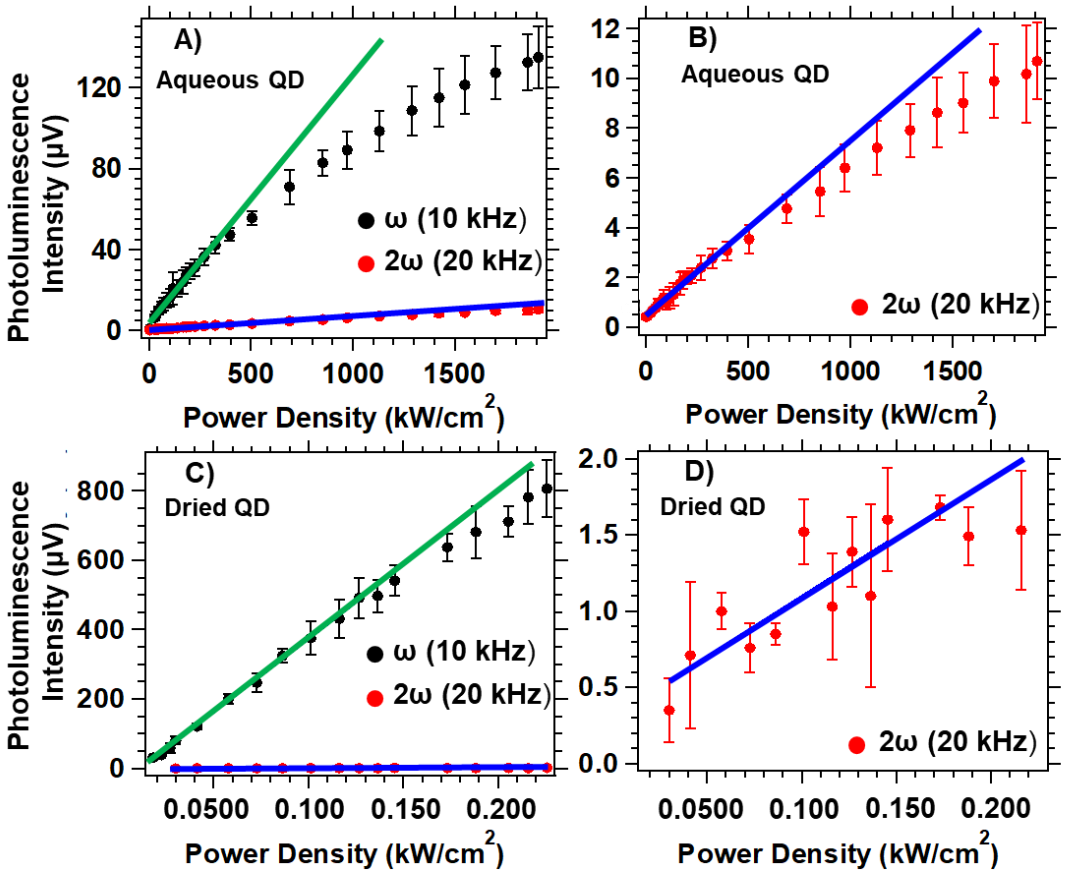

Figure 3: (**A**) Excitation power density vs PL intensity (measured in microvolts, μV) for QDs dispersed in water at the fundamental (ω) and second harmonic (2ω) frequencies. (**B**) An expanded view of the second harmonic plot for QDs dispersed in water. (**C**) Excitation power density vs PL intensity for QDs dried on a glass substrate at the fundamental (ω) and second harmonic (2ω). (**D**) An expanded view of the second harmonic plot for the dried QD sample. Note that the number of the data points for the second harmonic experiment was limited by detector saturation from the intense QD PL at higher power densities.

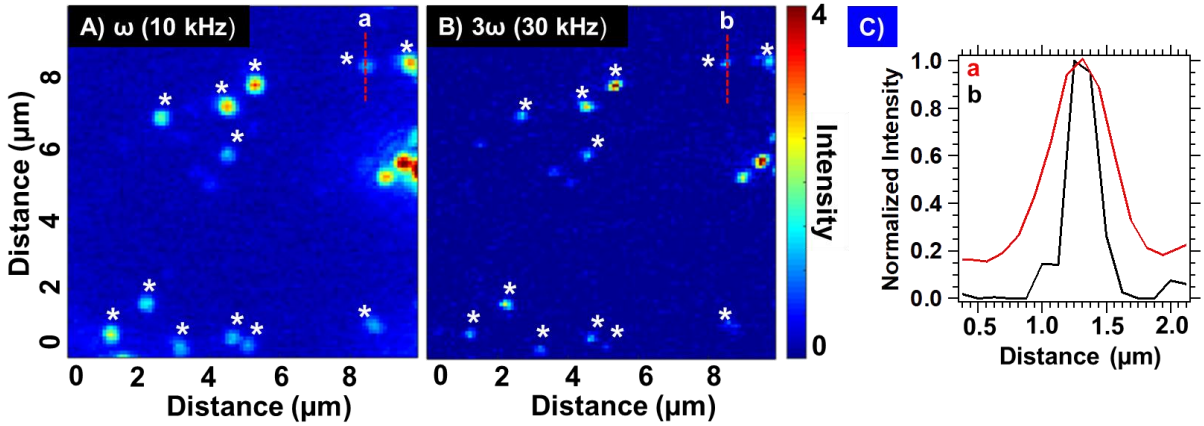

Figure 4. SAX images of QDs dried on a glass coverslip constructed by signal demodulation at the **(A)** fundamental frequency (ω =10 kHz) and (**B**) third harmonic frequency (3ω = 30 kHz). (**C**) Comparison of intensity profiles of the same QD from the fundamental (line a) and third harmoinc (line b) images. The images were collected with a step size of 100 nm, pixel dwell time of 1 ms and a lock-in time constant of 300 μs. The excitation power density in the sample plane was 270 kW/cm^2 and 2.7 MW/cm^2 for fundamental and third harmonic, respectively. The average full-width at half-maximum (FWHM) of 12 QDs (denoted by an asterisk) was calculated. The average FWHM of the intensity profiles was 430 ± 30 nm (i.e., dffraction limited) for the image acquired at ω and 260 ± 60 nm for image acquired at 3ω. It is unknown if these image features are isolated QDs or small aggregates, which may be the reason for relatively large standard deviations.

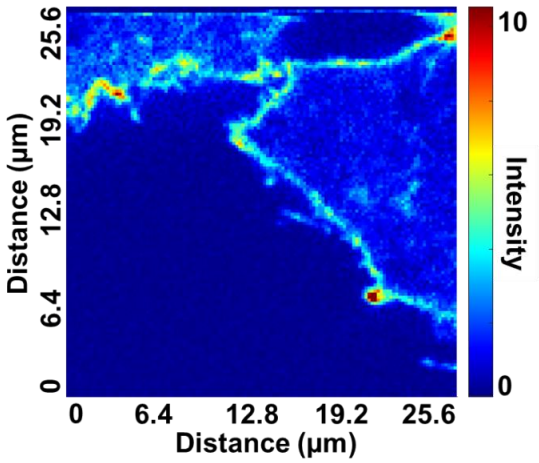

Figure 5: Fundamental frequency (ω =10 kHz) SAX image of HeLa cells labeled with Qdot® 655 ITK™ CdSe/ZnS core/shell QDs. Actin fibers in HeLa cells were first labeled with biotinylated phalloidin. Streptavidin-coated Qdot® 655 ITK™ CdSe/ZnS core/shell quantum dots were then bound to the biotinylated phalloidin. The image was collected with a step size of 100 nm, pixel dwell time of 1 ms, and a lock-in time constant of 300 μs. The excitation power density in the sample plane was 165 kW/cm^2. A representative optical image similar HeLa cells labeled with Qdot® 655 ITK™ quantum dots has been shown in supporting information (Figure S5).

Table 1: Fit parameters for the PL decay traces of the QDs.[a]

Sample	Excitation Power Density (kW/cm^2)	τ_1 (ns)[b]	τ_2 (ns)	A_1[c]	A_2	χ^2	τ_{av}(ns)[d]
Aqueous QD	200	6.8	30.2	0.32	0.68	1.04	22.7
	700	4.9	27.5	0.30	0.70	1.13	20.7
Dried QD	200	6.9	26.6	0.12	0.88	1.18	24.2
	700	6.9	26.7	0.10	0.90	1.14	24.6

[a] PL decay traces were fitted as a sum of exponential functions as $I(\lambda,t) = I_0(\lambda)\sum_i A_i\, e^{-t/\tau_i}$, where $\tau_i$and $A_i$are lifetime and amplitude associated with ith component.[25] [b] τ_1 and τ_2 are PL lifetimes obtained by the biexponential fit of the PL decay traces. [c] A_1 and A_2 are the normalized amplitude associated withτ_1 and τ_2, respectively. [d] τ_{av} is the average lifetime calculated using the relationship $\tau_{av} = \sum_{i=1}^{n} A_i\, \tau_i$.

Table 2: Photophysical properties of the Qdot® 655 ITK™

Sample	Φ	$k_R \times 10^7\ s^{-1}$	$k_{NR} \times 10^7 s^{-1}$
Aqueous QD	0.50	2.2	2.2
Dried QD	0.56	2.3	1.8

Φ is the relative quantum yield calculated at room temperature with Atto 590 dye in ethanol (Φ_{ref}= 0.80) as the reference. Wavelength of excitation was 532 nm. Average lifetimes reported in table 1 for 200 kW/cm^2 have been used for the calculation of radiative rate constant (k_R) and non-radiative rate constant (k_{NR}).

References

1. Hell, S. W.; Wichmann, J., Breaking the diffraction resolution limit by stimulated emission: stimulated-emission-depletion fluorescence microscopy. Opt. Lett. 1994, 19 (11), 780-782.

2. Gustafsson, M. G. L., Nonlinear structured-illumination microscopy: Wide-field fluorescence imaging with theoretically unlimited resolution. Proceedings of the National Academy of Sciences 2005, 102 (37), 13081-13086.

3. Haeberlé, O.; Simon, B., Saturated structured confocal microscopy with theoretically unlimited resolution. Opt. Commun. 2009, 282 (18), 3657-3664.

4. Wei, F.; Liu, Z., Plasmonic Structured Illumination Microscopy. Nano Lett. 2010, 10 (7), 2531-2536.

5. Fujita, K.; Kobayashi, M.; Kawano, S.; Yamanaka, M.; Kawata, S., High-Resolution Confocal Microscopy by Saturated Excitation of Fluorescence. Phys. Rev. Lett. 2007, 99 (22), 228105.

6. Yonemaru, Y.; Yamanaka, M.; Smith, N. I.; Kawata, S.; Fujita, K., Saturated Excitation Microscopy with Optimized Excitation Modulation. ChemPhysChem 2014, 15 (4), 743-749.

7. Patterson, G.; Davidson, M.; Manley, S.; Lippincott-Schwartz, J., Superresolution Imaging using Single-Molecule Localization. Annu. Rev. Phys. Chem. 2010, 61 (1), 345-367.

8. Rust, M. J.; Bates, M.; Zhuang, X., Sub-diffraction-limit imaging by stochastic optical reconstruction microscopy (STORM). Nature Methods 2006, 3 (10), 793-796.

9. Moerner, W. E., Single-molecule mountains yield nanoscale cell images. Nature Methods 2006, 3 (10), 781-782.

10. Singh, A. K.; Santra, K.; Song, X.; Petrich, J. W.; Smith, E. A., Spectral Narrowing Accompanies Enhanced Spatial Resolution in Saturated Coherent Anti-Stokes Raman Scattering (CARS): Comparisons of Experiment and Theory. The Journal of Physical Chemistry A 2020, 124 (21), 4305-4313.

11. Seigman, A. E., Lasers. University Science Books: Mill Valley, California, 1986; p 206.

12. Yamanaka, M.; Tzeng, Y.-K.; Kawano, S.; Smith, N. I.; Kawata, S.; Chang, H.-C.; Fujita, K., SAX microscopy with fluorescent nanodiamond probes for high-resolution fluorescence imaging. Biomedical Optics Express 2011, 2 (7), 1946-1954.

13. Nawa, Y.; Yonemaru, Y.; Kasai, A.; Oketani, R.; Hashimoto, H.; Smith, N. I.; Fujita, K., Saturated excitation microscopy using differential excitation for efficient detection of nonlinear fluorescence signals. APL Photonics 2018, 3 (8), 080805.

14. Nawa, Y.; Yonemaru, Y.; Kasai, A.; Smith, N. I.; Hashimoto, H.; Kawata, S.; Fujita, K. In Saturated excitation microscopy with extracting nonlinear fluorescence signals by signal subtraction, JSAP-OSA Joint Symposia 2016 Abstracts, Niigata, 2016/09/13; Optical Society of America: Niigata, 2016; p 15a_C31_7.

15. Chu, S.-W.; Su, T.-Y.; Oketani, R.; Huang, Y.-T.; Wu, H.-Y.; Yonemaru, Y.; Yamanaka, M.; Lee, H.; Zhuo, G.-Y.; Lee, M.-Y.; Kawata, S.; Fujita, K., Measurement of a Saturated Emission of Optical Radiation from Gold Nanoparticles: Application to an Ultrahigh Resolution Microscope. Phys. Rev. Lett. 2014, 112 (1), 017402.

16. Dabbousi, B. O.; Rodriguez-Viejo, J.; Mikulec, F. V.; Heine, J. R.; Mattoussi, H.; Ober, R.; Jensen, K. F.; Bawendi, M. G., (CdSe)ZnS Core−Shell Quantum Dots: Synthesis and Characterization of a Size Series of Highly Luminescent Nanocrystallites. The Journal of Physical Chemistry B 1997, 101 (46), 9463-9475.

17. Grecco, H. E.; Lidke, K. A.; Heintzmann, R.; Lidke, D. S.; Spagnuolo, C.; Martinez, O. E.; Jares-Erijman, E. A.; Jovin, T. M., Ensemble and single particle photophysical properties (two-photon excitation, anisotropy, FRET, lifetime, spectral conversion) of commercial quantum dots in solution and in live cells. Microsc. Res. Tech. 2004, 65 (4-5), 169-179.

18. Antelman, J.; Ebenstein, Y.; Dertinger, T.; Michalet, X.; Weiss, S., Suppression of Quantum Dot Blinking in DTT-Doped Polymer Films. The Journal of Physical Chemistry C 2009, 113 (27), 11541-11545.

19. Ai, X.; Xu, Q.; Jones, M.; Song, Q.; Ding, S.-y.; Ellingson, R. J.; Himmel, M.; Rumbles, G., Photophysics of (CdSe)ZnS colloidal quantum dots in an aqueous environment stabilized with amino acids and genetically-modified proteins. Photochemical & Photobiological Sciences 2007, 6 (9), 1027-1033.

20. Pechstedt, K.; Whittle, T.; Baumberg, J.; Melvin, T., Photoluminescence of Colloidal CdSe/ZnS Quantum Dots: The Critical Effect of Water Molecules. The Journal of Physical Chemistry C 2010, 114 (28), 12069-12077.

21. Schwartz, O.; Levitt, J. M.; Tenne, R.; Itzhakov, S.; Deutsch, Z.; Oron, D., Superresolution Microscopy with Quantum Emitters. Nano Lett. 2013, 13 (12), 5832-5836.

22. Visscher, K.; Brakenhoff, G. J.; Visser, T. D., Fluorescence saturation in confocal microscopy. Journal of Microscopy 1994, 175 (2), 162-165.

23. Ye, S.; Yan, W.; Zhao, M.; Peng, X.; Song, J.; Qu, J., Low-Saturation-Intensity, High-Photostability, and High-Resolution STED Nanoscopy Assisted by CsPbBr3 Quantum Dots. Adv. Mater. 2018, 30 (23), 1800167.

24. Hanne, J.; Falk, H. J.; Görlitz, F.; Hoyer, P.; Engelhardt, J.; Sahl, S. J.; Hell, S. W., STED nanoscopy with fluorescent quantum dots. Nature Communications 2015, 6 (1), 7127.

25. Singh, A. K.; Ghosh, S.; Kancherla, R.; Datta, A., Engineering the Excited-State Dynamics of 3-Aminoquinoline by Chemical Modification and Temperature Variation. The Journal of Physical Chemistry B 2016, 120 (50), 12920-12927.

26. Wang, X.; Qu, L.; Zhang, J.; Peng, X.; Xiao, M., Surface-Related Emission in Highly Luminescent CdSe Quantum Dots. Nano Lett. 2003, 3 (8), 1103-1106.

27. Adolfas K. Gaigalas, P. D., Lili Wang, and Yu-Zhong Zhang, Optical Properties of CdSe/ZnS Nanocrystals. Journal of Research of the National Institute of Standards and Technology 2014, 119, 19, 610-628.

28. Yeh, Y.-C.; Yuan, C.-T.; Kang, C.-C.; Chou, P.-T.; Tang, J., Influences of light intensity on fluorescence lifetime of nanorods and quantum dots. Appl. Phys. Lett. 2008, 93 (22), 223110.

29. Woggon, U.; Wind, O.; Gindele, F.; Tsitsishvili, E.; Müller, M., Optical transitions in CdSe quantum dots: From discrete levels to broad gain spectra. J. Lumin. 1996, 70 (1), 269-280.

30. van Sark, W. G. J. H. M.; Frederix, P. L. T. M.; Bol, A. A.; Gerritsen, H. C.; Meijerink, A., Blueing, Bleaching, and Blinking of Single CdSe/ZnS Quantum Dots. ChemPhysChem 2002, 3 (10), 871-879.

31. Fisher, B.; Caruge, J.-M.; Chan, Y.-T.; Halpert, J.; Bawendi, M. G., Multiexciton fluorescence from semiconductor nanocrystals. Chem. Phys. 2005, 318 (1), 71-81.

32. Boens, N.; Qin, W.; Basarić, N.; Hofkens, J.; Ameloot, M.; Pouget, J.; Lefèvre, J.-P.; Valeur, B.; Gratton, E.; vandeVen, M.; Silva, N. D.; Engelborghs, Y.; Willaert, K.; Sillen, A.; Rumbles, G.; Phillips, D.; Visser, A. J. W. G.; van Hoek, A.; Lakowicz, J. R.; Malak, H.; Gryczynski, I.; Szabo, A. G.; Krajcarski, D. T.; Tamai, N.; Miura, A., Fluorescence Lifetime Standards for Time and Frequency Domain Fluorescence Spectroscopy. Anal. Chem. 2007, 79 (5), 2137-2149.

33. Dolan, G.; Goldschmidt, C. R., A new method for absolute absorption cross-section measurements: rhodamine-6G excited singlet-singlet absorption spectrum. Chem. Phys. Lett. 1976, 39 (2), 320-322.

34. Yamanaka, M.; Kawano, S.; Fujita, K.; Smith, N.; Kawata, S., Beyond the diffraction-limit biological imaging by saturated excitation microscopy. Journal of Biomedical Optics 2008, 13 (5), 050507.

35. Yamanaka, M.; Saito, K.; Smith, N. I.; Kawata, S.; Nagai, T.; Fujita, K., Saturated excitation of fluorescent proteins for subdiffraction-limited imaging of living cells in three dimensions. Interface Focus 2013, 3 (5), 20130007.

36. Meiling, T. T.; Cywiński, P. J.; Löhmannsröben, H.-G., Two-Photon Excitation Fluorescence Spectroscopy of Quantum Dots: Photophysical Properties and Application in Bioassays. The Journal of Physical Chemistry C 2018, 122 (17), 9641-9647.

37. Ferrand, P., GPScan.VI: A general-purpose LabVIEW program for scanning imaging or any application requiring synchronous analog voltage generation and data acquisition. Comput. Phys. Commun. 2015, 192, 342-347.

Appendix. Supplemental Information

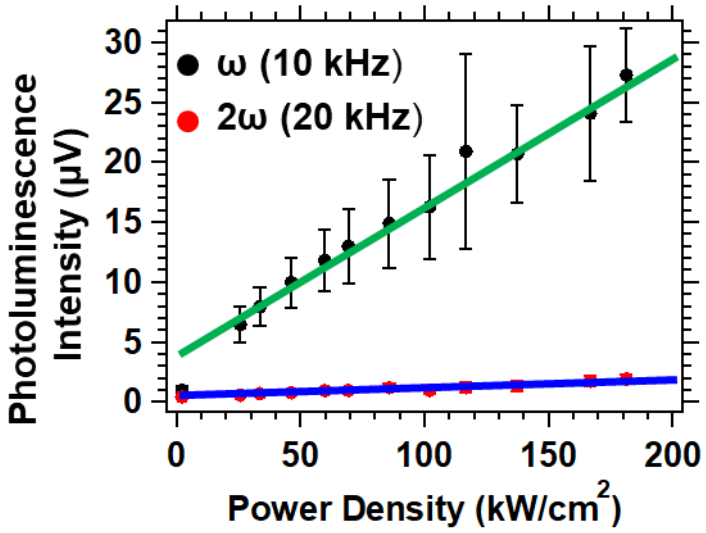

Figure S1. Photoluminescence (measured in microvolt, μV) measured by demodulating the photoluminescence signal from Qdot® 655 ITK™ quantum dots dispersed in aqueous media (with an optical density of 0.2 at 532 nm) at 10 kHz (black circle, the fundamental frequency) and 20 kHz (red circle, the second harmonic frequency). The error bars represent one standard deviation from 3 replicate measurements. The blue and green solid lines represent a linear fit of these data.

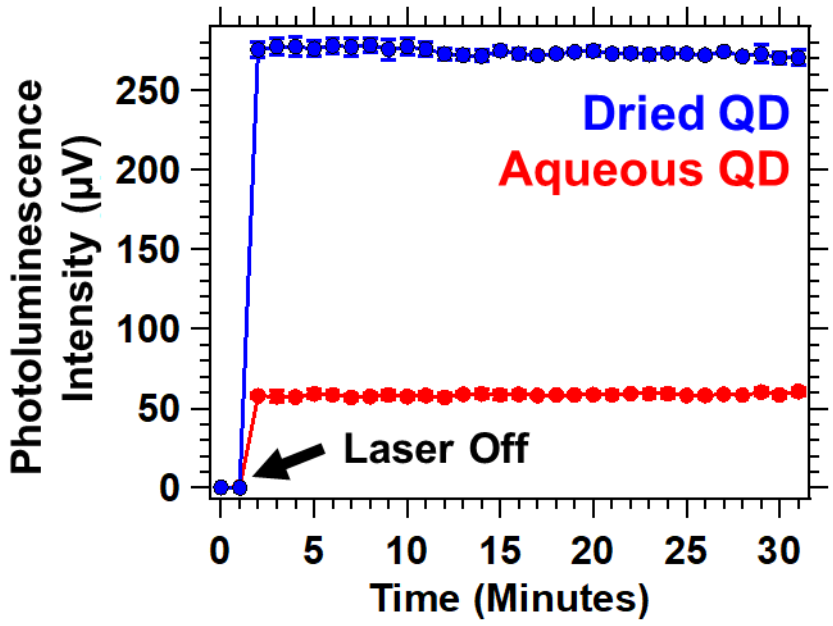

Figure S2. Photoluminescence Intensity vs Time plot for Qdot® 655 ITK™ quantum dots dispersed in aqueous media with an optical density of ~0.2 at 532 nm (red) and and Qdot® 655 ITK™ quantum dots drop casted and dried on a glass coverslip (blue). The excitation wavelength was 532 nm and the excitation power density was 235 kW/cm^2. The data points corresponding to "Laser off" are signal levels when no excitation light was present.

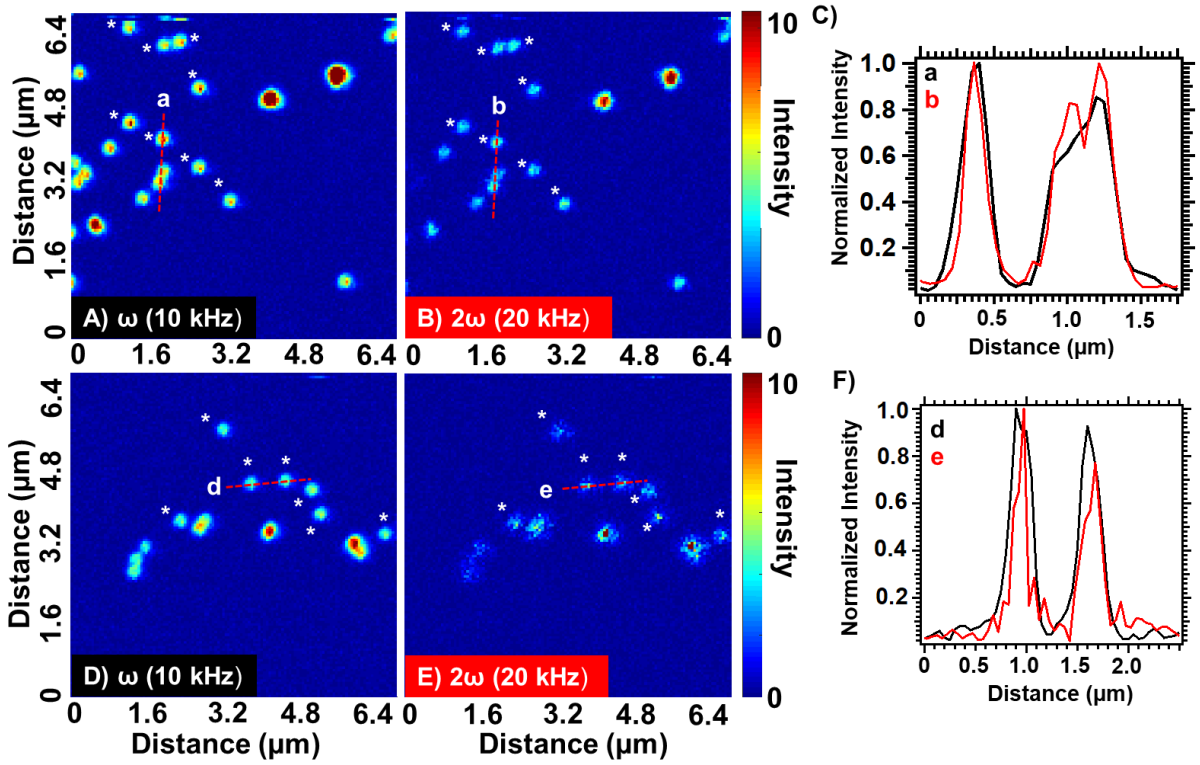

Figure S3. SAX microscopy images of 200-nm fluorescent polymer nanoparticles. Images constructed by signal demodulation at (**A**) the fundamental frequency of ω (10 kHz) and (**B**) the second harmonic frequency 2ω (20 kHz) by scanning the same region as in **A**. (**C**) The intensity profiles show the intensity across the lines indicated in the images A and B (labeled a, b, respectively). SAX microscopy images of a different 200-nm fluorescent polymer nanoparticles sample constructed by signal demodulation at (**D**) the fundamental frequency of ω (10 kHz) and (**E**) the second harmonic frequency 2ω (20 kHz) by scanning the same region as in **D**. (**F**) The intensity profiles show the intensity across the lines indicated in the images D and E (labeled d, e, respectively). The images were collected with a step size of 50 nm, pixel dwell time of 1 ms and a lock-in time constant of 300 μs. The excitation power density in the sample plane was 4 kW/cm^2 and 20 kW/cm^2 for the fundamental and second harmonic, respectively. These power densities are close to the values reported by Fujita and coworkers.[5] The average full-width at half-maximum (FWHM) of 15 polymer nanoparticles (denoted with an ***** in the images) was calculated. The average FWHM was 229 ± 5 (fundamental frequency) and 221 ± 8 nm (second harmonic frequency).

Preparation of fluorescence bead samples for imaging: Commercially available fluorescent polymer nanoparticles (FluoSpheres™ Carboxylate-Modified Microspheres, 0.2 μm, orange fluorescent (540 nm/560 nm), 2% solids) were diluted 1000 times in deionized water. The bead solution was sonicated prior to being drop casted on a clean glass coverslip, and the water was allowed to dry before imaging.

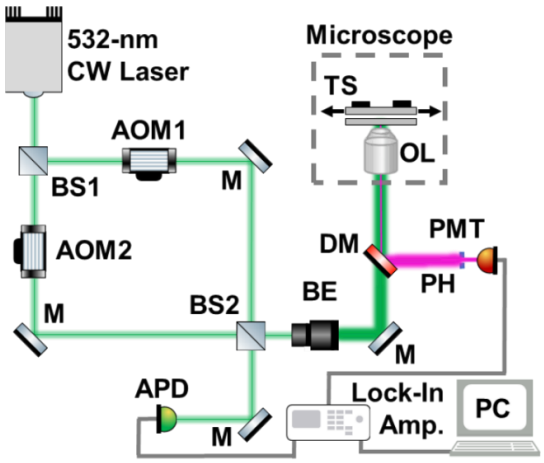

Figure S4: Schematic of saturated luminescence microscopy instrument. A 532-nm continuous wave (CW) laser is modulated using two acousto-optical modulators (AOMs). Demodulation is performed using a lock-in amplifier. Abbreviations: **BS** 50:50 beam splitter cube, **M** mirror, **BE** beam expander, **PC** personal computer, **DM** dichroic mirror, **OL** oil-immersion microscope objective, **TS** translational stage, **PH** pinhole, **PMT** photomultiplier tube, **APD** avalanche photodiode. The excitation path is colored with a green line and the detection path is colored with a pink line that goes from the TS back through the OL onto the DM and towards the PH and PMT. Other details are provided in the Experimental Section.

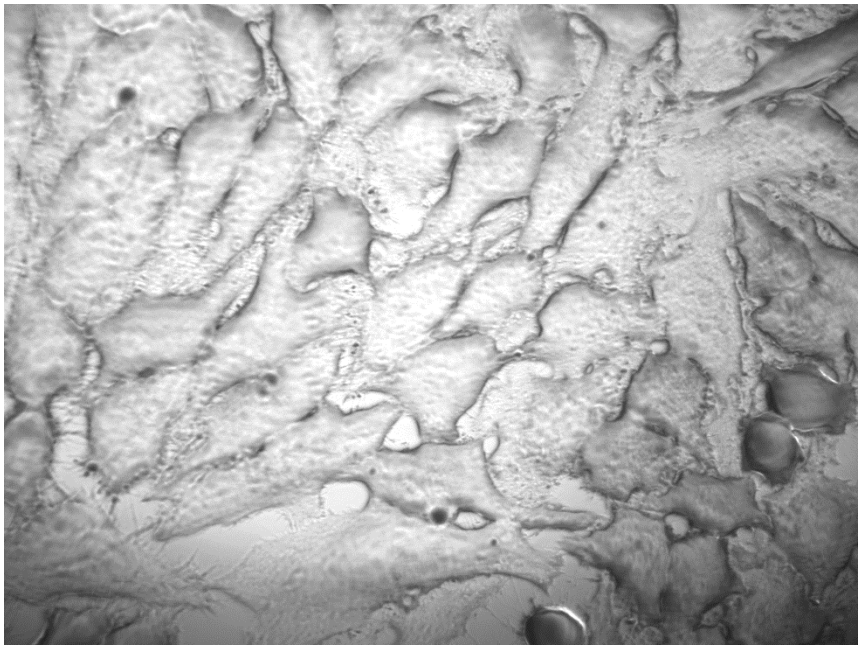

Figure S5: HeLa cells fixed with 4 % formaldehyde and stained with biotin phallloidin and streptavidin coated Qdot® 655 ITK™ quantum dots.

CHAPTER 5. PHOTOPHYSICAL PROPERTIES OF WAVELENGTH-TUNABLE METHYLAMMONIUM LEAD HALIDE NANOCRYSTALS

Daniel J. Freppon, Long Men, Sadie J. Burkhow, Jacob W. Petrich, Javier Vela[a], and Emily A. Smith[a]

[a]The Ames Laboratory, U.S. Department of Energy, and Department of Chemistry, Iowa State University, Ames, IA 50011-3111, USA

Modified from a manuscript published *J. Mater. Chem. C*, (2017) 5, 118, https://doi.org/10.1039/C6TC03886G.

Sadie J. Burkhow made significant contributions to this manuscript including data analysis, relevant literature review, all figure preparation, and relevant manuscript writing.

Abstract

We present the time-correlated luminescence of isolated nanocrystals of five methylammonium lead mixed-halide perovskite compositions ($CH_3NH_3PbBr_{3-x}I_x$) that were synthesized with varying iodide and bromide anion loading. All analyzed nanocrystals had a spherical morphology with diameters in the range of 2 to 32 nm. The luminescence maxima of $CH_3NH_3PbBr_{3-x}I_x$ nanocrystals were tuned to wavelengths ranging between 498 and 740 nm by varying the halide loading. Both $CH_3NH_3PbI_3$ and $CH_3NH_3PbBr_3$ nanocrystals exhibited no luminescence intermittency for more than 90% of the 250 s analysis time, as defined by a luminescence intensity three standard deviations above the background. The mixed halide $CH_3NH_3PbBr_{0.75}I_{0.25}$, $CH_3NH_3PbBr_{0.50}I_{0.50}$, and $CH_3NH_3PbBr_{0.25}I_{0.75}$ nanocrystals exhibited luminescence intermittency in 18%, 4% and 26% of the nanocrystals, respectively. Irrespective of luminescence intermittency, luminescence intensities were classified for each nanocrystal as: (a) constant, (b) multimodal, (c) photobrightening, and (d) photobleaching. Based on their

photophysics, the $CH_3NH_3PbBr_{3-x}I_x$ nanocrystals can be expected to be useful in a wide-range of applications where low and non-intermittent luminescence is desirable, for example as imaging probes and in films for energy conversion devices.

Introduction

Luminescent semiconductors are used in a variety of applications from microscopy probes[1-4] to thin film energy capture and conversion devices.[5-19] There is increasing interest in methylammonium lead halide perovskite ($CH_3NH_3PbX_3$, X= halide) materials due to their low cost, broad absorption as well as their charge transport diffusion lengths that range from ~100 nm to greater than 175 μm.[20-24] In energy capture and conversion films, large exciton diffusion lengths remove the need for a transport layer in perovskite-based solar cells, thus simplifying the device architecture. Single-crystalline nanocrystals, as opposed to polycrystalline films, could increase the efficiency of energy capture and conversion devices. $CH_3NH_3PbX_3$ nanocrystals are also being evaluated for use in light emitting diodes,[25] and as lasing materials.[26]

In addition to the energy capture and conversion applications outlined above, there are other uses for non-intermittent, photostable, as well as tunable nanocrystals. For example, as imaging probes the nanocrystal absorption and emission wavelengths should match wavelength criteria for the optical setup, so tunability can be advantageous. Tuning the luminescence wavelength of $CsPbX_3$[27–29] as well as $CH_3NH_3PbX_3$[30-33] perovskite nanocrystals across the visible spectrum has been reported.

Despite their promise, organometal halide perovskites have been reported to suffer from low photostability.[34,35] Superoxide (O_2), generated from the photoreaction of perovskites and oxygen, can accelerate their degradation to PbI_2, I_2 and CH_3NH_2.[36] Perovskite films degrade upon exposure to 457 nm light with a power density of 15 mW/cm^2 or higher.[37,38] Laser

illumination with 500 W/cm^2 was shown to cause photodamage to $CH_3NH_3PbI_3$ films within several seconds, leading to a decrease in luminescence.[39] However, little photobleaching (i.e., decreasing luminescence) or photobrightening (i.e., increasing luminescence) was observed for $CH_3NH_3PbI_3$ nanocrystals with wire, rod, and dot morphologies using mercury lamp illumination.[40] Matsumoto et al. and Manshor et al. report changes in surface morphology and reduced device efficiency for $CH_3NH_3PbI_3$-based films when exposed to both light and humidity, but claim the devices remain stable when exposed to light only.[41,42]

When illuminated with visible light, many types of semiconductor materials show luminescence intermittency (i.e., blinking), when the level of radiative decay drops below the background or other threshold intensity.[40,43–56] Luminescence intermittency has also been studied for $CH_3NH_3PbX_3$ materials[40,50,51,54] although the mechanism is still under debate.[34,35,38,39] One reported mechanism of luminescence intermittency in a dense $CH_3NH_3PbBr_3$ nanocrystal film is non-radiative Auger-like recombination of electrons and holes due to the accumulation of charge.[51] In closely packed nanocrystals, charge accumulates at the nanocrystal surface leading to intermittency; whereas, no intermittency was measured for well-dispersed nanocrystals. On the other hand, Tachikawa et al. reported intermittency in single $CH_3NH_3PbBr_3$ nanocrystals and postulated it is the result of charge trapping by surface lead sites reducing the probability of a recombination event.[54] They estimate 1 to 4 trap sites per 10 to 50 nm nanocrystal. The halide composition affected the trap density; an order of magnitude lower trap site density was measured in $CH_3NH_3PbI_3$ films grown in the presence of chloride compared to films in the absence of chloride.[57] In a $CH_3NH_3PbI_3$ film, a deep trap state 0.16 eV above the valence band was measured, and calculations showed this trap might arise from iodine defects.[58]

Zheng *et al.* report the differences in bulk crystals and nanocrystals of $CH_3NH_3PbBr_3$.[59] In bulk $CH_3NH_3PbBr_3$, filling of trap sites is dependent on the photon density, and luminescence lifetimes increase with higher photon densities. Compared to bulk, the luminescence lifetime of $CH_3NH_3PbBr_3$ nanocrystals is not as dependent on photon densities; 30% of the excitation photons undergo trap-free recombination; trap states are more likely to be present on the surface than in the volume of the crystal; and trap lifetimes can be short. Tian *et al.* have shown that light illumination removes traps leading to photobrightening in $CH_3NH_3PbI_3$ films, and that the size of $CH_3NH_3PbI_3$ crystallites (nanometers to microns) within the film has an effect on the rate of photobrightening.[60]

Here, we report the data from three luminescence techniques used to measure the photophysics of $CH_3NH_3PbBr_{3-x}I_x$ nanocrystals to gain a fundamental understanding of how composition affects their luminescence and, thus, their continued and potential usability in energy conversion and imaging applications. Ensemble luminescence measurements show the nanocrystal emission wavelengths are tunable across the visible wavelength region by varying the ratio of iodide and bromide salts in the synthetic loading. Due to heterogeneous crystal formation, individual nanocrystal photophysical properties vary with the type and number of defect and trap sites. Nanocrystal microscopy measures the luminescence intensity over time to reveal the temporal dynamics (*e.g.*, intermittency, flickering) as well as heterogeneity in the photophysical properties. Finally, nanocrystal microspectroscopy enables the full luminescence spectrum of isolated nanocrystals to be collected in order to monitor the stability of the emission peak over time.

Materials and Methods

Materials. Lead(II) iodide (PbI_2, 99%), lead(II) bromide ($PbBr_2$, ≥98%), methylamine (CH_3NH_2, 33 wt% in ethanol), N,N-dimethylformamide (DMF, 99.8%, anhydrous) and n-octylamine ($CH_3(CH_2)_7NH_2$, 99%) were purchased from Sigma-Aldrich; hydroiodic acid (ACS, 55-58%) and hydrobromic acid (ACS, 47.0-49.0%) from Alfa-Aesar; acetonitrile (99.9%) and toluene (99.9%) from Fisher Scientific. All chemicals were used as received.

Synthesis of Methylammonium Lead(II) Mixed-halide Nanocrystals

Precursor solutions. Alkylammonium halides were prepared by a slightly modified literature procedure.[31] Briefly, hydroiodic acid (10 mL, 0.075 mol) or hydrobromic acid (8.6 mL, 0.075 mol) was added to a solution of excess methylamine (24 mL, 0.19 mol) or *n*-octylamine (32 mL, 0.19 mol) in ethanol (100 mL) at 0 °C, and the mixture stirred at 0 °C for 2 h. The sample was concentrated under vacuum, first in a rotary evaporator at 70 °C, and then under dynamic vacuum at 60 °C for 12 h. The remaining solid was recrystallized from ethanol. *Br Solution.* $PbBr_2$ (2.9 mg, 0.008 mmol), CH_3NH_3Br (1.3 mg, 0.012 mmol) and $CH_3(CH_2)_7NH_3Br$ (2.5 mg, 0.012 mmol) were dissolved in a mixture of acetonitrile (20 mL) and DMF (0.2 mL). *I Solution.* PbI_2 (3.7 mg, 0.008 mmol), CH_3NH_3I (1.9 mg, 0.012 mmol) and $CH_3(CH_2)_7NH_3I$ (3.1 mg, 0.012 mmol) were dissolved in a mixture of acetonitrile (20 mL) and DMF (0.2 mL). *$CH_3NH_3Pb(Br_xI_{1-x})_3$ nanocrystals.* Portions of *Br* and *I* solutions were mixed according to the different desired halide loadings to a total volume of 4 mL, followed by the rapid addition of toluene (15 mL) while stirring. After 24 h stirring at room temperature, solids were isolated by centrifugation (5 min at 4500 rpm) and washed with toluene (5 mL). Solids were suspended into 10 mL toluene which resulted in a nanocrystal concentration of approximately 1 mM.

Nanocrystal Ensemble Characterization

XRD was measured using Cu Ka radiation on a Rigaku Ultima diffractometer. Solution extinction (absorption plus scattering) spectra were measured with a photodiode array Agilent 8453 UV-Vis spectrophotometer. Steady-state photoluminescence (PL) spectra were measured using a Horiba-Jobin Yvon Nanolog scanning spectrofluorometer.

Nanocrystal Luminescence Microscopy

$CH_3NH_3PbBr_{3-x}I_x$ nanocrystals were diluted to a tenth (/10) in toluene (~0.1 mM, 50 µL) and sonicated for 90 minutes before drop casting onto a glass microscope coverslip (Carlson Scientific, Peotone, IL, USA). Nanocrystal luminescence microscopy was performed using an upright microscope (Nikon Eclipse 80i, Melville, NY, USA). A mercury lamp was used for excitation (XCite 120 PC, EXFO Photonic Solutions Inc., Quebec City, Canada). Excitation and emission filters were from Omega Optical (Brattleboro, VT, USA), unless noted otherwise: 500 ± 5 nm excitation and 535 ± 7.5 nm emission filters were used for the $CH_3NH_3PbBr_3$, $CH_3NH_3Pb(Br_{0.75}I_{0.25})_3$, and $CH_3NH_3Pb(Br_{0.50}I_{0.50})_3$ samples; 500 ± 5 nm excitation and 615 ± 15 nm emission filters were used for the $CH_3NH_3Pb(Br_{0.25}I_{0.75})_3$ sample; 510 ± 5 nm excitation and 730 ± 40 nm emission filters (Semrock, Inc., Lake Forest, IL, USA) were used for the $CH_3NH_3PbI_3$ sample. A 100× Plan Apo, 1.49 numerical aperture oil-immersion objective was used and PL images were collected in the epi-direction using a charged-coupled device (CCD) camera (Photometrics Evolve, Tucson, AZ, USA) with a 250 ms exposure time and zero gain. Each PL movie consists of 1000 images collected sequentially for a total analysis time of 250 s. The signal-to-noise ratio was at least 2 at the start of each movie, and a diffraction-limited point spread function was measured for each analyzed nanocrystal.

Threshold Calculation

ImageJ was used to analyze the PL movies. For each nanocrystal analyzed, the nanocrystal's luminescence intensity and a background value were quantified in each of the 1000 frames using the Z-axis Profile function in ImageJ. The most intense pixel for the spheroid nanocrystals was used to plot the nanocrystal luminescence intensity over the entire 1000 frames (*i.e.*, over time). The background in each frame was measured approximately 8 pixels away from the center of each nanocrystal. The average background value (μ_{bg}) and background standard deviation (σ_{bg}) were calculated across all 1000 frames, and was used to calculate a threshold: Threshold = $\mu_{bg} + 3\sigma_{bg}$. Nanocrystals were considered intermittent in luminescence if their intensity fell below the threshold for more than 25 seconds over the entire movie (*i.e.*, 10% of the collection time).

Nanocrystal Microspectroscopy

The suspended $CH_3NH_3Pb(Br_{0.75}I_{0.25})_3$ nanocrystals prepared from precursor were diluted to a tenth (/10) in toluene (~0.3 mM, 50 μL) and sonicated for 60 min before drop casting onto a glass microscope coverslip (Carlson Scientific, Peotone, IL). A lab-built optical microscope based on a DM IRBE platform (Leica, Wetzlar, Germany) with 532-nm laser excitation (Sapphire SF 532 nm, Coherent, Santa Clara, CA, USA) was used to collect *emission spectra* as a function of illumination time. A 100× HCX PL APO, 1.49 numerical aperture oil-immersion objective (Leica) was used to achieve a laser spot with a diameter of 440 nm. The excitation power density at the sample was 1×10^5 W/cm^2. Photoluminescence was collected from the epi-direction and focused onto a HoloSpec f/1.8i spectrograph (Kaiser Optical Systems, Ann Arbor, MI, USA) equipped with a broad range grating (HFG-650, Kaiser Optical Systems) and then directed to a CCD (Newton 940, Andor Technology, Belfast, UK). A series of 2500 spectra

were collected for 0.1 second each. Spectra were then analyzed using IGOR Pro 6.34 batch fit (Wavemetrics, Lake Oswego, OR) and 3D images of the fits shown in Figure 5 were plotted in Matlab 2016a (Mathworks, Natick, MA).

Results and Discussion

Five $CH_3NH_3PbBr_{3-x}I_x$ nanocrystal compositions were prepared with X = 0, 0.75, 1.50, 2.25 and 3. Throughout, the presented formulas refer to the synthetic loading not a measured nanocrystal composition.[61] To control particle size, we used octylammonium halides ($CH_3(CH_2)_7NH_3X$) as surfactants, which we have shown passivate the surface and terminate/truncate further crystal growth.[40] All synthetic loadings produced primarily spherical nanocrystals, as shown by transmission electron microscopy (Fig. S1). The perovskites are nanocrystalline as evident by the peak broadness of their powder XRD patterns (Fig. S2). The XRD pattern shows a major peak at 30.2 degrees for $CH_3NH_3PbBr_3$ nanocrystals, which is typically assigned to a cubic crystal structure, and a peak at 28.7 for $CH_3NH_3PbI_3$ nanocrystals, which is typically assigned to a tetragonal crystal structure. According to the experimental patterns of $CH_3NH_3PbBr_{3-x}I_x$ (x=0.25, 0.50, 0.75), all three crystal structures are cubic. The mixed halide perovskites we studied are nanocrystalline. The reported XRD patterns of $CH_3NH_3PbI_3$ and $CH_3NH_3PbBr_3$ indicate the nanocrystals grow mainly along the [110] direction.[40] This preferred orientation is the main reason behind the differences observed between the experimental and standard XRD patterns (Fig. S2), which were collected from bulk single crystals.

The $CH_3NH_3PbBr_{3-x}I_x$ nanocrystals absorbed a broad range of visible wavelengths (Fig. 1). The luminescence spectra show a range in their wavelength of maximum emission with halide loading (Fig. 1). As the iodide content increased from 0 ($CH_3NH_3PbBr_3$) to 100%

($CH_3NH_3PbI_3$), the luminescence maximum shifted from 498 to 740 nm. The shift in luminescence maximum is not linear with halide loading (Fig. 2), which is consistent with previous reports.[30,62]

The luminescence intensity as a function of time was analyzed for up to 50 nanocrystals from each halide loading. The $CH_3NH_3(Br_{0.25}I_{0.75})_3$ nanocrystals were more dilute relative to the other compositions over replicate syntheses and the same sample preparation method only allowed 39 nanocrystals to be measured. An average luminescence intensity across the 250 second analysis time was calculated for each nanocrystal; histograms of the background subtracted values are shown in Fig. S3 for each halide loading. The absolute values on the x-axis cannot be compared across different compositions as the optical throughput of the instrument varies with wavelength (*e.g.*, filter bandwidth, *etc.*). The shapes of the distributions, however, can be compared. The mixed halide compositions of $CH_3NH_3Pb(Br_{0.75}I_{0.25})_3$, $CH_3NH_3Pb(Br_{0.50}I_{0.50})_3$, and $CH_3NH_3Pb(Br_{0.25}I_{0.75})_3$ had more outliers with intensities 13 to 230× higher than the intensity with the highest frequency compared to the single halide $CH_3NH_3PbBr_3$ and $CH_3NH_3PbI_3$ nanocrystals.

The single halide nanocrystals exhibit no luminescence intermittency as defined by a luminescence intensity above the calculated threshold for distinguishing luminescence from the background more than 90% of the analysis time (Table 1). The percentage of $CH_3NH_3Pb(Br_{0.75}I_{0.25})_3$, $CH_3NH_3Pb(Br_{0.50}I_{0.50})_3$, and $CH_3NH_3Pb(Br_{0.25}I_{0.75})_3$ nanocrystals that exhibit luminescence intermittency is 18, 4, and 26%, respectively. We hypothesize that the fraction of mixed halide nanocrystals that exhibit intermittency due to crystal defects or trap states. When electrons become trapped, luminescent recombination of excitons cannot occur, providing periods of no measured luminescence. Further, this leads to the assumption that

functional trap states are absent in the single halide nanocrystals. The single halide perovskites, $CH_3NH_3PbI_3$ and $CH_3NH_3PbBr_3$, have quantum yields of 1.5% and 44% respectively. These quantum yields are higher than the mixed halide perovskite nanocrystals (0.02 to 1.3%), which is consistent with the hypothesis that increased crystal defects or trap states are responsible for blinking in the mixed halide perovskites.

In addition to the percentage of nanocrystals that exhibit intermittency, it is also useful to consider the percentage of time the nanocrystals were above the threshold over the total analysis time (Table 1). The intensities of the $CH_3NH_3PbBr_3$ and $CH_3NH_3PbI_3$ nanocrystals are always above the threshold over the entire 208 minutes (*i.e.*, 50 nanocrystals analyzed for 250 seconds each). For the intermediate halide loadings, the percentage of non-intermittent nanocrystals and the percentage of the analysis time the nanocrystals are above the threshold are correlated. The latter, however, is always higher than the former. For example, 74% of the $CH_3NH_3Pb(Br_{0.25}I_{0.75})_3$ nanocrystals are not intermittent and are above the threshold 89% of the analysis time.

The luminescence signal over time was categorized into four different luminescence behaviors irrespective of the threshold or intermittency (Table 2). The behaviors are: (a) constant intensity, (b) multimodal intensity, (c) photobrightening, and (d) photobleaching. In order to be classified as constant luminescence intensity, shown in Fig. 3a, the slope of the line connecting the intensity at 0 seconds and 250 seconds was between -0.2 and 0.2 s^{-1}. The small fluctuations in intensity of a nanocrystal classified as constant luminescence are due to instrument noise; this produces an intensity histogram with a Gaussian distribution (Fig. 3a'). The $CH_3NH_3Pb(Br_{0.75}I_{0.25})_3$ and $CH_3NH_3Pb(Br_{0.50}I_{0.50})_3$ nanocrystals were the only compositions to exhibit type a constant intensities with populations of 28% for both compositions (Table 2).

If the intensity of a nanocrystal varied between two or three relatively constant values for a duration of at least 10 seconds with the transition between intensities occurring within 500 millisecond (*i.e.*, two times the acquisition time), this is classified as type b multimodal behavior, shown in Fig. 3b. The resulting intensity histogram is either a bimodal or trimodal distribution (Fig. 3b'). The number of nanocrystals that have a multimodal intensity profile decreased with the amount of bromide loading from $CH_3NH_3PbBr_3$ to $CH_3NH_3Pb(Br_{0.25}I_{0.75})$. The $CH_3NH_3PbI_3$ nanocrystals do not fit this trend with 18% of nanocrystals exhibiting this behavior. Across all nanocrystal compositions, 72 exhibited multimodal behavior, and this was the second most common behavior. Eight of the 72 total where trimodal (only found in the $CH_3NH_3PbBr_3$ and $CH_3NH_3Pb(Br_{0.75}I_{0.25})_3$ compositions) and 64 were bimodal. A possible mechanism for type b photophysics is considered: given the nanocrystals are smaller than the diffraction limit of light, it is possible that a bimodal luminescence intensity is from nanocrystal dimers or aggregates. Considering a bimodal distribution, the most common type b behavior, and a possible nanocrystal dimer, the high luminescence state would represent times when both nanocrystals are emitting; whereas, the low intensity state would represent times when only one nanocrystal is emitting. Statistically, there is a possibility that both nanocrystals are not emitting, and the intensity would drop below the threshold. This possibility increases as the duration of the low intensity state increases; however, an intensity below the threshold is never measured in this population. One may argue that the lower intensity state is one where the nanocrystal is not luminescent, and that an incorrect threshold has been applied. However, the image inset in Fig. 3b clearly show that the low intensity state is higher than the background. A low intensity, or gray state, has been reported for quantum dots, including ZnS capped CdSe[63] and CdS capped

CdSe.[64,65] The emitting low intensity state in $CH_3NH_3PbBr_{3-x}I_x$ nanocrystals may be a gray state, although the mechanism for the gray state may be unique and requires further study.

In up to 22% of the population, the luminescence intensity of a nanocrystal increased over the analysis time. If the slope of the intensity between the data points at time 0 seconds and 250 seconds was greater than 0.2 s^{-1}, then the nanocrystal was considered to be photobrightening, shown in Fig. 3c. Photobrightening results in an intensity histogram with an asymmetric distribution (Fig. 3c'). In the case of Fig. 3c, and whenever there is photobrightening, a skew does exist towards higher intensities. Photobrightening has been reported in $CH_3NH_3PbBr_3$ nanocrystals and $CH_3NH_3PbI_3$ films by Tachikawa *et al.* and deQuilettes *et al.*, respectively.[54,66] One mechanism reported for photobrightening is a photoinduced trap reduction caused by the movement of halides when illuminated with light. As the halides are transported about the nanocrystalline lattice, vacancies that make up trap sites are filled. Considering all nanocrystal compositions as an aggregate, this is the least common behavior.

Each nanocrystal composition produced a population where the luminescence intensity of a nanocrystal decreased over the analysis time. If the slope of the intensity between the data points at time 0 seconds and 250 seconds was less than -0.2 s^{-1}, then the nanocrystal was considered to be photobleaching, shown in Fig. 3d. Photobleaching generally results in an intensity histogram that skews to lower values (Fig. 3d'). Photobleaching was most common (74-95%) in the nanocrystals containing high amounts of iodide (*i.e.*, $CH_3NH_3Pb(Br_{0.25}I_{0.75})_3$ and $CH_3NH_3PbI_3$). We hypothesize that in cases of photobleaching, the nanocrystal lattice begins to decompose leading to higher non-radiative recombination events, which has also been observed in $CsPbX_3$ nanocrystals[52] and CdSe/ZnS quantum dots.[67] A small number of nanocrystals exhibited photobleaching as well as short periods of lower intensity up to 10 s in duration (*i.e.*,

below the 50 seconds used to categorize a nanocrystal as exhibiting a bimodal distribution). Each nanocrystal was analyzed for 250 seconds; it is possible that the percentage of nanocrystals with type d photobleaching behavior increases as the analysis time increases.

Flickering is defined here as less than 500 millisecond (*i.e.*, two times the acquisition time) periods of a drop in luminescence intensity. Flickering is observed in types b, c, and d luminescence behaviors. Examples of flickering are shown in Fig. 3b and d. In some instances of flickering, the luminescence intensity goes below the threshold, which represent brief intermittent events. For the events that do not go below the threshold, a faster acquisition rate may reveal whether these events represent intermittent events. A faster acquisition time of 20 millisecond was used to measure the time correlated luminescence intensity of all nanocrystal compositions; results for one composition are shown in Fig. 4 and for the other compositions in Fig. S4. A majority of the flickering measured with a 20 millisecond acquisition time remain above the threshold, revealing a mechanism faster than 20 milliseconds is responsible for a majority of these events.

In the nanocrystal luminescence microscopy experiments described above, increasing, decreasing or flickering luminescence could be explained by shifting luminescence spectra, which has been measured in similar nanocrystals.[31,68] If the luminescence shifts partially, or completely, outside the wavelength range of the filters used to collect the signal, then the luminescence intensity could increase, decrease, or disappear. In order to test for this, the emission spectrum of isolated $CH_3NH_3PbI_3$ nanocrystals was measured over 250 seconds under 1×10^5 W/cm^2 laser irradiance (Fig. 5). The emission maximum remained constant at 775 nm under continuous illumination with a 100 ms acquisition time. The emission does not shift outside the wavelength region of the filters used to collect the luminescence intensity *versus* time

data. This indicates that the blinking or other varying luminescence intensity states measured for the $CH_3NH_3PbI_3$ nanocrystals (Table 1) is not the result of shifting luminescence spectra. The instrument setup does not allow the measurement of the other nanocrystal compositions. Finally, this experiment shows that 50% of the nanocrystal exhibit photobrightening and 50% photobleaching under high irradiance, and overall better photostability than many reported in the literature for similar materials.[52,69]

Conclusion

The luminescence of a series of methylammonium lead halide nanocrystals has been reported. The wavelength of maximum luminescence was tunable within the range of 498-740 nm by controlling the bromide and iodide loading during nanocrystal synthesis. The $CH_3NH_3PbI_3$ and $CH_3NH_3PbBr_3$ nanocrystals exhibit no luminescence intermittency, while 82%, 96%, and 74% of the $CH_3NH_3Pb(Br_{0.75}I_{0.25})_3$, $CH_3NH_3Pb(Br_{0.50}I_{0.50})_3$, and $CH_3NH_3Pb(Br_{0.25}I_{0.75})_3$ nanocrystals exhibit no luminescence intermittency, respectively. It is likely that the mixed halide nanocrystals contain iodide-rich and bromide-rich domains when both halides are present in the nanocrystal.[38,61] It is also possible that domains form as a result of light-induced segregation. The low percentage of nanocrystals that exhibited intermittency, along with relatively good photostabilities at low (i.e., mercury lamp) and high (i.e., focused laser, up to 1×105 W/cm^2) photon fluxes, and the emission tunability of the nanocrystals will make these hybrid perovskite nanocrystals useful in a wide range of applications.

Declarations

Acknowledgements

This research is supported by the U.S. Department of Energy, Office of Basic Energy Sciences, Division of Chemical Sciences, Geosciences, and Biosciences through the Ames

Laboratory. The Ames Laboratory is operated for the U.S. Department of Energy by Iowa State University under Contract No. DE-AC02-07CH11358.

Figures and Tables

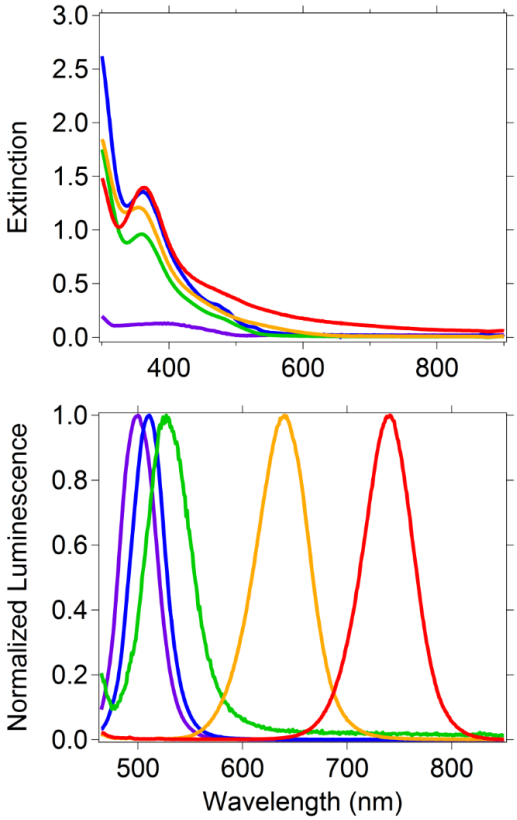

Fig. 1. (Top) Extinction (absorption plus scattering) and (bottom) normalized emission with 375 nm excitation spectra of $CH_3NH_3PbBr_3$ (purple), $CH_3NH_3Pb(Br_{0.75}I_{0.25})_3$ (blue), $CH_3NH_3Pb(Br_{0.50}I_{0.50})_3$ (green), $CH_3NH_3Pb(Br_{0.25}I_{0.75})_3$ (orange), $CH_3NH_3PbI_3$ (red). Extinction and emission spectra were collected in toluene as the solvent.

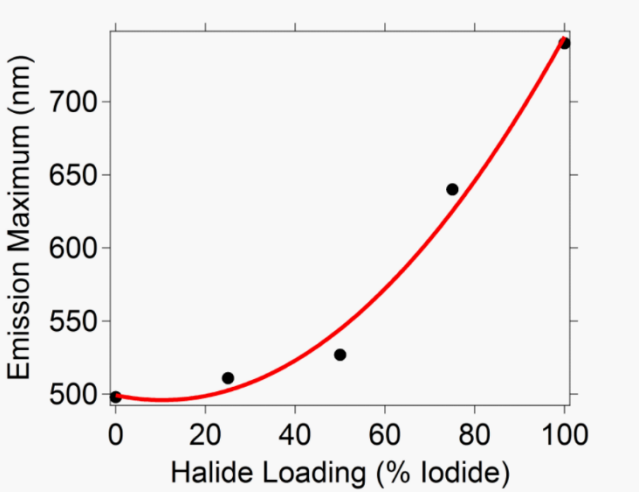

Fig. 2. Emission maximum wavelength versus iodide loading for the (0%) $CH_3NH_3PbBr_3$, (25%) $CH_3NH_3Pb(Br_{0.75}I_{0.25})_3$, (50%) $CH_3NH_3Pb(Br_{0.50}I_{0.50})_3$, (75%) $CH_3NH_3Pb(Br_{0.25}I_{0.75})_3$, and (100%) $CH_3NH_3PbI_3$ nanocrystals. The third-order polynomial fit line is shown in red. The equation for the best fit of the maximum emission wavelength (λ_{max}) versus percent iodide loading (x) is: $\lambda_{max} = -9 \times 10^{-5}x^3 + 0.04x^2 - x + 501$. The R^2 value for the fit is 0.99.

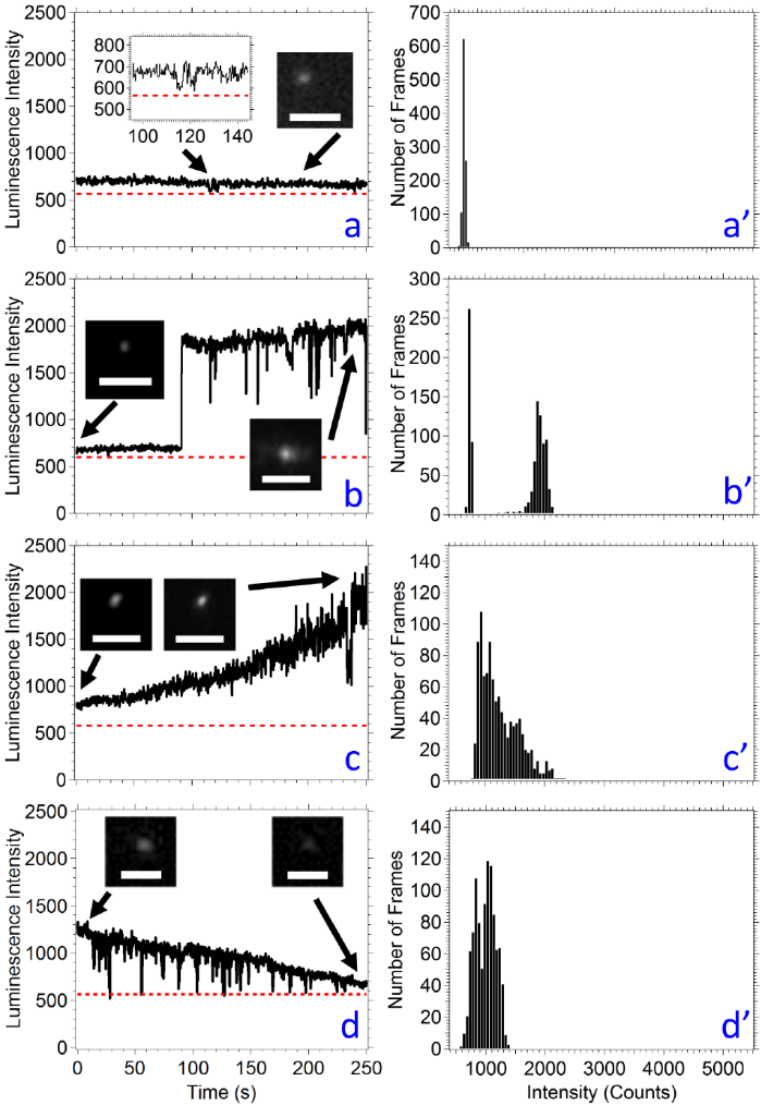

Fig. 3. Representative luminescence intensity versus time graphs for $CH_3NH_3Pb(Br_{0.75}I_{0.25})_3$ nanocrystals. The dotted red line is the threshold for distinguishing nanocrystal luminescence from the background. The panels represent four of the photophysical properties measured for all the perovskite compositions. The time-correlated luminescence intensity is found on the left. Histograms of the corresponding intensities are found on the right. Type (a) is representative of nanocrystals that only show fluctuations in luminescence intensity due to instrument noise. Type (b) is representative of nanocrystals that exhibit a multimodal luminescence intensity profile, in this case being bimodal, a low intensity and a high intensity or vice versa. Type (c) is representative of nanocrystals with luminescence intensities that photobrighten over time (a slope greater than 0.2 s^{-1}). Type (d) is representative of nanocrystals with luminescence intensities that photobleach over time (a slope smaller than -0.2 s^{-1}). Figures on the right show the intensity histograms for all 250 seconds. Each histogram corresponds to the similar letter (*e.g.* a' corresponds to a). The insets show the image at selected time points, as noted by the arrow. In all cases, the images show a nanocrystal intensity that can be differentiated from the background. The scale bar in each image is 2 μm and the acquisition time is 250 millisecond.

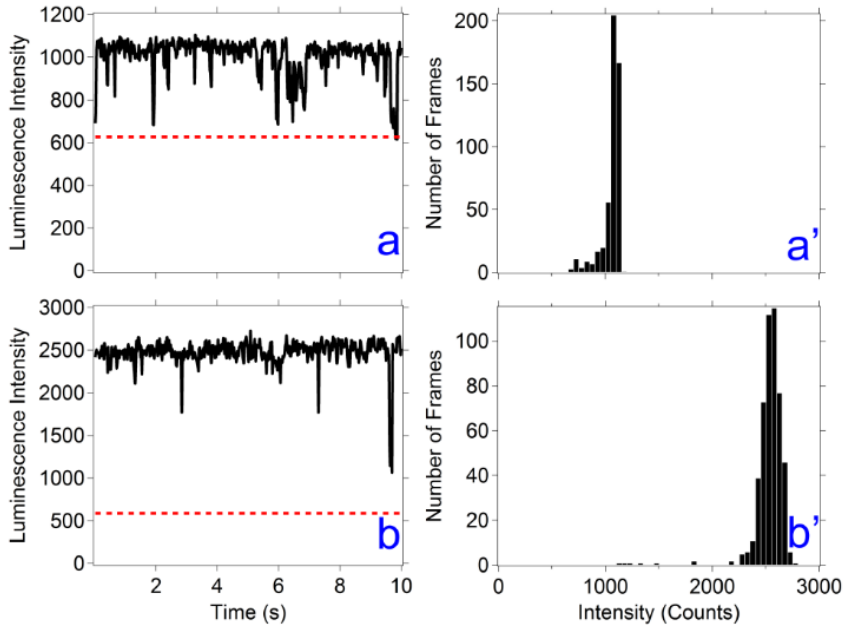

Fig. 4. Representative luminescence intensity versus time graphs for $CH_3NH_3PbBr_3$ nanocrystals. The acquisition time is 20 millisecond, collected over 10 seconds. The dotted red line is the threshold for distinguishing nanocrystal luminescence from the background.

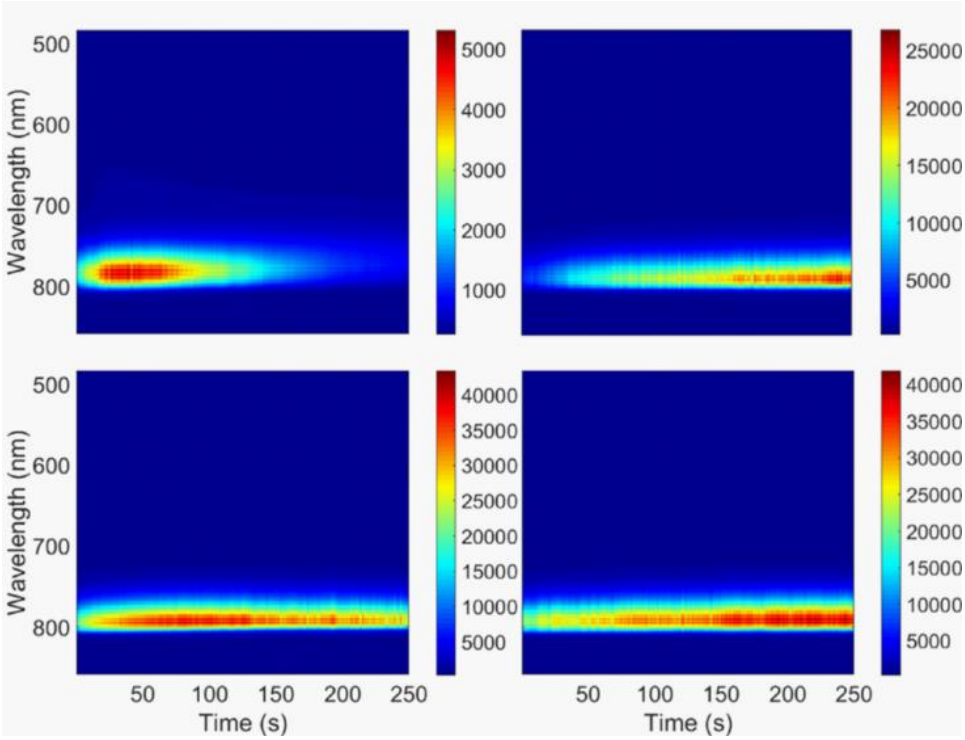

Fig. 5. Luminescence spectra of $CH_3NH_3PbI_3$ nanocrystals over time. Each panel represents a different nanocrystal. The luminescence maximum is constant over time at 775 nm. (This is shifted relative to the ensemble solution data shown in Fig. 1). The excitation wavelength is 532 nm; the acquisition time is 0.1 seconds.

Table 1. Percentage of nanocrystals within each composition that are above the calculated threshold over 90% of the analysis time (*i.e.*, "ON") and the percentage of time the nanocrystals are above the threshold.

Sample	Number of Nanocrystals Analyzed	Percentage **Nanocrystals** "ON"[a]	Percentage **Time** Above Threshold[b]
$CH_3NH_3PbBr_3$	50	100	100
$CH_3NH_3Pb(Br_{0.75}I_{0.25})_3$	50	82	93
$CH_3NH_3Pb(Br_{0.50}I_{0.50})_3$	50	96	99
$CH_3NH_3Pb(Br_{0.25}I_{0.75})_3$	39	74	89
$CH_3NH_3PbI_3$	50	100	100

[a] The nanocrystals are considered to be in an "ON" state if the luminescence intensity is above the calculated threshold at least 90% of the analysis time.
[b] Based on a total time of 250 seconds × number of nanocrystals analyzed.

Table 2. Number of nanocrystals analyzed for each halide loading and percentage that display type a, b, c, and d photoluminescence as defined in the text.

Sample	Number of Nanocrystals Analyzed	Type a: Constant Intensity	Type b: Multimodal Intensity Profile	Type c: Photo-brightening	Type d: Photo-bleaching
$CH_3NH_3PbBr_3$	50	0%	70%	4%	26%
$CH_3NH_3Pb(Br_{0.75}I_{0.25})_3$	50	28%	38%	22%	12%
$CH_3NH_3Pb(Br_{0.50}I_{0.50})_3$	50	28%	18%	8%	46%
$CH_3NH_3Pb(Br_{0.25}I_{0.75})_3$	39	0%	0%	5%	95%
$CH_3NH_3PbI_3$	50	0%	18%	8%	74%

References

1) Lane, L. A.; Smith, A. M.; Lian, T.; Nie, S., Compact and blinking-suppressed quantum dots for single-particle tracking in live cells. The Journal of Physical Chemistry B 2014, 118 (49), 14140-14147.

2) Luo, J.; Bai, H.; Yang, P.; Cai, J., One-pot aqueous synthesis of germanium-doped cadmium sulfide quantum dots as fluorescent probes for cell imaging. Materials Science in Semiconductor Processing 2015, 34 (0), 1-7.

3) Fernández-Suárez, M.; Ting, A. Y., Fluorescent probes for super-resolution imaging in living cells. Nature Reviews Molecular Cell Biology 2008, 9 (12), 929-943.

4) Orte, A.; Alvarez-Pez, J. M.; Ruedas-Rama, M. J., Fluorescence lifetime imaging microscopy for the detection of intracellular pH with quantum dot nanosensors. ACS Nano 2013, 7 (7), 6387-6395.

5) Patel, P.; Mitzi, D., Perovskites in the spotlight. MRS Bulletin 2014, 39 (09), 768-769.

6) Snaith, H. J., Perovskites: The Emergence of a New Era for Low-Cost, High-Efficiency Solar Cells. The Journal of Physical Chemistry Letters 2013, 4 (21), 3623-3630.

7) Park, N.-G., Organometal Perovskite Light Absorbers Toward a 20% Efficiency Low-Cost Solid-State Mesoscopic Solar Cell. The Journal of Physical Chemistry Letters 2013, 4 (15), 2423-2429.

8) Stranks, S. D.; Nayak, P. K.; Zhang, W.; Stergiopoulos, T.; Snaith, H. J., Formation of Thin Films of Organic–Inorganic Perovskites for High-Efficiency Solar Cells. Angewandte Chemie International Edition 2015, 54 (11), 3240–3248.

9) Edri, E.; Kirmayer, S.; Cahen, D.; Hodes, G., High open-circuit voltage solar cells based on organic–inorganic lead bromide perovskite. The Journal of Physical Chemistry Letters 2013, 4 (6), 897-902.

10) Edri, E.; Kirmayer, S.; Kulbak, M.; Hodes, G.; Cahen, D., Chloride Inclusion and Hole Transport Material Doping to Improve Methyl Ammonium Lead Bromide Perovskite-Based High Open-Circuit Voltage Solar Cells. The Journal of Physical Chemistry Letters 2014, 5 (3), 429-433.

11) De Wolf, S.; Holovsky, J.; Moon, S.-J.; Löper, P.; Niesen, B.; Ledinsky, M.; Haug, F.-J.; Yum, J.-H.; Ballif, C., Organometallic Halide Perovskites: Sharp Optical Absorption Edge and Its Relation to Photovoltaic Performance. The Journal of Physical Chemistry Letters 2014, 5 (6), 1035-1039.

12) Unger, E. L.; Hoke, E. T.; Bailie, C. D.; Nguyen, W. H.; Bowring, A. R.; Heumuller, T.; Christoforo, M. G.; McGehee, M. D., Hysteresis and transient behavior in current-voltage measurements of hybrid-perovskite absorber solar cells. Energy & Environmental Science 2014, 7 (11), 3690-3698.

13) Sum, T. C.; Mathews, N., Advancements in perovskite solar cells: photophysics behind the photovoltaics. Energy & Environmental Science 2014, 7 (8), 2518-2534.

14) Smith, I. C.; Hoke, E. T.; Solis-Ibarra, D.; McGehee, M. D.; Karunadasa, H. I., A Layered Hybrid Perovskite Solar-Cell Absorber with Enhanced Moisture Stability. Angewandte Chemie 2014, 126 (42), 11414-11417.

15) Zuo, L.; Gu, Z.; Ye, T.; Fu, W.; Wu, G.; Li, H.; Chen, H., Enhanced photovoltaic performance of CH3NH3PbI3 perovskite solar cells through interfacial engineering using self-assembling monolayer. Journal of the American Chemical Society 2015, 137 (7), 2674–2679.

16) Ono, L. K.; Raga, S. R.; Wang, S.; Kato, Y.; Qi, Y., Temperature-dependent hysteresis effects in perovskite-based solar cells. Journal of Materials Chemistry A 2015, 3, 9074-9080.

17) Jeon, N. J.; Noh, J. H.; Yang, W. S.; Kim, Y. C.; Ryu, S.; Seo, J.; Seok, S. I., Compositional engineering of perovskite materials for high-performance solar cells. Nature 2015, 517 (7535), 476-480.

18) Green, M. A.; Ho-Baillie, A.; Snaith, H. J., The emergence of perovskite solar cells. Nature Photonics 2014, 8 (7), 506-514.

19) Stender, A. S.; Marchuk, K.; Liu, C.; Sander, S.; Meyer, M. W.; Smith, E. A.; Neupane, B.; Wang, G.; Li, J.; Cheng, J.-X.; Huang, B.; Fang, N., Single Cell Optical Imaging and Spectroscopy. Chemical Reviews 2013, 113 (4), 2469-2527.

20) Stranks, S. D.; Eperon, G. E.; Grancini, G.; Menelaou, C.; Alcocer, M. J. P.; Leijtens, T.; Herz, L. M.; Petrozza, A.; Snaith, H. J., Electron-Hole Diffusion Lengths Exceeding 1 Micrometer in an Organometal Trihalide Perovskite Absorber. Science 2013, 342 (6156), 341-344.

21) Dong, Q.; Fang, Y.; Shao, Y.; Mulligan, P.; Qiu, J.; Cao, L.; Huang, J., Electron-hole diffusion lengths > 175 μm in solution-grown CH3NH3PbI3 single crystals. Science 2015, 347 (6225), 967-970.

22) Wehrenfennig, C.; Liu, M.; Snaith, H. J.; Johnston, M. B.; Herz, L. M., Charge-carrier dynamics in vapour-deposited films of the organolead halide perovskite CH3NH3PbI3-xClx. Energy & Environmental Science 2014, 7 (7), 2269-2275.

23) Xing, G.; Mathews, N.; Sun, S.; Lim, S. S.; Lam, Y. M.; Grätzel, M.; Mhaisalkar, S.; Sum, T. C., Long-Range Balanced Electron- and Hole-Transport Lengths in Organic-Inorganic CH3NH3PbI3. Science 2013, 342 (6156), 344-347.

24) Fu, Y.; Meng, F.; Rowley, M. B.; Thompson, B. J.; Shearer, M. J.; Ma, D.; Hamers, R. J.; Wright, J. C.; Jin, S., Solution Growth of Single Crystal Methylammonium Lead Halide Perovskite Nanostructures for Optoelectronic and Photovoltaic Applications. Journal of the American Chemical Society 2015, 137 (17), 5810-5818.

25) Li, G.; Tan, Z.-K.; Di, D.; Lai, M. L.; Jiang, L.; Lim, J. H.-W.; Friend, R. H.; Greenham, N. C., Efficient Light-Emitting Diodes Based on Nanocrystalline Perovskite in a Dielectric Polymer Matrix. Nano Letters 2015, 15 (4), 2640-2644.

26) Zhu, H.; Fu, Y.; Meng, F.; Wu, X.; Gong, Z.; Ding, Q.; Gustafsson, M.; Trinh, M.; Jin, S.; Zhu, X., Lead halide perovskite nanowire lasers with low lasing thresholds and high quality factors. Nature Materials 2015, 14, 636–642.

27) Protesescu, L.; Yakunin, S.; Bodnarchuk, M. I.; Krieg, F.; Caputo, R.; Hendon, C. H.; Yang, R. X.; Walsh, A.; Kovalenko, M. V., Nanocrystals of cesium lead halide perovskites (CsPbX3, X= Cl, Br, and I): novel optoelectronic materials showing bright emission with wide color gamut. Nano Letters 2015, 15 (6), 3692-3696.

28) Bekenstein, Y.; Koscher, B. A.; Eaton, S. W.; Yang, P.; Alivisatos, A. P., Highly luminescent colloidal nanoplates of perovskite cesium lead halide and their oriented assemblies. Journal of the American Chemical Society 2015, 137 (51), 16008–16011.

29) Akkerman, Q. A.; D'Innocenzo, V.; Accornero, S.; Scarpellini, A.; Petrozza, A.; Prato, M.; Manna, L., Tuning the optical properties of cesium lead halide perovskite nanocrystals by anion exchange reactions. Journal of the American Chemical Society 2015, 137 (32), 10276-10281.

30) Jang, D. M.; Park, K.; Kim, D. H.; Park, J.; Shojaei, F.; Kang, H. S.; Ahn, J.-P.; Lee, J. W.; Song, J. K., Reversible Halide Exchange Reaction of Organometal Trihalide Perovskite Colloidal Nanocrystals for Full-Range Band Gap Tuning. Nano Letters 2015, 15 (8), 5191-5199.

31) Di, D., Musselman, K. P., Li, G., Sadhanala, A., Ievskaya, Y., Song, Q., ... & Friend, R. H. (2015). Size-dependent photon emission from organometal halide perovskite nanocrystals embedded in an organic matrix. *The journal of physical chemistry letters*, *6*(3), 446-450.

32) Zhang, F.; Zhong, H.; Chen, C.; Wu, X.-g.; Hu, X.; Huang, H.; Han, J.; Zou, B.; Dong, Y., Brightly-Luminescent and Color-Tunable Colloidal CH3NH3PbX3 (X= Br, I, Cl) Quantum Dots: Potential Alternatives for Display Technology. ACS Nano 2015, 9 (4), 4533–4542.

33) Pathak, S.; Sakai, N.; Wisnivesky Rocca Rivarola, F.; Stranks, S. D.; Liu, J.; Eperon, G. E.; Ducati, C.; Wojciechowski, K.; Griffiths, J. T.; Haghighirad, A. A.; Pellaroque, A.; Friend, R. H.; Snaith, H. J., Perovskite Crystals for Tunable White Light Emission. Chemistry of Materials 2015, 27 (23), 8066-8075.

34) Berhe, T. A.; Su, W.-N.; Chen, C.-H.; Pan, C.-J.; Cheng, J.-H.; Chen, H.-M.; Tsai, M.-C.; Chen, L.-Y.; Dubale, A. A.; Hwang, B.-J., Organometal halide perovskite solar cells: degradation and stability. Energy & Environmental Science 2016, 9 (2), 323-356.

35) Niu, G.; Guo, X.; Wang, L., Review of recent progress in chemical stability of perovskite solar cells. Journal of Materials Chemistry A 2015, 3 (17), 8970-8980.

36) Aristidou, N.; Sanchez-Molina, I.; Chotchuangchutchaval, T.; Brown, M.; Martinez, L.; Rath, T.; Haque, S. A., The role of oxygen in the degradation of methylammonium lead trihalide perovskite photoactive layers. Angewandte Chemie International Edition 2015, 54 (28), 8208-8212.

37) Ito, S.; Tanaka, S.; Manabe, K.; Nishino, H., Effects of Surface Blocking Layer of Sb2S3 on Nanocrystalline TiO2 for CH3NH3PbI3 Perovskite Solar Cells. The Journal of Physical Chemistry C 2014, 118 (30), 16995-17000.

38) Hoke, E. T.; Slotcavage, D. J.; Dohner, E. R.; Bowring, A. R.; Karunadasa, H. I.; McGehee, M. D., Reversible photo-induced trap formation in mixed-halide hybrid perovskites for photovoltaics. Chemical Science 2015, 6 (1), 613-617.

39) Yuan, H.; Debroye, E.; Janssen, K.; Naiki, H.; Steuwe, C.; Lu, G.; Moris, M. l.; Orgiu, E.; Uji-i, H.; De Schryver, F., Degradation of Methylammonium Lead Iodide Perovskite Structures through Light and Electron Beam Driven Ion Migration. The Journal of Physical Chemistry Letters 2016, 7, 561-566.

40) Zhu, F.; Men, L.; Guo, Y.; Zhu, Q.; Bhattacharjee, U.; Goodwin, P. M.; Petrich, J. W.; Smith, E. A.; Vela, J., Shape Evolution and Single Particle Luminescence of Organometal Halide Perovskite Nanocrystals. ACS Nano 2015, 9 (3), 2948–2959.

41) Matsumoto, F.; Vorpahl, S. M.; Banks, J. Q.; Sengupta, E.; Ginger, D. S., Photodecomposition and Morphology Evolution of Organometal Halide Perovskite Solar Cells. The Journal of Physical Chemistry C 2015, 119 (36), 20810-20816.

42) Manshor, N. A.; Wali, Q.; Wong, K. K.; Muzakir, S. K.; Fakharuddin, A.; Schmidt-Mende, L.; Jose, R., Humidity versus photo-stability of metal halide perovskite films in a polymer matrix. Physical Chemistry Chemical Physics 2016, 18 (31), 21629-21639.

43) Barnes, M. D.; Mehta, A.; Thundat, T.; Bhargava, R. N.; Chhabra, V.; Kulkarni, B., On−Off Blinking and Multiple Bright States of Single Europium Ions in Eu3+:Y2O3 Nanocrystals. The Journal of Physical Chemistry B 2000, 104 (26), 6099-6102.

44) Glennon, J. J.; Buhro, W. E.; Loomis, R. A., Simple surface-trap-filling model for photoluminescence blinking spanning entire CdSe quantum wires. The Journal of Physical Chemistry C 2008, 112 (13), 4813-4817.

45) Glennon, J. J.; Tang, R.; Buhro, W. E.; Loomis, R. A., Synchronous photoluminescence intermittency (blinking) along whole semiconductor quantum wires. Nano letters 2007, 7 (11), 3290-3295.

46) Kuno, M.; Fromm, D. P.; Gallagher, A.; Nesbitt, D. J.; Micic, O. I.; Nozik, A. J., Fluorescence Intermittency in Single InP Quantum Dots. Nano Letters 2001, 1 (10), 557-564.

47) Kuno, M.; Fromm, D. P.; Hamann, H. F.; Gallagher, A.; Nesbitt, D. J., "On"/"off" fluorescence intermittency of single semiconductor quantum dots. The Journal of Chemical Physics 2001, 115 (2), 1028-1040.

48) Kuno, M.; Fromm, D. P.; Hamann, H. F.; Gallagher, A.; Nesbitt, D. J., Nonexponential "blinking" kinetics of single CdSe quantum dots: A universal power law behavior. The Journal of Chemical Physics 2000, 112 (7), 3117-3120.

49) Galland, C.; Ghosh, Y.; Steinbrück, A.; Sykora, M.; Hollingsworth, J. A.; Klimov, V. I.; Htoon, H., Two types of luminescence blinking revealed by spectroelectrochemistry of single quantum dots. Nature 2011, 479 (7372), 203-207.

50) Tian, Y.; Merdasa, A.; Peter, M.; Abdellah, M.; Zheng, K.; Ponseca, C. S.; Pullerits, T.; Yartsev, A.; Sundström, V.; Scheblykin, I. G., Giant Photoluminescence Blinking of Perovskite Nanocrystals Reveals Single-Trap Control of Luminescence. Nano Letters 2015, 15 (3), 1603-1608.

51) Wen, X.; Ho-Baillie, A.; Huang, S.; Sheng, R.; Chen, S.; Ko, H.-c.; Green, M. A., Mobile charge-induced fluorescence intermittency in methylammonium lead bromide perovskite. Nano Letters 2015, 15 (7), 4644-4649.

52) Park, Y.-S.; Guo, S.; Makarov, N. S.; Klimov, V. I., Room temperature single-photon emission from individual perovskite quantum dots. ACS Nano 2015, 9 (10), 10386-10393.

53) Seth, S.; Mondal, N.; Patra, S.; Samanta, A., Fluorescence Blinking and Photo-Activation of All-Inorganic Perovskite Nanocrystals, CsPbBr3 and CsPbBr2I. The Journal of Physical Chemistry Letters 2016, 7 (2), 266–271.

54) Tachikawa, T.; Karimata, I.; Kobori, Y., Surface Charge Trapping in Organolead Halide Perovskites Explored by Single-Particle Photoluminescence Imaging. The Journal of Physical Chemistry Letters 2015, 6 (16), 3195-3201.

55) Lidke, K. A.; Rieger, B.; Jovin, T. M.; Heintzmann, R., Superresolution by localization of quantum dots using blinking statistics. Opt. Express 2005, 13 (18), 7052-7062.

56) Banin, U.; Bruchez, M.; Alivisatos, A. P.; Ha, T.; Weiss, S.; Chemla, D. S., Evidence for a thermal contribution to emission intermittency in single CdSe/CdS core/shell nanocrystals. The Journal of Chemical Physics 1999, 110 (2), 1195-1201.

57) Wu, X.; Trinh, M. T.; Niesner, D.; Zhu, H.; Norman, Z.; Owen, J. S.; Yaffe, O.; Kudisch, B. J.; Zhu, X.-Y., Trap states in lead iodide perovskites. Journal of the American Chemical Society 2015, 137 (5), 2089-2096.

58) Duan, H.-S.; Zhou, H.; Chen, Q.; Sun, P.; Luo, S.; Song, T.-B.; Bob, B.; Yang, Y., The identification and characterization of defect states in hybrid organic-inorganic perovskite photovoltaics. Physical Chemistry Chemical Physics 2015, 17 (1), 112-116.

59) Zheng, K.; Zidek, K.; Abdellah, M.; Messing, M. E.; Al-Marri, M. J.; Pullerits, T., Trap States and Their Dynamics in Organometal Halide Perovskite Nanoparticles and Bulk Crystals. The Journal of Physical Chemistry C 2016, 120 (5), 3077–3084.

60) Tian, Y.; Merdasa, A.; Unger, E.; Abdellah, M.; Zheng, K.; McKibbin, S.; Mikkelsen, A.; Pullerits, T.; Yartsev, A.; Sundström, V.; Scheblykin, I. G., Enhanced Organo-Metal Halide Perovskite Photoluminescence from Nanosized Defect-Free Crystallites and Emitting Sites. The Journal of Physical Chemistry Letters 2015, 6 (20), 4171-4177.

61) Rosales, B. A., Men, L., Cady, S. D., Hanrahan, M. P., Rossini, A. J., & Vela, J. (2016). Persistent dopants and phase segregation in organolead mixed-halide perovskites. *Chemistry of Materials, 28*(19), 6848-6859.

62) Noh, J. H.; Im, S. H.; Heo, J. H.; Mandal, T. N.; Seok, S. I., Chemical Management for Colorful, Efficient, and Stable Inorganic–Organic Hybrid Nanostructured Solar Cells. Nano Letters 2013, 13 (4), 1764-1769.

63) Osborne, M.; Fisher, A., Charge-tunnelling and self-trapping: common origins for blinking, grey-state emission and photoluminescence enhancement in semiconductor quantum dots. Nanoscale 2016, 8 (17), 9272-9283.

64) Lesoine, M. D.; Bhattacharjee, U.; Guo, Y.; Vela, J.; Petrich, J. W.; Smith, E. A., Subdiffraction, Luminescence-Depletion Imaging of Isolated, Giant, CdSe/CdS Nanocrystal Quantum Dots. The Journal of Physical Chemistry C 2013, 117 (7), 3662-3667.

65) Malko, A. V.; Park, Y.-S.; Sampat, S.; Galland, C.; Vela, J.; Chen, Y.; Hollingsworth, J. A.; Klimov, V. I.; Htoon, H., Pump-Intensity- and Shell-Thickness-Dependent Evolution of Photoluminescence Blinking in Individual Core/Shell CdSe/CdS Nanocrystals. Nano Letters 2011, 11 (12), 5213-5218.

66) deQuilettes, D. W.; Zhang, W.; Burlakov, V. M.; Graham, D. J.; Leijtens, T.; Osherov, A.; Bulovic, V.; Snaith, H. J.; Ginger, D. S.; Stranks, S. D., Photo-induced halide redistribution in organic-inorganic perovskite films. Nat Commun 2016, 7, 1-9.

67) van Sark, W. G. J. H. M.; Frederix, P. L. T. M.; Van den Heuvel, D. J.; Gerritsen, H. C.; Bol, A. A.; van Lingen, J. N. J.; de Mello Donegá, C.; Meijerink, A., Photooxidation and Photobleaching of Single CdSe/ZnS Quantum Dots Probed by Room-Temperature Time-Resolved Spectroscopy. The Journal of Physical Chemistry B 2001, 105 (35), 8281-8284.

68) Fang, H. H.; Raissa, R.; Abdu-Aguye, M.; Adjokatse, S.; Blake, G. R.; Even, J.; Loi, M. A., Photophysics of organic–inorganic hybrid lead iodide perovskite single crystals. Advanced Functional Materials 2015, 25 (16), 2378-2385.

69) Luo, B.; Pu, Y.-C.; Yang, Y.; Lindley, S. A.; Abdelmageed, G.; Ashry, H.; Li, Y.; Li, X.; Zhang, J. Z., Synthesis, Optical Properties, and Exciton Dynamics of Organolead Bromide Perovskite Nanocrystals. The Journal of Physical Chemistry C 2015, 119 (47), 26672-26682.

Appendix. Supplemental Information

Transmission Electron Microscopy

Transmission Electron Microscopy (TEM). TEM was conducted using a FEI Technai G2 F20 field emission TEM operating at up to 200 kV with a point-to-point resolution of less than 0.25 nm and a line-to-line resolution of less than 0.10 nm. Samples were prepared by placing 2 or 3 drops of dilute toluene solutions onto carbon-coated copper grids.

Size and Morphology Analysis. Particle dimensions were measured manually and with ImageJ. Typically, more than 100 particles were counted in each case. Uncertainties in all measurements are reported as standard deviations.

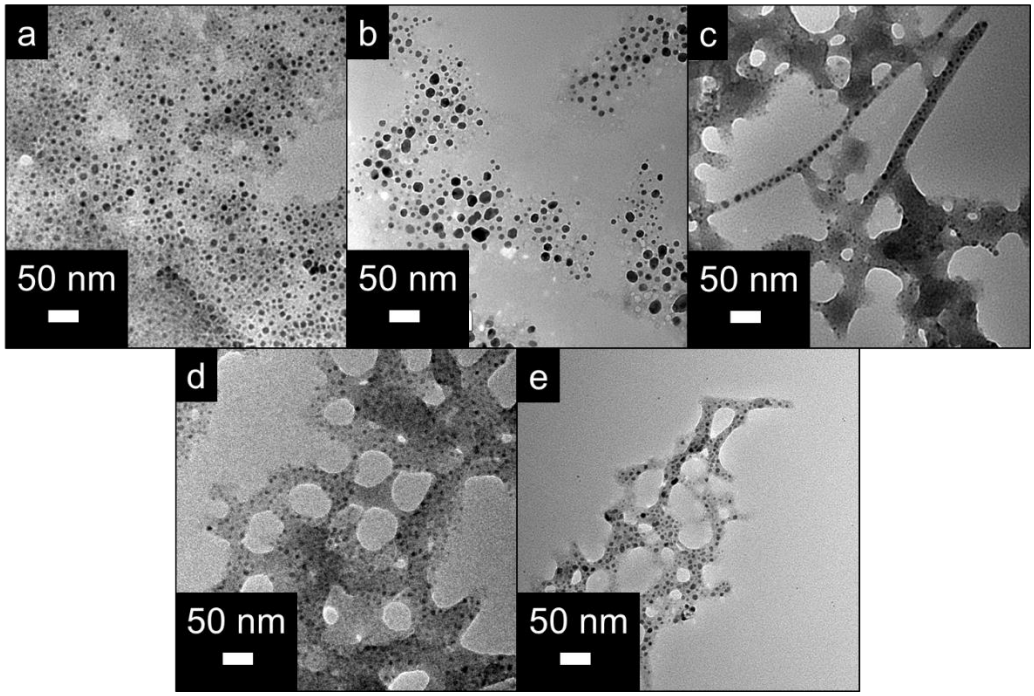

Fig. S1. TEM images of (a) $CH_3NH_3PbBr_3$, (b) $CH_3NH_3Pb(Br_{0.75}I_{0.25})_3$, (c) $CH_3NH_3Pb(Br_{0.50}I_{0.50})_3$, (d) $CH_3NH_3Pb(Br_{0.25}I_{0.75})_3$, and (e) $CH_3NH_3PbI_3$ nanocrystals.

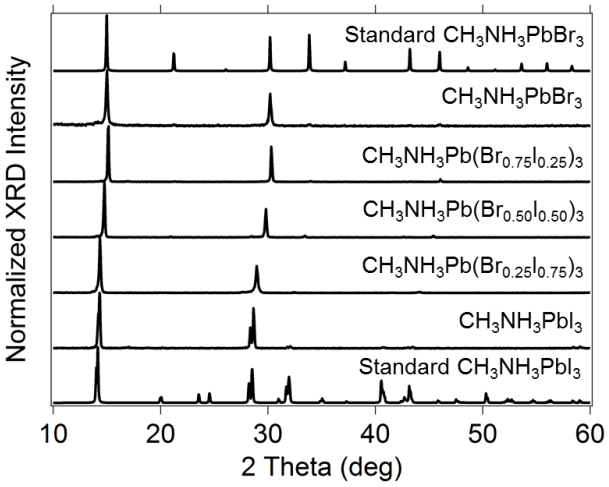

Fig. S2. X-ray diffraction (XRD) patterns of $CH_3NH_3PbBr_3$, $CH_3NH_3Pb(Br_{0.75}I_{0.25})_3$, $CH_3NH_3Pb(Br_{0.50}I_{0.50})_3$, $CH_3NH_3Pb(Br_{0.25}I_{0.75})_3$, and $CH_3NH_3PbI_3$ nanocrystals. Also included are the standard XRD patterns for the cubic $CH_3NH_3PbBr_3$ and tetragonal $CH_3NH_3PbI_3$ crystal structures, respectively. The various halide percentages stated in the formulas represent synthetic loading rather than a measured composition of the nanocrystals.

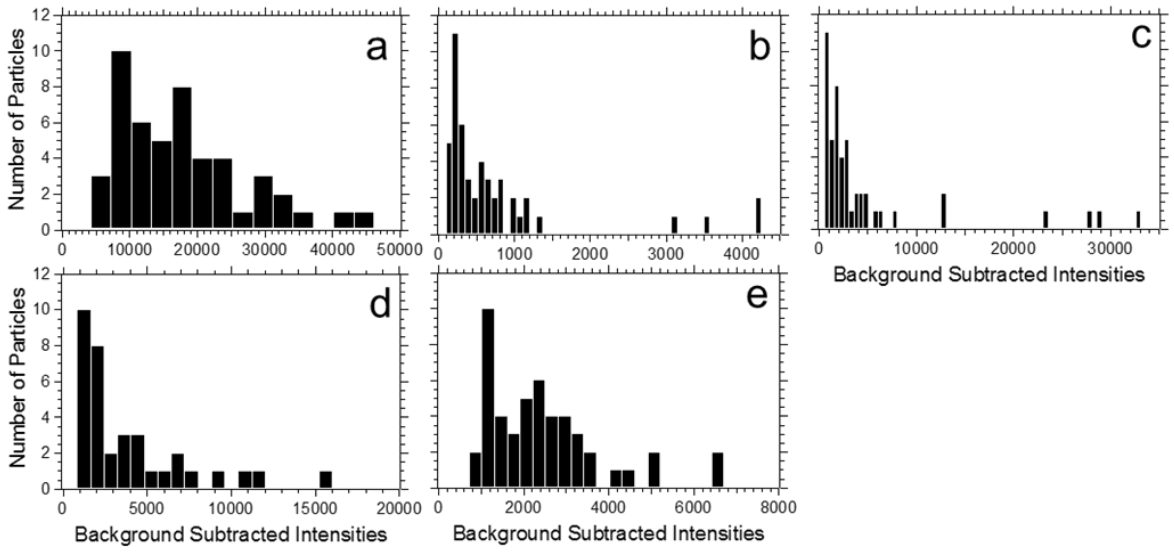

Fig. S3. Histograms of the average background subtracted nanocrystal luminescence intensity for the perovskite compositions: (a) $CH_3NH_3PbBr_3$, (b) $CH_3NH_3Pb(Br_{0.75}I_{0.25})_3$, (c) $CH_3NH_3Pb(Br_{0.50}I_{0.50})_3$, (d) $CH_3NH_3Pb(Br_{0.25}I_{0.75})_3$, and (e) $CH_3NH_3PbI_3$. Each histogram was generated to have 10 or 11 nanocrystals as a maximum frequency, so the bin size varies among each composition. A total of 50 nanocrystals were analyzed in all cases except (d), which had 39 nanocrystals analyzed.

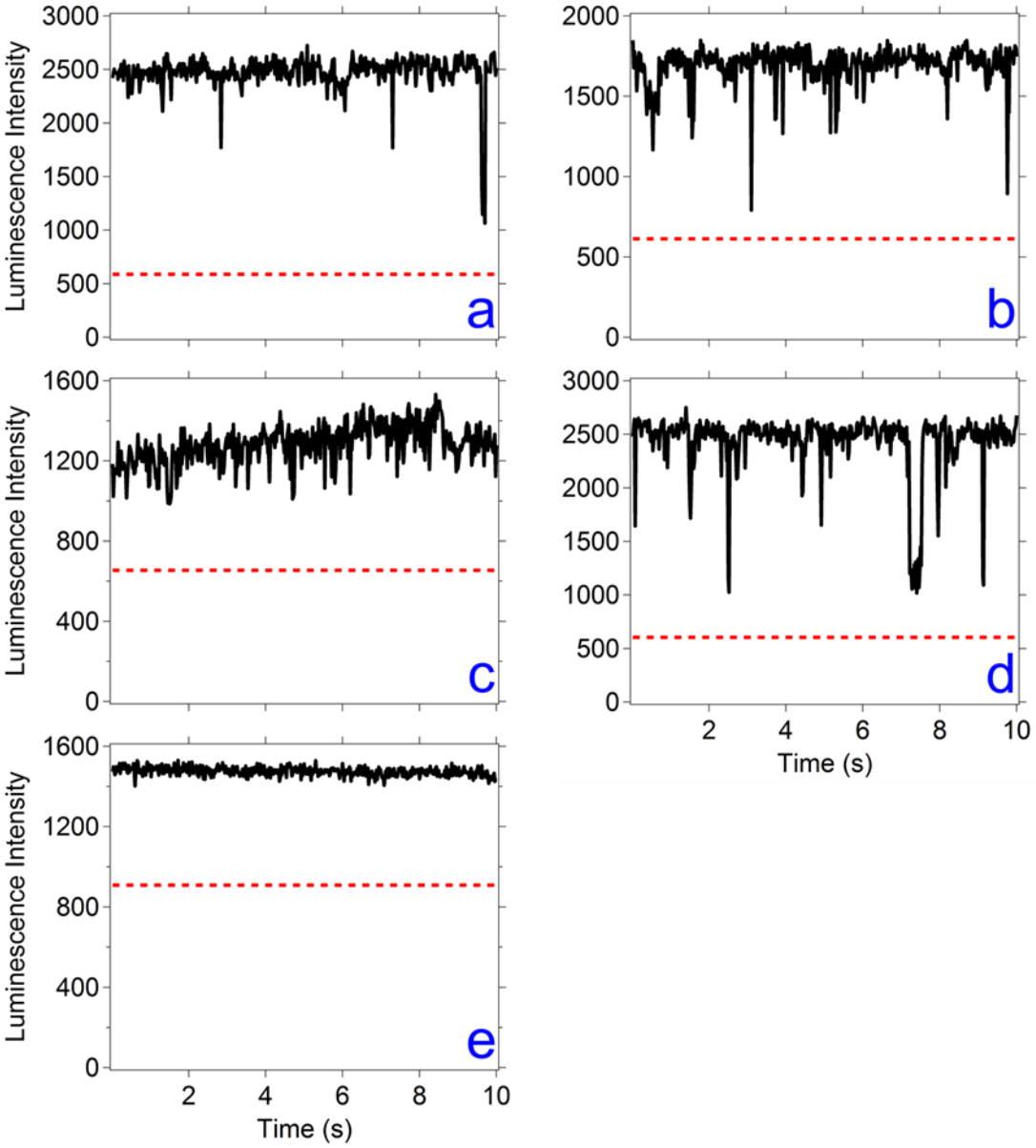

Fig. S4. Representative luminescence intensity versus time graphs for (a) $CH_3NH_3PbBr_3$, (b) $CH_3NH_3Pb(Br_{0.75}I_{0.25})_3$, (c) $CH_3NH_3Pb(Br_{0.50}I_{0.50})_3$, (d) $CH_3NH_3Pb(Br_{0.25}I_{0.75})_3$, and (e) $CH_3NH_3PbI_3$ nanocrystals. The acquisition time is 20 ms, collected over 10 s. The dotted red line is the threshold for distinguishing nanocrystal luminescence from the background.

CHAPTER 6. INTERFACIAL CONTROL OF CATALYTIC ACTIVITY IN THE ALDOL CONDENSATION: COMBINING THE EFFECTS OF HYDROPHOBIC ENVIRONMENTS AND WATER

Dilini Singappuli-Arachchige,[a,b], Takeshi Kobayashi, Zhuoran Wang,[a,b] Sadie J. Burkhow,[a,b] Emily A. Smith,[a,b] Marek Pruski,[a,b] and Igor Slowing,[a,b]

[a]The Ames Laboratory, U.S. Department of Energy

[b]Department of Chemistry, Iowa State University, Ames, IA 50011-3111, USA;

Modified from a manuscript published in *ACS Catalysis*, (2019) 9, 5574, https://doi.org/10.1021/acscatal.9b00195.

Sadie J. Burkhow made significant contributions to this manuscript including measuring all materials with Raman microscopy, all Raman data analysis, relevant literature review, figure preparation of Raman data, and relevant manuscript writing.

Abstract

Aminopropyl-functionalized mesoporous silica nanoparticles (AP-MSN) catalyze aldol condensations. The activity of AP-MSN decreases with increasing solvent polarity due to the stabilization of ion pairs formed between acidic silanol groups and the amines, which ultimately decreases the number of catalytically active amine sites. However, the reaction in water is faster than expected on the basis of polarity, because water limits the formation of Schiff bases that are also responsible for blocking active sites. In this work, we combined the action of water with a low-local-polarity environment around the catalytic sites of AP-MSN to maximize active site availability and catalyst performance. We specifically demonstrate how the local polarity of AP-MSN can be controlled by modifying its surface with varying concentrations of hexyl groups and how the dielectric constant of the silica−water interface can be determined using the solvatochromic probe Prodan. The catalytic activities of hexyl-modified AP-MSN in water were

inversely proportional to their interfacial dielectric constants and were significantly higher (roughly by a factor of 4) than those of AP-MSN in anhydrous solvents of comparable polarities. Producing low-local-polarity environments in aqueous AP-MSN also enhanced the sensitivity of the aldol reaction to the electronic effects of substituents in the substrate. The enhancement of catalytic activity by low interfacial polarity was also observed in other amine-catalyzed C−C bond forming reactions such as the Henry and vinylogous aldol reactions. Overall, our results demonstrate that the catalytic activity of AP-MSN can be controlled by the synergistic action of water and a low interfacial dielectric constant.

Keywords: interfacial catalysis, effective dielectric constant, hydrophobic environments, solvent effects, aldol condensation

Introduction

The effects of solvents on homogeneous catalytic reactions have been studied extensively.[1−7] In contrast, our understanding of solvent effects in heterogeneous catalysis remains fairly limited.[8−19] Examining the influence of solvents on heterogeneous reactions is complicated due to interfacial interactions,[15] competitive adsorption,[16] fractional solvation of adsorbed species,[10,17] and mass transfer kinetics.[20] Understanding the interplay among these factors is fundamental for the rational design of interfacial catalysts.

The study of interfacial catalysis can be simplified using benchmark reactions with mechanisms that are well understood in solution. A reaction that has been extensively used for this purpose is the aldol condensation.[19,21−29] This reaction has been recently included in the design of many biomass processing schemes,[30−36] and its study has provided clear examples of complex behaviors, such as acid−base cooperativity. Several groups have investigated the effects of different types of acidic sites on the activity of immobilized base catalysts, demonstrating that

cooperativity is affected by the strength, relative position, and structure of acid and base functionalities.[19,21−29,37] Additional studies have shown the role of properties more relevant to interfacial interactions such as the effects of support hydrophobicity[24,38−40] and solvents on the reaction.[18,19,41−43] For example, it has been shown that the catalytic activity of amine-functionalized mesoporous silicas decreases with increasing solvent polarity.[18,19] This drop in activity has been attributed to the increasing stabilization of ion pairs formed between acidic groups and amines that blocks a fraction of the active sites by turning them into nonnucleophilic ammonium cations.[18,19,44] Interestingly, in spite of its high dielectric constant, water deviates from this trend: the catalytic activity of primary amines is higher in water than in methanol.[18,19] This anomalous behavior has been explained by the role of water in limiting competing reactions such as the formation of the non-enolizable Schiff base 1 (pathway a, Scheme 1) [18,29] and the conjugated dehydration product 2 (pathway b, Scheme 1) [43] that deactivate another fraction of the active amine sites. In addition, water is required for the hydrolytic desorption of the product in the last step of the reaction (step c, Scheme 1), which drives the equilibrium toward completion.[18]

On the basis of these observations, we hypothesized that the catalytic performance of amines on silica could be enhanced by combining the effects of water and a low-polarity environment around the active sites, i.e., by simultaneously decreasing the number of sites deactivated through formation of Schiff bases and ammonium ions. We have recently used solvatochromic probes to measure the dielectric properties of water−silica interfaces and demonstrated that organo-functionalization of the surface produces local environments with polarities which differ from that of the bulk solvent.[45] Our measurements and DFT calculations suggested that molecular guests located at the interface between water and organo-functionalized

silica are indeed simultaneously surrounded by the tethered organic groups and water molecules.[45] This results in a mixed-solvation environment where the layer close to the silica surface has a lower polarity than the aqueous layer above it. Herein, we report the effects of organo-functionalization of aminopropyl mesoporous silica on its catalytic performance for the aldol condensation in water. We synthesized a series of hexyl modified 3-aminopropyl-functionalized mesoporous silica nanoparticles (Hex-AP-MSN) and used them as catalysts for the cross-aldol reaction between p-nitrobenzaldehyde and acetone in water. We examined the effect of hexyl group loading on the dielectric properties of the interface and the rate of the catalytic conversion and compared their activity with that of 3-aminopropyl mesoporous silica nanoparticles (APMSN) without any hexyl modification in water and in anhydrous solvents of varying dielectric constant.

Materials and Methods

Materials. Hexadecyltrimethylammonium bromide (CTAB), p-nitrobenzaldehyde, dimethyl sulfone (DMS), methanol, N-(3-dimethylaminopropyl)-N′-ethylcarbodiimide hydrochloride, N-hydroxysuccinimide sodium salt, resorcinol, anhydrous 2-butanol, anhydrous 1-propanol, and ninhydrin were purchased from Sigma-Aldrich. p-Bromobenzaldehyde, p-tolualdehyde, benzaldehyde, 3-buten-2-one, and tetrakis- (trimethylsilyl)silane (TTMS) were purchased from Aldrich. Tetraethyl orthosilicate (TEOS), 3-aminopropyltrimethoxysilane, 3-methoxypropyltrimethoxysilane, and hexyltrimethoxysilane were purchased from Gelest, Inc. NaOH, concentrated HCl, 2-propanol, and acetone were purchased from Fisher Scientific. Ethanol was purchased from Decon Laboratories and Prodan from Anapec, Inc. Butylamine was purchased from Fluka. Methanol, ethanol, 2-propanol, and acetone were dried with CaH_2 and distilled before use. All other reagents were used as received without further purification.

Synthesis of Functionalized MSNs. CTAB (1.0 g, 2.74 mmol) was dissolved in deionized water (480 mL) in a round-bottom flask followed by addition of 2 M NaOH (3.5 mL, 7.0 mmol). The solution was stirred for 1 h at 80 °C. TEOS (5.0 mL, 22.6 mmol) and organosilanes (amounts according to Table S6) were then added dropwise over 7 min to the CTAB solution. Magnetic stirring was continued for another 2 h at 80 °C. The solution was filtered, washed with abundant water and methanol, respectively, and vacuum-dried overnight. The CTAB template was removed by refluxing 1.0 g of dry solid with 100 mL of methanol and concentrated HCl (0.8 mL, 9.7 mmol) at 60 °C for 6 h. The surfactant removal step was repeated one more time. The surfactant-removed samples were then filtered, washed with abundant methanol and water, and vacuum-dried at 100 °C overnight.

Characterization of Catalysts. XRD patterns were recorded on a Bruker X-ray diffractometer equipped with Cu Kα radiation (40 kV, 44 mA) over the range of 1−10° 2θ. The nitrogen adsorption/desorption isotherms were measured in a Micromeritics Tristar surface area and porosity analyzer. The surface areas and pore size distributions were calculated by the Brunauer−Emmett−Teller (BET) and Barrett−Joyner−Halenda (BJH) methods, respectively. Elemental analyses of the dry samples were done in triplicate on a PerkinElmer 2100 series II CHNS analyzer, using acetanilide as a calibration standard and combustion and reduction temperatures of 925 and 640 °C, respectively.

Homogeneous Synthesis of Schiff-Base Intermediate (Analogous to Species 1 in Scheme 1).

p-Nitrobenzaldehyde (0.40 mmol) and butylamine (0.50 mmol) were mixed in methanol-d4 (1 mL) and stirred at 60 °C for 24 h. 1 H NMR (600 MHz, methanol-d4; δ, ppm): 8.46 (s,1H), 8.29 (d, J = 8.1 Hz, 2H), 7.96 (d, J = 8.1 Hz, 2H), 3.68 (td, J = 7.4 Hz, 1.49 Hz, 2H), 1.72 (m,

2H), 1.43 (m, 2H), 0.95 (t, 3H). 13C{1 H} NMR (600 MHz, methanol-d4; δ, ppm): 160.0, 149.0, 141.5, 128.6 (2C), 123.5 (2C), 60.8, 32.5, 20.0, 12.8.

Solid-State NMR. The concentrations of silanols in the MSN were determined by ^{29}Si direct polarization magic-angle spinning (DPMAS) NMR spectroscopy.[60] The ^{29}Si DPMAS NMR spectra were acquired on an Agilent NMR spectrometer operated at 9.4 T, equipped with a Chemagnetics 5 mm MAS probe. The samples were packed in a zirconia MAS rotor and spun at 8 kHz. The ^{1} H spectrum of predried Hex(1.0)-APMSN was acquired at 14.1 T on a Varian NMR System 600 spectrometer, using a FastMAS 1.6 mm probe operated at 25 kHz.

To characterize the spent catalysts, DNP-enhanced ^{13}C{^{1} H} CPMAS experiments were carried out on a Bruker Avance III spectrometer operated at 9.4 T, equipped with a 3.2 mm cryoMAS probe and a 263 GHz gyrotron. The samples were mixed with 10 mM AMUPol dissolved in water, packed in a sapphire rotor, and spun at 7 kHz at 105 K.

The experimental parameters used to acquire ^{29}Si and ^{13}C spectra are given in the captions to Figures S1 and S8 in the Supporting Information.

Raman Spectroscopy. An XploRA Plus Raman confocal upright microscope with a Synapse EMCCD camera was used for all Raman measurements (HORIBA Scientific, Edison, NJ). A 785 nm solid state diode laser with a 26000 W/cm^2 irradiance was used for the spent catalysts, and due to the strong Raman scattering from p-nitrobenzaldehyde and the homogeneously synthesized intermediate, 3000 and 500 W/cm^2 irradiances were used, respectively. Raman data were collected in the epi-direction with a 20× magnification, a 0.4 numerical aperture objective, a 600 grooves/millimeter grating, a 200 μm monochromator slit, and a 500 μm confocal pinhole. The acquisition time was 50 s with three accumulations. To

obtain a representative signal, three different sample areas were measured and averaged for the spectra shown within Figure S6.

FTIR Spectroscopy. Diffuse reflectance infrared Fourier transform (DRIFT) measurements were made on a Bruker Vertex 80 FT-IR spectrometer equipped with a HeNe laser and photovoltaic MCT detector and OPUS software, to characterize the spent catalysts. Before measurements, samples were vacuum-dried overnight after a 24 h reaction. Then, they were mixed with KBr and finely ground to ensure a smooth surface in the sample chamber. p-Nitrobenzaldehyde and homogeneously synthesized intermediate were also analyzed in the same manner for comparison.

Active Site Quantification. Measurement of amine sites in the materials was performed using a modified ninhydrin method.[48,49] Different AP-MSN samples (15.0 mg each) were suspended in absolute ethanol (3.0 mL). An aliquot (0.5 mL) of ninhydrin in EtOH (56 mM) solution was added to the suspension, and the mixture was heated for 10 min at 100 °C. After the samples were cooled for 5 min, the absorption of the resultant Ruheman's purple complex was measured at 588 nm in a microplate reader against a blank consisting of MSN (15.0 mg), absolute ethanol (3.0 mL), and ninhydrin solution (56 mM, 0.5 mL). Butylamine was used as a calibration standard for quantification purposes.

Fluorescence Measurements of Prodan-Loaded MSN Samples. Measurement of the samples' dielectric constants was done according to our previously published method.[45] A solution of Prodan in acetone (0.010 mL, 1.0 mM) was added to the dry samples (10.0 mg each) and ground. The mixture was left to dry and then suspended in water (2.0 mL). The suspensions were analyzed by fluorescence spectroscopy in a Cary Eclipse spectrophotometer. The excitation wavelength was set at 337 nm, and both excitation and emission slit widths were set at 5 nm. The

fluorescence spectra were then fitted in OriginPro using a Gaussian distribution model. The maximum fluorescence emission wavelength of each sample was used to assign dielectric constants on the basis of probe fluorescence in reference solvents (Figure S1 and eq S1).[45] To test if the dye was associated to the materials, the suspensions were centrifuged. Fluorescence spectroscopy analysis of the supernatants gave no signal, indicating the dye was not present in water. Resuspension of the solids in fresh water restored the signal, indicating the dye remained associated to the MSN.

Aldol Reaction between Para-Substituted Benzaldehydes and Acetone. Para-substituted benzaldehydes (0.20 mmol) were dissolved in excess acetone (1.5 mL, 20 mmol), followed by the addition of a suspension of functionalized APMSN (35−38 mg, corresponding to 1.0 mol % amine based on the aldehyde substrate) in the corresponding solvent (1.5 mL). The solution was stirred for different amounts of time ranging from 2 to 75 h at 60 °C. Reactions for p-tolualdehyde and benzaldehyde were performed using twice the amount of reactants. The reaction mixtures were quenched with ice and centrifuged; the supernatant was then concentrated under reduced pressure in a rotary evaporator. The products were redissolved in CDCl3 and quantified by 1 H NMR using DMS or TTMS as the internal standards. All mass balances were 100% ± 10%.

Because of their lower boiling points, the reactions using ptolualdehyde and benzaldehyde were also analyzed by GC-MS, to verify the mass balance. These samples were centrifuged, and an aliquot (0.200 mL) was diluted in ethanol (1.0 mL) and analyzed in an Agilent GC-MS instrument (7890A, 5975C) with a HP-5MS column, with resorcinol as the internal standard.

TOFs were calculated from the slope of the kinetic plots (time versus turnover number). The turnover number was defined as mmol of product divided by mmol of aminopropyl groups in the reaction system (based on ninhydrin quantification). Selectivities were calculated as 100% times the mmol of each product divided by the mmol of the sum of the products at the longest time of sampling.

Henry Reaction between p-Nitrobenzaldehyde and Nitromethane. p-Nitrobenzaldehyde (30 mg, 0.20 mmol) was dissolved in excess nitromethane (1.5 mL, 28 mmol), followed by the addition of a suspension of functionalized MSN (35 mg, 1.0 mol % AP) in water (1.5 mL). The solution was stirred for 24 h at 60 °C. The reaction mixture was quenched with ice and centrifuged; the supernatant was then concentrated under reduced pressure. The products were quantified by 1 H NMR using TTMS as the internal standard.

Vinylogous Aldol Reaction between p-Nitrobenzaldehyde and 3-Buten-2-one.

p-Nitrobenzaldehyde (30 mg, 0.20 mmol) and 3-buten-2-one (16.2 μL, 0.20 mmol) were added to a a suspension of functionalized MSN (35 mg, 1.0 mol % AP) in water (3 mL). The solution was stirred for 24 h at 60 °C. The reaction mixture was quenched with ice and centrifuged; the supernatant was then concentrated under reduced pressure. The products were quantified by 1 H NMR using DMS as the internal standard.

Results and Discussion

First, we tested the catalytic activity of vacuum-dried AP-MSN (0.07 ± 0.02 mmol aminopropyl/g) for the cross-aldol condensation between p-nitrobenzaldehyde and excess acetone (Scheme 2) in anhydrous methanol, 1-propanol, and water. Consistent with previous reports, AP-MSN showed low catalytic activity in methanol (TOF 0.43 ± 0.02 h−1 , dielectric constant ε 32.6; Figure 1), likely due to the solvent stabilization of non-nucleophilic

ammonium−silanoxy ion pairs and formation of inhibited states 1 and 2 (Scheme 3, case I).[18,19] Replacing methanol with the less polar 1-propanol (ε 20.1) led to a ca. 50% enhancement in AP-MSN activity (TOF 0.65 ± 0.02 h^{-1}), suggesting that destabilization of protonated amines by decreasing solvent polarity increases the number of active nucleophilic sites, even though the persistence of inhibition products 1 and 2 prevents a further increase in reactivity (Scheme 3, case II).[18] Use of water as a solvent led to an AP-MSN activity (TOF 0.58 ± 0.05 h−1) higher than that in methanol but slightly lower than that in propanol, suggesting that the role of water in the hydrolysis of inhibited states 1 and 2 is more significant than its dielectric stabilization of the protonated ammonium ions (Scheme 3, case III).[18,19,43] These results indicate that AP-MSN catalytic activity can be improved either by decreasing the dielectric constant of the solvent or by utilizing the hydrolytic action of water. Attempts to combine both effects using a 1-propanol/ water mixture failed to further increase the activity, giving a rate lower than those of the pure solvents (TOF 0.44 ± 0.01 h^{-1}). The lack of activity enhancement in the solvent mixture was likely due to its high dielectric constant (ε 44).[46,47] Thus, to effectively combine the hydrolytic effect of water with the destabilization of ammonium−silanoxy pairs, it is necessary to prevent water from significantly increasing the dielectric constant at the reaction site.

We clarify that the TOF values are calculated on the basis of the amine content of the original catalysts as measured by reaction with ninhydrin.[48,49] Because both inhibitory processes (formation of ammonium−silanoxy ion pairs and products 1 and 2) imply deactivation of a fraction of the amine groups, the variations in TOF should account for the differences in number of free active sites that result from these inhibitory mechanisms.

An alternate way to control the dielectric properties around a supported active site is to immobilize organic groups next to it.[9,50] Because the tethered organic groups can interfere with

solvation at the solid−water boundary, the dielectric properties of the interface can be decoupled from those of the bulk solvent, resulting in a lower local polarity.[45] Following this idea, we synthesized a new catalyst by incorporating hexyltrimethoxysilane along with 3-aminopropyltrimethoxysilane in MSN. Amine quantification by reaction with ninhydrin combined with elemental (CHN) analysis of the material indicated aminopropyl and hexyl group loadings of 0.06 ± 0.01 and 1.02 ± 0.02 mmol/g, respectively (Table S1). The new catalyst was designated Hex(1.0)-AP-MSN.

To measure the effective dielectric constant of the catalyst− water interface, we used the fluorescent solvatochromic probe Prodan.[51−53] Because of its zwitterionic structure, the stability of Prodan's excited state is greatly affected by the dielectric properties of its environment.[45] This results in a dependence of the probe's Stokes shift on the dielectric constant of the solvent (Figure S1). Impregnation of the probe on Hex(1.0)- AP-MSN followed by suspension in water and fluorescence spectroscopy analysis resulted in a Stokes shift of 151.0 ± 0.6 nm, which, on the basis of the solvent calibration (eq S1), corresponded to an interfacial dielectric constant (ε_i) of 21.6 ± 0.5. Note that because the probe remains adsorbed on the surface without leaching out to the solvent, it must directly reflect the dielectric properties of the interface. Importantly, the interfacial dielectric constant of Hex(1.0)-AP-MSN in water was significantly lower than that measured for AP-MSN in the same solvent (ε_i 74.8 ± 0.8; Figure 1b) and was very close to the dielectric constant of 1-propanol (ε 20.1).[47]

Remarkably, the catalytic activity of Hex(1.0)-AP-MSN for the reaction in water (TOF 3.2 ± 0.2 h^{-1}) was about 5 times higher than those of AP-MSN in water or 1-propanol. These results suggest that the combination of a low dielectric environment around the active sites due to the hexyl groups and the availability of water at the interface decreases the extent of catalyst

deactivation by species such as Schiff base 1 (Scheme 3, case IV). The coexistence of water and hexyl groups on the surface of Hex(1.0)-AP-MSN was evidenced by exposing a vacuum-dried sample to ambient humidity and acquiring its ^{1}H solid state (SS)NMR (Figure S2). In addition to the signals corresponding to the hexyl and amine groups, the spectrum presents two resonances at 4.8 and 4.0 ppm attributed to weakly adsorbed water and rapidly exchanging SiOH−(H2O)n species, respectively.[54,55]

Elemental analysis of the spent and washed AP-MSN after the reaction in 1-propanol and Hex(1.0)-AP-MSN after the reaction in water indicated increases in N content of 78% and 56%, respectively. In addition, the spent AP-MSN changed in color from the original white to yellow (Figure S3), which may be indicative of the inhibitory Schiff base 1. 18,29,43 In contrast, Hex(1.0)-AP-MSN retained its white color after reaction in water. Whereas these observations suggest formation of imine intermediate 1, analyses by dynamic nuclear polarization (DNP) enhanced 13C SSNMR, Raman, and FTIR spectroscopy (Figures S4−S7) could not distinghuish this species from the potentially physisorbed p-nitrobenzaldehyde substrate. All of the collected spectra indicate the presence of aromatic species in the spent catalysts; however, the observed signals could be assigned to either the starting p-nitrobenzaldehyde or the hypothetical Schiff base intermediate 1. While signals specific to the intermediate 1 can be observed by SSNMR at much higher AP loadings (1 mmol/g),[18,29,43] the low active site loadings in this study (ca. 0.06 mmol/g) prevented unequivocal identification of the molecules. Importantly, however, amine quantification with ninhydrin indicated that the spent AP-MSN after reaction in 1-propanol had 0.03 mmol/g of available sites (i.e., a ca. 60% loss of active sites), while the spent Hex(1.0)-AP-MSN after reaction in water retained 0.04 mmol sites/g (a 33% loss after reaction). This result confirms that both catalysts are partially poisoned during the reaction but that the combination of

hexyl groups and interfacial water decreased the extent of deactivation. Recycling of both catalysts indicated a steady drop in activity over four cycles, with Hex(1.0)-AP-MSN in water giving always higher product yields in comparison to AP-MSN in 1-propanol (Figure S8).

The dependence of the AP-MSN-catalyzed reaction on the polarity of the medium can be analyzed following the Eyring− Laidler formalism for reactions involving dipoles. According to this model, the logarithm of the rate constant has a linear dependence on the reciprocal of the medium's ε value (eq S2).[1,56−59] Consistent with this theory, the AP-MSN-catalyzed aldol reaction in different solvents shows a linear relationship between the log(TOF) and the inverse of the solvents' ε value (Figure 2, red squares and Table S2 and Figure S9). The positive slope of the correlation likely reflects the increasing availability of nucleophilic amine groups with decreasing ε, because higher ε media should increase the extent of amine protonation and thereby decrease the rate of the aldol pathway (Scheme 3, case I). This dependence should also be valid for the interfacial dielectric constant (εi) of hexyl-substituted APMSN in water. To examine this hypothesis, we synthesized additional bifunctional Hex-AP-MSN materials loaded with amounts of 3-aminopropyl groups similar to those before (0.06−0.07 mmol/g) but varying amounts of hexyl groups (Hex(0.5)-AP-MSN, Hex(0.7)-AP-MSN, and Hex(0.9)-APMSN). The hexyl groups were incorporated in 10-fold excess with respect to the amines to ensure they could affect the solvation environment of the active sites. Again, group loadings were measured by a combination of elemental (CHN) analysis and amine quantification via reaction with ninhydrin (Table S1). Because silanol groups participate in the reaction as cooperative partners of the amines, they were also quantified by ^{29}Si DP MAS SSNMR.[60] The analysis indicated that all the materials had similar amounts of silanols (Figure S10), more than enough to ensure effective cooperativity with the catalytic amines.[25] Nitrogen physisorption and powder X-ray diffraction

analyses of the samples showed that the organic groups had no significant effects on the textural properties and pore structure of the materials (Table S3 and Figure S11). The εi values of the materials suspended in water were obtained by fluorescence spectroscopy analysis of adsorbed Prodan. The εi values decreased with the hexyl group loadings of the materials, confirming that interfacial polarity can be fine-tuned via surface functionalization (Table S3 and Figure S12).[45]

The reaction was then performed in water using the hexylfunctionalized materials as catalysts. The catalytic activities of the Hex-AP-MSN varied significantly, despite all reactions being conducted in water under the same conditions. Moreover, the dependence of the catalytic activity on the interfacial dielectric constant shows a trend analogous to that of AP-MSN in water-free solvents, i.e., the log(TOF) increased as a function of $1/\varepsilon_i$ (Figure 2, blue circles, and Table S4 and Figure S13). Three important features can be observed here. First, the activities of the Hex-AP-MSN catalysts used in water were significantly higher than those of AP-MSN in water-free solvents with comparable ε values. This upward shift in activity is likely due to the presence of water at the interface, which improves the reactivity as described above. Second, the reactions performed in aqueous media (blue) displayed a higher rate sensitivity to changes in polarity in comparison to those performed in water-free media (red), as indicated by the difference in the slopes of their $1/\varepsilon$−log(TOF) linear correlations (21.3 for aqueous versus 12.6 for water-free reactions). This difference in sensitivity indicates that the effect of water on the reaction is more important at low interfacial polarities in comparison to that when the local environment is highly polar. Finally, the nonzero slope of the aqueous HexAP-MSN-catalyzed reactions confirms that the dielectric properties at the active site differ from those of the bulk solvent and are controlled by the organic functionalities.

An alternative explanation to the increase in activity of APMSN with hexyl loading could be the steric destabilization of bulky species such as 1 and 2 by the long hydrocarbon chains. To examine this possibility, we synthesized 3-methoxypropyland 2-cyanoethyl-modified AP-MSN (MeOP-AP-MSN, 1.25 ± 0.01 mmol methoxypropyl/g; CNEt-AP-MSN, 0.90 ± 0.01 mmol cyanoethyl/g) with AP loadings similar to those for the Hex-AP-MSN materials (0.05 ± 0.01 and 0.07 ± 0.02 mmol/g, respectively). Fluorescence spectroscopy measurements with adsorbed Prodan indicated that the materials had interfacial dielectric constants (εi 49 ± 1, MeOP-AP-MSN; εi 53 ± 1, CNEt-AP-MSN) between those of AP-MSN (74.8 ± 0.8) and Hex-AP-MSN (<35), which is consistent with the higher polarity of methyl ether and nitrile groups in comparison to the hexyl chain. In spite of the presence of a large amount of organic groups on the surface, the TOF of the aldol reaction using these materials in water were between those of AP-MSN and the Hex-AP-MSN (1.32 ± 0.09 h−1 , MeO-AP-MSN; 0.68 ± 0.03 h−1 , CNEt-AP-MSN). This result indicates that the effect of the organic groups on the catalytic activity of the materials was not due to sterics but likely due to the differences in the dielectric properties of the interfaces. Importantly, the activities of both MeOP-AP-MSN and CNEt-AP-MSN fit in the 1/ε−log(TOF) trend for aqueous media (Figure 2, black and white triangles respectively).

Hammett analysis of the reaction indicates a small difference in its sensitivity to the electronic effects of benzaldehyde substituents when Hex(1.0)-AP-MSN versus AP-MSN is used as a catalyst in water (Figures S13 and S14 and Table S5). The positive slope obtained with both materials is consistent with previous reports[21] and suggests that there are no fundamental differences in the reaction mechanism using these catalysts. The positive slope is indicative of a negative charge buildup in the transition state of the rate-limiting step. This step has been proposed as the nucleophilic attack of the enamine on the benzaldehyde carbonyl (bottom of

catalytic cycle in Scheme 1).[21,23,25,26] Electron-withdrawing groups lower the activation barrier by decreasing the negative charge density at the reaction center. This effect is more relevant in nonpolar environments because they have less capacity to stabilize charges in comparison to high-dielectric media. This was recognized in the initial work by Hammett, when he showed that the reaction constant (ρ) is inversely proportional to the dielectric constant of the media (eqs S3 and S4).[61] Thus, the slightly larger slope in the Hammett plot for Hex(1.0)- APMSN than for AP-MSN in water (Figure S14) is consistent with the lower ε_i of the former. The difference in substituent sensitivities between the two catalysts appears small in the Hammett plot because it is based on the logarithm of the TOF ratios of substituted and nonsubstituted benzaldehyde; however, it becomes more obvious in direct comparisons of the substrates' TOFs (Figure 3).

We also observed some variations in product selectivity as a function of hexyl substitution of the catalyst. Under all the conditions tested, the aldol product was favored over the enone regardless of the catalyst employed. It is known that the selectivity for enone is typically favored by increasing reaction temperatures.[34] On the basis of the reaction equilibrium, one could also expect that the presence of anhydrous media would give higher enone selectivity in comparison to water. Indeed, while all the AP-MSN-catalyzed reactions run in anhydrous solvents showed enone selectivities between 19 and 28%, the reaction conducted in water with the same catalyst gave lower aldol product (5%) (Table S2). Reactions with hexylsubstituted catalysts in water also showed lower enone selectivities (3−4%) (Table S4).

Overall, our results suggest that lowering the interfacial polarity of aqueous AP-MSN enhances its catalytic activity toward the aldol condensation because it increases the availability of the nucleophilic amines. On the basis of this postulate, the same approach should favor other reactions catalyzed by silica-supported amines. For example, Ballini and Bosica have reported

that the amine-catalyzed Henry reaction (Scheme 4a) is improved when organic solvents are replaced with water.[62] While this reaction proceeds through a different mechanism than the aldol condensation, the rate-limiting step requires the availability of free amines[21,62,63] and should therefore benefit from a lower interfacial polarity. To examine this hypothesis, we performed the Henry reaction between pnitrobenzaldehyde and nitromethane using aqueous Hex(1.0)- AP-MSN and AP-MSN as catalysts. Our measurements indicated that, indeed, the hexyl-modified catalyst was twice as active as AP-MSN (Figure 4, black bars), which is consistent with the proposed hypothesis. Similarly, the activity of aqueous Hex(1.0)-AP-MSN for the vinylogous aldol reaction between p-nitrobenzaldehyde and 3-buten-2-one (Scheme 4b)64 was about 50% higher than that of AP-MSN (Figure 4, white bars), further supporting the idea that low interfacial polarity enhances the activity of these catalysts by increasing the availability of the amine active sites.

Conclusion

This work demonstrates that nonpolar and aqueous media can be combined in interfacial systems to enhance the performance of supported catalysts. The activity of the AP-MSN-catalyzed aldol reaction can be improved by both (1) low-polarity media because they disfavor silanol-mediated amine protonation and (2) water because it destabilizes inhibitory pathways. The synergistic combination of low-polarity local environments and water can be achieved by introducing alkyl groups along with the catalyst on MSN and suspending the composite in water. The dielectric constant at the MSN−water interface (ε_i) can be determined by fluorescence spectroscopy using solvatochromic probes such as Prodan and calibrating the fluorescence with standard solvents. The ε_i of Hex-AP-MSN in water is directly proportional to the surface density of alkyl groups. Decreasing the εi of aqueous Hex-AP-MSN leads to enhancements in the TOF

of the aldol reaction comparable to those on decreasing the ε of the solvent; however, for a given ε_i or ε the aqueous reaction is about 4 times faster than the reaction using anhydrous alcohols as solvents. Decreasing the ε_i of Hex-AP-MSN in water enhances the sensitivity of the aldol reaction to substituent effects, as probed by studying the Hammett linear structure−activity relationships of the system. Electron-withdrawing groups particularly enhance the activity of Hex-AP-MSN for this reaction because they disperse the charge density in the transition state of the rate-limiting step, compensating for the inability of the low-polarity media to stabilize charges. Understanding the role of local environment on the catalysis of the aldol reaction enables controlling other amine-mediated transformations, as demonstrated by the higher activity of aqueous Hex-AP-MSN in comparison to AP-MSN in the Henry and vinylogous aldol reactions. Ultimately, controlling the interfacial dielectric properties of heterogeneous catalysts will enable designing advanced systems that replace nonpolar organic solvents with water, an economical and an environmentally friendly solvent.

Declarations

Acknowledgements

This research was supported by the U.S. Department of Energy, Office of Basic Energy Sciences, Division of Chemical Sciences, Geosciences, and Biosciences, through the Ames Laboratory Catalysis Science program. The Ames Laboratory is operated for the U.S. Department of Energy by Iowa State University under Contract No. DE-AC02-07CH11358.

Schema and Figures

Scheme 1. Proposed Cycle of the Aldol Reaction between p-Nitrobenzaldehyde and Acetone Catalyzed by 3-Amino-Functionalized Mesoporous Silica Nanoparticles (AP-MSN): Main Reaction (Black) and Possible Inhibitory Pathways (Red)[a], Ar = p-nitrophenyl

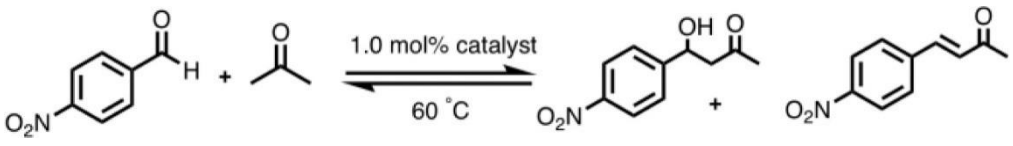

Scheme 2. Cross-Aldol Condensation between p-Nitrobenzaldehyde and Acetone

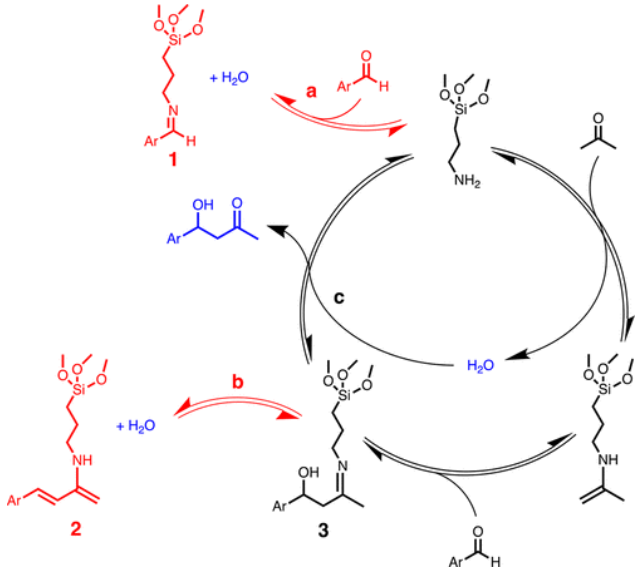

Scheme 4. (a) Henry Reaction between pNitrobenzaldehyde and Nitromethane and (b) Vinylogous Aldol Reaction between p-Nitrobenzaldyhde and 3-Buten-2- one

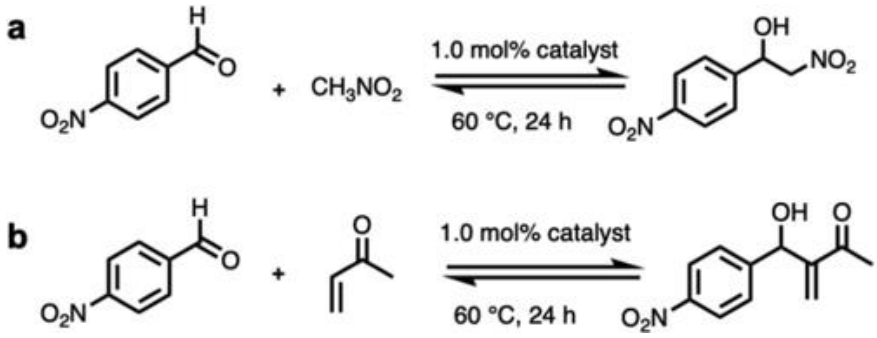

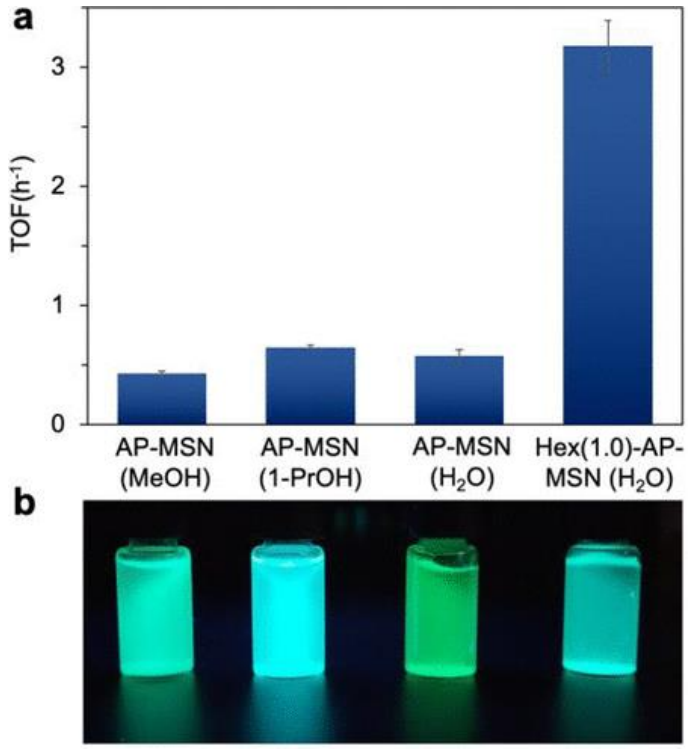

Figure 1. (a) Catalytic activities of AP-MSN in different solvents and Hex(1.0)-AP-MSN in water for the aldol reaction between p-nitrobenzaldehyde and acetone (1.0 mol % AP, 60 °C). (b) Suspensions of the Prodan-loaded materials in the solvents (corresponding to the materials and solvents in (a)) under a 355 nm lamp. The color of the fluorescent emission is indicative of the dielectric constant (ε).

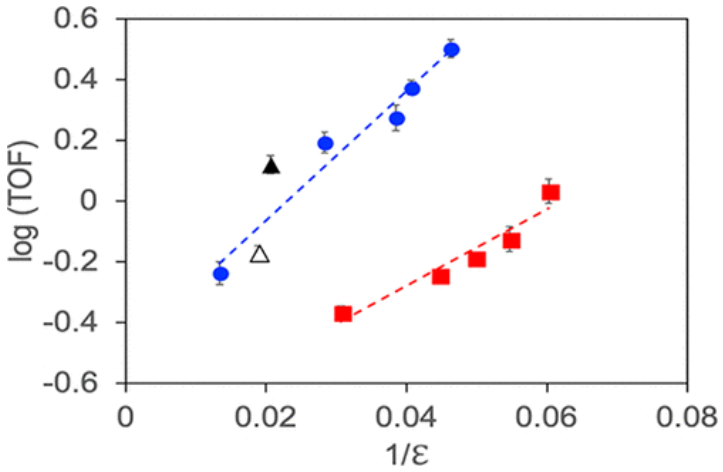

Figure 2. Variation of log(TOF) of the aldol reaction between p-nitrobenzaldehyde and acetone with the reciprocal of the dielectric constant of Hex-AP-MSN having different hexyl group loadings in water (blue circles), MeOP-AP-MSN in water (black triangle), CNEt-AP-MSN in water (white triangle), and AP-MSN in anhydrous solvents (red squares) (1.0 mol % AP, 60 °C).

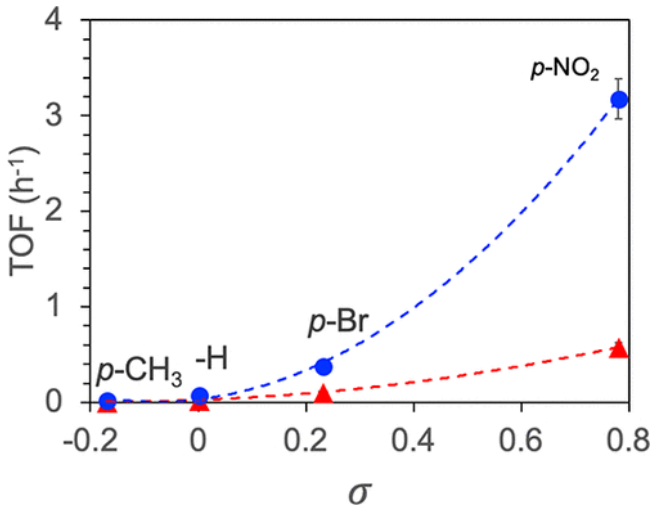

Figure 3. Hammett constants (σ) of para-substituted benzaldehydes versus the TOFs of their aldol reaction with acetone using Hex(1.0)- AP-MSN (blue circles) and AP-MSN (red triangles) as catalysts in water (1.0 mol % amine, 60 °C).

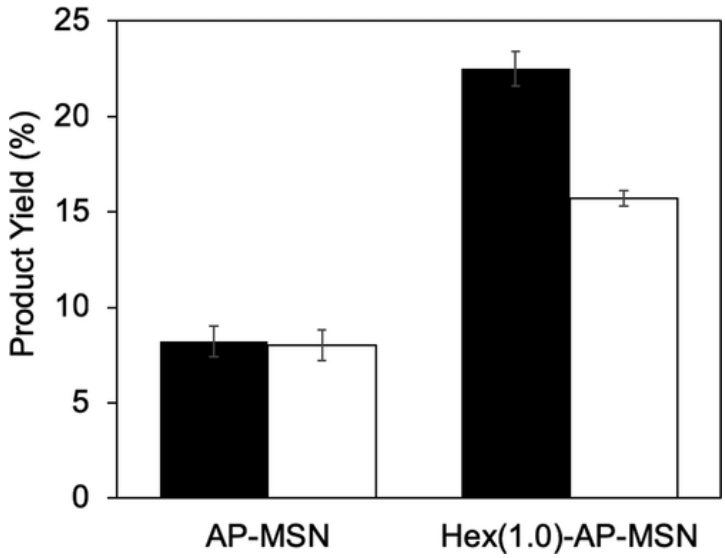

Figure 4. Differences in catalytic activities between aqueous AP-MSN and Hex(1.0)-AP-MSN for the Henry (black) and vinylogous aldol reactions (white ×100) (1.0 mol % amine, 24 h, 60 °C).

References

1) Reichardt, C. Solvents and Solvent Effects in Organic Chemistry, 4th ed.; Wiley-VCH: Weinheim, Germany, 2011.

2) Reichardt, C. Solvents and Solvent Effects: an Introduction. Org. Process Res. Dev. 2007, 11, 105−113.

3) Ruiz-Pernía, J. J.; Martí, S.; Moliner, V.; Tuñon, I. A Novel Strategy to Study Electrostatic Effects in Chemical Reactions: Differences Between the Role of Solvent and the Active Site of Chalcone Isomerase in a Michael Addition. J. Chem. Theory Comput. 2012, 8, 1532−1535.

4) Theilacker, K.; Buhrke, D.; Kaupp, M. Validation of the DirectCOSMO-RS Solvent Model for Diels-Alder Reactions in Aqueous Solution. J. Chem. Theory Comput. 2015, 11, 111−121.

5) Bernasconi, L.; Baerends, E. J. A Frontier Orbital Study with ab Initio Molecular Dynamics of the Effects of Solvation on Chemical Reactivity: Solvent-Induced Orbital Control in FeO-Activated Hydroxylation Reactions. J. Am. Chem. Soc. 2013, 135, 8857−8867.

6) Jalan, A.; West, R. H.; Green, W. H. An Extensible Framework for Capturing Solvent Effects in Computer Generated Kinetic Models. J. Phys. Chem. B 2013, 117, 2955−2970.

7) Horn, M.; Matyjaszewski, K. Solvent Effects on the Activation Rate Constant in Atom Transfer Radical Polymerization. Macromolecules 2013, 46, 3350−3357.

8) Narske, R. M.; Klabunde, K. J.; Fultz, S. Solvent Effects on the Heterogeneous Adsorption and Reactions of (2-Chloroethyl)ethyl Sulfide on Nanocrystalline Magnesium Oxide. Langmuir 2002, 18, 4819−4825.

9) Bass, J. D.; Solovyov, A.; Pascall, A. J.; Katz, A. Acid-Base Bifunctional and Dielectric Outer-Sphere Effects in Heterogeneous Catalysis: A Comparative Investigation of Model Primary Amine Catalysts. J. Am. Chem. Soc. 2006, 128, 3737−3747.

10) Brindza, M. R.; Walker, R. A. Differentiating Solvation Mechanisms at Polar Solid/Liquid Interfaces. J. Am. Chem. Soc. 2009, 131, 6207−6214.

11) Alam, T. M.; Hibbs, M. R. Characterization of Heterogeneous Solvent Diffusion Environments in Anion Exchange Membranes. Macromolecules 2014, 47, 1073−1084.

12) Xu, X.; Zhang, C.; Zhai, Y.; Liu, Y.; Zhang, R.; Tang, X. Upgrading of Bio-Oil Using Supercritical 1-Butanol over a Ru/C Heterogeneous Catalyst: Role of the Solvent. Energy Fuels 2014, 28, 4611−4621.

13) Fridkin, G.; Yehezkel, L.; Columbus, I.; Zafrani, Y. Solvent Effects on the Reactions of the Nerve Agent VX with KF/Al2O3: Heterogeneous or Homogeneous Decontamination? J. Org. Chem. 2016, 81, 2154−2158.

14) Sievers, C.; Noda, Y.; Qi, L.; Albuquerque, E. M.; Rioux, R. M.; Scott, S. L. Phenomena Affecting Catalytic Reactions at Solid-Liquid Interfaces. ACS Catal. 2016, 6, 8286−8307.

15) Weber, D.; Mitchell, J.; McGregor, J.; Gladden, L. F. Comparing Strengths of Surface Interactions for Reactants and Solvents in Porous Catalysts Using Two-Dimensional NMR Relaxation Correlations. J. Phys. Chem. C 2009, 113, 6610−6615.

16) Copeland, J. R.; Shi, X.-R.; Sholl, D. S.; Sievers, C. Surface Interactions of C2 and C3 Polyols with γ-Al2O3 and the Role of Coadsorbed Water. Langmuir 2013, 29, 581−593.

17) Faheem, M.; Suthirakun, S.; Heyden, A. New Implicit Solvation Scheme for Solid Surfaces. J. Phys. Chem. C 2012, 116, 22458−22462.

18) Kandel, K.; Althaus, S. M.; Peeraphatdit, C.; Kobayashi, T.; Trewyn, B. G.; Pruski, M.; Slowing, I. I. Solvent-Induced Reversal of Activities between Two Closely Related Heterogeneous Catalysts in the Aldol Reaction. ACS Catal. 2013, 3, 265−271.

19) Zeidan, R. K.; Hwang, S.-J.; Davis, M. E. Multifunctional Heterogeneous Catalysts: SBA-15-Containing Primary Amines and Sulfonic Acids. Angew. Chem., Int. Ed. 2006, 45, 6332−6335.

20) Farnesi Camellone, M.; Negreiros Ribeiro, F.; Szabová, L.; Tateyama, Y.; Fabris, S. Catalytic Proton Dynamics at the Water/Solid Interface of Ceria-Supported Pt Clusters. J. Am. Chem. Soc. 2016, 138, 11560−11567.

21) Collier, V. E.; Ellebracht, N. C.; Lindy, G. I.; Moschetta, E. G.; Jones, C. W. Kinetic and Mechanistic Examination of Acid-Base Bifunctional Aminosilica Catalysts in Aldol and Nitroaldol Condensations. ACS Catal. 2016, 6, 460−468.

22) Kim, K. C.; Moschetta, E. G.; Jones, C. W.; Jang, S. S. Molecular Dynamics Simulations of Aldol Condensation Catalyzed by Alkylamine-Functionalized Crystalline Silica Surfaces. J. Am. Chem. Soc. 2016, 138, 7664−7672.

23) Brunelli, N. A.; Venkatasubbaiah, K.; Jones, C. W. Cooperative Catalysis with Acid-Base Bifunctional Mesoporous Silica: Impact of Grafting and Co-condensation Synthesis Methods on Material Structure and Catalytic Properties. Chem. Mater. 2012, 24, 2433−2442.

24) Lauwaert, J.; Ouwehand, J.; De Clercq, J.; Cool, P.; Van Der Voort, P.; Thybaut, J. W. Tuning component enrichment in amino acid functionalized (organo)silicas. Catal. Commun. 2017, 88, 85−89.

25) Lauwaert, J.; De Canck, E.; Esquivel, D.; Thybaut, J. W.; Van Der Voort, P.; Marin, G. B. Silanol-Assisted Aldol Condensation on Aminated Silica: Understanding the Arrangement of Functional Groups. ChemCatChem 2014, 6, 255−264.

26) Lauwaert, J.; De Canck, E.; Esquivel, D.; Van Der Voort, P.; Thybaut, J. W.; Marin, G. B. Effects of amine structure and base strength on acid-base cooperative aldol condensation. Catal. Today 2015, 246, 35−45.

27) Lewis, J. D.; Van de Vyver, S.; Román-Leshkov, Y. Acid-Base Pairs in Lewis Acidic Zeolites Promote Direct Aldol Reactions by Soft Enolization. Angew. Chem., Int. Ed. 2015, 54, 9835−9838.

28) Hoyt, C. B.; Lee, L.-C.; Cohen, A. E.; Weck, M.; Jones, C. W. Bifunctional Polymer Architectures for Cooperative Catalysis: Tunable Acid-Base Polymers for Aldol Condensation. ChemCatChem 2017, 9, 137−143.

29) Kandel, K.; Althaus, S. M.; Peeraphatdit, C.; Kobayashi, T.; Trewyn, B. G.; Pruski, M.; Slowing, I. I. Substrate Inhibition in the Heterogeneous Catalyzed Aldol Condensation: A Mechanistic Study of Supported Organocatalysts. J. Catal. 2012, 291, 63−68.

30) Tarabanko, V. E.; Hendogina, Y. V.; Petuhov, D. V.; Pervishina, E. P. On the Role of Retroaldol Reaction in the Process of Lignin Oxidation into Vanillin. Kinetics of the Vanillideneacetone Cleavage in Alkaline Media. React. Kinet. Catal. Lett. 2000, 69, 361−368.

31) Fan, H.; Yang, Y.; Song, J.; Ding, G.; Wu, C.; Yang, G.; Han, B. One-pot Sequential Oxidation and Aldol-Condensation Reactions of Veratryl Alcohol Catalyzed by the Ru@ZIF-8 + CuO/Basic Ionic Liquid System. Green Chem. 2014, 16, 600−604.

32) Sasaki, M.; Furukawa, M.; Minami, K.; Adschiri, T.; Arai, K. Kinetics and Mechanism of Cellobiose Hydrolysis and Retro-Aldol Condensation in Subcritical and Supercritical Water. Ind. Eng. Chem. Res. 2002, 41, 6642−6649.

33) Liang, G.; Wang, A.; Zhao, X.; Lei, N.; Zhang, T. Selective Aldol Condensation of Biomass-derived Levulinic Acid and Furfural in Aqueous-phase over MgO and ZnO. Green Chem. 2016, 18, 3430−3438.

34) Nelson, N.; Chaudhary, U.; Kandel, K.; Slowing, I. Heterogeneous Multicatalytic System for Single-Pot Oxidation and C-C Coupling Reaction Sequences. Top. Catal. 2014, 57, 1000−1006.

35) Dabral, S.; Hernández José, G.; Kamer Paul, C. J.; Bolm, C. Organocatalytic Chemoselective Primary Alcohol Oxidation and Subsequent Cleavage of Lignin Model Compounds and Lignin. Chem. Sus Chem. 2017, 10, 2707−2713.

36) Bui, T. V.; Sooknoi, T.; Resasco, D. E. Simultaneous Upgrading of Furanics and Phenolics through Hydroxyalkylation/Aldol Condensation Reactions. Chem. Sus Chem. 2017, 10, 1631−1639.

37) Pham, T. N.; Zhang, L.; Shi, D.; Komarneni, M. R.; Ruiz, M. P.; Resasco, D. E.; Faria, J. Fine-Tuning the Acid-Base Properties of Boron-Doped Magnesium Oxide Catalyst for the Selective Aldol Condensation. Chem. Cat Chem. 2016, 8, 3611−3620.

38) Lee, K. S.; Parquette, J. R. A self-assembled nanotube for the direct aldol reaction in water. Chem. Commun. 2015, 51, 15653−15656.

39) Lu, A.; Moatsou, D.; Hands-Portman, I.; Longbottom, D. A.; O'Reilly, R. K. Recyclable l-Proline Functional Nanoreactors with Temperature-Tuned Activity Based on Core-Shell Nanogels. ACS Macro Lett. 2014, 3, 1235−1239.

40) Eymur, S.; Akceylan, E.; Sahin, O.; Uyanik, A.; Yilmaz, M. Direct Enantioselective Aldol Reactions Catalyzed by Calix[4]Arene-Based L-Proline Derivatives in the Water. Tetrahedron 2014, 70, 4471−4477.

41) Doyagüez, E. G.; Calderón, F.; Sánchez, F.; Fernández-Mayoralas, A. Asymmetric Aldol Reaction Catalyzed by a Heterogenized Proline on a Mesoporous Support. The Role of the Nature of Solvents. J. Org. Chem. 2007, 72, 9353−9356.

42) Schmid, M. B.; Zeitler, K.; Gschwind, R. M. The Elusive Enamine Intermediate in Proline-Catalyzed Aldol Reactions: NMR Detection, Formation Pathway, and Stabilization Trends. Angew. Chem., Int. Ed. 2010, 49, 4997−5003.

43) De Vylder, A.; Lauwaert, J.; Esquivel, D.; Poelman, D.; De Clercq, J.; Van Der Voort, P.; Thybaut, J. W. The Role of Water in the Reusability of Aminated Silica Catalysts for Aldol Reactions. J. Catal. 2018, 361, 51−61.

44) Cummings, T. F.; Shelton, J. R. Mannich Reaction Mechanisms. J. Org. Chem. 1960, 25, 419−423.

45) Singappuli-Arachchige, D.; Manzano, J. S.; Sherman, L. M.; Slowing, I. I. Polarity Control at Interfaces: Quantifying Pseudosolvent Effects in Nano-confined Systems. ChemPhysChem 2016, 17, 2982−2986.

46) Méndez-Bermúdez, J. G.; Dominguez, H.; Pusztai, L.; Guba, S.; Horváth, B.; Szalai, I. Composition and Temperature Dependence of the Dielectric Constant of 1-Propanol/Water Mixtures: Experiment and Molecular Dynamics Simulations. J. Mol. Liq. 2016, 219, 354−358.

47) Smallwood, I. Handbook of Organic Solvent Properties; Elsevier Science: Burlington, 1996.

48) Soto-Cantu, E.; Cueto, R.; Koch, J.; Russo, P. S. Synthesis and Rapid Characterization of Amine-Functionalized Silica. Langmuir 2012, 28, 5562−5569.

49) Manzano, J. S.; Weinstein, Z. B.; Sadow, A. D.; Slowing, I. I. Direct 3D Printing of Catalytically Active Structures. ACS Catal. 2017, 7, 7567−7577.

50) Bass, J. D.; Anderson, S. L.; Katz, A. The Effect of Outer-Sphere Acidity on Chemical Reactivity in a Synthetic Heterogeneous Base Catalyst. Angew. Chem. 2003, 115, 5377−5380.

51) Weber, G.; Farris, F. J. Synthesis and Spectral Properties of a Hydrophobic Fluorescent Probe: 6-Propionyl-2-(Dimethylamino)-Naphthalene. Biochemistry 1979, 18, 3075−3078.

52) Cerezo, F. M.; Rocafort, S. C.; Sierra, P. S.; García-Blanco, F.; Oliva, C. D.; Sierra, J. C. Photophysical Study of the Probes Acrylodan (1-[6-(Dimethylamino)naphthalen-2-yl]prop-2-en-1-one), ANS (8-Anilinonaphthalene-1-sulfonate) and Prodan (1-[6 (Dimethylamino)naphthalen-2-yl]propan-1-one) in Aqueous Mixtures of Various Alcohols. Helv. Chim. Acta 2001, 84, 3306−3312.

53) Catalan, J.; Perez, P.; Laynez, J.; Blanco, F. G. Analysis of the Solvent Effect on the Photophysics Properties of 6-Propionyl-2-(dimethylamino)naphthalene (PRODAN). J. Fluoresc. 1991, 1, 215−223.

54) Trébosc, J.; Wiench, J. W.; Huh, S.; Lin, V. S. Y.; Pruski, M. Solid-State NMR Study of MCM-41-type Mesoporous Silica Nanoparticles. J. Am. Chem. Soc. 2005, 127, 3057−3068.

55) Grünberg, B.; Emmler, T.; Gedat, E.; Shenderovich, I.; Findenegg, G. H.; Limbach, H.-H.; Buntkowsky, G. Hydrogen Bonding of Water Confined in Mesoporous Silica MCM-41 and SBA-15 Studied by 1H Solid-State NMR. Chem. - Eur. J. 2004, 10, 5689−5696.

56) Laidler, K. J.; Landskroener, P. A. The Influence of the Solvent on Reaction Rates. Trans. Faraday Soc. 1956, 52, 200−210.

57) Yakupov, M. Z.; Lyapina, N. K.; Shereshovets, V. V.; Imashev, U. B. The Solvent Effect on the Rate of Reaction between Propanethiol and Chlorine Dioxide. Kinet. Catal. 2001, 42, 609−612.

58) Yutilova, K.; Shved, E.; Shuvakin, S. Behavior of epichlorohydrin catalytic acidolysis reaction with the variation of solvent polarity. React. Kinet., Mech. Catal. 2018, 125, 15−24.

59) Karthikeyan, G.; Anbalagan, K.; Elango, K. P. Correlation Analysis of Reactivity in the Reduction of Trans-Chloro-(RC6H4NH2)Bis(1,2-Diaminoethane)Cobalt(III) Complexes by Hexacyanoferrate(II) in Aqueous Methanol. Transition Met. Chem. 2000, 25, 213−218.

60) Huh, S.; Wiench, J. W.; Yoo, J.-C.; Pruski, M.; Lin, V. S.-Y. Organic Functionalization and Morphology Control of Mesoporous Silicas via a Co-Condensation Synthesis Method. Chem. Mater. 2003, 15, 4247−4256.

61) Hammett, L. P. The Effect of Structure upon the Reactions of Organic Compounds. Benzene Derivatives. J. Am. Chem. Soc. 1937, 59, 96−103.

62) Ballini, R.; Bosica, G. Nitroaldol Reaction in Aqueous Media: An Important Improvement of the Henry Reaction. J. Org. Chem. 1997, 62, 425−427.

63) Motokura, K.; Tada, M.; Iwasawa, Y. Heterogeneous Organic Base-Catalyzed Reactions Enhanced by Acid Supports. J. Am. Chem. Soc. 2007, 129, 9540−9541.

64) Casiraghi, G.; Battistini, L.; Curti, C.; Rassu, G.; Zanardi, F. The Vinylogous Aldol and Related Addition Reactions: Ten Years of Progress. Chem. Rev. 2011, 111, 3076−3154.

65) Trébosc, J.; Wiench, J. W.; Huh, S.; Lin, V. S. Y.; Pruski, M., J. Am. Chem. Soc. 2005, 127, 3057-3068.

66) Kandel, K.; Althaus, S. M.; Peeraphatdit, C.; Kobayashi, T.; Trewyn, B. G.; Pruski, M.; Slowing, I. I., ACS Catal. 2013, 3, 265-271.

67) Kandel, K.; Althaus, S. M.; Peeraphatdit, C.; Kobayashi, T.; Trewyn, B. G.; Pruski, M.; Slowing, I. I., J. Catal. 2012, 291, 63-68.

68) Kalaichelvan, S., N. Sundaraganesan, and B.D. Joshua, FT-IR, FT-Raman spectra and ab initio HF and DFT calculations of 2-nitro-and 4-nitrobenzaldehydes. 2008.

69) Lambert, J.B., et al., Introduction to organic spectroscopy. 1987: Macmillan Publishing Company.

Appendix. Supplemental Information

Table S1. Concentrations of surface species on MSN samples.

Sample	AP[a] (mmol/g)	Organic group[b] (mmol/g)
AP-MSN	0.07 ± 0.02	-
Hex(0.5)-AP-MSN	0.07 ± 0.03	0.48 ± 0.01
Hex(0.7)-AP-MSN	0.07 ± 0.01	0.74 ± 0.05
Hex(0.9)-AP-MSN	0.07 ± 0.02	0.94 ± 0.01
Hex(1.0)-AP-MSN	0.06 ± 0.01	1.02 ± 0.02
MeOP-AP-MSN	0.05 ± 0.01	1.25 ± 0.01
CNEt-AP-MSN	0.07 ± 0.02	0.90 ± 0.01

[a]From quantification by reaction with ninhydrin.
[b]Calculated as a difference between AP concentration obtained from ninhydrin quantification and total organics obtained from elemental analysis.

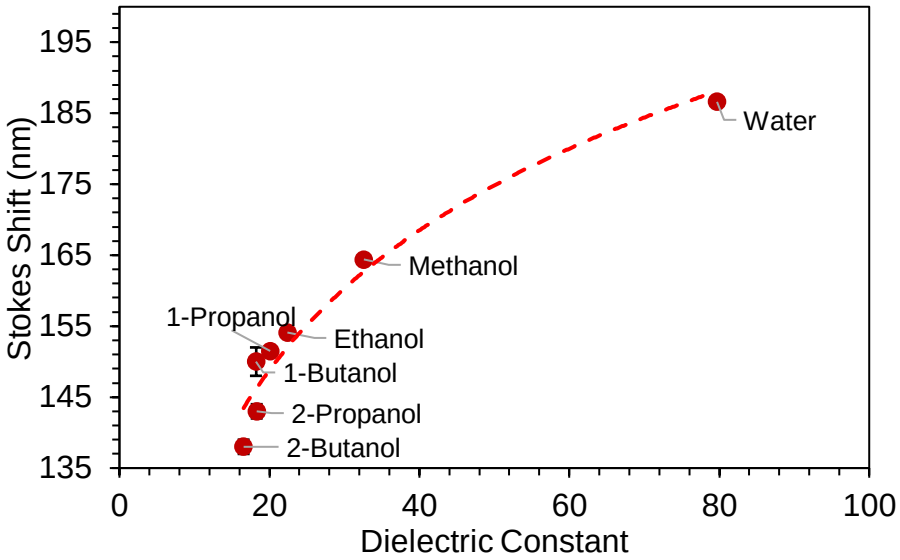

Figure S1. Stokes shifts of Prodan in pure solvents of varying dielectric constants (ε values from Smallwood, I., *Handbook of Organic Solvent Properties*. Elsevier: Burlington, 1996).

Equation S1. Correlation between Prodan's Stokes shift and solvent dielectric constants.

$$Stokes\ Shift = 28.4 \ln(\varepsilon) + 63.7$$

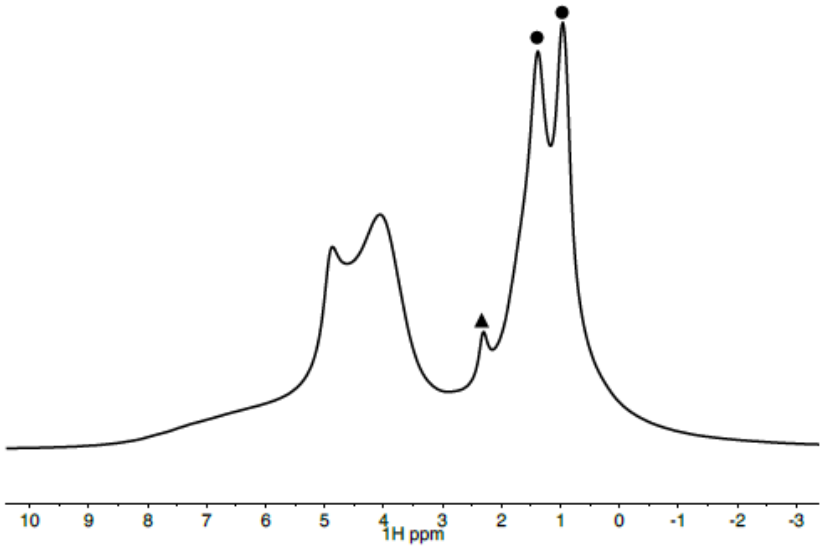

Figure S2. 1H SS NMR spectrum of pre-dried Hex(1.0)-AP-MSN and then exposed to ambient humidity. Signals at 0.9 and 1.4 ppm are assigned to protons in hexyl group (black circles), aminopropyl protons on the alpha carbon can be observed at 2.3 (black triangle) while the other protons overlap with those of hexyl. Peaks at 4.8 and 4.0 ppm correspond to weakly adsorbed water and rapidly exchanging SiOH-(H2O)n species, respectively.[65]

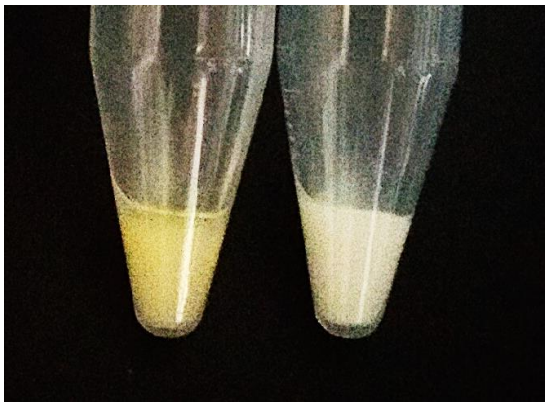

Figure S3. Photographs of the spent AP-MSN (left) and Hex(1.0)-AP-MSN (right) catalysts after reaction in 1-propanol and water, respectively.

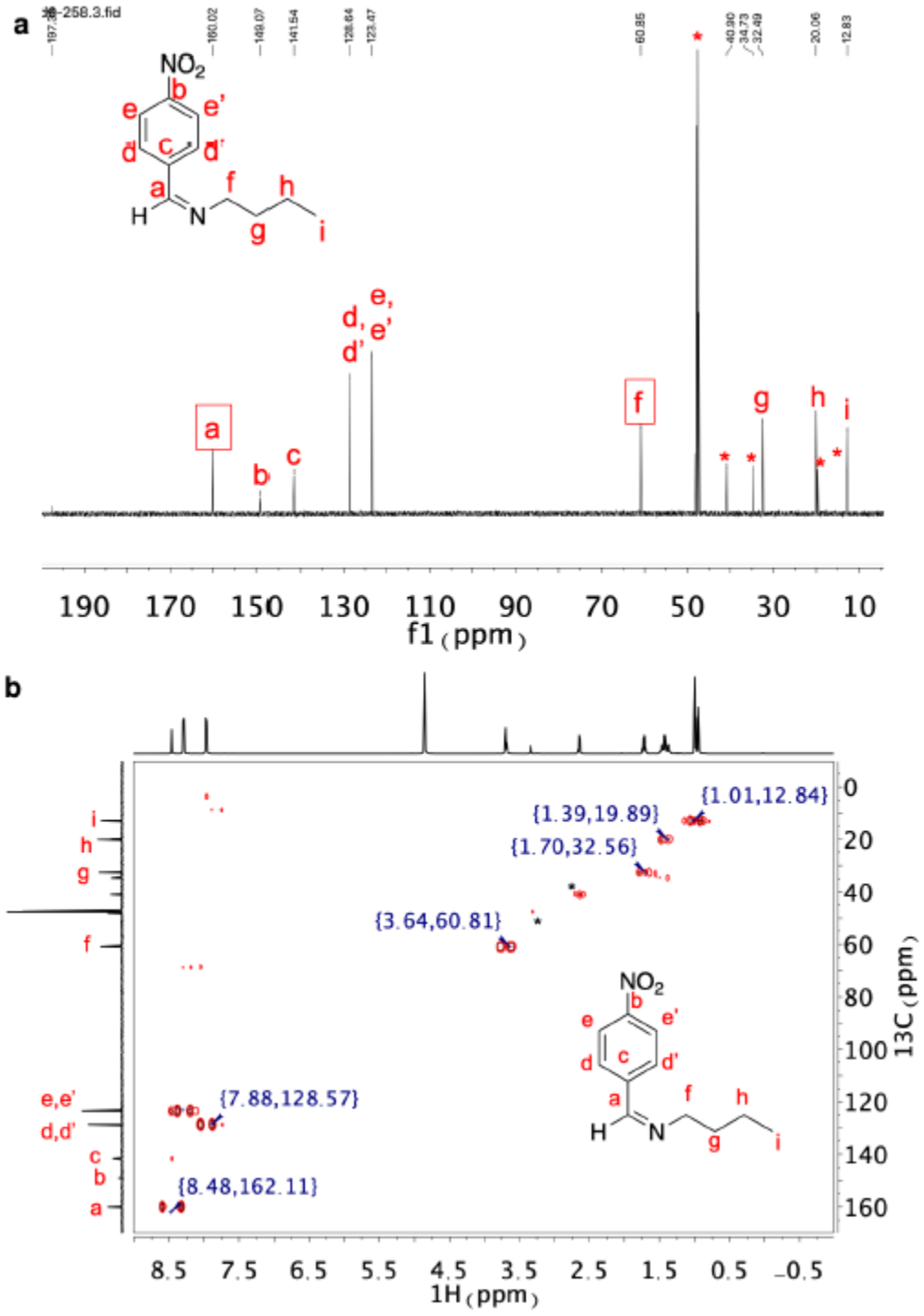

Figure S4. Schiff base model of intermediate **1** obtained by reaction between *p*-nitrobenzaldheyde and butylamine. a) $^{13}C\{^{1}H\}$ NMR spectra b) HSQC (* excess butylamine and solvent), peaks a and f are absent in any of the starting materials.

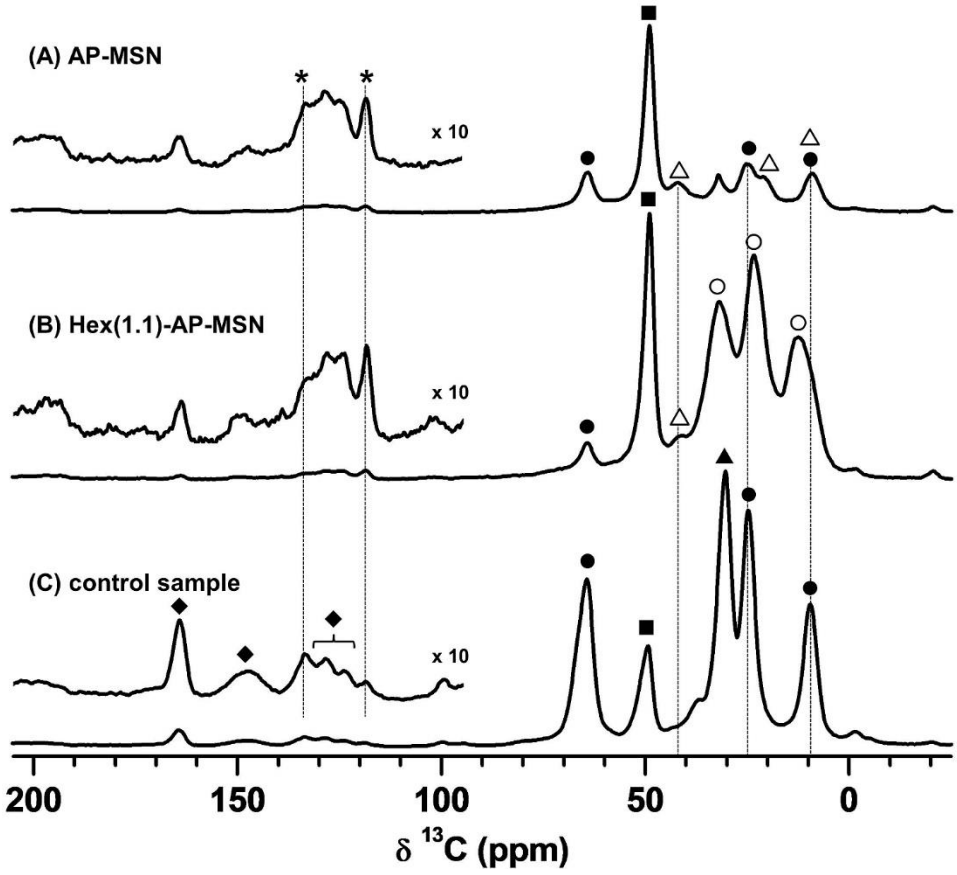

Figure S5. DNP-enhanced $^{13}C\{^{1}H\}$ CPMAS spectra of AP-MSN after reaction in 1-propanol (A), Hex(1.1)-AP-MSN after reaction with water (B), and control sample (C). The spectra were obtained using $\nu_{RF}(^{1}H)$ = 100 kHz during short pulse and heteronuclear ^{1}H decoupling (TPPM), $\nu_{RF}(^{1}H)$ = 85 kHz during CP, $\nu_{RF}(^{13}C)$ = 71 kHz during CP, contact time τ_{CP} = 0.5 ms, recycle delay τ_{RD} = 6.0 (s), number of scans = 800 (A, B), and 3200 (C). The spectra were normalized based on the number of scans and the sample amount packed in the NMR rotor. The control sample was prepared as follows: the mixture containing non-functionalized MSN (60 mg), 1-propanol (3 mL), *p*-nitrobenzaldehyde (60 mg) and acetone (3 mL) was stirred for 24 h at 60 °C, centrifuged, decanted, and washed with methanol. The sample was again centrifuged, decanted, and then dried for 2 h under vacuum. The open triangles (△) and circles (○) represent the signals assigned to AP and Hex, respectively. The filled symbols represent 1-propanol (●), CTAB (▲) , methoxy (CH_3–O–Si) (■) and *p*-nitrobenzaldehyde derivative(s) (♦). Asterisks denote the spinning sidebands.

The spectra of AP-MSN and Hex(1.1)-AP-MSN showed the signals attributed to the functional groups. However, due to the very low loading (~0.06 mmol/g), the AP resonances in the AP-MSN were dominated by additional peaks representing residual solvent, reactants, and products, which remained even after vacuum drying. As expected, in the Hex(1.1)-AP-MSN, the aliphatic spectral region was dominated by the silica-bound hexyl functionalities. Unfortunately, resonances representing the Schiff base products, which we were

able to identify in the heavily AP-loaded MSNs (>1 mmol/g),[66,67] could not be unambiguously discerned in neither sample, as they overlapped with those representing residual *p*-nitrobenzaldehyde derivatives and the spinning sidebands originating from the strong aliphatic peaks. This is not surprising, given that the concentration of Schiff base in these samples is even smaller than AP. However, in addition to elemental analysis, Schiff base formation was indicated by comparing the color of the spent catalysts (Figure S4).

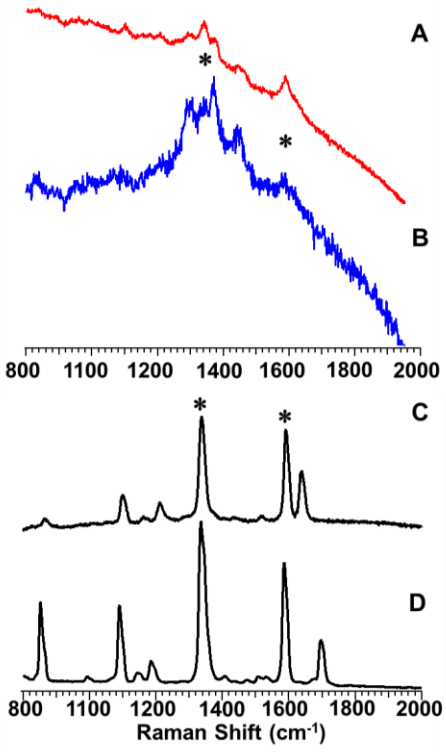

Figure S6. Raman spectra of (A) spent AP-MSN, (B) spent Hex(1.0)-AP-MSN, (C) model Schiff base intermediate obtained from reaction between *p*-nitrobenzaldehyde and butylamine, and (D) *p*-nitrobenzaldehyde. The Raman peaks at approximately 1590 cm^{-1} and 1350 cm^{-1} correspond to aromatic NO_2 antisymmetric and symmetric stretching respectively.[68,69] The y-axis is relative Raman scattering intensity (a.u.).

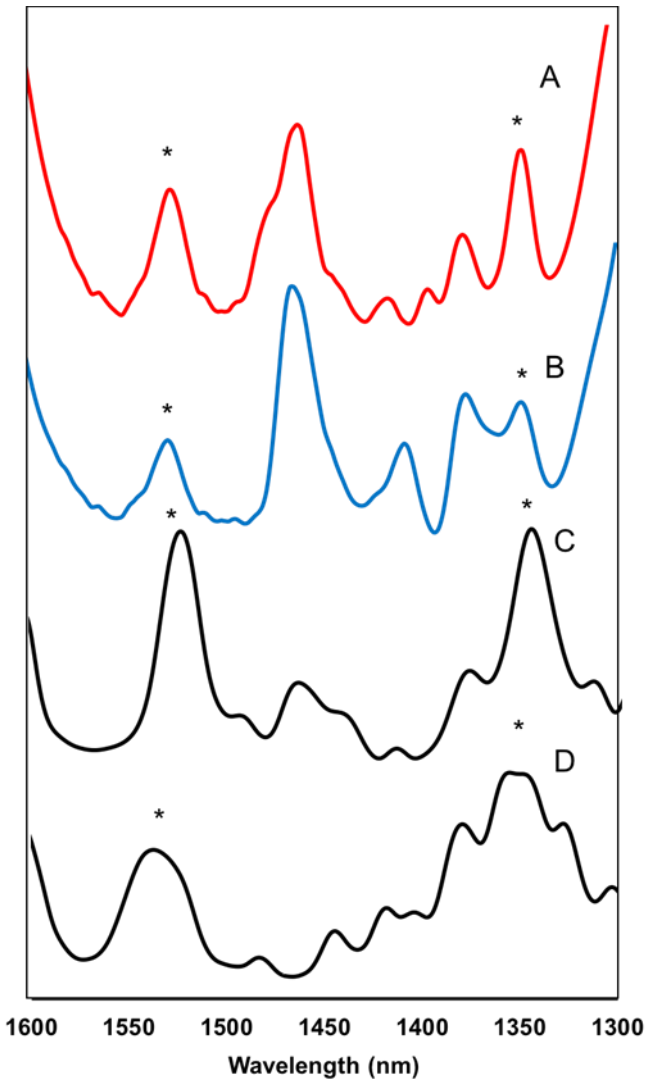

Figure S7. DRIFT-IR spectra in the fingerprint region of (A) spent AP-MSN, (B) spent Hex(1.0)-AP-MSN, (C) Schiff base intermediate from reaction between *p*-nitrobenzaldehyde and butylamine, and (D) *p*-nitrobenzaldehyde. The IR bands at approximately 1520 cm^{-1} and 1350 cm^{-1} correspond to aromatic NO_2 antisymmetric and symmetric stretching, respectively.

Equation S2.
For a bimolecular reaction between two dipoles having no net charge;

$$\ln k \approx \ln k_0 + \frac{3e^2}{8KT}\left(\frac{2}{\varepsilon} - 1\right)\left(\frac{G_A}{b_A^3} + \frac{G_B}{b_B^3} - \frac{G_{\neq}}{b_{\neq}^3}\right)$$

ε	Dielectric constant of the medium
k	Rate constant in a medium of dielectric constant ε
k_0	Rate constant in a medium of dielectric constant ε =1
K	Boltzmann constant
T	Temperature
e	Charge on surface
b	Radius of molecule
G	Charge distribution parameter, proportional to the dipole moment

(A and B correspond to two reactant dipoles and ≠ sign corresponds to the activated complex)
(From: Laidler, K. J.; Landskroener, P. A., The influence of the solvent on reaction rates. *Trans. Faraday Soc.* **1956,** *52*, 200-210)

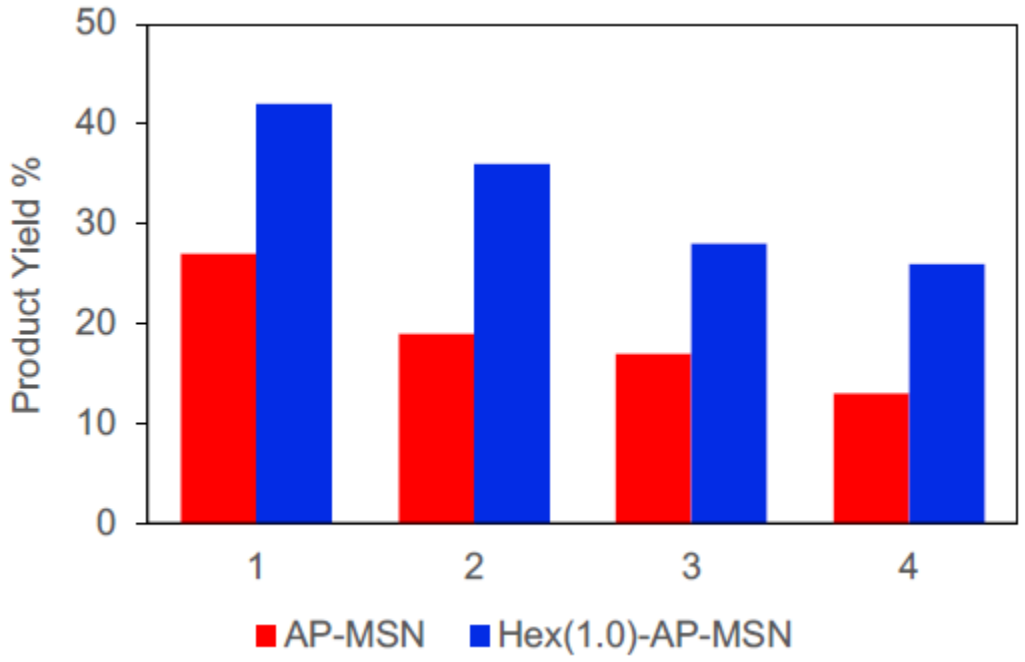

Figure S8. Catalyst recycling for AP-MSN in 1-propanol (red) and Hex(1.0)-AP-MSN in water (blue). Conditions: 60 °C, 12 h, 60 mg catalyst. Catalysts were washed with acetone after each cycle to remove physisorbed unreacted *p*-nitrobenzaldehyde.

Table S2. Catalysis data for AP-MSN in different solvents.

Sample	ε	TOF (h-1)	% Selectivity	
			Aldol	Enone
Water	65.8±1.4	0.58±0.05	95	5
Methanol	32.6	0.43±0.02	77	23
Ethanol	22.4	0.57±0.02	72	28
1-Propanol	20.1	0.65±0.02	73	26
2-Propanol	18.3	0.75±0.07	81	19
2-Butanol	16.6	1.1±0.1	80	20

Reaction conditions:1.0 mol% AP, 60 °C, 8 h.

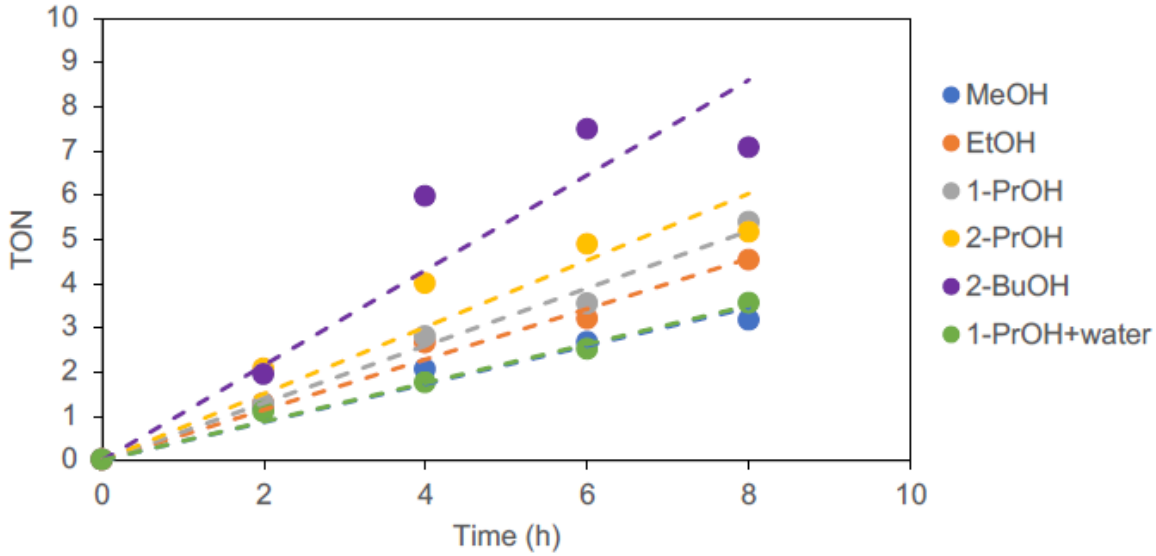

Figure S9. Kinetic plots for AP-MSN in different solvents. Reaction conditions:1.0 mol% AP, 60 °C, 8 h.

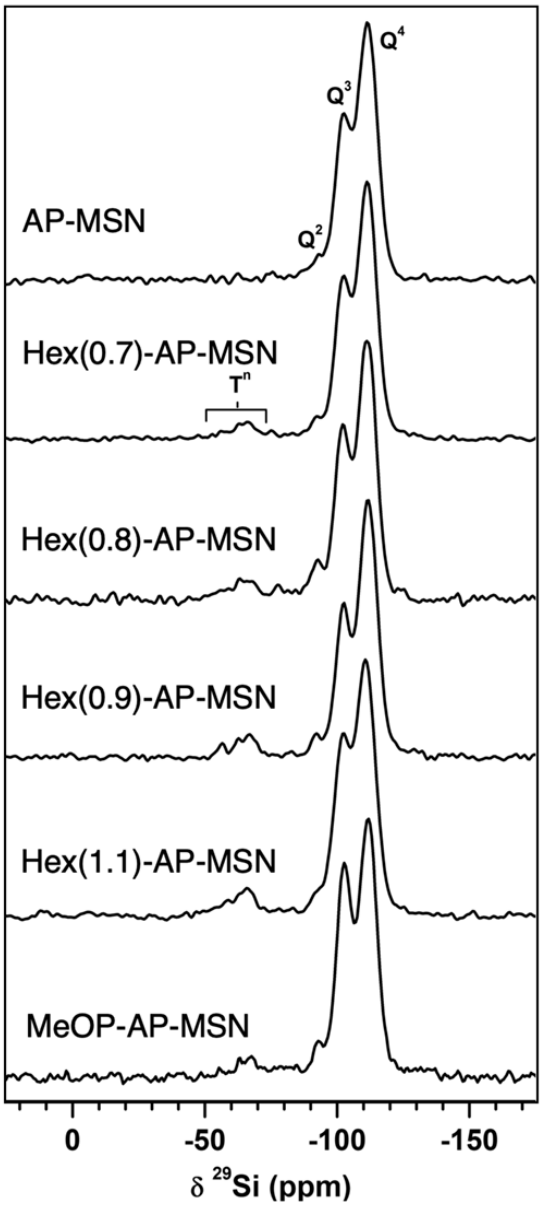

Figure S10. ^{29}Si DPMAS-NMR spectra of different MSN samples. The spectra were obtained using excitation with a single π/2 pulse of 5 μs followed by data acquisition under TPPM ^{1}H decoupling, using the magnitude of the RF magnetic field $\nu_{RF}(^{1}H)$ = 40 kHz. 296 transients were accumulated with a recycle delay of 300 s. The resonances are assigned as follows: Q^4 represents core sites connected to four Si neighbors via siloxane bridges ($(\equiv SiO)_4\mathbf{Si}$), whereas surface sites are denoted as Q^3 ($(\equiv SiO)_3\mathbf{Si}(OH)$) and Q^2 ($(\equiv SiO)_2\mathbf{Si}(OH)_2$). Functionalization with R groups generates the so-called T^n sites, with a general formula ($(\equiv SiO)_n\mathbf{Si}R(OH)_{3-n}$).

Table S3. Surface properties of the functionalized MSN samples.

Sample	SABET (m2/g)	WBJH (nm)	Stokes Shift(nm)	Interfacial Dielectric Constant in Water (εi)
AP-MSN	1234	2.9	186.3±0.3	74.8±0.8
Hex(0.5)-AP-MSN	803	2.0	164.9±0.4	35.3±0.5
Hex(0.7)-AP-MSN	1181	2.4	156.2±0.1	26.0±0.1
Hex(0.9)-AP-MSN	1053	2.3	154.7±0.1	24.6±0.1
Hex(1.0)-AP-MSN	1126	2.6	151.0±0.6	21.6±0.5
MeOP-AP-MSN	1119	2.6	174.0±0.8	49±1.4
CNEt-AP-MSN	1180	2.7	176.6±0.6	53±1.1

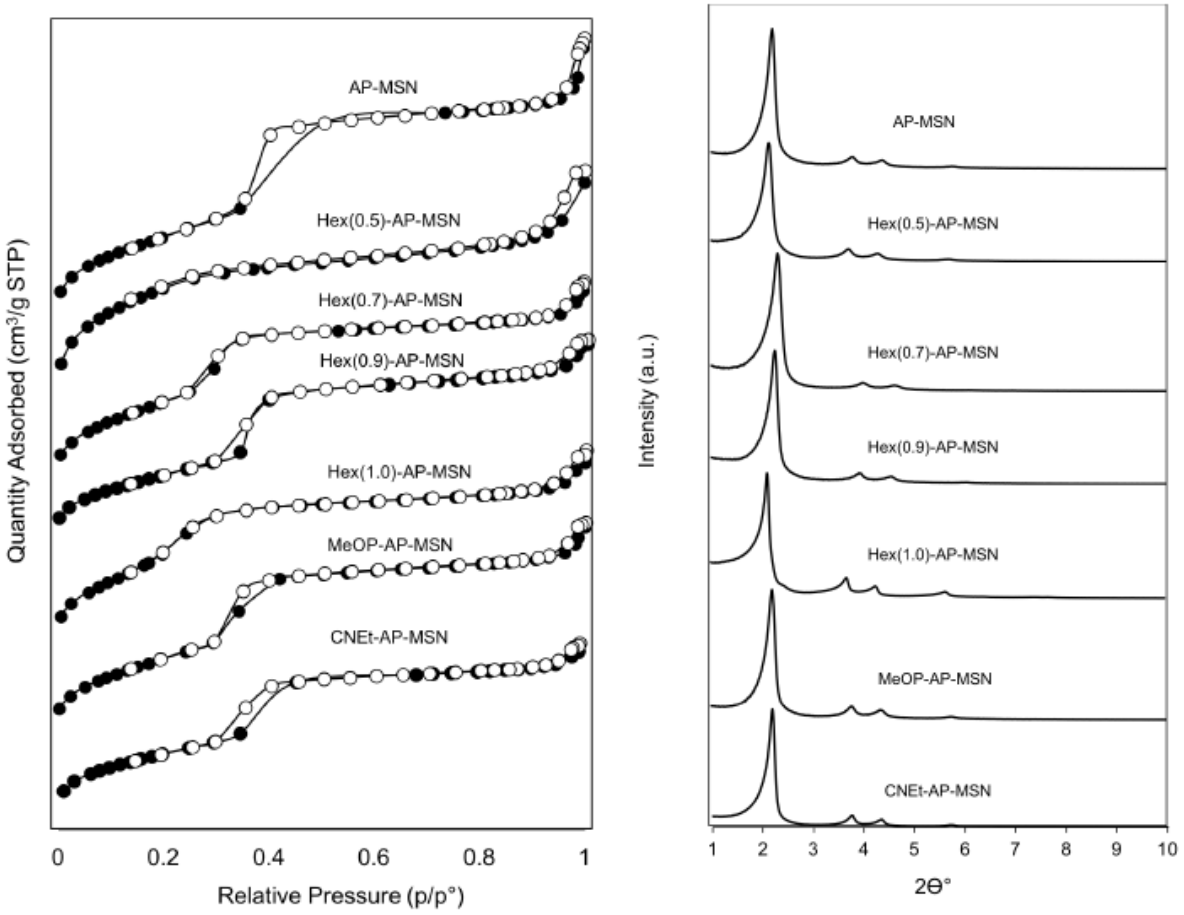

Figure S11. a) Nitrogen physisorption isotherms, and b) powder x-ray diffraction patterns of the functionalized MSN samples.

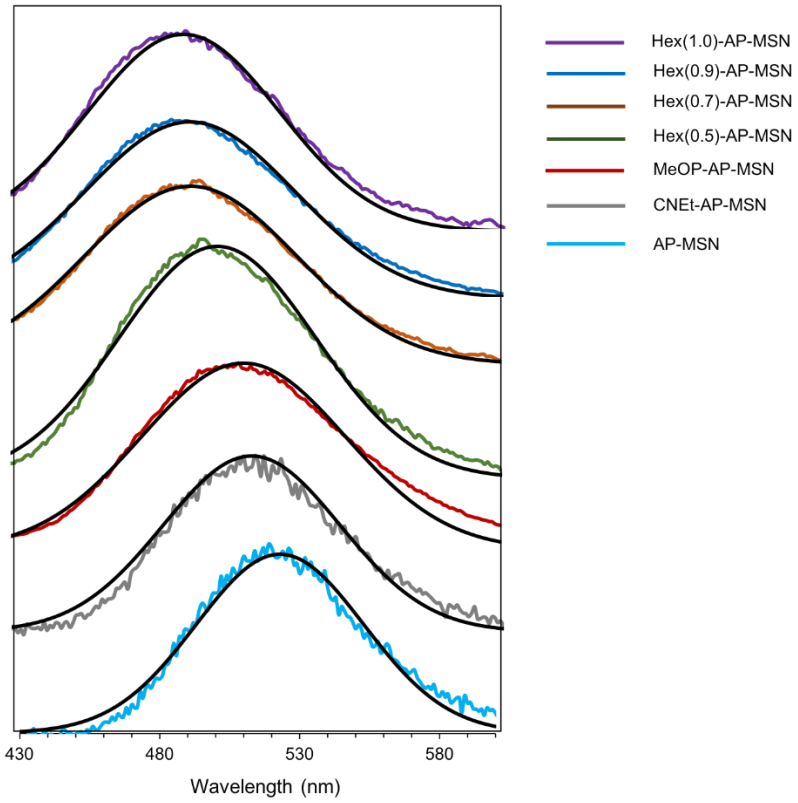

Figure S12. Fluorescence emission spectra of water suspensions of Prodan-loaded MSN samples fitted (black trace) with a Gaussian function in OriginPro. Excitation wavelength: 337 nm, slit widths: 5 nm each.

Table S5. Catalysis data for Hex-AP-MSN in water.

Sample	ε_i	TOF (h^{-1})	% Selectivity	
			Aldol	Enone
AP-MSN	74.8±0.8	0.58±0.05	95	5
Hex(0.5)-AP-MSN	35.3±0.5	1.6±0.1	96	4
Hex(0.7)-AP-MSN	26.0±0.1	1.9±0.2	97	3
Hex(0.9)-AP-MSN	24.6±0.1	2.4±0.1	97	3
Hex(1.0)-AP-MSN	21.6±0.5	3.2±0.2	96	4
MeOP-AP-MSN	48.5±1.4	1.32±0.09	91	9
CNEt-AP-MSN	53.1±1.1	0.68±0.03	94	6
AP-MSN (water+1-propanol)	44[a]	0.44±0.01	72	28

[a]From: Méndez-Bermúdez, J. G.; Dominguez, H.; Pusztai, L.; Guba, S.; Horváth, B.; Szalai, I., Composition and temperature dependence of the dielectric constant of 1-propanol/water mixtures: Experiment and molecular dynamics simulations. *J. Mol. Liq.* 2016, *219*, 354-358. Reaction conditions:1.0 mol% AP, 60 °C, 8 h.

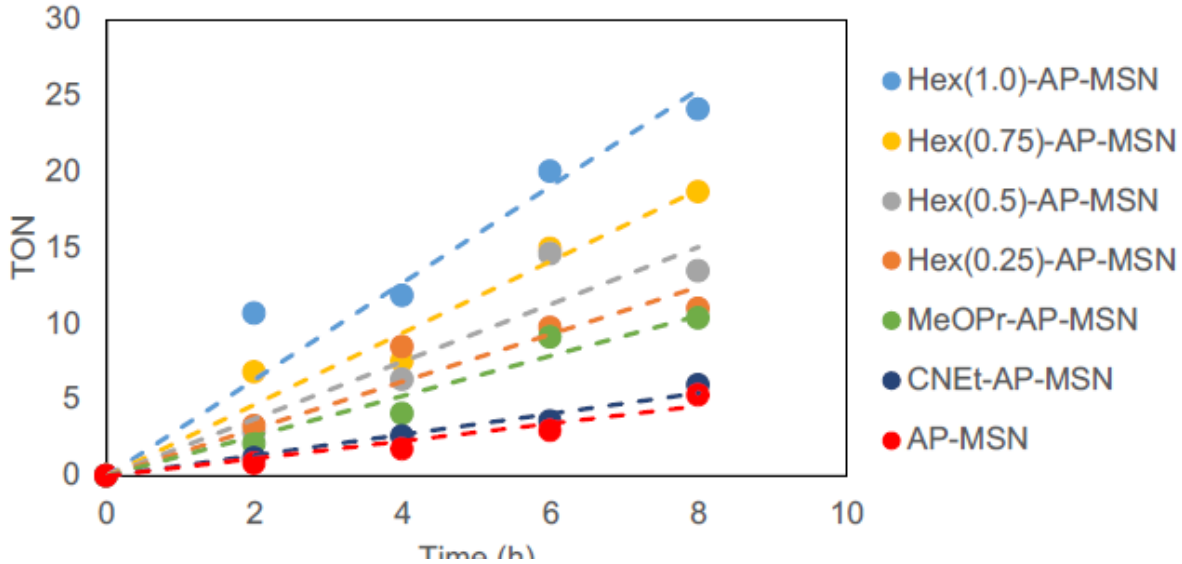

Figure S13. Kinetic plots for substituted AP-MSN in water. Reaction conditions:1.0 mol% AP, 60 °C.

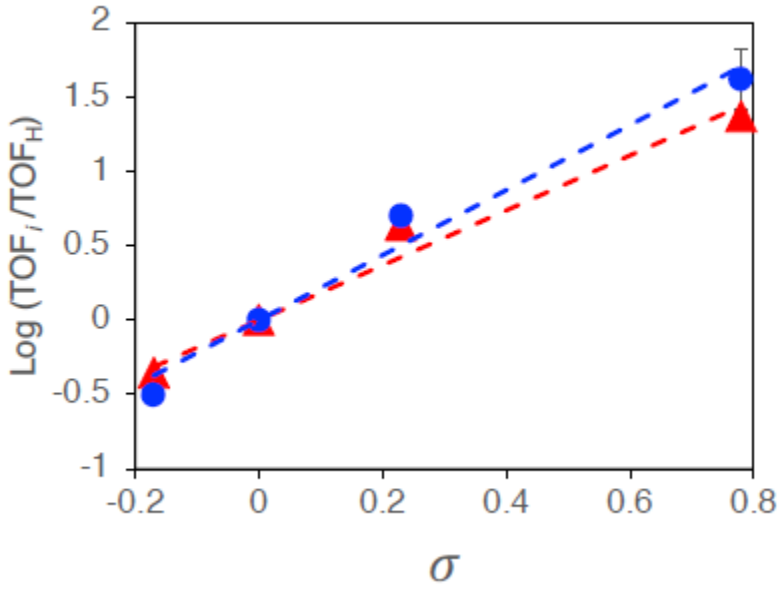

Figure S14. Hammett plots for the aldol reaction between *p*-substituted benzaldehydes and acetone using Hex(1.0)-AP-MSN (blue circles) and AP-MSN (red triangles) as catalysts in water (1.0 mol% amine, 60 °C).

Table S5. Catalysis data for Hammett relationships studies.

Substituent	AP-MSN			Hex(1.0)-AP-MSN		
	TOF (h^{-1})	%Aldol	%Enone	TOF (h^{-1})	%Aldol	%Enone
$-NO_2$	0.58±0.05	95	5	3.2±0.2	96	4
-Br[a]	0.109±0.004	78	20	0.39±0.04	86	14
-H[b]	0.025±0.004	88	12	0.077±0.009	88	12
$-CH_3$[c]	0.011±0.003	82	18	0.024±0.003	83	17

Reaction conditions:1.0 mol% AP, 60 °C. Selectivities reported for [a]8, [b]24 h and [c]72 h.

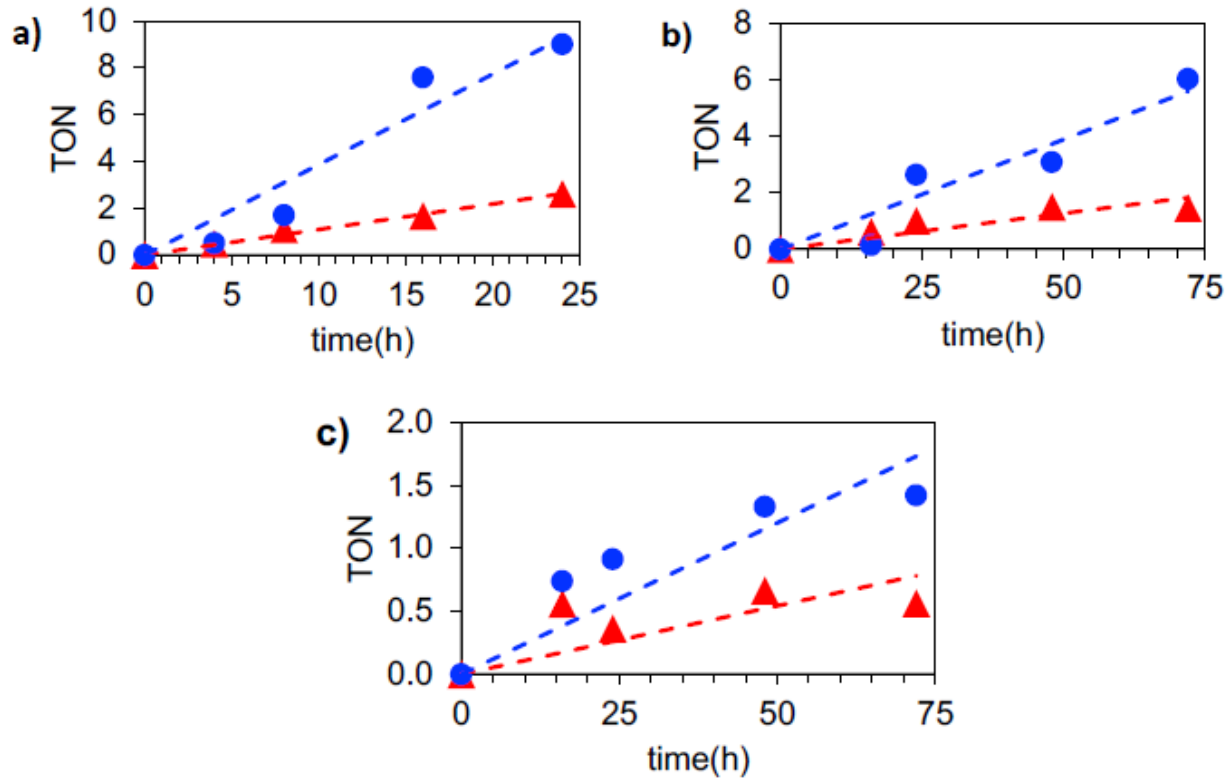

Figure S15. Kinetic plots for Hammett relationship studies. a) *p*-Br-, b) unsubstituted (-H), and c) *p*-methyl- benzaldehyde substrates. The plots for *p*-nitrobenzaldehyde are shown in Figures S12 and S13.

Equation S3.

$$Log\ \frac{TOF}{TOF_0} = \rho\sigma$$

TOF turnover frequency for the substituted benzaldehyde
TOF_0 turnover frequency for the unsubstituted benzaldehyde
ρ reaction constant
σ substituent constant
(From: Hammett, L. P., The Effect of Structure upon the Reactions of Organic Compounds. Benzene Derivatives. *J. Am. Chem. Soc.* **1937,** *59*, 96-103)

Equation S4.

$$\rho = \frac{1}{d^2\,T}\left(\frac{B_1}{\varepsilon} + B_2\right)$$

T temperature,
d the distance from the substituent to the reacting group (carbonyl group)
ε the dielectric constant of the reaction medium
B_1,B_2 constants depend on the reaction and independent of temperature and solvent
(From: Hammett, L. P., The Effect of Structure upon the Reactions of Organic Compounds. Benzene Derivatives. *J. Am. Chem. Soc.* **1937,** *59*, 96-103.

Table S6. Amounts of organosilanes used in the synthesis of functionalized MSN samples.

Sample	Ligand	Volume (µL)
AP-MSN	3-aminopropyltrimethoxysilane	35
Hex(0.5)-AP-MSN	3-aminopropyltrimethoxysilane	35
	hexyltrimethoxysilane	55
Hex(0.7)-AP-MSN	3-aminopropyltrimethoxysilane	35
	hexyltrimethoxysilane	110
Hex(0.9)-AP-MSN	3-aminopropyltrimethoxysilane	35
	hexyltrimethoxysilane	170
Hex(1.0)-AP-MSN	3-aminopropyltrimethoxysilane	35
	hexyltrimethoxysilane	220
MeOP-AP-MSN	3-aminopropyltrimethoxysilane	35
	3-methoxypropyltrimethoxysilane	190
CNEt-AP-MSN	3-aminopropyltrimethoxysilane	35
	2-cyanoethyltriethoxysilane	154

Spectral data of substrates and reaction products.

1. Aldol reaction: p-Nitrobenzaldehyde (PNB) and acetone

PNB: ^{1}H NMR (500 MHz, $CDCl_3$) 10.17 (s, 1H), 8.41 (d, J = 8.5 Hz, 2H), 8.09 (d, J = 8.6 Hz, 2H); *aldol product*: ^{1}H NMR (500 MHz, $CDCl_3$) 8.23 (d, J = 8.7 Hz, 2H), 7.57 (d, J = 8.6 Hz, 2H), 5.29 (dt, J = 7.6,3.4, Hz, 1 H), 2.87 (m, 2H), 2.25 (s, 3H); *enone product*: ^{1}H NMR (500 MHz, $CDCl_3$) 8.28 (d, J = 8.8 Hz, 2H), 7.72 (d, J = 9.0 Hz, 2H), 7.55 (d, J = 16.3 Hz, 1H), 6.84 (d, J = 16.3 Hz, 1H), 2.44 (s, 3H).

2. Aldol reaction: p-Bromobenzaldehyde (PBB) and acetone

PBB: ^{1}H NMR (500 MHz, $CDCl_3$) 9.98 (s, 1H), 7.75 (d, J = 8.5 Hz, 2H), 7.69 (d, J = 8.5 Hz, 2H); *aldol product*: ^{1}H NMR (500 MHz, $CDCl_3$) 7.47 (d, J = 8.4 Hz, 2H), 7.24 (d, J = 8.3 Hz, 2H), 5.12 (dd, J = 8.7,3.6 Hz, 1 H), 2.83 (d, J = 8.7 Hz, 1H), 2.81 (d, J = 3.7 Hz, 1H), 2.20 (s, 3H); *enone product*: ^{1}H NMR (500 MHz, $CDCl_3$) 7.53 (d, J = 8.5 Hz, 2H), 7.44 (d, J = 16.3 Hz, 1H), 7.41 (d, J = 8.5 Hz, 2H), 6.70 (d, J = 16.3 Hz, 1H), 2.38 (s, 3H)

3. Aldol reaction: Benzaldehyde and acetone

Benzaldehyde: ^{1}H NMR (500 MHz, $CDCl_3$) 10.03 (s, 1H), 7.89 (d, J = 7.6 Hz, 2H), 7.64 (t, J = 7.4 Hz, 1H), 7.54 (t, J = 7.5 Hz, 2H), GC-MS, *m/z*: $[M]^+$ (106), 105 $[M-H]^+$, 77 $[M-CHO]^+$, *aldol product*: ^{1}H NMR (500 MHz, $CDCl_3$) 7.64 (m, 2H), 7.38 (m, 2H), 7.32 (m, 1H), 5.20 (dd, J = 9.3, 3.1 Hz, 1 H), 2.93 (dd, J = 17.6, 9.4 Hz, 1H), 2.86 (dd, J = 17.6, 3.2 Hz, 1H), 2.08 (s, 3H); *enone product*: ^{1}H NMR (500 MHz, $CDCl_3$) 7.58 (dd, J = 6.7, 3.0 Hz, 2H), 7.55 (d, J = 16.4 Hz, 1H), 7.43 (m, 3H), 6.76 (d, J = 16.3 Hz, 1H), 2.42 (s, 3H), GC/MS, *m/z*: $[M]^+$ (146), 131 $[M-CH_3]^+$, 103 $[M-COCH_3]^+$ (Quantifications were done with combined NMR and GC-MS data)

4. Aldol reaction: p-Tolualdehyde (PT) and acetone

PT: ^{1}H NMR (500 MHz, $CDCl_3$) 9.97 (s, 1H), 7.81 (d, J = 7.8 Hz, 2H), 7.33 (d, J = 7.8 Hz, 2H), 2.44 (s,3H); GC-MS, *m/z*: $[M]^+$ (120), 119 $[M-H]^+$, 91 $[M-CHO]^+$, *aldol product*: ^{1}H NMR (600 MHz, $CDCl_3$) 7.25 (d, J = 8.0 Hz, 2H), 7.17 (d, J = 7.8 Hz, 2H), 5.13 (dd, J = 9.4, 3.1 Hz, 1 H), 2.89 (dd, J = 17.5,9.4 Hz, 1H), 2.80 (dd, J = 17.5,3.1 Hz, 1H)2.01 (s, 3H); *enone product*: ^{1}H NMR (500 MHz, $CDCl_3$) 7.50 (d, J = 16.2 Hz, 1H), 7.45 (d, J = 8.1 Hz, 2H), 7.21 (d, J = 7.9 Hz, 2H), 6.69 (d, J = 16.3 Hz, 1H), 2.27 (s, 3H),GC/MS, *m/z*: $[M]^+$ (160), 145 $[M-CH_3]^+$, 117 $[M-COCH_3]^+$ (Quantifications were done with combined NMR and GC-MS data)

5. Henry reaction: p-Nitrobenzaldehyde (PNB) and nitromethane

PNB: ^{1}H NMR (500 MHz, Acetone- d_6)) 10.00 (s, 1H), 8.22 (d, J = 9.0 Hz, 2H), 7.99 (d, J = 9.0 Hz, 2H); *condensation product*: ^{1}H NMR (500 MHz, Acetone-D6) 8.04 (m, 2H), 7.60 (d, J = 9.0 Hz, 2H), 5.42 (m, 1 H), 4.68 (dd, J = 12.9,3.4 Hz, 1H), 2.47 (m, 1H); *dehydration product*: ^{1}H NMR (500 MHz, Acetone-d_6) 8.11 (d, J = 8.7 Hz, 1H), 8.03 (m, 2H), 7.92 (d, J = 10.8 Hz, 2H), 7.89 (d, J = 6.7 Hz, 1H)

6. Vinylogous aldol reaction: p-Nitrobenzaldehyde (PNB) and 3-butan-2-one

PNB: ^{1}H NMR (500 MHz, $CDCl_3$) 10.17 (s, 1H), 8.41 (d, J = 8.5 Hz, 2H), 8.09 (d, J = 8.6 Hz, 2H); *condensation product*: ^{1}H NMR (500 MHz, $CDCl_3$) 8.23 (d, J=8.8 Hz, 2H), 7.59 (d, J = 8.9 Hz, 2H), 6.06 (d, J=1.1 Hz, 1 H), 5.71 (d, J = 1.1Hz, 1H), 4.87 (s, 1H), 2.39 (s, 3H)

7. Homogeneous model of intermediate 1: (p-nitrobenzaldehyde reacted with butylamine, N-butyl-1-(4-nitrophenyl)methanimine)
^{1}H NMR (600 MHz, Methanol-d_4) 8.46 (s,1H), 8.29 (d, J=8.1 Hz, 2H), 7.96 (d, J=8.1 Hz, 2H), 3.68 (td, J=7.4 Hz, 1.49Hz, 2H), 1.72 (m, 2H), 1.43 (m, 2H), 0.95 (t, 3H)

Solvent purification procedures.

Commercial anhydrous 1-propanol and anhydrous 2-butanol were used without any further purification. Acetone, methanol, ethanol and 2-propanol were treated with CaH_2 at room temperature overnight. Acetone (b.p. 56 °C), and methanol (b.p. 64 °C) were then purified using simple distillation from the CaH_2-containing mixture. Ethanol (b.p. 78 °C) and 2-propanol (b.p. 82 °C) were purified from the CaH_2-containing mixture using fractional distillation column. The solvents were sealed and used for reactions immediately after distillation.

CHAPTER 7. GENERAL CONCLUSION

This dissertation focused on using Raman spectroscopy and SAX microscopy to investigate the properties of plants and biological materials, and collaborative research works on inorganic materials and catalysts. Raman and mass spectrometry imaging were used to understand the downstream effects of gene silencing at the cellular level within maize. Raman spectroscopy was deemed suitable as a fast alternative method for determining the rosmarinic acid concentration and relative abundance in spearmint to assess the optimal plant harvest time. Furthermore, the compatibility of CdSe/ZnS QDs with SAX imaging for biological materials was evaluated.

In Chapter two, the spatial dependence of gene silencing at the cellular level was studied with a multimodal Raman and mass spectrometry imaging method for maize. The cellular level spatial correlation from VIGS was measured with Raman and mass spectrometry imaging and compared to an average percentage in the mRNA levels obtained via qRT-PCR. We determined the leaf regions that showed a visible mosaic phenotype had a reduced carotenoid expression but were not eliminated. From *pds* silencing via VIGS, the Raman and mass spectrometry imaging techniques revealed complementary information. We concluded that *pds* silencing reduced the downstream carotenoid Raman signal and therefore increased the phytoene mass spectrometry signal. The multimodal imaging approach shows great utility to spatially characterize the distribution of biochemical changes that result from gene silencing in plant tissues. We propose this approach can be used in addition to a gene analysis method such as qRT-PCR to confirm gene silencing.

In Chapter three, a fast and straightforward analysis method using Raman spectroscopy was developed to find the relative abundance of rosmarinic acid within spearmint leaves. The

peak area for cellulose and rosmarinic acid were used for a ratio analysis to determine the rosmarinic acid abundance. The spatial distribution of rosmarinic acid abundance between trichomes and epidermal cells was divulged for KI110 and Native plants. Overall, the rosmarinic acid abundance in trichomes was at least 6-fold higher than in epidermal cells. No statistical difference was observed for rosmarinic acid abundance between leaf ages except in the KI110 and Native trichomes. A calibration model to obtain rosmarinic acid concentration using only Raman spectroscopy was developed with partial least squares regression. This calibration model can be directly used with no sample preparation on *in situ* plants and has the potential for in-field analysis.

In Chapter four, the CdSe/ZnS core/shell inorganic semiconductor QD compatibility as a luminescent probe for SAX microscopy and biological materials was investigated. The QDs revealed two behaviors dependent upon the sample environment. Once the QDs were in a dried state the photoluminescence saturation was achieved with excitation power densities less than 1 kW/cm^2. An average of 40% spatial resolution improvement was achieved with a third-harmonic signal of the dried QDs; however, no improvement was observed between the fundamental frequency (10 kHz) and second-harmonic frequency (20 kHz) constructed images. For QDs dispersed in an aqueous environment, the excitation power densities needed to extract the second harmonic signal were greater than 200 kW/cm^2, which is unfavorable for live cellular studies. The HeLa cells labeled with the QDs in an aqueous environment also manifested this phenomenon for higher harmonics, but the fundamental frequency was obtained. A promising route for biological SAX imaging may be attained using QDs tailored to have longer lifetimes at lower power densities, which are more favorable for cellular studies in aqueous environments.

In Chapters, five and six, fluorescence microscopy and Raman spectroscopy characterized a series of inorganic materials and catalysts.